

## Orbital dynamics in the vicinity of contact binary asteroid systems

Feng, Jinglang

**DOI**

[10.4233/uuid:d8d5d083-5027-4468-9cb2-21a691dcdc72](https://doi.org/10.4233/uuid:d8d5d083-5027-4468-9cb2-21a691dcdc72)

**Publication date**

2016

**Document Version**

Final published version

**Citation (APA)**

Feng, J. (2016). *Orbital dynamics in the vicinity of contact binary asteroid systems*. [Dissertation (TU Delft), Delft University of Technology]. <https://doi.org/10.4233/uuid:d8d5d083-5027-4468-9cb2-21a691dcdc72>

**Important note**

To cite this publication, please use the final published version (if applicable).  
Please check the document version above.

**Copyright**

Other than for strictly personal use, it is not permitted to download, forward or distribute the text or part of it, without the consent of the author(s) and/or copyright holder(s), unless the work is under an open content license such as Creative Commons.

**Takedown policy**

Please contact us and provide details if you believe this document breaches copyrights.  
We will remove access to the work immediately and investigate your claim.

# **Orbital Dynamics in the Vicinity of Contact Binary Asteroid Systems**

## **Proefschrift**

ter verkrijging van de graad van doctor  
aan de Technische Universiteit Delft,  
op gezag van de Rector Magnificus prof. ir. K.C.A.M. Luyben;  
voorzitter van het College voor Promoties,  
in het openbaar te verdedigen op  
woensdag 8 juni om 12:30 uur

Door

**Jinglang FENG**

School of Astronautics,  
M.Sc., Northwestern Polytechnical University,  
Xi'an, China  
geboren te Henan, China

This dissertation has been approved by the  
promotor: Prof. dr. ir. P.N.A.M. Visser  
copromotor: Ir. R. Noomen

Composition of the doctoral committee:

Rector Magnificus,	voorzitter
Prof. dr. ir. P.N.A.M. Visser,	promotor
Ir. R. Noomen,	copromotor

Independent members:

Prof. dr. E.K.A. Gill,	Technische Universiteit Delft
Prof. ir. K.F. Wakker,	Technische Universiteit Delft
Prof. dr. D.J. Scheeres,	University of Colorado
Prof. dr. G. Gómez,	University of Barcelona
Dr. H. Hussmann,	Institute of Planetary Research/DLR Berlin
Prof. dr. ir. J.M. Hoekstra	Technische Universiteit Delft, reservelid



Keywords: Orbital dynamics, Contact binary asteroid system, Stability, Resonance

Printed by: Ridderprint

Front & Back: Image credit: ESA/Rosetta/MPS (comet 67P)

Copyright © Jinglang Feng

ISBN 978-94-6299-355-6

An electronic version of this dissertation is available at

<http://repository.tudelft.nl/>.

All rights reserved. No parts of this publication may be reproduced, stored in a retrieval system, or transmitted, in any form or by any means, electronic, mechanical, photocopying, recording, or otherwise, without the prior written permission of the author.

# Contents

<b>Acknowledgements .....</b>	<b>I</b>
<b>Summary .....</b>	<b>III</b>
<b>Samenvatting .....</b>	<b>VII</b>
<b>Chapter 1 Introduction .....</b>	<b>1</b>
1.1 Classification .....	1
1.2 Exploration.....	4
1.3 Dynamical Environment .....	6
1.4 Current Research Status .....	10
1.5 Related Methods .....	16
1.6 Research Motivation.....	18
1.7 Thesis Outline .....	20
<b>Chapter 2 Numerical analysis of orbital motion around contact binary asteroid system .....</b>	<b>21</b>
2.1 Introduction.....	21
2.2 Dynamical Model.....	24
2.3 Contact Binary System 1996 HW1 .....	26
2.3.1 Zero-velocity Curves and EPs.....	26
2.3.2 Location and Stability of EPs at Different Values of $\mu$ and $\delta$ .....	28
2.4 POs in the vicinity of the EPs .....	30
2.4.1 Lyapunov Orbits.....	31
2.4.2 Halo Orbits.....	33
2.4.3 Vertical Orbits.....	34
2.5 Orbital Motion around the System.....	37
2.5.1 Equatorial Orbits.....	37
2.5.2 Effect of Parameter $\delta$ on Retrograde A and B Orbits .....	39
2.5.3 Resonant Orbits .....	41
2.6 Conclusions .....	43
<b>Chapter 3 Orbital Motion in the Vicinity of the Non-collinear Equilibrium Points.....</b>	<b>45</b>
3.1 Introduction.....	45



## Contents

3.2	Dynamical Model .....	48
3.3	Non-collinear EPs and their Stability .....	50
3.4	Motion Around the Stable Non-collinear EPs.....	52
3.4.1	The Third-order Analytical Orbits .....	53
3.4.2	Numerical Verification .....	55
3.5	Motion around the Unstable Non-collinear EPs.....	58
3.5.1	Linear Feedback Control .....	59
3.5.2	Controlled Motion Tracking the Third-order Analytical Orbit .....	59
3.5.3	Controlled Motion Tracking the Numerical Orbit.....	62
3.6	Conclusions .....	64
<b>Chapter 4 Modelling and Analysis of Periodic Orbits Around a Contact Binary Asteroid .....</b>		<b>69</b>
4.1	Introduction .....	69
4.2	Shape Model and Geometrical Potential.....	72
4.3	Spherical Harmonics Expansion.....	73
4.3.1	Method .....	73
4.3.2	Verification .....	74
4.4	Hamiltonian of the Truncated System.....	77
4.4.1	Single-averaged Model .....	78
4.4.2	Double-averaged Model .....	79
4.5	Poincaré Sections of the Single-averaged Model .....	83
4.6	Periodic Orbits .....	87
4.6.1	POs in the Single-averaged Model.....	87
4.6.2	POs in the Non-averaged Model .....	87
4.6.3	POs of Faster Rotating Asteroid.....	91
4.7	Conclusions .....	95
<b>Chapter 5 1:1 Ground-track resonance in a uniformly rotating 4<sup>th</sup> degree and order gravitational field.....</b>		<b>99</b>
5.1	Introduction .....	99
5.2	Dynamical Modelling .....	101

## Contents

5.2.1	Hamiltonian of the system .....	101
5.2.2	1:1 Resonance.....	101
5.3	Primary Resonance .....	103
5.3.1	EPs and Resonance Width .....	103
5.3.2	Numerical results.....	103
5.4	Second Resonance .....	108
5.4.1	The location and width of $\mathcal{H}_{reson2}$ .....	109
5.4.2	1996 HW1 .....	110
5.4.3	Vesta .....	115
5.4.4	Betulia.....	119
5.5	The Maximal Lyapunov Characteristic Exponent of Chaotic Orbits .....	122
5.6	Conclusions.....	124
<b>Chapter 6 Conclusions and Recommendations .....</b>		<b>129</b>
6.1	Conclusions.....	129
6.2	Recommendations.....	132
<b>References.....</b>		<b>135</b>
<b>Curriculum Vitae .....</b>		<b>143</b>
<b>List of Author's Publications.....</b>		<b>145</b>



# Acknowledgements

First of all, I would like to give my thanks to Prof. Boudewijn Ambrosius and Prof. Bert Vermeersen for offering me the opportunity to pursue my PhD in the Astrodynamics and Space Missions group. This group covers a broad range of topics about space, e.g. orbital mechanics, orbit determination, solar system exploration and dynamics, reentry systems and geosciences, which made me really feel working in a 'space environment'. Furthermore, I appreciate your encouragements and support for me to come through the hard times, as well as your inspiring discussions for helping me shaping my PhD topic.

My thanks go to my promotor Prof. Pieter Visser, whose critical feedback improved the quality of my research and made sure that it is good enough for submission. In addition, thanks for offering me an extension that allowed me to finish this dissertation efficiently. Many thanks I like to give to Ron Noomen, my daily supervisor. I really appreciate your effort that has been put in during the past years. It is impossible to count the number of meetings we have had and how many iterations of the draft of the papers and this dissertation came from you. I would also like to give you special thanks for guiding me patiently through my PhD and for the freedom to address my curious problems.

I give my thanks to Prof. Karel Wakker for insightful discussions about averaging techniques. I would like to thank Erwin for your help on dealing with the control problem and on sharing some tricks in MATLAB programming. Thanks go to Wouter for the help on parallel computing in MATLAB, which really saved me a huge amount of time to get the results. My thanks also go to Ernst, who had a helpful discussion with me about the fundamentals of gravity that impressed me a lot. Bart and Dominic, I appreciate your help on managing my spherical harmonics expansion from a coding and theoretical point of view, respectively. Hermes, your insightful discussions and also your book about solar system dynamics were really helpful. Thanks go to Joao for always sharing with me newly published journal papers about asteroids. I would like thank Jeroen and Kartik for your explanations of many basic aspects about asteroids at the very beginning of my PhD and for leaving me with a huge collection of useful literature. Tatiana, I appreciate your company in the office, since we always worked 'face to face' and very often moved 'shoulder by shoulder'. Your optimistic and open attitude towards work and life had a very positive influence on me undoubtedly. Mao, Black and Haiyang, thank you for being accompanies as compatriots. Thanks go to Tim and Jacco for translating the summary and propositions of this dissertation from English to Dutch. Thanks go to my other colleagues, Jose, Daphne, Eelco, Marc, Svenja, Carlos, Gunther, Bas, Loic, Sowmini, Wim and also to our secretary Relly, as you provided me an open and friendly environment and shared

## Acknowledgements

your experiences. I will always miss the scientific and unscientific discussions at our lunch table, in the office and after we enjoyed the movies (Gravity, Interstellar, The Martian, Star Wars) together. The time spent with you guys, your passion for space and the open culture in The Netherlands really assisted me to explore my personality and myself.

Furthermore, I give my gratitude to Prof. Jianping Yuan for your support and encouragements for pursuing my PhD about astrodynamics in The Netherlands. Thanks go to Prof. Xiyun Hou for your detailed help to figure out the headache problems. I'm very grateful to Prof. Daniel Scheeres, for your discussions about my research at conferences and providing constructive suggestions that helped me treat the problem from a higher level. I would like to thank Prof. Gerard Gómez for providing me your expertise and feedback about my research. I also give my thanks to Dr. Stella Tzirti who helped me on Poincaré sections method. Thanks go to Dr. Xiaodong Liu for the timely help on detailed technical problems and also for your professional discussions about asteroids. Thanks also go to Jian Guo for the insightful suggestions and encouragement, especially at the hardest time during my PhD. Prof. Leonid Gurvits, thank you for providing me the up-to-date information about deep space exploration and about the up-to-date Chinese space science programs.

To my dear friends Ying Li, Weiling Zheng, Xuexue Chen, Zhenpei Wang, Le Li, Xi Zhang, Lixia Niu, thank you all for sharing my ups and downs during the past years. Thank you for being there on my journey to develop into a mature person.

I give my thanks to the Chinese Scholarship Council (CSC) for funding me to do this research.

The committee members of my PhD are also greatly acknowledged, for the devotion of time to read my dissertation and for being a part of my defense ceremony.

Finally, I give my thankfulness to my parents and my brother. Thank you for your love and support. You have always been my strong background and have given me the determination to persist on the way to my destinations.

Delft, The Netherlands, January 2016

Jinglang Feng

# Summary

In recent years, space missions with the destination of small solar system bodies have become more and more important. For missions to such kind of bodies, one of the biggest challenges comes from the perturbation on the spacecraft's motion by the highly irregular gravitational field. Therefore the dynamical environment in the vicinity of these bodies needs to be characterized. Many studies about orbital dynamics around single asteroids and binary asteroid systems have been performed.

With this background, my PhD research focuses on orbital dynamics in the vicinity of contact binary asteroids, which is estimated to constitute 10-20% of all small solar system bodies (including comets). This kind of bodies is also characterized by their highly bifurcated shape. In August 2014, ESA's Rosetta arrived at its target comet 67P/Churyumov-Gerasimenko after a ten years journey in space. The comet, impressing many by virtue of its shape with two lobes in contact, belongs to contact binary bodies. In addition, in October 2015, the images sent back by NASA's New Horizons revealed that Pluto's tiny moon Kerberos also consists of two lobes. These discoveries provide good support for the selection of this topic. In addition, this characterization also can give us hints on the formation and evolution of such small solar system bodies. Specifically, the objective of this research is to perform a systematic study on the orbital motion around contact binary asteroid systems.

For the purpose of this study, first, the gravitational field needs to be modeled. There are three main methods: (1) the spherical harmonics expansion; (2) the polyhedron model that approximates the body with large numbers of polyhedra, given the detailed shape model of the body is available; (3) geometric shape models whose closed-form potentials can be usually obtained. To fulfill the purpose for a systematic study about the dynamical environment around contact binary bodies, the configuration of a combination of a sphere and an ellipsoid is applied. The gravitational field can be obtained in the closed-form potential from the two components and the equations of motion can be built in the rotating frame.

Actually, this model is analogous to that of the Restricted Three Body Problem (RTBP), with the same common definition of the mass ratio, which is the ratio of mass of the smaller component to the total mass of the two main bodies. However, an important difference is that the ratio of gravitational acceleration to centrifugal acceleration equals one for the two main bodies of the RTBP, but it can be any number for our model. With the rigid-body assumption, for two contacted spheres, there is compression between the two lobes if the ratio is larger than one, and stretching occurs for ratios smaller than one. The value of one indicates that there is no internal force between the two. For contacted ellipsoid and sphere, this ratio deviates slightly from the critical value one, due to the non-spherical potential of the ellipsoid component. Therefore, our model can be viewed as a generalization of the RTBP. By varying the

values of these two ratios in our model, contact binary asteroids with this kind of shape and with a wide range of physical parameters can be covered. Due to this similarity, the methods that apply to the RTBP for characterizing orbital motion are obtained and examined for the first time in application to contact binary asteroid system 1996 HW1, which is known to be the most bifurcated asteroid.

Accordingly, equilibrium points (EPs) and their stability are first obtained and examined for HW1. By varying the values of the two ratios in the model, their influence on the location and stability of the EPs is examined. Second, Lyapunov, Halo and vertical (the motion is mostly along the  $z$ -direction) families of periodic orbits (POs) are obtained for HW1. The fast rotation of the asteroid has a stabilizing effect on equatorial orbital motion. Orbits that are in resonance with the rotation of the asteroid are also obtained, and they can provide good coverage of the polar region of the body for spacecraft observations.

In the RTBP, there is a well-known Richardson third-order analytical solution of Halo orbits obtained with the Lindstedt-Poincaré (LP) method. In this research, the same method is applied to obtain the third-order analytical solution of orbital motion in the vicinity of the non-collinear EPs with non-spherical gravitational field. This solution is tested against numerical simulations and it proves to have a very good accuracy for moderate-amplitude orbital motion. With the increase of orbital amplitude and rotation rate of the asteroid, the solution becomes less accurate, due to the application of linear expansion of the LP method.

By expanding the closed-form gravitational potential into spherical harmonics to degree and order 4, frozen orbits can be obtained by applying the Lagrange Planetary Equations (LPE). They have large eccentricities and are available within limited inclination ranges, which are quite different from those of the planets. This is due to the large  $C_{20}$  and  $C_{40}$  terms resulting from the highly irregular gravitational field. In addition, families of 3-dimensional POs around the entire asteroid in the original full gravitational field are obtained, although most of them prove to be unstable. The fast rotation of the asteroid is also found to have a stabilizing effect on the 3-dimensional orbital motion.

At the end of this research, the underling dynamics of this 1:1 ground-track resonance (i.e. the 1:1 commensurability between the mean motion rate of the spacecraft and the rotation rate of the asteroid) is studied with a two degree of freedom (2-DOF) Hamiltonian, which consists of a main part of a 1-DOF Hamiltonian and a perturbation part of a 2-DOF Hamiltonian. For a generalization of this study, the spherical harmonics up to degree and order 4 are taken into account. The characteristics of three asteroids (Vesta, 1996 HW1 and Betulia) are used. The high-order harmonics are found to introduce new EPs and asymmetry to the dynamics. The perturbation Hamiltonian, which is treated as a second resonance, gives rise to chaos in the phase space. The extent of chaos is estimated by the distance between the two

## Summary

resonances and their respective strengths, also for orbits at different combinations of eccentricity and inclination. The near polar orbits are found to be robust against the perturbation Hamiltonian. With maximum Lyapunov Characteristic Exponents, it is found that the more irregular the gravitational field, the stronger the resulting chaos.

Finally, the methods developed in this thesis can also be applied to the study of orbital dynamics in binary asteroid systems, planet-moon systems and binary star systems.





# Samenvatting

In de afgelopen jaren zijn ruimtemissies naar kleine hemellichamen in ons zonnestelsel in populariteit toegenomen. Voor missies naar dergelijke lichamen vormt het zeer grillige gravitatieveld één van de grootste uitdagingen. Daarom is het belangrijk de dynamische omgeving van deze lichamen te beschrijven. In het verleden zijn al vele studies uitgevoerd naar baandynamica rond enkele planetoïden en planetoïdeparen.

Met deze studies als basis, richt mijn promotieonderzoek zich op baandynamica in de nabijheid van dubbel-planetoïden (dat wil zeggen: twee planetoïden die elkaar raken), die naar schatting 10-20% uitmaken van de totale populatie van kleine lichamen in ons zonnestelsel (inclusief kometen). Dit soort lichamen wordt gekenmerkt door hun sterk tweeledige vorm. Na een ruimtereis van tien jaar, in augustus 2014, arriveerde ESA's Rosetta bij zijn doel, de komeet 67P/Churyumov-Gerasimenko. De komeet wekte grote belangstelling door zijn tweeledige vorm, karakteristiek voor dubbel-planetoïden. Bovendien onthulden foto's van NASA's New Horizons in oktober 2015 dat Kerberos, de zeer kleine maan van Pluto, een soortgelijke tweeledige vorm heeft. Daarnaast kan deze karakterisatie ons inzicht verschaffen in het vormingsproces en de levensloop van dergelijke kleine hemellichamen. De hierboven beschreven ontdekkingen leveren een goede basis voor dit promotieonderzoek, dat zich het best laat omschrijven als een systematische studie van de baanbewegingen rond dubbel-planetoïden.

De eerste, voorbereidende stap in dit onderzoek omvat het modeleren van het gravitatieveld. Hiervoor worden de volgende modellen aangewend: (1) de sferisch harmonische benadering; (2) een benadering van het lichaam door grote aantallen polyeders, gegeven een gedetailleerd ruimtelijk model; (3) geometrische ruimtelijke modellen. Voor de systematische studie van de dynamische omgeving van dubbellichamen wordt gebruik gemaakt van een model bestaande uit een bol en een ellipsoïde die aan elkaar verbonden zijn. Het complete gravitatieveld kan worden verkregen uit de gesloten vorm van de potentiaal van de twee delen, en de bewegingsvergelijkingen kunnen in het roterende assenstelsel worden beschreven.

Dit model is in de kern analoog aan het Beperkte Drielichamenprobleem (Restricted Three Body Problem, RTBP), waarbij dezelfde definitie van de massaverhouding wordt gebruikt, namelijk de ratio van de massa van het kleine hoofdlichaam en de som van de massa's van de twee hoofdlichamen. Een belangrijk verschil is echter dat, waar de gravitatieversnelling en de middelpuntvliedende versnelling voor de twee hoofdlichamen altijd gelijk zijn in een RTBP, de ratio tussen deze twee versnellingen een willekeurige waarde kan aannemen in ons model. In het geval van een ratio groter dan één worden de twee delen samengedrukt, terwijl een waarde kleiner dan één een staat van uitrekking impliceert. Een ratio gelijk aan één duidt op een situatie zonder interne krachten tussen de twee delen. In dit opzicht kan ons model worden gezien als

een generalisatie van het RTBP. Door de waarden van de twee hierboven besproken ratio's te variëren, kunnen dubbel-planetoïden met een dergelijke vorm en een groot bereik aan fysieke eigenschappen gemodelleerd worden. Door de overeenkomsten tussen ons model en het RTBP kunnen methoden voor baanbewegingsbeschrijvingen uit het RTBP ook op ons model worden toegepast. In dit onderzoek geldt dubbel-planetoïde 1996 HW1 als archetype, aangezien deze bekend staat als de duidelijkst tweeledige planetoïde.

Overeenkomstig de methode worden allereerst de evenwichtspunten (equilibrium points, EP) van HW1 verkregen en onderzocht. Door de twee verhoudingen in het model te variëren wordt hun invloed op de locatie en de stabiliteit van de EPs in kaart gebracht. Ten tweede worden Lyapunov, Halo en verticale (de beweging is grotendeels in  $z$ -richting) families van periodieke banen (Periodic Orbits, PO) om HW1 beschreven. De snelle draaiing van de planetoïde heeft een stabiliserend effect op de equatoriale baanbeweging. Bovendien worden banen die resoneren met de draaiing van de planetoïde afgeleid, die een goede dekking van de polen van het lichaam kunnen verschaffen.

In het RTBP wordt een bekende Richardson derde orde analytische oplossing beschreven voor Halo banen die verkregen zijn volgens de Lindstedt-Poincaré methode. In dit onderzoek wordt dezelfde methode toegepast om een derde orde analytische oplossing te vinden voor de baanbeweging in de buurt van niet-collineaire EPs met een niet-bolvormig gravitatieveld. Uit een vergelijking met numerieke simulaties blijkt dat deze oplossing een grote nauwkeurigheid heeft voor baanbewegingen van gemiddelde amplitude. De nauwkeurigheid neemt af met toenemende amplitude, alsmede met toenemende draaisnelheid van de planetoïde, door het gebruik van een lineaire benadering in de LP-methode.

Door de gesloten vorm van de gravitatiepotentiaal te benaderen met sferische harmonischen tot en met graad en orde 4 kunnen zgn. frozen orbits worden verkregen door de Lagrange Planetaire Vergelijkingen toe te passen. Deze banen hebben een grote excentriciteit en zijn slechts beschikbaar voor een beperkt inclinatiebereik, dat sterk verschilt van dat rond planeten. Dit komt door de grote  $C_{20}$  en  $C_{40}$  termen, veroorzaakt door het zeer grillige gravitatieveld. Daarnaast worden families van driedimensionale POs geformuleerd rond de hele planetoïde in het originele, gehele gravitatieveld, al blijken de meeste daarvan instabiel. De snelle draaiing van de planetoïde blijkt ook een stabiliserend effect te hebben op de driedimensionale baanbeweging.

Aan het eind van dit onderzoek wordt de achterliggende dynamica van deze 1:1 resonantie nader onderzocht met een Hamiltoniaan met twee vrijheidsgraden (two degrees of freedom, 2-DOF), bestaande uit een 1-DOF Hamiltoniaan als basis en het verstoringsdeel van een 2-DOF Hamiltoniaan. Ter generalisatie van deze studie worden de sferische harmonischen tot de vierde graad en orde in ogenschouw

genomen. De kenmerken van drie planetoïden (Vesta, 1996 HW1 en Betulia) worden gebruikt. De hoge orde harmonischen worden gebruikt om nieuwe EPs en asymmetrie te introduceren in de dynamische vergelijkingen. De verstorings-Hamiltoniaan, die wordt verwerkt als een secundaire resonantie, veroorzaakt chaos in de faseruimte. De mate van chaos wordt benaderd door de afstand tussen de twee resonanties en hun respectievelijke sterkte, ook voor banen met verschillende combinaties van excentriciteit en inclinatie. De bijna-polare banen blijken robuust te zijn tegen de verstorings-Hamiltoniaan. Met maximale Lyapunov Karakteristieke Exponenten wordt aangetoond dat hoe grilliger het gravitatieveld is, hoe groter de resulterende chaos is.

Ten slotte kunnen de methoden die in deze proefschrift worden ontwikkeld ook worden toegepast op de bestudering van baandynamica in dubbel-planetoïdesystemen, planeet-maan systemen en dubbel-stersystemen.



# Chapter 1 Introduction

---

Missions to asteroids and comets have received much attention in recent years. For the design of such missions an important issue is to identify the dynamical environment for a spacecraft orbiting around the asteroid, which usually possesses an irregular gravitational field. This brings a great challenge for mission design. From a more general perspective, uncovering the motion of arbitrary particles in such a dynamical environment also gives us a clue on the evolution history of the body itself. In this thesis, the orbital dynamics of a spacecraft (or a particle) in the vicinity of contact binary asteroids, characterized by highly bifurcated gravitational fields, is studied. The challenge comes from the resulting highly perturbed environment.

In this introduction chapter, a classification of asteroids is presented first to give some basic insight into the spatial distribution, composition and shape of asteroids. Then the status of asteroid exploration is reviewed, which reflects the significant science return of asteroid missions. The dynamical environment around asteroids related to mass, density, rotation rate and gravitational field is summarized. The current research status and methods related to the study of orbital dynamics about asteroids are reported. Finally, the research questions of our study are formulated and the structure of the thesis is presented.

## 1.1 Classification

Asteroids are small rocky bodies, the majority of which probably consists of collisional fragments of the original planetesimals (Bottke, 2002) with the exception of a number of spherical and big ones, e.g. Vesta whose self-gravity is strong enough to retain an almost spherical shape. Typically, most of them do not have any signature of volatile activities. However, occasional activities have been observed on a number of them recently, which makes the distinction between asteroids and comets (characterized by volatiles and lower density) less obvious. Asteroids can be classified according to their spatial distribution, chemical composition and shape.

### Spatial Distribution

According to their location in the Solar System, asteroids in general can be classified as Near-Earth asteroids (NEAs), Main Belt asteroids (MBAs), Trojans, Centaurs and Trans-Neptunian objects (Bottke, 2002), as shown in Fig.1. NEAs with a perihelion radius of less than 1.3 AU have significant interaction with the inner planets and are often mentioned as Near Earth Objects (NEOs). A special kind of NEAs is known as the Potentially Hazardous Asteroids (PHAs), which have a possibility of impacting Earth. MBAs range from large-sized bodies (e.g. Ceres and Vesta) to dust located between the orbits of Jupiter and Mars, in which region the larger bodies are

continually eroded and broken up into smaller bodies. Trojans are asteroids that are captured at Sun-major planets' L4 and L5 Lagrange points and are in 1:1 resonant motion with the major planet. Centaurs are in orbit between Jupiter and Neptune. Trans-Neptunian objects (TNOs) are bodies that travel beyond the orbit of Neptune, which include the Kuiper Belt Objects (KBOs) as well as some quite large bodies, e.g. Pluto (demoted to be a dwarf planet in 2006) and Charon, one of its moons.

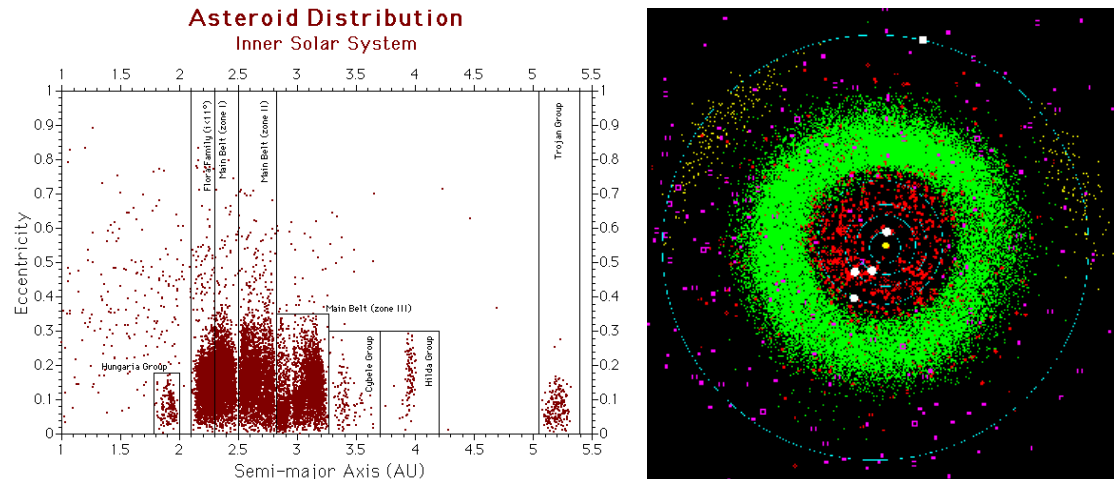


**Figure 1** Left: Distribution of semi-major axes and eccentricities for asteroids in the inner Solar System. Source: <http://www.reocities.com/szygywjp/HarmonicSpec.html>. Right: A snapshot of asteroids and comets in the inner Solar System. The white dots are planets with the outermost one being Jupiter; the red and green dots represent NEAs and MBAs, respectively; the yellow dots illustrate the Trojans; the purple ones represent comets. Source: [www.uwgb.edu/dutchs/planets/asteroid.htm](http://www.uwgb.edu/dutchs/planets/asteroid.htm).

## Composition

The chemical composition of asteroids is quite diverse, ranging from rock and metal to hydrated minerals and organics. According to spectrophotometric observations, asteroids can be divided into different types by their compositions of different minerals, e.g. A-type with olivine and metal, B-, C-, F-, G-type with silicate chondrules, D-, P-, T-type with silicates and carbon etc.. (Nelson et al., 1993).

Among them, C-, S- and M-types are the three main categories (Bottke, 2002). C-type asteroids are carbon-rich and have spectra similar to that of carbonaceous chondrite meteorites. They are extremely dark, with a low geometric albedo. They are abundant in the outer region of the MBAs, and Ceres is a typical example. S-type asteroids have a metallic composition, and are primarily made of silicates, and are relatively bright. They are the most common class in the inner MBAs and also constitute a large fraction of NEAs. It is believed that they are associated with the ordinary chondrites, which are the most abundant meteorites that can be found on Earth's surface. C- and S-type asteroids are estimated to account for about 75% and 17% of all known asteroids, respectively. The third-largest population is the M-type asteroids, which are bright and metal-rich. They contain large amounts of iron and

nickel and dominate the middle MBAs. These three classes of asteroids are interesting candidates for future mining missions.

## Shape

Depending on their shape, asteroids can be divided into single asteroids, contact binary asteroids and binary asteroid systems. The single asteroid is a body with one component typically of irregular shape (like a potato), e.g. 433 Eros and 25143 Itokawa. Contact binaries consist of two components that are in physical contact and are referred to as bifurcated bodies, e.g. 4769 Castalia (Hudson, 1994) and 1996 HW1 (Magri et al., 2011). Including comets, these kinds of bodies are estimated to constitute approximately 20% of all small Solar System bodies (Harmon et al., 2010). Rosetta's targeted comet 67P/Churyumov-Gerasimenko (denoted as 67P) was found to be a contact binary accretion of two distinct objects (Massironi et al., 2015). Finally, a binary asteroid system always includes a primary asteroid accompanied by a secondary orbiting body, e.g. system 1999 KW4 (Scheeres et al., 2006, Ostro et al., 2006) on system Ida-Dactyl, and constitutes approximately 15% of the NEAs (Pravec et al., 2006). Examples of the different asteroid types are displayed in Fig.2.

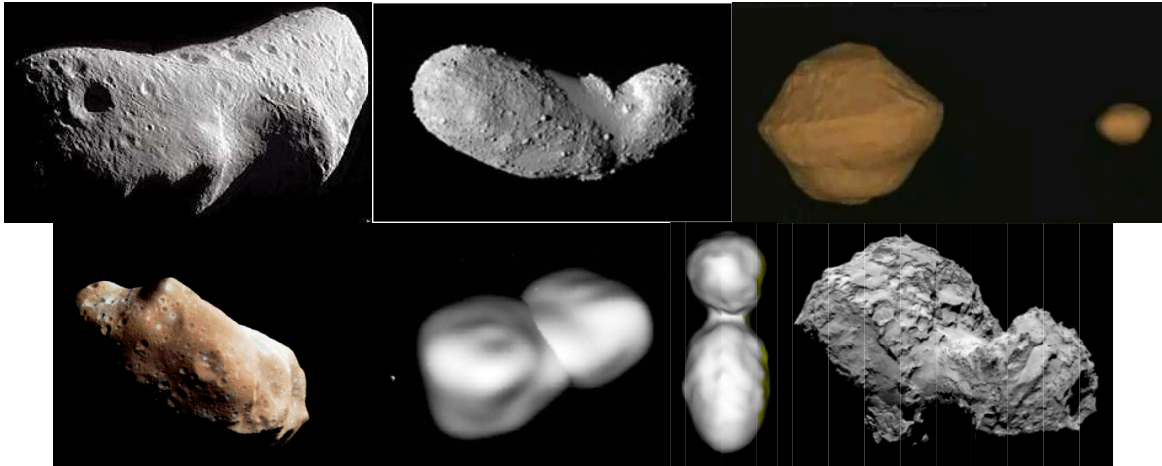


**Figure 2** Top: 433 Eros (NASA/JPL); 25143 Itokawa (JAXA); system 1999 KW4 (NASA/JPL and Ostro). Bottom: system Ida-Dactyl (NASA/JPL); 4769 Castalia (NASA/JPL); 1996 HW1 (Magri et al., 2007); 67P (ESA/Rosetta/MPS).

From radar observations, the NEA Castalia was found to have a bifurcated shape consisting of two lobes in contact. In recent years, more and more contact binaries have been observed. Combining radar images and spectra, 1996 HW1 was revealed to have a contact binary shape and to be the most bifurcated near-Earth asteroid ever studied. It is a  $3.8 \times 1.6 \times 1.5$  km elongated body with a rotation period of 8.76243 hours. The two lobes are very similar to a big ellipsoid and a small sphere, respectively. This shape model is the most bifurcated one among all the potential models of asteroids (Magri et al., 2011) and therefore will serve as our prime study object in the entire research performed in this thesis. Comet 67P probably has a comparable or even more bifurcated shape than asteroid 1996 HW1.



More examples of contact binaries are given in Fig.3. According to photometric observations in the infrared and visible regions in 1977, the Trojan asteroid 624 Hektor was estimated to be the largest and most elongated known Trojan and was considered to have a dumbbell shape with two spherical lobes (Hartmann and Cruikshank, 1978). It was found to have a small satellite later on (Marchis et al., 2014). In 2005, asteroid 2005 CR37 was found as a candidate contact binary with an extremely bifurcated shape of two round lobes with almost similar size (Benner et al., 2006). Images from the Arecibo observatory in Puerto Rico revealed that Comet 8P/Tuttle has a 10 km long nucleus of a highly bifurcated shape with two components, consisting of a larger sphere and a smaller elongated body (Harmon et al., 2010). From Doppler radar images, asteroid 4486 Mithra was found to be an extremely slow rotator and to have an irregular and significantly bifurcated body; it was recommended as a contact binary body with an initial shape model of two identical ellipsoids (Brozovic et al., 2010). According to the up-to-date images sent back by NASA's New Horizons spacecraft in October 2015, Pluto's tiny moon Kerberos was shown to have a double-lobed shape, with the larger lobe approximately 8 km across and the smaller lobe 5 km across. It is speculated that Kerberos was formed from two icy bodies bumping into each other (NASA, 2015a).

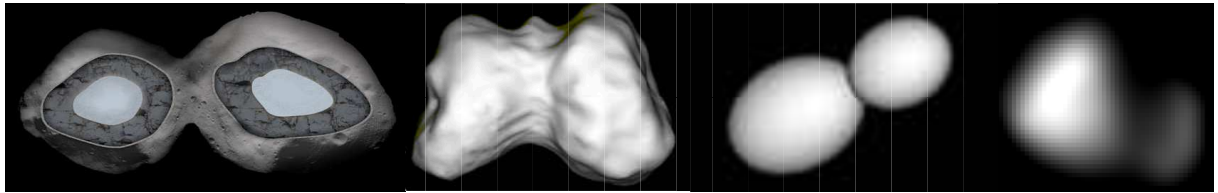


**Figure 3** Shape models of contact binaries: 624 Hektor (Marchis et al., 2014), 4486 Mithra (Brozovic et al., 2010), 8P/Tuttle (Harmon et al., 2010), Kerberos (NASA/JHUAPL/SwRI).

## 1.2 Exploration

In early days, asteroids (or small Solar System bodies) could only be detected and measured by ground-based observations, i.e. optical and radar observations. With these techniques, the body's overall size, shape, spin period, brightness and orbit could be estimated albeit with limited accuracies.

Since the 1990s, the technique of distant flybys was not only developed but actually practiced by various space agencies, which was a big step in determining the total mass and better constraining the density of an asteroid, e.g. the Galileo (NASA) flyby of Ida in 1993 (Belton et al., 1996) and the Chang'e (CNSA) flyby of Toutatis in 2012 (Zhao et al., 2015). Later on, rendezvous missions, e.g. NASA's NEAR and Dawn and JAXA's Hayabusa, followed and explored asteroids in detail at close distance, greatly advancing our understanding of the small bodies. During the orbiting of asteroid Eros in 2000, NEAR determined its gravity, mass, spin rate and orientation, density and internal mass distribution (Veeverka et al., 2000). In 2005, Hayabusa characterized

Itokawa's surface thoroughly and provided the observations to develop a precise model of its shape (Fujiwara et al., 2006). Samples of regolith were collected with this spacecraft's touchdown on the asteroid and were returned to Earth in June 2010. Dawn observed Vesta's surface geology on small scale and revealed through the image-derived shape model and the mass determined by radio-metric tracking that the asteroid is indeed a differentiated body (Russell et al., 2012). Bright spots (most of them within impact craters) on Ceres and also haze above some of these spots were observed by Dawn. These spots were found to be probably made of salt, ice and frozen water (Nathues et al., 2015).

Although Rosetta is an ESA mission targeted at a comet, it is to be mentioned here. After having travelled for ten years, Rosetta had a rendezvous with its target comet 67P in June 2014 and released the lander Philae for the first landing on a comet even in October. The comet is revealed to have the highly irregular shape of a contact binary body (Sierks et al., 2015), which is analogous to the shape model that this thesis focuses on. The two lobes were identified as two distinct bodies (Massironi et al., 2015). The orbiter is still in operation and uncovered more and more scientific aspects of the body, especially during the comet's approach to its perihelion in August 2015. The lander provided images of the comet with unprecedented details.



**Figure 4** Left: artist's impression of Rosetta and Philae at the comet. *Credit: ESA/ATG medialab; Comet image: ESA/Rosetta/NavCam; Right: jet event at 67P's perihelion. Image: ESA/Rosetta/MPS.*

The OSIRIS-REx asteroid sample return mission was approved as the next New Frontiers mission of NASA. The target is Bennu, which is one of the PHAs and which is estimated to have a relatively high probability (approximately 0.0041%) of impacting Earth around 2175 (NASA, 2016). This mission is scheduled to be launched in September 2016 and will arrive at its target in 2018 (Lauretta et al., 2015). After characterization of the body's physical and chemical properties, samples will be returned to Earth in 2023. It will provide crucial information to develop an impact mitigation mission in the future. Recently, a new mission named AIDA (Asteroid Impact and Deflection Assessment) was proposed with binary asteroid 65803 Didymos as its destination (Abell et al., 2012). AIDA is collaboration among ESA, DLR, NASA

and others. At the binary's close encounter with Earth in October 2022, an asteroid impactor developed by NASA will be sent to the secondary body with the purpose to change its orbital period around the primary. This will provide the opportunity for the observing spacecraft sent by ESA to gather data on the deflection and on the potential alteration of other physical properties of the system.

Instead of capturing a complete asteroid and putting it into orbit around the Moon, in April 2013 NASA decided to design a mission to drag a boulder from a large asteroid and send the rock in orbit around the Moon around 2025, which is called the Asteroid Redirect Mission (NASA, 2015b). The Orion spacecraft with solar electric propulsion will descend on a large asteroid which still needs to be selected and capture a boulder with a robotic arm. Then it will transfer to a stable retrograde orbit around the Moon. Two astronauts in the crew vehicle will go aboard the Orion spacecraft and conduct spacewalks to investigate the captured boulder before returning samples to Earth. This mission also aims at testing key techniques for future manned Mars missions.

In 'China's Deep-space Exploration to 2030' program (Yongliao et al., 2014), a sample-return mission to main belt asteroid Ceres is proposed, with the science objectives of characterizing its topography, structure and composition, detecting the asteroids weathering layers and the interaction between the solar wind and the asteroid, and finally uncovering the origin and evolution of the body as well as the potential origin of life.

### **1.3 Dynamical Environment**

The dynamical environment of an asteroid is important not only for understanding the characteristics and evolution of the body, but also for characterizing the orbital motion of a spacecraft around it. Closely related physical properties are mass, density, shape and rotation rate, since they determine the gravitational field in which the spacecraft moves and typically also the rotation frame in which the dynamics is studied.

#### **Mass and Density**

An asteroid's mass can primarily be determined from its perturbation on neighboring (encountering or orbiting) spacecraft (NEAR), and from the interaction between asteroids (Ceres and Vesta) (Britt et al., 2002). These methods mainly take advantage of the irregularities in the trajectory or orbit of the perturbed objects, i.e. a spacecraft or another asteroid. In addition, the mass can also be determined from the orbital motion of the natural satellites by Kepler's third law, e.g. the system Ida-Dactyl. Among them, the most accurate method relies on tracking the motion of a spacecraft orbiting around the asteroid.

The volume of asteroids is often estimated from infrared astronomical observations. The bulk density can then be calculated by dividing mass over volume and generally

ranges between 2-3 g/cm<sup>3</sup>, with small fractions of lower or higher values. Only a limited number of asteroids' bulk density estimates are available. Occasionally, the internal structure of asteroids can be directly characterized by in-situ investigations by space missions (Takeuchi, 2009).

## Rotation

The rotation of an asteroid in general also has a great influence on the orbiting spacecraft. The rotation rate is observed to have a relationship with the size of the body (Pravec et al., 2002), as shown in Fig.5. As can be seen, most asteroids are uniformly rotating with rates ranging from extremely fast (rotation period of 1.3 min) to extremely slow (rotation period of 2400 hours).

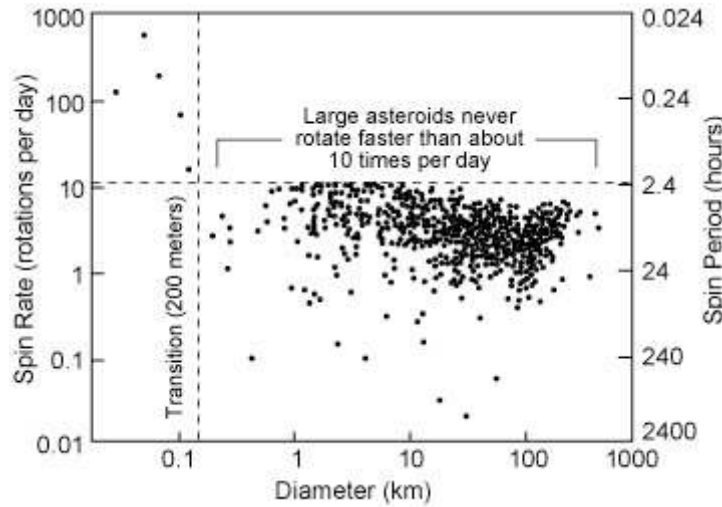


**Figure 5** Spin rate of asteroids as function of diameter (Pravec et al., 2002).

Large asteroids (diameter  $D > 40$  km) have a maximum spin rate of about 2.4 hours. This is probably due to the fact that most of these asteroids are rubble piles that fall apart if the bodies spin too fast. Very small-sized asteroids ( $D < 0.15$  km) can rotate extremely fast (the period of the fastest known rotator 2000 DO<sub>8</sub> is 1.3 min only) and are concluded to be primarily made of monolithic rocks. Normal small-sized bodies ( $0.15 \text{ km} < D < 10 \text{ km}$ ) are shown to be strengthless bodies with a rubble pile or a shattered interior structure. In addition, binary asteroid systems with fast rotating primaries were found as a significant subset among NEAs.

A small fraction of asteroids exhibits a non-principal-axis rotation, where the rotation axis shows an additional precession and nutation, which was termed 'tumbling'. Such a body demonstrates quasi-periodic motion with more than one non-constant fundamental frequency. Toutatis is one example that was observed by Ostro et al. (1999) with such kind of rotation. Based on the flyby data of Chang'e-2, its two major periods were confirmed to be 5.38 days for the principal rotation and 7.40 days for the precession with an amplitude of up to 60° (Zhao et al., 2015), in agreement with the results from Ostro. This kind of body is not considered in this thesis.

## Gravitational Field

The irregular shape of an asteroid induces a complex gravitational field, which is responsible for a strongly perturbed dynamical environment compared with that of the planets. Because of such irregularities, it can be very challenging to design and maintain suitable spacecraft orbits around such bodies. Even more, the spacecraft might escape from or impact on the asteroid due to the large perturbations. The gravitational field can typically be represented by three different methods.

#### (a) Spherical harmonics expansion

The gravitational potential can be expressed as an infinite spherical harmonics series expansion. The Laplace equation of the gravity potential was solved in terms of spherical coordinates, and it can be written as (Kaula, 1966, Wakker, 2010)

$$V = \frac{GM}{r} \left\{ 1 + \sum_{n \geq 1} \sum_{m=0}^n \left( \frac{R_e}{r} \right)^n P_{nm}(\sin(\theta)) [C_{nm} \cos(m\lambda) + S_{nm} \sin(m\lambda)] \right\},$$

where  $R_e$  is the reference radius (often chosen as the maximum radius of the body),  $(\lambda, \theta)$  are the longitude and latitude, respectively, and  $r$  is the distance from the particle (or spacecraft) to the center of the body.  $C_{nm}$  and  $S_{nm}$  are the spherical harmonic coefficients, and  $P_{nm}$  are the associated Legendre functions. This potential  $V$  can be truncated at arbitrary degree  $n$  and order  $m$  to achieve the desired accuracy. According to the definition, the first-degree and order harmonics are all zero if the centre of mass of the body is chosen as the origin of the body-fixed frame, which can be the case provided that mass distribution and the exact shape of the body are known. Therefore, the gravitational potential in addition to that of the point mass starts from the second-degree harmonics. Since this method actually expands the potential into a spherical harmonics series, it diverges within the circumscribing sphere and therefore the potential  $V$  is only valid outside this sphere. Accelerations can be obtained by differentiating the potential w.r.t. the directions of interest (e.g. radial).

#### (b) Polyhedron model

Any celestial body with arbitrary shape can be approximated by a polyhedron model. Werner (1994) developed the closed-form solution of the potential for an arbitrary polyhedron split into triangular faces and edges (Fig.6). With this technique, the general formula for the potential can be written as

$$U(r) = \frac{G\sigma}{2} \left( \sum_{e \in \text{edges}} \mathbf{r}_e \cdot \mathbf{E}_e \cdot \mathbf{r}_e L_e - \sum_{f \in \text{faces}} \mathbf{r}_f \cdot \mathbf{F}_f \cdot \mathbf{r}_f \omega_f \right),$$

where  $G$  is the gravitational constant and  $\sigma$  is the density of the body (assumed to be constant). The two sums are the contributions from points located on all edges and all faces, respectively, for covering the entire volume of the body.  $\mathbf{r}_e$  and  $\mathbf{r}_f$  denote the vector from any point on the edge and on the face to the exterior particle, respectively, cf. Fig. 6.  $\mathbf{E}_e$  and  $\mathbf{F}_f$  are on edge dyad and face dyad.  $L_e$  represents the potential of the

general edge  $e$ , and  $\omega_f$  denotes the signed area of the face  $f$  projected onto a unit sphere centered on the exterior particle. The detailed explanation of all the symbols can be found in Werner and Scheeres (1997). The solution satisfies Laplace's equation outside the body and Poisson's equation inside the body, and therefore can be used to compute the gravitational field close to and on the surface of the body. Given a polyhedron shape model of a complex asteroid, its gravitational potential (up to the surface) can be obtained with high accuracy, compared to the spherical harmonics model (Werner and Scheeres, 1997). This model was used for the mission operation of NEAR. In addition, Werner also developed the method for converting the polyhedron potential into a spherical harmonics series (Werner, 1997). Again, the acceleration is obtained by differentiation. This approach is computationally heavy.

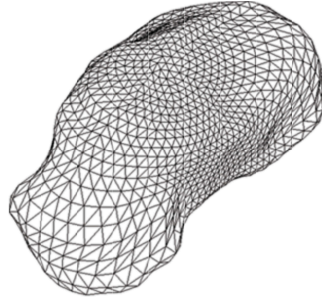


**Figure 6** The polyhedron shape model of Itokawa with 3688 faces (Park et al., 2010).

A related modelling method is called the 'mascons', where the mass distribution of a body is approximated by a collection of point masses. This method was firstly used to estimate the lunar gravitational potential (Muller and Sjogren, 1968) and then was applied to approximate the irregular gravitational field of asteroid Itokawa for JAXA's Hayabusa mission (Maruya et al., 2006). However, this method has relatively low precision at the surface of the asteroid and is computationally heavy compared to the polyhedron model, as shown in Werner's study.

### (c) Geometrical shapes

A constant-density ellipsoid is one typical geometrical shape for approximating the asteroid. Given an ellipsoid with semi-axes  $\alpha > \beta > \gamma$  (Figure 7), its gravitational potential can be expressed as (MacMillan, 1958)

$$U_E(\mathbf{s}) = -\frac{3GM}{4} \int_{\lambda(\mathbf{s})}^{\infty} \phi(\mathbf{s}, v) \frac{dv}{\Delta(v)},$$

$$\phi(\mathbf{s}, v) = 1 - \frac{s_x^2}{\alpha^2 + v} - \frac{s_y^2}{\beta^2 + v} - \frac{s_z^2}{\gamma^2 + v},$$

$$\Delta(v) = \sqrt{(\alpha^2 + v)(\beta^2 + v)(\gamma^2 + v)},$$

in which  $\mathbf{s} = (s_x, s_y, s_z)$  is the vector from the center of the ellipsoid to the particle and  $\lambda(\mathbf{s})$  is defined as the maximum real root of  $\phi(\mathbf{s}, \lambda) = 0$ . The integral can be numerically evaluated with the first and second kind of Carlson's Elliptic Integrals



(Press, 2007). In analogy to the polyhedron method, this potential is also valid close to and on the surface of the body. The calculation of the acceleration needs Carlson's Elliptic Integral of the third kind. The potential of a straight segment, two orthogonal segments and two connected spheres can be found in Riaguas et al. (1999) , Bartczak and Breiter (2003) , Prieto-Llanos and Gomez-Tierno (1994), respectively.

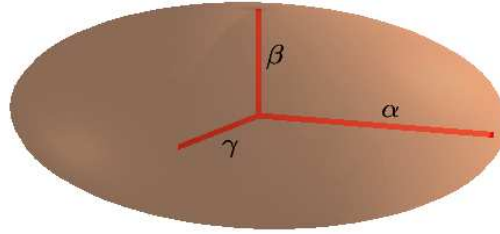


**Figure 7** An ellipsoid with three semi-axes  $\alpha, \beta, \gamma$ .

### Other Perturbations

In addition to the irregular gravitational attraction by the asteroid, the orbiting particle or spacecraft also suffers from perturbations from solar and planetary gravitations and solar radiation pressure (SRP). The planetary perturbation is negligible unless there is a close encounter of the asteroid with the planet. The SRP is dominant over solar gravitation especially for spacecraft with a large area-to-mass ratio, since it is generated primarily due to the reflection of solar photons on the surface of an area (Scheeres, 2012). If the spacecraft is far from the asteroid, SRP is recognized as the main perturbation over the irregular gravitation from the body. For sufficiently large asteroids (e.g. Eros), the perturbation from SRP is very limited. When the asteroids have the size on the order of a few kilometers or less, SRP needs to be taken into account for determining the stability of orbiting spacecraft. Some detailed studies of SRP on spacecraft motion around asteroids will be covered in the next section.

## 1.4 Current Research Status

There has been extensive research about orbital motion around irregular asteroids (Scheeres, 2012). For the aspect of dynamics, various main topics can be identified. The location and linear stability of the EPs of the system are one highlight. A single asteroid usually has four EPs, while Betulia is an exception (so far) that hosts six EPs due to its diamond shape (Magri et al., 2007). It is known that the collinear EPs are always unstable, whereas the non-collinear EPs transit from stable to unstable when the rotation rate of the asteroid increases. A second main topic is to characterize the orbital motion around the whole asteroid, and to design orbits and examine their stabilities, to identify stable regions. Frozen orbits and POs are usually investigated. Therefore, the phase space of the asteroid can be characterized. In addition, another interesting aspect is to study the ejection and capture dynamics at the periapsis passage of a given orbit, to identify the mechanisms of ejection and capture of the particles on

the surface of an asteroid, and even the capture of other small objects. In general, these studies can be classified by the way in which the gravitational field has been modeled.

### **Geometrical Shapes**

With the uniformly rotating triaxial ellipsoid model, Scheeres (1994) made a systematic investigation about the surrounding dynamics. An asteroid is classified as Type I in the case of stable non-collinear EPs (e.g. Vesta) and Type II in the case of unstable ones (e.g. Eros). Objects in the vicinity of the stable EPs oscillate around them indefinitely, while near the unstable EPs particles travel close to or even crash with the asteroid or escape from the body by following the related unstable manifolds. Two main families of planar POs were identified. The prograde (or direct) family is stable at large distances from the body and becomes unstable when it comes close, while the retrograde family is always stable and is a good candidate for actual space missions.

To approximate elongated irregular bodies (Eros, Ida), the shape model of a straight segment with constant density was applied (Riaguas et al., 1999). Equations of motion (EOM) were derived for the situation that the segment was fixed in inertial space, and families of POs were found by applying the Poincaré map; their bifurcations were identified using numerical continuation methods. One step further, the model of two perpendicular segments of different length and mass to describe cigar-shaped or ellipsoid-shaped bodies was proposed (Bartczak and Breiter, 2003). With application to the elongated sphere and the three-axis ellipsoid cases, this model was found to be computationally efficient and especially suitable for motions that approach the surface of the body. Prieto-Llanos and Gomez-Tierno (1994) introduced the rotating mass dipole model (dumbbell) to represent natural elongated bodies in rotation, which can be viewed as a generalization of the Circular Restricted Three Body Problem (CRTBP). The location of the EPs was obtained and their stability was investigated. A modal control technique was developed to stabilize a mission at the collinear EPs for the purpose of close survey of the body. As an extension, the same dynamical system with the difference that the centrifugal force is larger than the gravitational force was studied (Hirabayashi et al., 2010), which is the case for fast-rotating asteroids. By introducing the ratio of gravitational to centrifugal force, the conditions for stable collinear EPs were defined. The method was applied to fast-rotating asteroid 2000 EB<sub>14</sub>.

### **Spherical Harmonics Model**

With the assumption of constant-density, values of the harmonics coefficients were generated from the gravitational field of a triaxial ellipsoid and a bifurcated shape of two ellipsoidal components (German and Friedlander, 1991). Numerical simulations were then performed to study the stability of orbits around them.



The effects of low degree and order spherical harmonics (mainly  $C_{20}$  and  $C_{22}$ ) on the stability of general orbits and on the solution of frozen orbits have respectively been examined and obtained both numerically and analytically. Given a rotational second degree and order gravitational field, the stable and unstable regions were characterized for initially circular, equatorial orbits by detecting the changes of the semi-major axis (indicating orbital energy) through numerical integration for the case of Castalia (Hu and Scheeres, 2004). In addition, the resonance between the orbital period and the rotation of the asteroid was found to play a crucial role on the stability of orbits and was recommended for further study.

For Eros, the  $C_{20}$  term was also found to introduce large secular variations of the argument of periapsis, the longitude of the ascending node and the mean anomaly for orbits within several radii of the body (Scheeres et al., 2000), which needs to be taken into account for real mission operations. With the averaging method and Lagrange Planetary Equations (LPE), the effect of  $C_{22}$  was identified as making changes in orbital energy, angular momentum and its projection on the rotation axis. The interaction between the rate of change of the true anomaly of the orbit and the asteroid rotation rate was expressed explicitly with a further application of designing safe close flybys over the asteroid. The  $C_{30}$  and  $C_{40}$  terms were shown to make the eccentricity oscillate with a long period and boost its maximal value (Scheeres et al., 2003), respectively.

For Castalia, a 16<sup>th</sup> degree and order spherical harmonics model was used to obtain the EPs and the associated stable and unstable manifolds (Scheeres et al., 1996). Prograde, retrograde and vertical orbits were obtained. As mentioned before, the  $C_{22}$  term has the effect of changing orbital energy, the increase and decrease of which was revealed to be closely related to the quadrant of the orbit's periapsis passage. The possibility of an elliptical prograde orbit to be transformed into a hyperbolic trajectory and vice versa was identified, as well as the capture and escape radius.

For the non-principal-axis rotator Toutatis, the Hamiltonian is non-integrable and no Jacobi integral exists (Scheeres et al., 1998), as the EOM is time-periodic due to the nutation of the asteroid. Using the LPE, families of quasi-frozen orbits with minimal variations of orbital elements were found very close to the asteroid, among which retrograde ones proved especially robust. Stable and unstable POs with periods commensurate to the rotation period of the body were obtained in the body-fixed frame.

For fast-rotating irregular gravitational fields, an explicit analytical formulation for high-altitude motion under the influence of an arbitrary degree and order gravitational field was developed by applying Lie transformations (Ceccaroni and Biggs, 2013). The non-integrable Hamiltonian was reduced to an integrable one. For application, the initial conditions of frozen orbits were obtained given a 15<sup>th</sup> degree and order spherical harmonics model of Eros.

## Polyhedron Approximation

For the study of motions around Eros (Scheeres et al., 2000), Castalia (Scheeres et al., 1996) and Toutatis (Scheeres et al., 1998), spherical harmonics expansions up to degree and order 16, 16 and 20 respectively were applied outside the circumscribing sphere; once within this sphere a polyhedron model was used. For all of them, the EPs and prograde and retrograde POs were characterized by applying the Poincaré maps and numerical correction and continuation methods.

In addition, a model for the dynamics of a particle on the surface of an asteroid was built. Depending on the location on the asteroids' surface, limitations on the velocities of the ejecta either escaping from or re-impacting on Castalia and Toutatis were determined. For ejecta coming from the uniform rotator Castalia, they are probably transported into a stable retrograde orbit rather than into a prograde one. Castalia was found to accumulate ejecta on its leading sides. Particles on the surface of non-uniformly rotating Toutatis suffer time-varying forces. Ejecta that persist in the phase space of a frozen orbit for long time durations and then impacted were found. Toutatis was revealed to accumulate ejecta over its surface uniformly.

Based on the polyhedron model, Yu and Baoyin (2012a) developed a hierarchical grid search method for systematically looking for general three-dimensional POs around asteroids. Their topological classification and stability were also examined. 29 Families of POs were generated as the result of the study case 216 Kleopatra, a small fraction of which were stable.

With a polyhedron-represented gravitational field, the EPs were classified into eight cases according to their associated eigenvalues (Jiang et al., 2014). Then a first-order analytical solution of the motion in the vicinity of the EPs was constructed. Asteroids Kleopatra, Geographos and Castalia were found to have four unstable EPs, while Golevka has two stable and two unstable ones. By applying the polyhedron method, the potential of a cube was modeled (Liu et al., 2011b). The POs in the symmetry planes parallel to the face of the cube and in the diagonal plane were obtained with the Poincaré maps. The POs in other planes were found with the homotopy method. All these families of POs were revealed to be stable.

## Binary Asteroid System

For binary asteroid systems, the relative motion of the asteroid pair has to be modeled first before the motion of a massless particle in the vicinity of the system can be investigated.

With the Full Two Body Problem (F2BP) model, the stability of a binary asteroid system consisting of arbitrary mass distributions has been investigated (Scheeres, 2002). By studying the energy and momentum transfer between the rotational and translational momenta, sufficient conditions for stability against escape and impact were developed. As an example, the binary asteroid system 1996 FG3 was evaluated.

By assuming that one body of the binary pair is a sphere, the F2BP was reduced to a sphere-restricted F2BP (Scheeres, 2006). The conditions for the relative equilibrium of the system were derived, together with their spectral and energetic stability.

Hirabayashi and Scheeres (2013) derived recursive formulas for computing the mutual potential, force and torque of the asteroid pair represented by polyhedrons, with applications to compute the dynamics of a binary system with two equal-sized parallelepipeds orbiting each other. Given an ellipsoidal satellite (i.e. secondary) orbiting an oblate primary in an equatorial orbit, McMahon and Scheeres (2013) studied its planar motion and identified the stable EPs around which the secondary can librate. The sufficient condition for bounded motion was determined. With a Lagrangian approach, the binary system was modelled as the F2BP (Woo et al., 2013). The resultant planar motion of the two bodies was obtained numerically. For the particular case that the bodies have inertial symmetry, the dynamics was reduced and a first-order solution was obtained. Truncated-cone-shaped and peanut-shaped bodies were investigated as examples.

Bellerose and Scheeres (2008) introduced the spacecraft motion into this problem and came up with the Restricted Full Three Body Problem (RFTBP). They made further simplifications by representing the two bodies as an ellipsoid and a sphere, and investigated the equilibrium conditions for the two bodies. Given the stable configuration that the longest principal axis of the ellipsoid points to the sphere, the EOM of the spacecraft was built and EPs of the dynamics and their stability were investigated. POs around one of the bodies and the entire system were obtained. In addition, the transit paths between the two bodies, the impact dynamics and also the control of a probe hopper were evaluated. The binary system 1999 KW4 was used as an example for mission design.

Chappaz and Howell (2015) extended this work by finding the POs in the ellipsoid-ellipsoid system and also by investigating the non-synchronous ellipsoid-sphere and ellipsoid-ellipsoid systems. For the synchronous case, families of Halo orbits and resonant orbits were generated; and their stability was investigated. The ellipsoidal shape of the secondary body was found to have a significant impact on the dynamics of its nearby EPs and to destabilize some of the stable POs around the EPs. The increasing non-sphericity of the primary and secondary bodies was seen to introduce a rich dynamical behavior of the system from the Poincaré maps. For the non-synchronous case, since the secondary body is in a distinct periodic motion itself, only discrete sets of POs were found which have commensurate periods with respect to the period of the secondary body.

In addition to the orbital dynamics from the irregular gravitational field, there are also studies about the effects of SRP on orbits, as well as resonant dynamics.

### **Solar Radiation Pressure**

Taking into account SRP, Dankowicz (1994) showed the existence of a family of circular orbits for which the centers of their orbital plane have a displacement with respect to the center of the primary body (point mass) and in the direction of the solar radiation. The necessary condition to stay bounded around the central body was obtained. Scheeres and Marzari (2002) extended this work by introducing the ellipticity of the central body's orbit around the Sun and tidal effects. They also investigated the stability of sun-synchronous orbits in the terminator plane without offset. The sufficient condition for stable motion was derived.

As one application of these analyses, the minimum radius for being trapped in orbit around Itokawa was estimated to be around 1.73 km (Scheeres et al., 2004). Only taking into account SRP, frozen orbits were obtained with the LPE and their stability was checked. With the inclusion of the  $C_{20}$  term, the stable frozen orbits were destabilized if they are close to the body. For the perturbation from  $C_{22}$ , the destabilization is weaker for an orbit around a fast rotating body than that around a slowly rotating one at a given distance.

Combining the previous work, Byram and Scheeres (2009) identified stable sun-synchronous orbits hovering about a comet with the Hill Three-Body Problem model (HTBP), which is known as a solar terminator orbit (STO). Control strategies were also investigated to bound the spacecraft's motion in the allowable region. By including the irregular gravity of the small body, Broschart and Villac (2009) built an augmented HTBP model and developed a procedure for identifying the resultant non-chaotic long-term stable terminator orbits. Asteroid 6489 Golevka with a 12<sup>th</sup> degree and order spherical harmonics gravity model was used as a study case. Hussmann et al. (2012) performed numerical simulations of spacecraft motion around binary asteroid system 1996 FG3, taking into account solar radiation pressure and the 4<sup>th</sup> degree and order gravitational fields of both primary and secondary asteroids. Generally, the orbital motion was found to be unstable. However, stable STOs were obtained, especially for circular and low-eccentricity orbits. They were not affected by the perturbations from the irregular shape and rotation rate of the primary asteroid as well as perturbations from the secondary asteroid. These STOs were suitable for studying the gravitational field of the primary.

### **Resonant Dynamics**

For orbiting an asteroid, ground-track resonances happen between the rotation period of the asteroid and the orbital period of the spacecraft or particle, given the proper initial conditions. They were shown to have a strong influence on the stability of orbits (Hu and Scheeres, 2004). Hu found the orbits at the 1/2, 1/1, 3/2 resonances etc. to be stable only when the  $C_{20}$  and  $C_{22}$  terms are small (weak perturbations) for the uniformly rotating 2<sup>nd</sup> degree and order gravitational fields. With the same gravitational field, Olsen (2006) studied the widths of the mean motion resonances (defined as the width of the separatrix). Their widths were revealed to be independent

of the rotation rate and mass of the central body, but closely related to the eccentricity and inclination of the orbit. For the slow rotation case, orbital stability was explained by the overlap criteria and the distance between the resonances. The dynamics within the resonance was recommended for further study.

For a gravitational field up to degree and order 4, Delsate (2011) investigated the low-order main resonances of Dawn around Vesta. With numerical integrations, the 1:1 resonance was found to be largest and the 2:3 resonance had the strongest effect on increasing eccentricity. Analytical approximations of these resonances were studied with the 1 degree of freedom (1-DOF, i.e. with one pair of free variables) pendulum model. The resonant angle was found to be the key element during the operational phase.

By applying the ellipsoid shape model, stable resonances were numerically detected using the MEGNO (Mean Exponential Growth factor of Nearby Objects) indicator for fast and slowly uniformly rotating cases (Compère et al., 2012). Compère also developed an analytical model with a truncated ellipsoidal potential at degree and order 2. This model explained the MEGNO maps of the 1:1 and 2:1 resonances for polar and circular orbits, and indicated the effects of the body's shape and orbital eccentricity and inclination on the location of the resonances.

Tzirti and Varvoglis (2014) extended the analytical model by including the  $C_{30}$  term into the 1:1 ground-track resonance which introduced a second angle and resulted in a 2-DOF (with two pairs of free variables) dynamics. For non-circular and non-polar orbits, the characteristics of the resonance were investigated. Due to the term  $C_{30}$ , chaotic layers were created around the separatrix, although the resonance width was not significantly influenced.

## 1.5 Related Methods

Some general tools for studying celestial mechanics (or orbital dynamics) that are also closely related to our current studies are briefly introduced here. Detailed descriptions can be found in related literature (Ferraz-Mello, 2007, Morbidelli, 2002, Wiggins, 2003).

### Hamiltonian Dynamics

An N-degree of freedom dynamical system can be defined by N generalized coordinates  $q_i$  ( $i = 1, 2, \dots, N$ ) and their associated momenta  $p_i$  ( $i = 1, 2, \dots, N$ ). Its Hamiltonian  $\mathcal{H}$  is the Legendre transformation of its Lagrangian which is the summation of the kinetic energy  $T$  and potential energy  $V$  of the system. It can be written as (Ferraz-Mello, 2007)

$$\mathcal{H} = \sum_{i=1}^N p_i \cdot \dot{q}_i - T(\dot{q}_i, q_i) + V(q_i, t).$$

The Hamilton equations of the system are defined as

$$\dot{q}_i = \frac{\partial \mathcal{H}}{\partial p_i}, \dot{p}_i = -\frac{\partial \mathcal{H}}{\partial q_i},$$

which are also called the canonical equations of the system. When  $\mathcal{H}$  is time-independent, it is the energy constant of the system. For celestial mechanics and astrodynamics, it is convenient to write the system in Hamiltonian form when orbital elements and a rotating frame are used (Morbidelli, 2002). Usually the Hamiltonian of such systems can be written as

$$\mathcal{H} = \mathcal{H}_0 + \mathcal{H}_{rotation} + \mathcal{H}_{perturbation}(L, G, H, l, g, h, t),$$

in which  $\mathcal{H}_{perturbation}$  is the perturbation from any gravitational potential that disturbs the system from the Keplerian motion  $\mathcal{H}_0$ , and  $l, g, h$  are the Delaunay variables as function of orbital elements with their corresponding canonical momenta  $L, G, H$ . For some problems,  $\mathcal{H}$  is time-independent and integrable, which means that the Hamiltonian value is a constant. Either perturbation techniques can be applied to study the dynamics through canonical transformations that make the Hamiltonian to have a simpler form, or numerical integrations can be done to get the evolution of  $q_i$  and  $p_i$  which is called Hamiltonian flow. Due to a perturbation,  $\mathcal{H}$  might become time-dependent and non-integrable. For the study of this kind of system, an additional coordinate  $\tau$  and its corresponding momentum are usually introduced to make a new time-independent Hamiltonian that can be solved by Fourier expansion and perturbation techniques. In conclusion, the theory of the Hamiltonian is well settled for systems with small perturbations.

### Poincaré Map and Reduction Method

Poincaré developed the idea of reducing continuous time systems (flows) to the associated discrete time system (map) (Wiggins, 2013). This method is quite suitable for studying ordinary differential equations (ODEs). At least one of the variables of the dynamical system can be eliminated by constructing a Poincaré map. In doing so, a lower-dimensional system is obtained, from which the local and global dynamics of the original system can be examined.

In addition, the periodic solutions of a dynamical system and their stability can be identified by searching for stationary points on the map and checking their stability, which can be characterized in terms of the eigenvalues of the linearization of the map about these points. This map is especially suitable for the study of a 2-DOF system, as the reduction map is two-dimensional and allows visible inspection. The construction of the map needs a proper surface of cross-section, which can be chosen depending on the geometrical structure of the system. Then initial points are sampled for integration, during which the epochs and the coordinates of the points that satisfy the conditions of the section are recorded. Since the Hamiltonian of the time-invariant 2-DOF dynamical system is a constant, it can be used as a restriction of the section, as all points on the map must have the same value of it.

In our study, the map is mainly used for finding POs and checking their stability, which is called the reduction method. Having chosen a map perpendicular to the Hamiltonian flow and an initial point close to the real solution on that map, the differential equations of the system are integrated until the first return on the map. The initial condition is then differentially corrected with the derivative of the final state with respect to the initial one and the linearized dynamics for several iterations, until it has converged to the real solution at the desired accuracy. Once the solution is found, its transition matrix (also called monodromy matrix), which is obtained by integrating the variational equations for a full period, is used to determine the stability of the orbit. The PO is stable if all eigenvalues of the monodromy matrix have a magnitude of one; otherwise it is unstable. This is one of the most popular numerical correction methods.

## 1.6 Research Motivation

Since extensive studies of the dynamics in the single and binary asteroid systems have already been done, this thesis focuses on a new topic: the systematic study of orbital dynamics around a contact binary asteroid. As mentioned in previous sections, contact binary bodies (including comets) constitute 10-20% of all small Solar System bodies and represent the most bifurcated shape. Since contact binary bodies are created by the impact and merger of two small objects, follow-up future missions devoted to such kind of body, no matter whether they are asteroids or planetary moons (e.g. Kerberos), will be appealing (although there are already large science returns from the Rosetta mission to 67P, a contact binary comet). The science objectives could aim at characterizing the physical and chemical properties of the neck region, where the two lobes are connected. The diversity of the density and composition of the two lobes is also of high interest. These investigations will give us hints on the evolution history of such kind of bodies and further on the evolution of our Solar System. Therefore, it is interesting and worthwhile to investigate orbital dynamics in such highly perturbed environments, for both mission and science aspects.

The general research question can be formulated as follows:

***What are the main characteristics of orbital motion around contact binary asteroids?***

Before going into detail, the dynamical environment needs to be defined. The gravitational field needs to be defined first for solving the dynamics. Compared to the two-connected sphere model, the configuration of an ellipsoid and a sphere is applied since it breaks one element of symmetry. Therefore, this model goes one step further to study bifurcated bodies. For this specific configuration, possible formation mechanisms and the relationship between the relative configuration and the rotational angular momentum have been studied in detail (Scheeres, 2007). However, the orbital dynamics around such kind of configuration has not been explored in detail, which is addressed in this thesis. In addition, neither high-order solutions around the EPs nor

the resonant dynamics in a highly irregular gravitational field have been studied for highly bifurcated asteroids.

Despite it being simplified from the real situation, this model captures the main mass distribution of this kind of body, and also the main dynamics around it. Since the gravitational potential of the sphere and the ellipsoid can both be expressed in closed-form formulas, the combined gravitational field can be obtained by superimposing one upon the other. This method is mainly applied for the numerical exploration of the system. In addition, we are also interested in the properties of spherical harmonics induced for this highly bifurcated body. Given a gravitational field represented by spherical harmonics, both a numerical and an analytical study can be performed for identifying the dynamics. The contact binary 1996 HW1 serves as the study case throughout this thesis, since it is the most bifurcated asteroid ever found as mentioned in the previous section.

Since we focus more on the characteristics of an irregular gravitational field and its effect on orbital dynamics in its vicinity, solar perturbations are ignored in this research. They only play a significant role when the motion is in moderate distance or far away from the asteroid, as has been mentioned in a previous section. Based on the above, secondary research questions are formulated.

***(a) What is the phase space of the whole system when the gravitational field is given by the closed-form formulas? How can an analytical solution of the motion in the vicinity of the EPs be constructed?***

For characterizing the phase space, the number and locations of the EPs and their stability need to be identified, together with the properties of orbital motion in their vicinity. The prograde and retrograde POs around the entire body and also their stability need to be investigated, to identify the stable regions for potential mission orbits. To construct the analytical solution of the motion around the EPs, the Lindstedt-Poincaré (LP) method will be applied. Its accuracy has to be examined against the magnitude of the motion and the rotation of the system, to give a clue of when this solution can be applied.

***(b) Given the gravitational field represented by truncated spherical harmonics, how can the dynamics be addressed? What are the characteristics of the resonant dynamics resulting from the harmonics of a highly bifurcated configuration?***

First, the gravitational field needs to be expanded into spherical harmonics coefficients. With the averaging method, frozen orbits and POs can be obtained. Their stability and other characteristics can be identified. With the relatively large spherical harmonics coefficients, the model of resonant dynamics needs to be built and investigated. For the 1-DOF model, the locations and widths of the resonance need to be solved for non-circular and non-polar orbits. For the 2-DOF system, the chaos appears as the



inclusion of a second resonance. Its region needs to be estimated for different eccentricities and inclinations.

## 1.7 Thesis Outline

All research questions are addressed in Chapters 2-5. Chapters 2 and 3 focus on research question (a), while Chapters 4 and 5 address research question (b).

Chapter 2 primarily focuses on characterizing the phase space of the entire contact binary system. Based on the physical parameters of the system 1996 HW1, the EPs, their linear stability and the associated manifolds are identified. The planar, Halo-like and vertical orbits are determined. In addition, the equatorial prograde, retrograde POs and three-dimensional resonant orbits together with their linear stability around the entire system are investigated over large regions for different rotation rates.

Next, Chapter 3 zooms in on the phase space of the system to non-collinear EPs and is devoted to the analytical solutions of the motion around them. For the motion around the stable EPs, a third-order analytical solution is constructed by the LP method. Its accuracy decreases when the orbit goes further away from the EPs and when the asteroid rotates faster. For the motion around the unstable EPs, a linear feedback control law based on low thrust is introduced to stabilize the motion and track the reference trajectory.

In Chapter 4, the frozen orbits and the three-dimensional (3D) POs around the whole body are investigated. The gravitational field is expanded into a spherical harmonics model up to degree and order 8. The Hamiltonian taking into account harmonics coefficients up to degree and order 4 is developed. Frozen orbits are identified with the double-averaged Hamiltonian. By applying Poincaré maps and a numerical correction method, 3D POs are obtained around the whole body at different rotation rates in the single-averaged model and further in the full non-averaged model.

For a generalization of the study of the current gravitational field, Chapter 5 mainly investigates the 1:1 resonant dynamics of the 4<sup>th</sup> degree and order spherical harmonics gravitational field. The dynamical model is built as a 2-DOF Hamiltonian. The 1-DOF resonant dynamics is first solved by finding the EPs of the resonance and checking their stability under different combinations of eccentricity and inclination for asteroids Vesta, 1996 HW1 and Betulia. The 2-DOF dynamics is then investigated in the libration region and around the separatrix of the stable EPs. The relationship between the extent of the chaotic region and the distance of the primary and second resonances are studied qualitatively with Poincaré maps and the overlap criteria, also with different eccentricities and inclinations for all three asteroids. The boundaries of the chaotic layers are estimated from the modulated-pendulum approximation.

Chapter 6 concludes this thesis and gives recommendations for future work.

# Chapter 2 Numerical analysis of orbital motion around contact binary asteroid system

---

J. Feng, R. Noomen, P.N.A.M. Visser, J. Yuan

Submitted to *Advances in Space Research*, January 2016

## Abstract

The general orbital motion around a contact binary asteroid system is investigated in this study. System 1996 HW1 is explored in detail, as it is the mostly bifurcated asteroid known to date. The location of its equilibrium points (EPs) is obtained and their linear stability is studied. Families of Lyapunov, Halo and vertical periodic orbits (POs) in the vicinity of these EPs as well as their stability are found and examined, respectively. The influence of the relative size of each lobe and the shape of the ellipsoidal lobe and the rotation rate of the asteroid on the location and stability of the EPs are studied. Additionally, two families of equatorial orbits are obtained at a wide range of distances: from far away to nearby. Their stability is examined against the distance to the asteroid and the rotation rate of the asteroid, to uncover the influence of highly non-spherical gravitational field and the rotation of the asteroid on the orbital motion. Finally, resonant orbits in  $N$  commensurability with the rotation of the asteroid are found and their stability is discussed. The fast rotation of the asteroid has a stabilizing effect on the equatorial orbital motion.

## 2.1 Introduction

Up to now, several space missions destined for small solar system bodies, e.g. asteroids and comets, have been launched. Close proximity operations are challenging for these missions due to perturbations caused by the irregular gravitational fields of these bodies. Comet 67P/Churyumov-Gerasimenko, the target of ESA's Rosetta mission, was found to be a contact body of two lobes with different origin (probably indicating different densities) recently (Sierks et al., 2015). NASA's New Horizon mission discovered that one of Pluto's tiny moons Kerberos is also a double-lobed body. From radar and optical observations, many near-Earth asteroids (NEAs), main-belt and Trojan asteroids, and even comets are found to be contact binaries; they are estimated to constitute 10-20% of all small solar system bodies (Harmon et al., 2010). This study focuses on investigating the general properties of orbital motion in the strongly perturbed environment induced by these highly bifurcated bodies.

Traditionally, the shape of an asteroid was approximated by a triaxial or oblate ellipsoid. With this model and the closed-form ellipsoidal potential, Chauvineau et al. (1993) investigated planar orbits by numerical integration and identified chaotic and regular orbits by varying the mass distribution and rotation rate of the body. Scheeres

(1994) performed systematic studies about the equilibrium points (EPs) and periodic orbits (POs) in its vicinity, from which an asteroid was classified as type I if the non-collinear EPs are stable and type II if they are unstable. Werner (1994) developed the polyhedron method to approximate the shape and gravitational field of asteroids by means of thousands of polyhedra. This is the most accurate approach, especially for studying motion extremely close to and on the surface of an asteroid. It has been widely applied for identifying the dynamical environment, e.g. EPs, POs and particle motions, around asteroids with detailed shape models (Scheeres et al., 1996, 1998, 2000). A closely related model is the so-called ‘mascons’ model that represents the asteroid with a collection of point masses, which was first used to estimate the lunar gravitational potential (Muller and Sjogren, 1968). However, it is less accurate on the surface of the body, compared to the polyhedron model (Werner and Scheeres, 1997). The spherical harmonics model was also widely applied for general analytical and averaging studies of orbital motion around asteroids. From this model, the  $C_{20}$ ,  $C_{30}$  and  $C_{40}$  terms were found to introduce secular rates of the argument of periapsis, the ascending node, mean anomaly and eccentricity for orbits close to the asteroid. The  $C_{22}$  term was identified to change orbital energy and angular momentum (Scheeres, 2012). Even with higher degree and order spherical harmonics, frozen orbits were obtained (Ceccaroni and Biggs, 2013). In addition, the geometrical shapes of a cube, a straight segment, and two orthogonal segments were also applied (Liu et al., 2011b, Bartczak and Breiter, 2003, Riaguas et al., 1999). Families of POs were generated in their vicinity and the stability of the orbits was investigated. The three-dimensional region for stable orbital motion around an asteroid represented by an ellipsoid was identified in Lara and Scheeres (2002).

For our exploration of the dynamical environment around contact binary bodies, a shape model consisting of two lobes (an ellipsoidal component and a spherical component) that are in physical contact, is applied. Based on it, the effects of system configuration (varying the relative size of each lobe and the shape of the ellipsoidal lobe) and the rotation rate of the asteroid on the orbital motion can be studied in a systematic way. For this kind of shape, Scheeres (2007) discussed formation mechanisms and studied the relationship between the relative configuration and the rotational angular momentum. The motion of an orbiting spacecraft or a particle in its vicinity will be investigated in detail in this study. Here, the ellipsoid and the sphere are combined in one body, which breaks the symmetry along one axis of the system. This is different from the previous models that approximate the bifurcated body by two connected spheres (German and Friedlander, 1991) and two mass dipoles (Prieto-Llanos and Gomez-Tierno, 1994), which have complete symmetry in three axes.

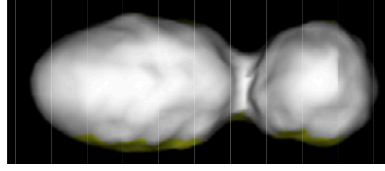


**Figure 1** The shape model of 1996 HW1 (Magri et al., 2011).

Following the definition in Magri et al. (2011), bifurcation is defined as a penalty function that identifies the body's deepest neck. It reflects the concavity of the shape and the narrow extent of the neck region. Contact binary system 1996 HW1 was found to be the mostly bifurcated asteroid until recently, as shown in Fig.1. However, comet 67P observed by the Rosetta mission might be more bifurcated since it has a deep neck region. Therefore, it serves as the basic model of a contact binary asteroid and its physical parameters are applied in our simulations. Although there are several methods to represent the gravitational field of this highly bifurcated shape, e.g. the spherical harmonics expansion and the polyhedron approximation as mentioned, in this study the potential from the combination of an ellipsoidal potential and a spherical potential is directly applied, with the constant-density and rigid-body assumptions. Since the orbital motion in the vicinity of a highly perturbed gravitational field is the focus, other perturbations, e.g. solar radiation pressure and third-body gravitation (e.g. solar gravitation), are not considered here.

For this kind of shape model, there are two free system parameters: the mass ratio  $\mu$  that reflects the mass distribution between two components and the gravitational-centripetal acceleration ratio  $\delta$  that indicates the rotation rate (fast or slow) of the asteroid. Therefore, this study is arranged as follows. First, based on the physical parameters of the system 1996 HW1, the EPs and their linear stability are identified. Second, the influence of  $\mu$  and  $\delta$  on the location and stability of the EPs is investigated. Third, with approximated analytical initial conditions and the differential correction (DC) method and continuation process, families of Lyapunov, Halo and vertical POs are generated, and their stability is studied. In addition, equatorial POs around the entire system and their linear stability are investigated, and the effect of the parameter  $\delta$  on their stability is examined. Finally, resonant orbits that are in  $N$  commensurability with the rotation of the asteroid, are obtained for different  $\delta$ , and their stability is discussed.

## 2.2 Dynamical Model

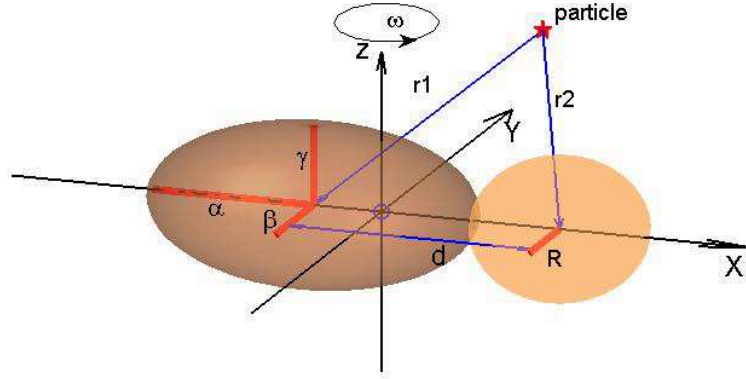


**Figure 2** The ellipsoid-sphere configuration in the rotating frame  $XYZ$  with rotation rate  $\omega$ .

The geometry of the ellipsoid-sphere configuration is illustrated in Fig.2. The parameters that characterize this configuration are: the three semi-axes of the ellipsoid  $\alpha, \beta, \gamma$ , the radius of the sphere  $R$  and the uniform rotation rate  $\omega$ , which is aligned with the axis of the maximum moment of inertia. The system is assumed to be homogeneous, with a constant density  $\rho$ . The vector between the centers of mass of the two components is defined to be  $\vec{d}$  (from ellipsoid to sphere), where  $|\vec{d}| = \alpha + R$ , and the mass ratio  $\mu$  is equal to  $m_s/(m_s + m_e) = R^3/(R^3 + \alpha\beta\gamma)$  ( $m_s$  and  $m_e$  being the mass of the sphere and the ellipsoid, respectively). In the body-fixed frame ( $XYZ$ -frame in Fig.2), the gravitational potential is invariant, and the equations of motion for an object located at  $\vec{r} = (x, y, z)$  in the vicinity of the asteroid can be written as

$$\ddot{\vec{r}} + 2\omega \times \dot{\vec{r}} + \omega \times (\omega \times \vec{r}) = \frac{\partial U_{se}}{\partial \vec{r}}, \quad (1)$$

where the potential of the asteroid  $U_{se}$  is expressed as

$$U_{se} = U_s + U_e = G(m_s + m_e) \left( \frac{\mu}{|\vec{r} - (1-\mu)\vec{d}|} + (1-\mu)U_E(\vec{r} + \mu\vec{d}) \right), \quad (2)$$

in which  $U_s$  and  $U_e$  are the potential of the spherical lobe and ellipsoidal lobe, respectively, and  $U_E$  is the ellipsoid potential of unit mass and is expressed as (MacMillan, 1958)

$$U_E(\vec{s}) = \frac{3}{4} \int_{\lambda}^{\infty} \phi(\vec{s}, v) \frac{dv}{\Delta(v)},$$

$$\phi(\vec{s}, v) = 1 - \frac{x^2}{\alpha^2 + v} - \frac{y^2}{\beta^2 + v} - \frac{z^2}{\gamma^2 + v}, \quad (3)$$

$$\Delta(v) = \sqrt{(\alpha^2 + v)(\beta^2 + v)(\gamma^2 + v)},$$

where  $\phi(\vec{s}, v) = 0$ ,  $\vec{s} = (x, y, z)$ , and  $\lambda$  is defined as the maximum real root of  $\phi(\vec{s}, \lambda) = 0$ . Taking the length and time units as the distance  $d$  and  $\omega^{-1}$ , respectively, after normalization, Eq.(1) becomes

$$\begin{cases} \ddot{x} - 2\dot{y} = x - \delta \left[ \frac{\mu(x-1+\mu)}{|\vec{r}_2|^3} - \frac{(1-\mu)\partial U_E(\vec{r}_1)}{\partial x} \right] \\ \ddot{y} + 2\dot{x} = y - \delta \left[ \frac{\mu y}{|\vec{r}_2|^3} - \frac{(1-\mu)\partial U_E(\vec{r}_1)}{\partial y} \right] \\ \ddot{z} = -\delta \left[ \frac{\mu z}{|\vec{r}_2|^3} - \frac{(1-\mu)\partial U_E(\vec{r}_1)}{\partial z} \right] \end{cases}, \quad (4)$$

where  $\vec{r}_1$  and  $\vec{r}_2$  are the vectors from the particle  $(x, y, z)$  to ellipsoid center  $(-\mu, 0, 0)$  and the sphere center  $(1 - \mu, 0, 0)$ , respectively, and  $\delta = G(m_s + m_e)/\omega^2 d^3$  is a dimensionless scaling parameter that represents the ratio of the gravitational acceleration to centrifugal acceleration. The derivatives of the ellipsoid potential with respect to  $x, y, z$  are

$$\begin{cases} U_{Ex} = -\frac{3}{2}x \int_{\lambda}^{\infty} \frac{dv}{(\alpha^2 + v)\Delta(v)} \\ U_{Ey} = -\frac{3}{2}y \int_{\lambda}^{\infty} \frac{dv}{(\beta^2 + v)\Delta(v)} \\ U_{Ez} = -\frac{3}{2}z \int_{\lambda}^{\infty} \frac{dv}{(\gamma^2 + v)\Delta(v)} \end{cases}, \quad (5)$$

in which the parameters  $x, y, z, \alpha, \beta, \gamma$  are all normalized, and these integrals are Carlson Elliptic Integrals of the second kind that can be obtained by Carlson's algorithms evaluated in Press (2007). The second derivatives of  $U_E$  with respect to  $x, y, z$  can be found in Scheeres (2012). Therefore, for orbital motion in the vicinity of the asteroid, the potential  $U_E$  can be rewritten as

$$U_E = \frac{3}{2} \cdot R_0 + \frac{1}{2} (x \cdot U_{Ex} + y \cdot U_{Ey} + z \cdot U_{Ez}), \quad (6)$$

where

$$R_0 = \frac{1}{2} \int_0^{\infty} \frac{dv}{\Delta(v + \lambda)}$$

is the Carlson Elliptic Integral of the first kind that also can be obtained by Carlson's algorithms evaluated in Press (2007). The integral for this Hamiltonian system is

$$C = \frac{1}{2} (\dot{x}^2 + \dot{y}^2 + \dot{z}^2) - \frac{1}{2} (x^2 + y^2) - \delta U_{se} = T - V, \quad (7)$$

in which  $T = \frac{1}{2} (\dot{x}^2 + \dot{y}^2 + \dot{z}^2)$  is the specific kinetic energy,  $V = \frac{1}{2} (x^2 + y^2) + \delta U_{se}$  is the effective potential, and  $C$  is the Jacobi integral or Jacobi constant.

The free parameters of system (4) are  $\mu$  and  $\delta$ . The former one reflects the relative mass distribution within the system and the relative size (or mass) of the two components. The latter one indicates the rotation situation of the asteroid. For two connected spheres,  $\delta = 1$  represents the case that the two lobes are just touching one another without any internal forces, while the components are in compression for  $\delta > 1$  and stretch for  $\delta < 1$ . However, for our model,  $\delta$  deviates slightly from 1 for the touching case due to the non-spherical property of the ellipsoid component. It is pointed out here that the Restricted Three Body Problem (RTBP) can be viewed as a particular situation in which both of the two lobes are spheres with  $\delta = 1$ . The influence of  $\mu$  and  $\delta$  on the dynamical environment in the vicinity of the asteroid will be investigated in the following sections.

## 2.3 Contact Binary System 1996 HW1

Firstly, numerical studies are performed for 1996 HW1, whose detailed shape model was obtained by Magri et al. (2011) (Fig.1). It is found to be the most bifurcated bodies among the currently known elongated asteroids, with a pronounced ‘neck’ separating two lobes in a roughly 1:2 mass ratio. Since the two components can be represented by an ellipsoid and a sphere, Table 1 gives their physical dimensions, the bulk density and the rotational period of the entire system. It rotates in align with the axis of the maximum moment of inertia. Given these rotational period and the bulk density, the system is not in a minimum energy state as described in Scheeres (2007) as  $\delta$  is 2.1682, implying the existence of internal tension between the two components. For the minimum energy state of 1996 HW1, its rotation rate should be 7.4 h, rather than its current value of 8.76243 h. Due to this slow rotation, there exists internal compression between the two components (Magri et al., 2011).

Table 1 The main parameters of 1996 HW1 (Magri et al., 2011)

Overall dimensions (km)	X: 3.78±0.05; Y: 1.64±0.1; Z: 1.49±0.15
Sidereal rotational period (h)	8.76243±0.00004
Average sphere radius (km)	1.32
Triaxial ellipsoid principal axes size (km)	2.46×1.64×1.49
Bulk density (g·cm <sup>-3</sup> )	2.0

### 2.3.1 Zero-velocity Curves and EPs

Similar to the RTBP, for our model  $C = -V$  also defines the zero-velocity surfaces with  $T = 0$ , which divides the space into an accessible region ( $T > 0$ ) and a forbidden region ( $T < 0$ ). Unlike the RTBP where the zero-velocity curves are largely determined by the mass ratio  $\mu$ , the curves of our model are determined by  $\mu$  together with  $\delta$ . Given a value of the Jacobi constant  $C$ , the motion is bounded to the accessible

region. In the  $xy$  plane, the zero-velocity curves for different  $C$  levels of system 1996 HW1 are shown in Fig.3.

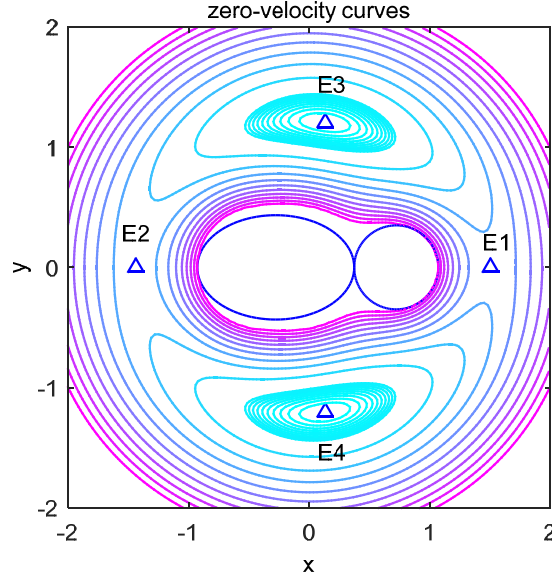


**Figure 3** The zero-velocity curves and positions of four EPs of system 1996 HW1 in the  $xy$ -plane (the color corresponds to the Jacobi constant  $C$  of the system).

EPs are fixed points in the rotating (body-fixed) frame, where velocity and accelerations are zero. They can be interpreted as synchronous orbits around the asteroid in the inertial frame. In Fig.3, four EPs can be identified, among which E1, E2 are the collinear ones and E3, E4 are the non-collinear ones. According to Scheeres (1994), E1 and E2 are referred to as saddle EPs, while E3 and E4 are the so-called center EPs. As this configuration is symmetric in the  $z$ -plane, the EPs are all situated in the  $xy$ -plane. Their exact positions can be computed by setting the right-hand sides of Eq.(4) to zero and are denoted as  $(x_e, y_e, z_e)^T$ . According to differential theory (Meiss, 2007), the linear stability of the EPs can be determined from the linearized dynamics of Eq.(4). Given a small perturbation from an EP  $\mathbf{X} = (\xi, \eta, \zeta, \dot{\xi}, \dot{\eta}, \dot{\zeta})^T$ , in which  $(\xi, \eta, \zeta)^T = (x, y, z)^T - (x_e, y_e, z_e)^T$ , the linearized equation of motions for a perturbation (variational equations) in the neighborhood of an EP is written as

$$\dot{\mathbf{X}} = \mathbf{A} \cdot \mathbf{X} \quad (8)$$

where

$$\mathbf{A} = \begin{bmatrix} \mathbf{0}_{3 \times 3} & \mathbf{I}_{3 \times 3} \\ V_{xx} & V_{xy} & V_{xz} & 0 & 2 & 0 \\ V_{xy} & V_{yy} & V_{yz} & -2 & 0 & 0 \\ V_{xz} & V_{yz} & V_{zz} & 0 & 0 & 0 \end{bmatrix}$$

is the Jacobi matrix calculated at the corresponding EP and  $V$  is the effective potential defined in Eq. (7). The characteristic equation of  $\mathbf{A}$  can be written as

$$\lambda^6 + a\lambda^4 + b\lambda^2 + c = 0$$



in which  $\lambda$  is the eigenvalue and coefficients  $a, b, c$  are determined by the second derivatives of  $V$  that are closely related to the rotation rate of the body. If all the eigenvalues have non-positive real parts, the EP is Lyapunov stable (or linearly stable), otherwise it is unstable. The positions of the four EPs of 1996 HW1 and their corresponding eigenvalues are given in Tables 2 and 3.

Table 2 Location and linear stability of the EPs in the rotating frame

EP	$x$	$y$	stability
E1	1.50397208867676	0	U
E2	-1.43907984894912	0	U
E3	0.142251271693655	1.20262697830487	U
E4	0.142251271693655	-1.20262697830487	U

Table 3 The eigenvalues of the EPs

EPs	$\lambda_{1,2}$	$\lambda_{3,4}$	$\lambda_{5,6}$
E1	$\pm 1.15329441819126$	$\pm 1.327198177844053i$	$\pm 1.252450802130986i$
E2	$\pm 0.90255553930741$	$\pm 1.21107228063561i$	$\pm 1.16099544900511i$
E3/E4	$-0.480938988379065 \pm 0.852439624239106i$	$0.480938988379066 \pm 0.852439624239106i$	$\pm 1.004638240930704i$

Since both E1 and E2 have positive real eigenvalues, they are hyperbolically unstable. E3 and E4 have eigenvalues with positive real parts, and they are complex unstable. The positions and stability of the EPs obtained here are highly consistent with those obtained by Magri et al. (2011), in which study the polyhedron model of the body was used. This proves the validity of our model that approximates the body with the combination of an ellipsoid and a sphere. In addition, system 1996 HW1 can be classified as a type II asteroid, according to Scheeres (1994).

The eigenvalues and eigenvectors determine the orbital motion in the vicinity of the EPs. For E1 and E2, the pair of real eigenvalues and their corresponding eigenvectors define the 1-dimensional stable and unstable manifolds. For E3 and E4, the two pairs of complex eigenvalues and eigenvectors define the spiral stable and unstable manifolds. The pure imaginary eigenvalues and the corresponding eigenvectors of all four EPs generate two 2-dimensional center manifolds, on which POs can be found. These POs are obtained in Section 4 of this study. In addition, since all the EPs are located in the  $xy$ -plane, the motion in  $z$ -direction decouples from the motion in  $xy$ -plane, which is analogous to the RTBP. With the purely imaginary eigenvalues, small oscillations in the  $z$ -direction are expected.

### 2.3.2 Location and Stability of EPs at Different Values of $\mu$ and $\delta$

Having obtained the EPs of system 1996 HW1 and their stability, a systematic study on the effects of  $\mu$  and  $\delta$  on the location and stability of the EPs is carried out for the same shape model of two connected lobes. As  $\mu$  is closely related to the configuration of the system, Table 4 gives its value for different dimensions of the ellipsoid and the

sphere, respectively, assuming a homogenous density. The parameters in Table 4 include the sphere-sphere and ellipsoid-sphere configurations. The former configuration includes the case of two equal-sized spheres but also two configurations with a big and a small sphere. For the latter configuration, the ellipsoid ranges from mild to strong elongation. Therefore, these configurations cover almost all possible configurations of a contact binary asteroid system.

Table 4 The mass ratio  $\mu$  of contact binary asteroid systems with different configurations

Sphere Radius/km	Ellipsoid Semi-axis/km		
	A:1×1×1	B:1×0.75×0.5	C:1×0.5×0.25
1	0.5	0.7273	0.8889
0.5	0.1111	0.25	0.5
0.25	0.0154	0.04	0.1111

In addition to  $\mu$ , the parameter  $\delta$  ranges from the critical value to the value of 10 for each configuration. Here the critical value is the value for which at least one of the EPs is located on the surface of the asteroid (Vasilkova, 2005). The positions of the EPs are given in Fig.4. For all the configurations, the EPs move further away from the asteroid as  $\delta$  increases, i.e. the rotation slows down and the centripetal contribution becomes smaller. Since the sets of three lines for E1 and E2 tend to overlap, the location of them are slightly influenced by  $\mu$ , compared to  $\delta$ . However, the dependence of the location of E3 on  $\mu$  is strong. On the other hand, for E3 and a given value of  $\mu$ , with an increment of  $\delta$ , the  $y$  coordinate increases while the  $x$  coordinate does not change much. In addition,  $\delta$  does not have much influence on the stability of E1 and E2, as both of them are always hyperbolically unstable. This is different for E3, which transits from linearly stable to unstable with the decrease of  $\delta$  (fast rotation), as indicated in the bottom plots of Fig.4. The red dots represent that E3 is linearly stable, while the blue ones indicate complex instability. The transitions always occur approximately at  $\delta = 5$  or  $\delta = 6$ , which is worth further study on this specific value. Fast rotation (small  $\delta$ ) of the asteroid makes the E3 points unstable, which is consistent with the conclusion in Scheeres (2012).

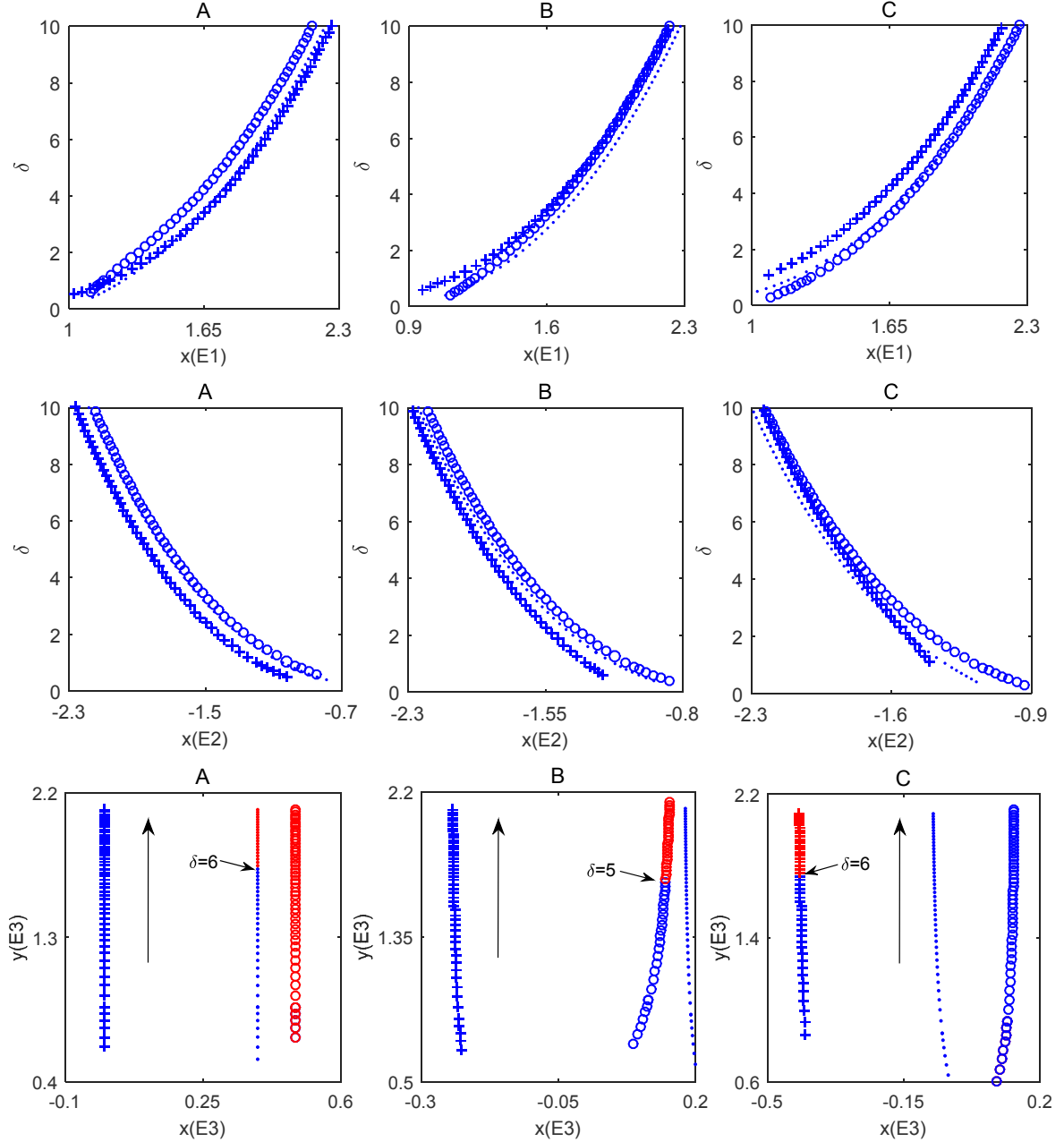


**Figure 4** The coordinates of E1 (upper), E2 (middle) and E3 (bottom) for the A, B and C configurations in Table 4, where the circles, dots and plus markers represent sphere components with radius of 0.25, 0.5 and 1 km, respectively. The blue and red dots indicate the unstable and stable EPs, respectively.

## 2.4 POs in the vicinity of the EPs

For the linearized system Eq. (8), provided that the initial conditions are restricted so that only the non-divergent mode is allowed, the 3-dimensional solution around the collinear EPs can be written as

$$\begin{cases} \xi = A_1 \cos \lambda t + A_2 \sin \lambda t & (a) \\ \eta = -\alpha A_1 \sin \lambda t + \alpha A_2 \cos \lambda t & (b), \\ \zeta = B_1 \sin \lambda_v t + B_2 \cos \lambda_v t & (c) \end{cases} \quad (10)$$

in which  $\lambda$  and  $\lambda_v$  are the frequency of the motion in the  $xy$ -plane and  $z$ -plane, respectively. After Moulton et al. (1920), the POs are classified into three categories

- (1)  $\xi = \eta = 0$  and  $\zeta$  is in the form of (c).
- (2)  $\zeta = 0$  and  $\xi, \eta$  are in the form of (a), (b) respectively.
- (3)  $\xi, \eta, \zeta$  are of the form of (a), (b), (c) respectively,  $\lambda$  and  $\lambda_v$  are commensurable.

Each of these options will be discussed later. In addition, from the linearized system of the RTBP, Szebehely (1967) studied the possibility of short-period and long-period periodic motions around the EPs and their stability. Similarly, Lara and Elife (2002) investigated the linearized motion in the vicinity of the geostationary points and obtained families of planar periodic orbits. For our study, when E3 is stable for some rotation rates of the asteroid as studied in Section 3.2, there exist both short- and long-period motions in the vicinity of it.

According to the Floquet Theorem (Meiss, 2007), the linear stability of POs can be determined from their State Transition Matrix (STM)  $\Phi(t)$ , which reflects the change of state variables at epoch  $t$  due to a small deviation of the state at initial time. It is defined as a nonsingular matrix which satisfies the matrix differential equation

$$\dot{\Phi}(t) = \mathbf{A} \cdot \Phi(t)$$

where  $\mathbf{A}$  is the matrix defined in the linearized system Eq. (8) and  $\Phi(0) = \mathbf{I}_{6 \times 6}$ . For a PO with period  $T_p$ , the STM after completion of one full period is named the monodromy matrix  $\mathbf{M}$ , i.e.  $\mathbf{M} = \Phi(T_p)$ . The eigenvalues of  $\mathbf{M}$  are called Floquet multipliers and  $\mathbf{M}$  was proven to be symplectic for the autonomous Hamiltonian system. Therefore,  $\mathbf{M}$  has eigenvalues in the form of  $\lambda_1, 1/\lambda_1, \lambda_2, 1/\lambda_2, 1, 1$ . Following Broucke (1969) and Gómez et al. (2005), the stability index here is defined as  $s_i = |\lambda_i + 1/\lambda_i|, i = 1, 2$ . The PO is stable if  $s_i < 2$ , while unstable if  $s_i > 2$ . Bifurcations might occur and new families of POs are expected to be generated at  $s_i = 2$ . In the following study, only the pairs of non-unit eigenvalues are considered.

#### 2.4.1 Lyapunov Orbits

The second category of Moulton's classification is considered first, which corresponds to planar motion. Therefore, the general solution of the linearized system can be written as

$$\begin{cases} \xi = A \sin(\lambda t + \phi) \\ \eta = \alpha A \cos(\lambda t + \phi) \end{cases} \quad (11)$$

where  $\lambda$  is the mode of the first pair of pure imaginary eigenvalues of E1 and E2 (listed in Table 3),  $\alpha = (\lambda + V_{xx}/\lambda)/2$ , and  $A$  is the amplitude. As our model is

symmetric with respect to the  $x$ -axis in the  $xy$ -plane, the initial condition of the PO is chosen as the point that intersects the  $x$ -axis perpendicularly:

$$x_0 = x_{E1} + A, y_0 = 0, \dot{x}_0 = 0, \dot{y}_0 = -\alpha\lambda A, T = 2\pi / \lambda$$

Based on the differential correction (DC) process that has been widely applied for finding POs around asteroids (Scheeres et al., 2000) and planetary moons (Russell and Lara, 2007), these approximate initial conditions are adjusted and the exact solutions of the full non-linearized model are obtained. With the numerical continuation method (Osinga and Krauskopf, 2007, Russell and Lara, 2007) a family of POs with variations of orbital period is obtained. Longer orbital periods come with larger amplitudes as well.

With the increase of orbital amplitude  $A$ , the Lyapunov orbits expand from the vicinity of the EP to the surface of the asteroid. Orbits around E1 and E2 that do not intersect with the asteroid are illustrated in Fig.5, as well as the stability index and periods. It can be seen that all orbits are highly unstable with large  $s$  values. There are two blue dash-dotted lines in each stability plot. The upper one is  $s_1$  that indicates the in-plane stability, while the lower one is  $s_2$  that represents the vertical (or  $z$ -direction) stability, and  $s_3 = 2$  is the pair of unit eigenvalues and is not shown in the plot. The closer the orbit to E1 and E2, the larger the instability is. For orbits around E1 and E2, their  $s_2$  pass the critical line  $s = 2$  at  $x \approx 1.77$  and  $x \approx -1.1$  (marked as pentagrams in the plot), respectively, which means that bifurcations occur and new families of POs are generated at these locations. This phenomenon also exists in the RTBP, for which the new family orbits are actually the Halo orbits. Whether it is the case for the current model will be discussed in Section 4.2. Furthermore, for all these orbits, their periods become longer with an increase of the orbital amplitudes.

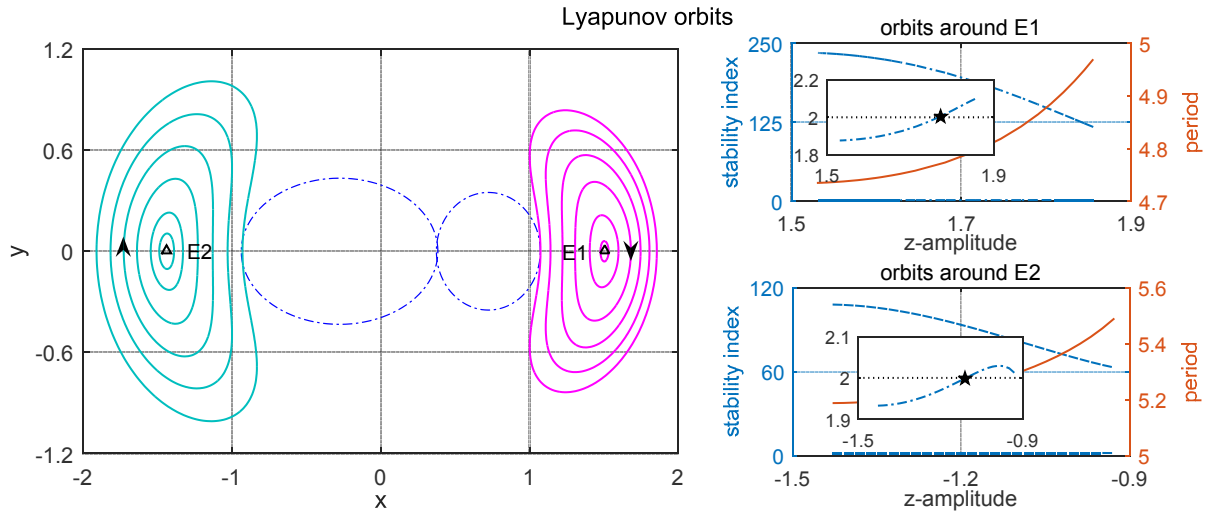


**Figure 5** Left: Lyapunov orbits around E1 and E2; Right: their stability index  $s_1$  and  $s_2$  (blue dash-dotted lines) and corresponding periods (orange lines).

### 2.4.2 Halo Orbits

The general 3-dimensional orbits around EPs are known as Lissajous orbits in the RTBP. They are quasi-periodic. Halo orbits are a special classification where the frequency of the orbit in the  $xy$ -plane is equal to that in the  $z$ -direction, i.e.  $\lambda = \lambda_z$ . Therefore, Eq.(10) can be written as (Richardson, 1980)

$$\begin{cases} \xi = A_x \cos(\lambda t + \phi) \\ \eta = \alpha A_x \sin(\lambda t + \phi) \\ \zeta = A_z \sin(\lambda t + \psi) \end{cases}, \quad (12)$$

$$\psi = \phi + n\pi/2, n = 1, 3$$

in which  $A_x$  and  $A_z$  are the amplitudes in the  $x$ -direction and  $z$ -direction, respectively. Richardson (1980) derived the third-order analytical solution of the above system and gave solutions explicitly. This approximation has been primarily used in the RTBP. However, in our current numerical study, we use the initial conditions that are directly obtained from Eq.(12) and are written as

$$x_0 = x_{E1} + A_x, y_0 = 0, z_0 = \pm A_z, \dot{x}_0 = 0, \dot{y}_0 = -\alpha\lambda A_x, \dot{z}_0 = 0, T = 2\pi/\lambda.$$

The conditions  $A_z$  and  $-A_z$  generate two families of Halo orbits, respectively, which are known as the northern Halo orbits and southern Halo orbits in the RTBP (Howell, 1984). By applying the same DC method, orbits around both E1 and E2 are obtained and the ones that do not intersect with the asteroid are depicted in Fig.6. For a good visualization, their projections on the  $xy$ -,  $xz$ - and  $yz$ -planes are given in Fig.7. It can be seen that the  $z$ -amplitude  $A_z$  controls the size and the shape of the orbits. The purple and green orbits are the so-called northern and southern Halo orbits, respectively. When  $A_z$  increases, the orbits become more inclined and move further away from E1 and E2 but close to the surface of the asteroid. From the stability index, it can be found that the closer the orbit to E1 and E2 the larger its instability. These orbits all have stability in the  $z$ -direction, as shown by the fact that  $s_2$  has values no larger than 2. However, there is a tendency that the orbit will become  $z$ -direction unstable if its  $A_z$  becomes larger. The orbital period reduces with the increase of  $A_z$ .

As shown in Fig.7, the projections of Halo orbits on the  $xy$ -plane have a similar shape with that of the Lyapunov orbits. For extremely small  $A_z$ , the orbits approach to the  $xy$ -plane infinitely which is witnessed by the projection in the  $xz$ -plane. They originate from the planar motion as their vertical stability starts from value 2, which is the bifurcation point. The  $x$  coordinates of the near planar Halo orbits (marked in pentagrams in Fig.7) are approximately the same with those of the bifurcation points for the Lyapunov orbits in Fig.5. Therefore, similar to the RTBP, Halo orbits are actually bifurcations of the Lyapunov family orbits for our model.

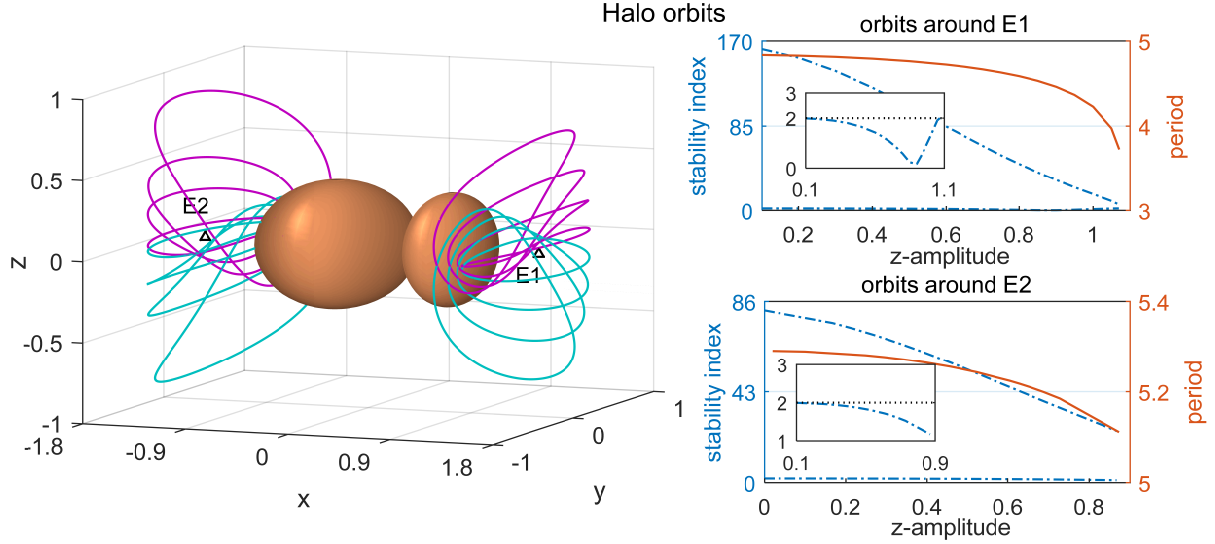


**Figure 6** Left: Halo orbits around E1 and E2; Right: their stability index  $s_1$  and  $s_2$  (blue dash-dotted lines) and corresponding periods (orange lines) as a function of z-amplitude.

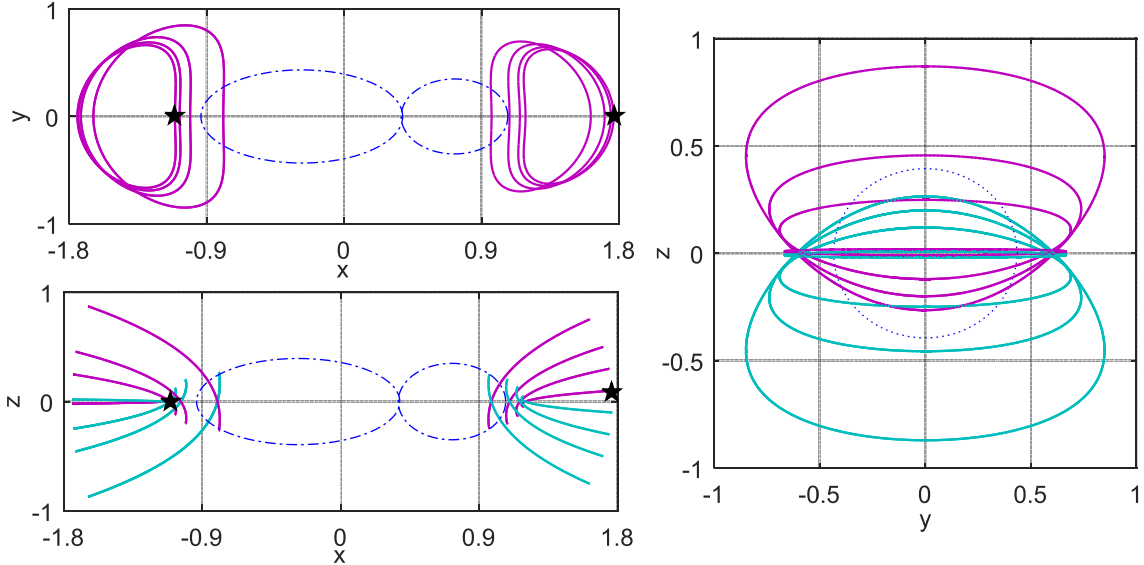


**Figure 7** The projections of the Halo orbits around E1 and E2 on the  $xy$ -,  $xz$ - and  $yz$ -planes.

### 2.4.3 Vertical Orbits

The vertical orbits are defined as orbits with motion mostly in the  $z$ -direction. For this kind of orbits, the initial conditions from Eq.(10) are

$$\xi_0 = \eta_0 = \zeta_0 = 0, \dot{\xi}_0 = \dot{\eta}_0 = 0, \dot{\zeta}_0 = \epsilon,$$

from which it is difficult to get the expected orbit. This is because there is no estimation about the  $y$ -axis velocity  $\dot{\eta}_0$ , which is necessary to generate the vertical orbit. Since the vertical orbit originates from the center manifolds generated from the third pair of pure imaginary eigenvalues and eigenvectors, the initial conditions  $\mathbf{S}$  that are used to generate the manifolds are applied here for searching for the vertical POs. If this pair of eigenvalues and their corresponding eigenvectors are denoted as  $\pm i\beta$  and  $\mathbf{u}_{Re} \pm i\mathbf{u}_{Im}$ , respectively, then  $\mathbf{S}$  can be expressed as (Scheeres, 2012)

$$\mathbf{S} = \mathbf{S}_{EP} + 2\varepsilon [\cos(\beta(t-t_0) + \varphi)\mathbf{u}_{Re} - \sin(\beta(t-t_0) + \varphi)\mathbf{u}_{Im}], \quad (13)$$

in which  $\mathbf{S}_{EP}$  is the state vector of the EP and  $\varepsilon$  and  $\varphi$  are the arbitrary amplitude and initial phase angle, respectively. At  $t = t_0$ , the initial state  $\mathbf{S}_0$  is obtained as

$$\mathbf{S}_0 = \mathbf{S}_{EP} + 2\varepsilon [\cos(\varphi)\mathbf{u}_{Re} - \sin(\varphi)\mathbf{u}_{Im}], \quad (14)$$

For E1 and E2, this family of orbits is symmetric w.r.t. the  $xy$ - and  $xz$ -planes. Therefore,  $\mathbf{S}_0$  serves as the input of the DC method to obtain the vertical POs around E1 and E2 at small amplitudes, and similarly the continuation process is applied to generate POs with large amplitudes. However, for the vertical family around E3, due to the asymmetry of the system w.r.t. the  $xz$ -plane, the Levenberg-Marquardt method (Lourakis, 2005), whose application has no requirement on the symmetric property of the system, is applied to find orbits and the continuation process is then applied for large-amplitude orbits. Since E4 is symmetric with E3 with respect to the  $xz$ -plane and they share the same eigenvalues (Table 3), the vertical families around E4 are also symmetric with the families of POs around E3 and are not shown here.

All the vertical families are illustrated in Fig.8. For E1, E2 and E3, the vertical orbits bend more towards the  $xy$ -plane and come close to the surface of the asteroid, as the  $z$ -amplitude increases. Similarly, the closer the orbit to the EPs, the stronger in-plane instability it has. However, orbits change from stable to unstable in  $z$ -direction when their  $z$ -amplitude exceeds 1.04 and 1.08 for E1 and E2, respectively, as indicated by the pentagrams of  $s_2$ . The orbits around E3 first reach the largest  $z$ -amplitude 1.31, and then bend back down to the asteroid. They always have vertical stability. However, the in-plane motion around E3 change from unstable to stable in the process of the orbits coming back to the body at a  $z$ -amplitude of 0.77. Similarly, new families of orbits are expected to be generated at the pentagram points.



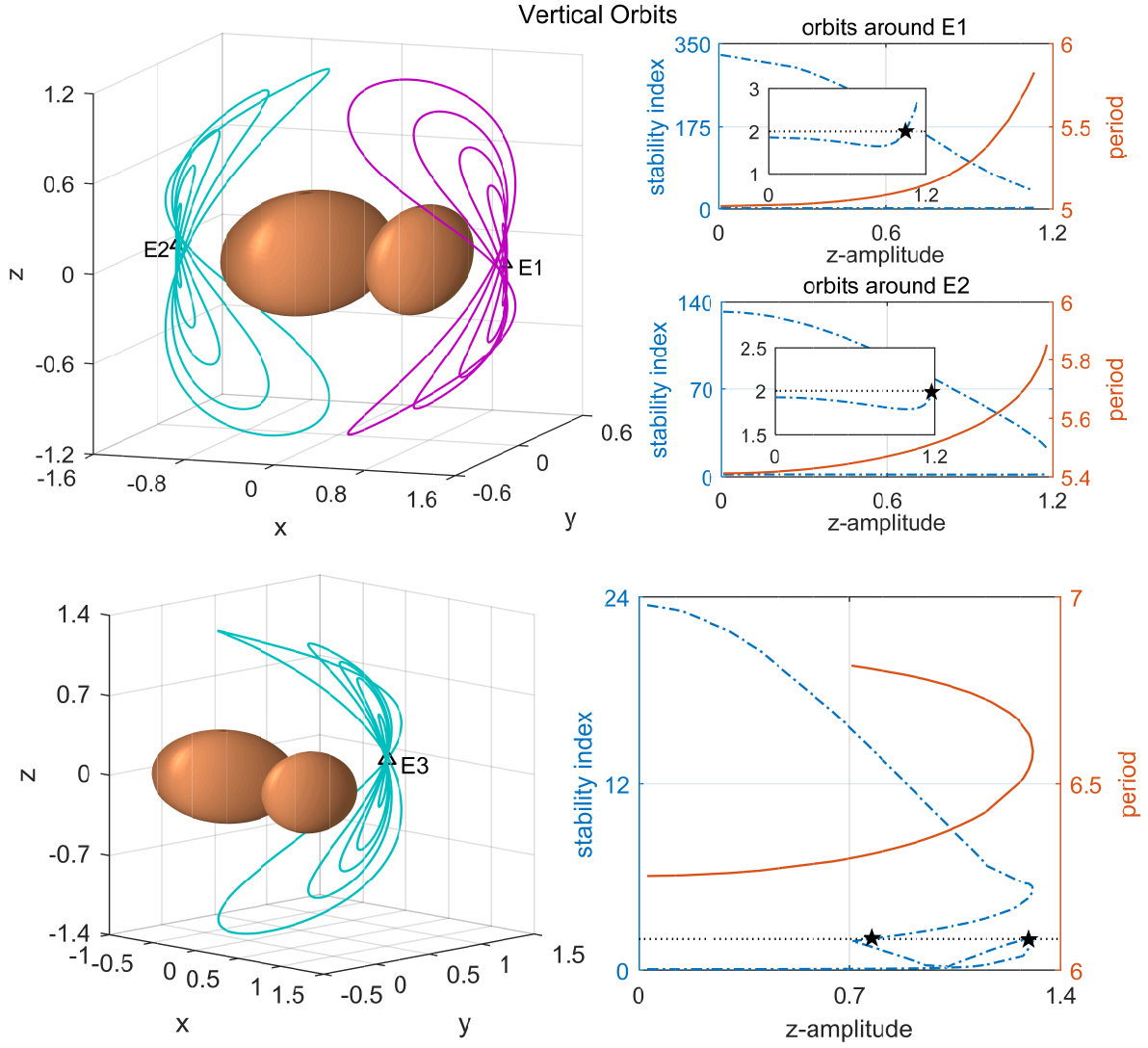


**Figure 8** Left: Vertical orbits in the vicinity of E1, E2 and E3; Right: their stability index  $s_1$  and  $s_2$  (blue dash-dotted lines) and corresponding periods (orange lines) as a function of the z-amplitude.

In summary, for the above three kinds of POs, the closer the orbit to the EPs, the larger in-plane instability it has. The Lyapunov orbits change from vertically stable to unstable with the increase of orbital amplitudes in the  $xy$ -plane. For Halo and Vertical families around E1 and E2, orbits with small z-amplitudes have vertical stability and then become unstable when their z-amplitudes are larger. However, they always have strong in-plane instability. Compared to orbits around E1 and E2, the orbits with similar size around E3 are less unstable. And a small portion of orbits around E3 even have in-plane stability. This is due to the fact that E3 (complex unstable) is less unstable than E1 and E2 which are hyperbolically unstable. Therefore, the general properties of orbital motion in the vicinity of the unstable EPs are characterized. For real missions, orbital control is required to stabilize the unstable orbits.

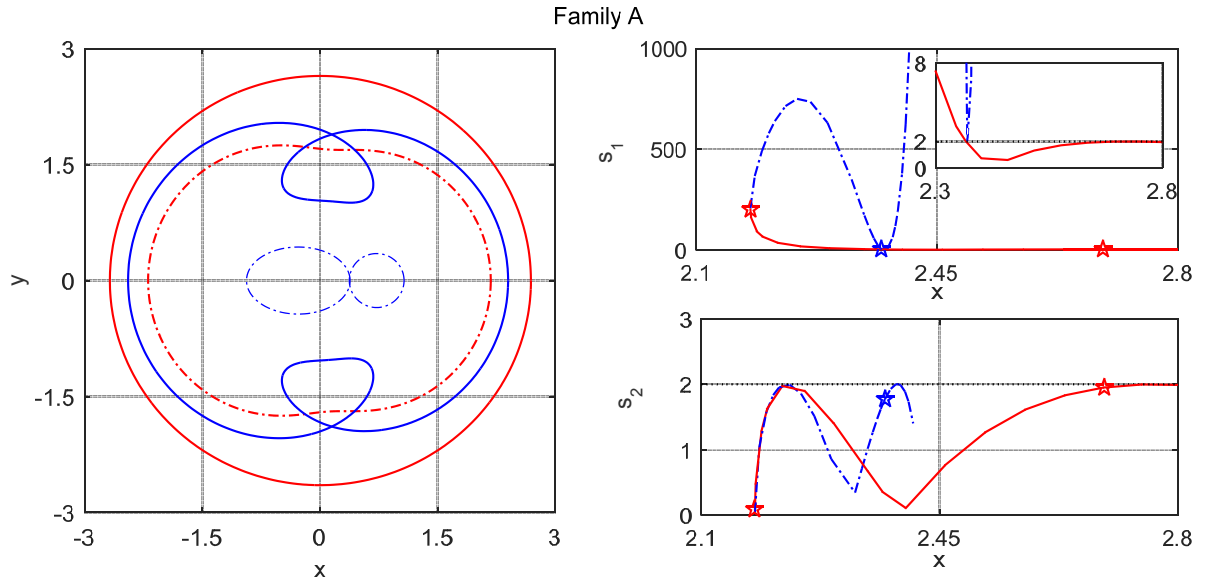
## 2.5 Orbital Motion around the System

### 2.5.1 Equatorial Orbits

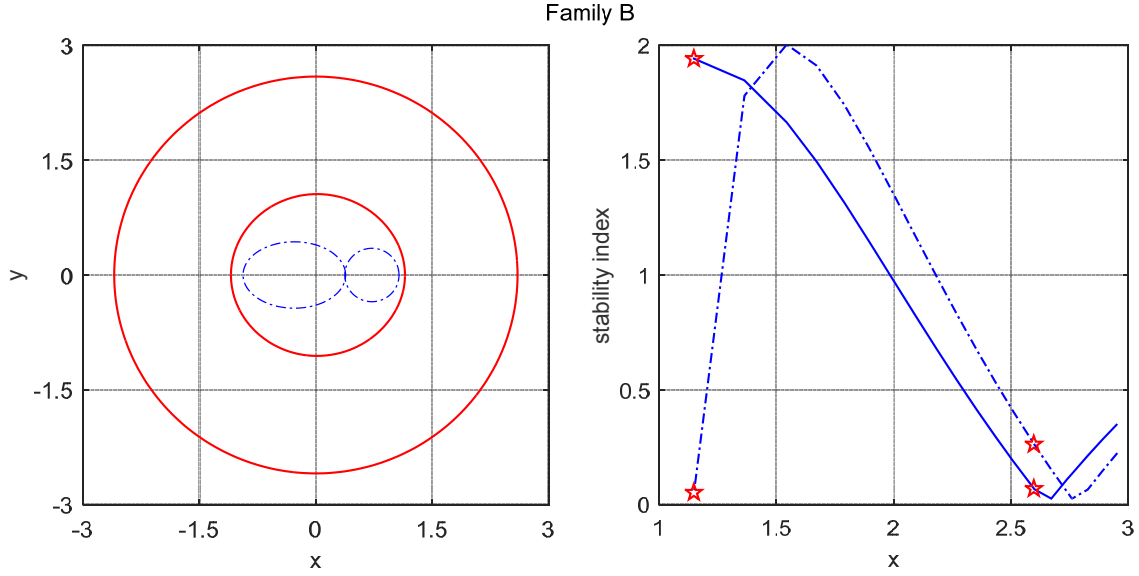
This section focuses on orbits around the entire asteroid system. Given that the rotation rate of the asteroid has value '1' in the normalized system, the initial conditions for an equatorial circular orbit in the rotating frame are expressed as

$$x_{rot} = r, y_{rot} = 0, \dot{x}_{rot} = 0, \dot{y}_{rot} = \pm\sqrt{GM/r} - r = \pm\sqrt{\delta/r} - r,$$

where the '+' and '-' signs represent prograde and retrograde orbits in the inertial frame, respectively. The prograde motion in the inertial frame is also prograde in the rotating frame if  $\dot{y}_{rot} = \sqrt{\delta/r} - r > 0$  given  $\delta > r^3$ , and becomes retrograde if  $\dot{y}_{rot} = \sqrt{\delta/r} - r < 0$  given  $\delta < r^3$ . The retrograde motion in the inertial frame is always retrograde in the rotating frame as  $\dot{y}_{rot} = -\sqrt{\delta/r} - r < 0$ . Therefore, the prograde and retrograde orbits in the inertial frame are denoted as families A and B, respectively. Examples of orbits of families A and B and their stability index are given in Figs.9 and 10.



**Figure 9** Left: three orbits of family A; Right: the stability indices  $s_1$  and  $s_2$ . The pentagrams represent the orbits in the left plot.



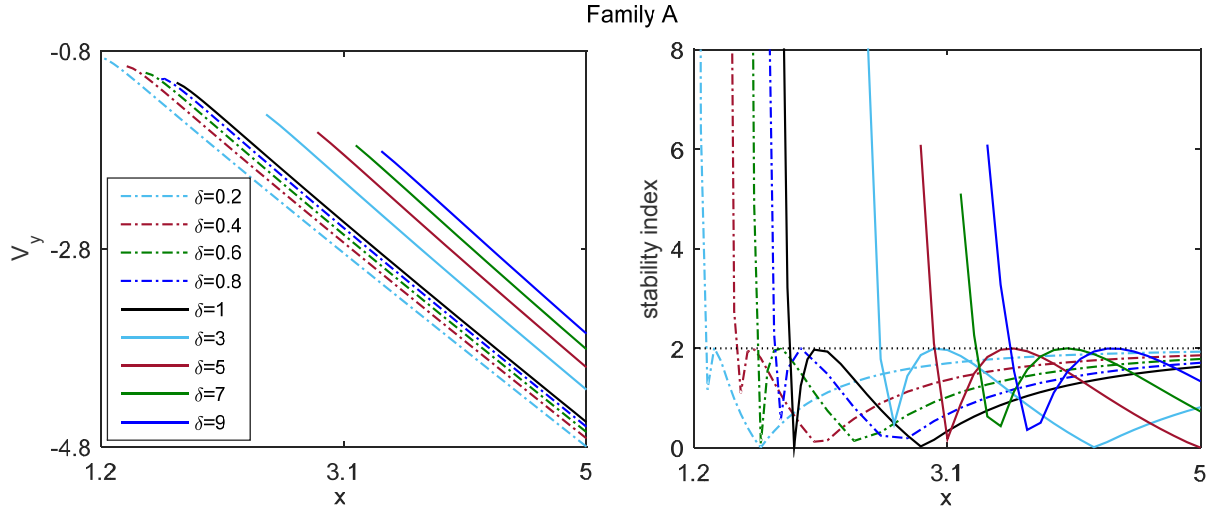
**Figure 10** Left: two orbits of family B; Right: the stability indices  $s_1$  (solid line) and  $s_2$  (dash-dotted line). The pentagrams represent orbits in the left plot.

Fig.9 illustrates three orbits around the contact binary system of family A, which is found to be all retrograde in the rotating frame. As the orbit comes close to the asteroid, it evolves from circular and stable (red solid) to distorted and unstable (red dash dotted). This is also reflected in the stability index plot: the closer the orbit to the asteroid the more unstable it is. In addition, a new family of orbits (blue) is generated at  $x \approx 2.4$  as the stability index reaches the value 2, when the bifurcation is expected. The blue orbit in the left plot of Fig.9 belongs to this family, which is characterized by two extra loops in the middle region. Similarly, this family of orbits also becomes highly unstable when approaching the asteroid. However, they all have vertical stability as illustrated by  $s_3$ . Therefore, the irregular shape of the asteroid is revealed to have a destabilizing effect on the retrograde A orbits.

Two orbits of family B are shown in the left plot of Fig.10; one is the closest orbit of this family around the asteroid with  $r \approx 1.2$  and the other one has a radius of 2.6. This family of orbits keeps the circular geometry even when it is in close vicinity of the asteroid. As indicated in the right plot, all these orbits are stable, as their stability indices are not larger than 2. Compared to family A, family B is more robust against the perturbing gravitational field and is preferable for a mission close to the asteroid. This is due to the fact that the relative rotation between family B orbits and the asteroid is generally faster than that of family A, and the perturbation is averaged (or smoothed) to some extent. This analysis is consistent with that of Scheeres et al. (2000). The influence of the parameter  $\delta$  on the stability and energy of these retrograde A and B orbits is studied quantitatively in the following section.

### 2.5.2 Effect of Parameter $\delta$ on Retrograde A and B Orbits

The above simulations are based on the physical parameters of the system 1996 HW1 with  $\delta = 2.1682$ . Now the value of  $\delta$  will be varied from 0.2 to 9, representing a wide range of the rotation rate of the asteroid. The value for  $\mu$  is kept at the value of 1996 HW1, i.e. 0.2767. Parameter  $\delta = 1$  is the situation for fast rotating asteroids, e.g. 2000EB<sub>14</sub> (Whiteley et al., 2002). The case  $\delta > 1$  is the more general situation as most contact binary asteroids rotate slowly, where a squeezing force exists between the two components.



**Figure 11** The position-velocity curves and position-stability index curves of family A orbits at different values of  $\delta$ . The horizontal dotted line in the right plot corresponds to stability index  $s = 2$ ; the dashed lines are for  $\delta < 1$  while the solid lines hold for  $\delta \geq 1$ .

Fig.11 gives the position-velocity curves and the position-stability index curves of family A orbits at different values of  $\delta$ , respectively. It is mentioned that all the orbits obtained here do not include the bifurcation families of orbits (which have been shown as the blue orbit in Fig.9), as the main purpose of this section is studying the effect of rotation rate of the asteroid on the orbital motion. It can be seen that all these orbits are retrograde ( $V_y < 0$ ) in the rotating frame. As the asteroid rotates faster (smaller  $\delta$ ) the orbits can be continued to the close vicinity of the asteroid, especially for the case  $\delta \leq 1$ . For the slowly rotating asteroids (large  $\delta$ ), family A orbits at close distance are not found. For the same  $x$ , the faster the rotation of the asteroid, the more initial velocity it requires for the orbital motion in the rotating frame.

The stability index is only plotted for  $s_1$ , since all orbits have vertical stability. Different with velocity, the stability index does not show a simple change tendency. For all  $\delta$ , as the orbits come close to the asteroid, after passing a bottom value the stability index touches the line  $s = 2$  (indicating bifurcations) and then experiences a low value again. After that it goes up sharply, indicating a fast growth of instability. Furthermore, the faster the rotation of the asteroid, the less the instability of the orbits have and a closer distance to the asteroid stable orbits can be obtained. This is in

contrast with the case of the non-collinear EPs (belong to the 1:1 resonance), which transform from stable to unstable when the rotation rate of the asteroid increases beyond a certain value.

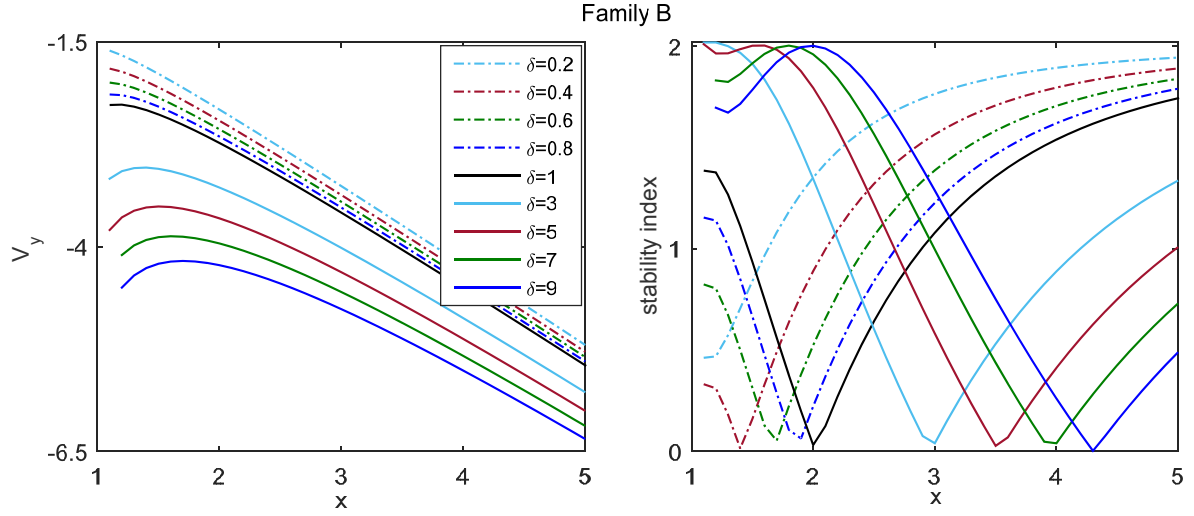


**Figure 12** The position-velocity curves and position-stability index curves of retrograde B orbits for different values of  $\delta$ . The dashed lines are for  $\delta < 1$  while the solid lines hold for  $\delta \geq 1$ .

For family B orbits, the position-velocity curves and the position-stability index curves at different values of  $\delta$ , respectively, are given in Fig.12. In general, for all  $\delta$ , stable orbits can be obtained in close vicinity of the asteroid, again proving the robustness property of family B orbits against gravitational perturbations. In contrast with family A, for the same  $x$ , the faster the rotation of the asteroid (small  $\delta$ ), the less initial velocity it requires for orbital motion in the rotating frame. All these orbits are linearly stable, as their stability index is within the range from 0 to 2. Similar to that of family A, the stability index arrives at the bifurcation point (namely  $s = 2$ ) after experiencing a bottom value close to 0 for the slow rotation cases. For the fast rotation situations, the stability index has a delay to reach the value of 2. In addition, from our simulations, it is also found that these orbits are stable at a further distance (e.g.  $x = 30$ ) from the asteroid.

In summary, both families of orbits obtained are retrograde in the rotating frame, in which family A has slow retrograde motion and family B has faster one. At the same distance to the asteroid, the orbits are more stable around a fast rotating asteroid than around a slow one. This emphasizes the stabilization effect of the fast rotation of the gravitational field on the equatorial motion, due to the averaging effect of the perturbation. In addition, as the orbit comes close to the asteroid, the dynamics will be subjected to bifurcation earlier for the slowly rotating asteroids. However, when the orbit is extremely close to the asteroid, the fast rotation can no longer diminish the effect of irregular gravity on family A orbits anymore. In general, family B is more stable than family A, and is more suitable for mission orbits.

### 2.5.3 Resonant Orbits

For completeness, the resonant orbits around the entire body are also explored in the rotating frame. Here we define the resonant orbit (with mean angular velocity rate  $\omega_{res}$ ) with commensurability  $N$  to the rotation of the asteroid with normalized velocity ‘1’, namely  $\omega_{res} = N$ . The initial conditions for this  $N$ -resonance orbit and its orbital period can be derived as

$$x_0 = \sqrt[3]{\delta/N^2}, y_0 = 0, z_0 = 0, \dot{x}_0 = 0, \dot{y}_0 = -N \cdot x_0 - x_0 = -\sqrt[3]{\delta N} - \sqrt[3]{\delta/N^2},$$

$$\dot{z}_0 = \sqrt{\delta/x_0} = \sqrt[3]{\delta N}, T = \begin{cases} 2\pi/N, N < 1 \\ 2\pi, N \geq 1 \end{cases}.$$

With these initial conditions, the DC method is applied and the polar resonant orbits can be obtained accurately. Examples of orbits at  $\delta = 1$  and  $\delta = 100$ , which respectively represent fast and slow rotation of the asteroid, are given in Figs.13 and 14. It can be seen that all these orbits have coverage of the polar region of the asteroid, which is interesting from the perspective of mission design.

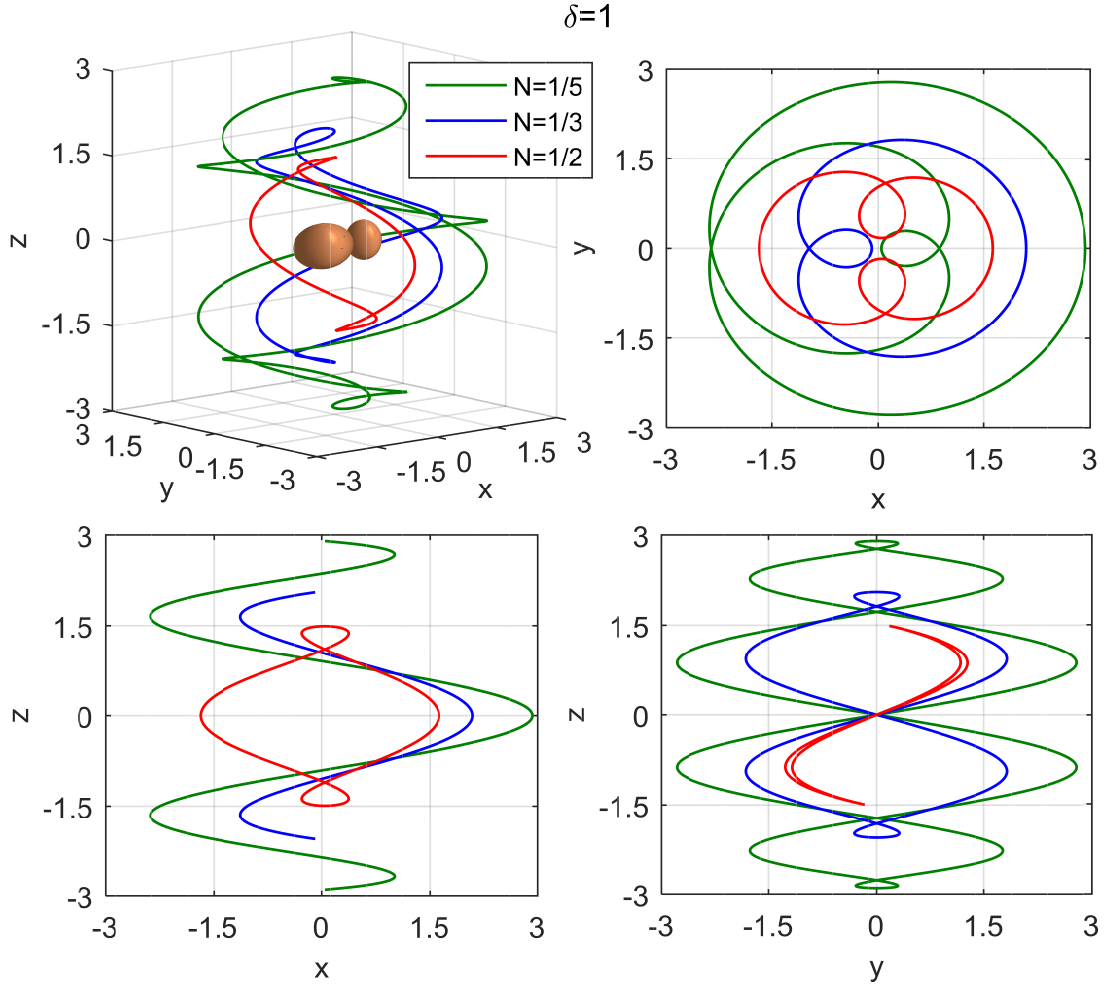


**Figure 13** 3-dimensional resonant orbits with  $N = 1/5, 1/3, 1/2$  at  $\delta = 1$  and their projections on the  $xy$ -,  $xz$ - and  $yz$ -planes.

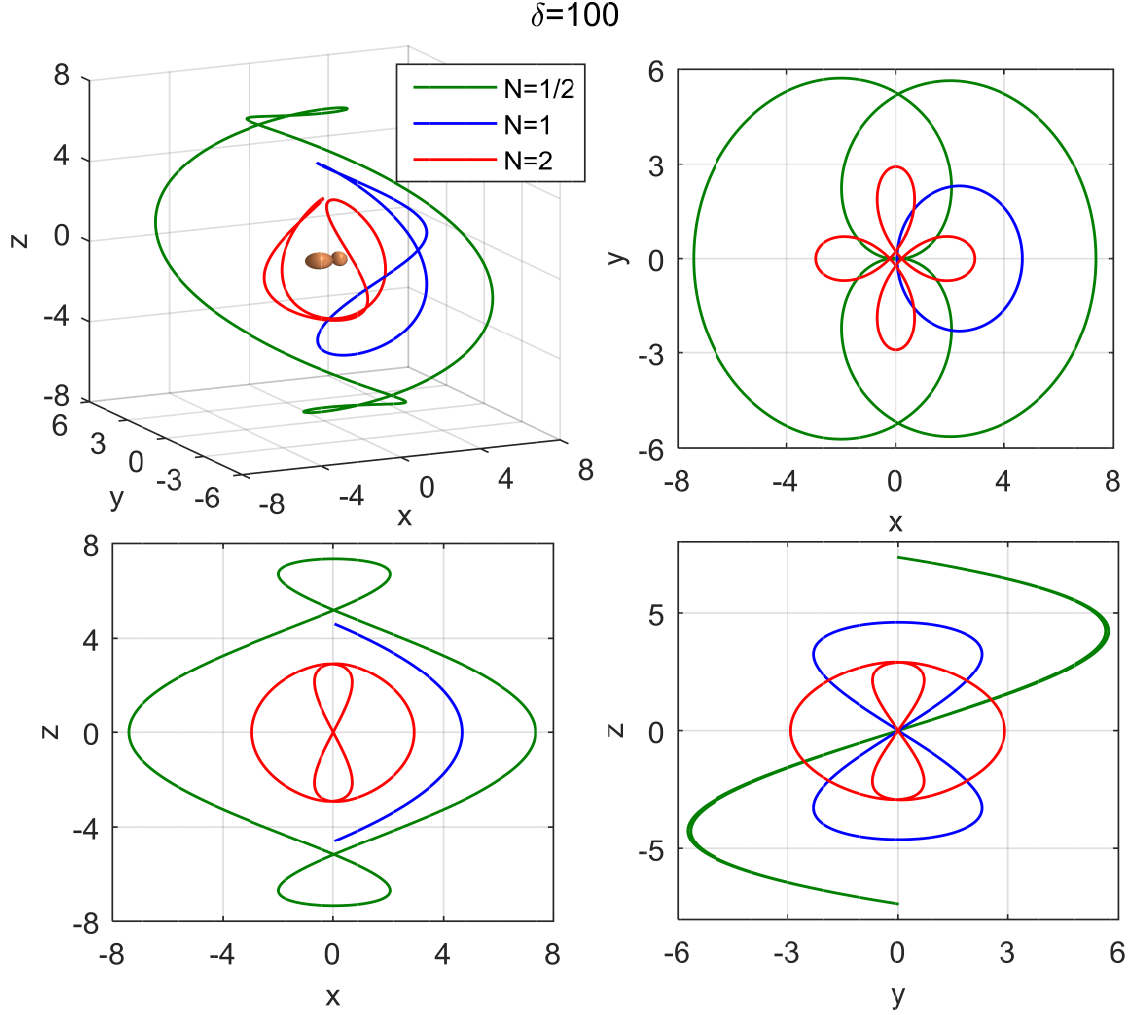


**Figure 14** 3-dimensional resonant orbits with  $N = 1/2, 1, 2$  at  $\delta = 100$  and their projections on the  $xy$ -,  $xz$ - and  $yz$ -planes.

For  $\delta = 1$ , only orbits with  $N < 1$  are studied as they physically exist. It is also found that as the orbit comes close to the asteroid, it transits from linearly stable to highly unstable, due to the increasing perturbations from the irregular gravitational field. The three orbits illustrated in Fig.13 are all unstable. For  $\delta = 100$ , orbits with  $N \leq 1$  and with small  $N > 1$  (e.g.  $N = 1$  and  $N = 2$ ) are obtained, but it is still difficult to identify orbits with large  $N$  values. The orbits shown in Fig.14 are also unstable. Different from the equatorial case, for the situation of resonance there is no general conclusion here about the influence of  $\delta$  on the resonant orbits. The absolute fast rotation of the asteroid is unable to guarantee the stability, as it is already known that the non-collinear EPs that belong to the 1:1 resonance become unstable at the fast rotation case. The commensurability  $N$  between the rotation of the asteroid and mean motion of the orbit and  $\delta$  both play a role on the stability of the resonant orbits.

In addition, according to Lara (2003), the resonant 3-dimensional orbits are the outcome of bifurcations that may appear along the family of planar periodic orbits. For the resonant orbits that have been obtained above, it is found that for  $\delta = 1$ , only the orbit with  $N = 1/3$  is close to the bifurcation that appears along the retrograde family

A. For  $\delta = 100$ , the orbits with  $N = 1/2$  and  $N = 1$  originate from the corresponding bifurcations generated from the retrograde family A and family B, respectively. This indicates that the highly non-spherical gravitational field and the rotation rate of the central body probably have an influence on the location of the bifurcations.

## 2.6 Conclusions

The general dynamical environment around contact binary asteroid systems is explored. Based on the physical parameters of 1996 HW1, four EPs were obtained and their stability was investigated. Families of the Lyapunov, Halo and vertical POs were found in the vicinity of these EPs. It was found that the closer the PO to the EPs, the more unstable it is. The locations of collinear E1 and E2 are sensitive to the change of rotation rate, but not to the system configuration; and they are always unstable. For the non-collinear E3 and E4, system configuration does have a significant influence on their locations. They transit from linear stability to complex instability with increasing rotation rate of the asteroid.

The equatorial orbits of families A and B around system 1996 HW1 were addressed. When family A orbits change size from further away from the asteroid to its close vicinity, they transit from stable to highly unstable. This is due to the perturbation from the highly irregular gravitational field. Family B orbits were found to remain stable even when they are extremely close to the asteroid and are robust against the gravitational perturbation. Therefore, family B is more preferable for mission orbits. In contrast to the stability of the non-collinear EPs, the fast rotation of the asteroid was proven to have a stabilizing effect on both family A and B orbits, namely the equatorial orbital motion, due to the averaging effect of the irregular gravitation. However, this stabilization cannot diminish the effect of irregular gravity on orbits in the extreme proximity to the asteroid for family A POs. Finally, resonant orbits were obtained at two rotation rates of the asteroid, i.e. fast case and slow case. They are all unstable but have a good coverage of the polar region of the body.

Overall,  $\mu$  and  $\delta$  were revealed to have significant influence on the orbital dynamics in the vicinity of the asteroids, and this study contributes to the exploration of the dynamical environment around highly bifurcated bodies.





# Chapter 3 Orbital Motion in the Vicinity of the Non-collinear Equilibrium Points

---

J. Feng, R. Noomen, J. Yuan

Published in *Planetary and Space Science*, Vol.117, p. 1-14, 2015

## Abstract

The orbital motion around the non-collinear equilibrium points (EPs) of a contact binary asteroid is investigated in this paper. A contact binary asteroid is an asteroid consisting of two lobes that are in physical contact. Here, it is represented by the combination of an ellipsoid and a sphere. The gravity field of the ellipsoid is approximated by a spherical harmonic expansion with terms  $C_{20}$ ,  $C_{22}$  and  $C_{40}$ , and the sphere by a straightforward point mass model. The non-collinear EPs are linearly stable for asteroids with slow rotation rates, and become unstable as the rotation rate goes up. To study the motion around the stable EPs, a third-order analytical solution is constructed, by the Lindstedt-Poincaré (LP) method. A good agreement is found between this analytical solution and numerical integrations for the motion in the vicinity of the stable EPs. Its accuracy decreases when the orbit goes further away from the EPs and the asteroid rotates faster. For the unstable EPs, the motions around them are unstable as well. Therefore, the linear feedback control law based on low thrust is introduced to stabilize the motion and track the reference trajectory. In addition, more control force is required as any of the injection error, the amplitude of the analytical reference orbit or the rotation rate of the asteroid increases. For small orbits around the EPs, the third-order analytical solution can serve as a good reference trajectory. However, for large amplitude orbits, accurate numerical orbits are to be used as reference. This avoids an extra control force to track the less accurate third-order analytical solution.

## 3.1 Introduction

This paper focuses on one specific type of asteroid, i.e. the contact binary asteroid, which consists of two lobes that are in physical contact and which represents the most bifurcated body. Together with comets, the contact binary body is estimated to constitute 10-20% of all small solar system bodies (Harmon et al., 2011). Rosetta's target comet (67P/Churyumov-Gerasimenko) was found to be probably a contact binary very recently (August 2014). A detailed investigation of the dynamical environment around them can shed light on the dynamical evolution of our solar system.

The highly irregular gravity field induced by such an asteroid can be modelled with different methods (Scheeres, 2012). Outside of the circumscribing sphere, a spherical

harmonic expansion truncated at arbitrary degree and order can be used. When closer to the body, the polyhedron method of approximation of the shape of a body with triangular faces is more valid (Werner and Scheeres, 1997). Another option is to approximate the gravity field by that of geometrical shapes (e.g. an ellipsoid<sup>1</sup>), in which case closed-form potentials can usually be obtained. Many studies have been carried out on the dynamical environment around highly bifurcated bodies, e.g. Castalia, Eros and Itokawa (Scheeres et al., 1996, Scheeres et al., 2004, Scheeres et al., 2000), mainly focusing on equilibrium points and periodic orbits. The polyhedron method is usually applied for the precise modelling of the gravity field, since it is robust and accurate.

Analytical work is typically to give a more general insight into dynamics, but this is difficult to perform with such a precise model. Therefore, for a general study of this kind of contact binary body, a simplified model of a combination of a sphere and an ellipsoid is applied here, as shown in Fig.1. For this specific configuration, possible formation mechanisms and the relationship between the relative configuration and the rotational angular momentum have been studied in detail in (Scheeres, 2007). This simplified model captures the main characteristics of the mass distribution of a contact binary body. Additionally, it breaks one-axial symmetry, which is one step further compared with other totally symmetrical shapes, e.g. two connected spheres (Prieto-Llanos and Gomez-Tierno, 1994), two orthogonal segments (Bartczak and Breiter, 2003), which were applied for analytical work. In (Tzirti and Varvoglis, 2014), the ellipsoid and the sphere components are separated and serve as the basic model of a binary asteroid pair.

Generally, the single-asteroid system has four EPs for the asteroid system, except for Betulia (Magri et al., 2007) which is known to have six ones due to its irregular gravity field. The linear stability of the EPs of an ellipsoid-shaped asteroid has been identified by (Scheeres, 1994), in which the asteroid is classified as Type I in the case of stable non-collinear EPs and Type II in the case of unstable ones. It is known that the collinear EPs are always unstable, whereas the non-collinear EPs transit from stable to unstable when the rotation rate of the asteroid increases. This is similar to the restricted three body problem (RTBP), for which the linear stability of the non-collinear EPs (known as the  $L_4$  and  $L_5$  points) bifurcates at the mass ratio  $\mu_c = 0.03852$  (Routh's critical value). Purely numerical methods have been applied for studying the motion around the EPs for a binary asteroid system (Gabern et al., 2006). In (Jiang et al., 2014), the first-order solution was described in the form of a series expansion form for motion around the EPs of asteroids with a gravity field from the

---

<sup>1</sup> According to Scheeres (2012), the 'closed-form' refers to an exact solution to Laplace's equation. The gravitational potentials of a bar, a straight segment and a polyhedron with constant density can also be expressed in closed form.

polyhedron method. However, little work has been done about high-order expansion of the motion around the non-collinear EPs of a contact binary body. This is the focus of the current study, in which the motion is expanded to the third order with the simplified gravity field and the influence of the rotation of the asteroid on the accuracy of the expansion is investigated.

For the stable EPs, a straightforward analytical technique for investigating this motion is the Lindstedt-Poincaré (LP) method. Its basic idea is that the non-linearity of the system alters the frequencies of the linearized system (Mickens, 1981). Extensive use of this technique has been made to obtain periodic solutions of various non-linear systems. One typical application of the LP method in celestial mechanics is the construction of third-order halo orbits around the collinear EPs in the RTBP (Richardson, 1980). Afterwards, extended work has been carried out by (Gómez, 2001, Jorba and Masdemont, 1999, Lei and Xu, 2013), in which analytical solutions in the vicinity of the collinear and non-collinear EPs have been constructed to arbitrary order. Additionally, taking into account the effects of the lunar orbital eccentricity and the solar gravity field in the Earth-Moon system, halo orbits and Lissajous orbits around the trans-lunar libration points have been obtained to the third order (Farquhar and Kamel, 1973). In Gómez and Marcote (2006), periodic orbits of the Hill model have been constructed, also by applying the LP method. With the real Earth-Moon model, the EPs of the original RTBP have been replaced by special quasi-periodic orbits, which are called dynamical substitutes (Hou and Liu, 2010). With the LP method, higher order analytical solutions of the periodic motion in the vicinity of these dynamical substitutes can be constructed (Hou and Liu, 2011). Therefore, the LP method is also applied in this paper but with a highly irregular gravity field.

As for the unstable EPs, the orbital motion around them is also unstable. Therefore, a low-thrust control strategy with the optimal linear feedback control law is employed for tracking the nominal orbital motion. The basic idea of this control method is to eliminate the unstable component of the motion and follow the desired trajectory. This method is widely applied for stabilizing unstable non-linear dynamical systems, and is well suited for orbit maintenance around the collinear EPs in the RTBP (Farquhar, 1970, Gurfil and Meltzer, 2006).

This paper is organized as follows. Firstly, a simplified model of a rotating contact binary asteroid is introduced. Secondly, based on the parameters of the system 1996 HW1 which is one of the most bifurcated body known to date (Magri et al., 2011), the location of the non-collinear EPs and their linear stability are investigated at different rotation rates of the asteroid. Thirdly, for the stable EPs, periodic and quasi-periodic orbits are analytically constructed to the third order by means of the LP method. The accuracy of these analytical orbits and the influence of the orbit amplitude and the rotation rate of the asteroid are investigated by numerical integration. Finally, for the unstable EPs, linear feedback control is applied to track the third-order analytical orbit.

Again, the influence of the rotation of the asteroid and the orbit amplitude on the propellant consumption is also studied. In addition, for large orbit amplitudes, an accurate orbit numerically derived from the third-order analytical solution is also tracked, to quantify the extra control force consumed by following the less accurate analytical solution.

This study provides a method of studying the dynamics around contact binary bodies, i.e. taking the two components individually from the gravity field point of view. The analytical solutions obtained here can serve as the initial point for solving dynamics in the precise gravity field, once the two components of the body are determined from observations.

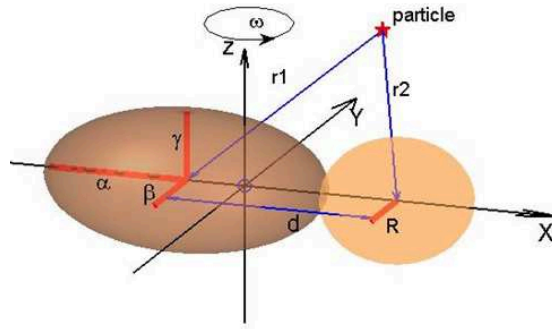


**Figure 1** The ellipsoid-sphere configuration of a contact binary asteroid system.

### 3.2 Dynamical Model

The geometry of the ellipsoid-sphere configuration is illustrated in Fig.1. The system is assumed to be homogeneous (i.e. the same density for both components) and to rotate uniformly with rotation velocity  $\vec{\omega}$ . The mass ratio  $\mu$  is equal to  $m_s/(m_s + m_e) = R^3/(R^3 + abc)$  ( $m_s$  and  $m_e$  are the mass of the sphere and the ellipsoid, respectively;  $a, b, c$  are the three semi-axes of the ellipsoid and  $R$  is the radius of the sphere). The total mass is denoted as  $M = m_s + m_e$ . The vector between the centers of mass of the two components is defined to be  $\vec{d}$  (from ellipsoid to sphere), where  $|\vec{d}| = a + R$ . In the body-fixed frame ( $XYZ$ -frame), the gravitational potential is invariant. The equation of motion in the vicinity of the asteroid is expressed in this frame as

$$\ddot{\vec{r}} + 2\vec{\omega} \times \dot{\vec{r}} + \vec{\omega} \times (\vec{\omega} \times \vec{r}) = \frac{\partial U_{se}}{\partial \vec{r}}, \quad (1)$$

where  $\vec{r} = (\tilde{x}, \tilde{y}, \tilde{z})$  is the state vector and

$$\begin{aligned}
 U_{se} &= U_s + U_e = GM \cdot \left[ \frac{\mu}{r_1} + (1-\mu) \cdot U_e(\vec{r}_2) \right] \\
 &= GM \cdot \left\{ \frac{\mu}{r_1} + \frac{1-\mu}{r_2} + (1-\mu) \cdot \left( \tilde{C}_{20} \left( \frac{3\tilde{z}^2}{2r_2^5} - \frac{1}{2r_2^3} \right) + \tilde{C}_{22} \frac{3[(\tilde{x}+\mu)^2 - \tilde{y}^2]}{r_2^5} + \frac{\tilde{C}_{40}}{8} \left( \frac{35\tilde{z}^4}{r_2^9} - \frac{30\tilde{z}^2}{r_2^7} + \frac{3}{r_2^5} \right) \right) \right\},
 \end{aligned}
 \tag{2}$$

in which  $U_e$  is the ellipsoid potential of unit mass in spherical harmonics,  $\vec{r}_2 = (\tilde{x}, \tilde{y}, \tilde{z}) - (1-\mu)\vec{d}$  and  $\vec{r}_1 = (\tilde{x}, \tilde{y}, \tilde{z}) + \mu\vec{d}$  are the vectors from the sphere center at  $(1-\mu, 0, 0)$  and ellipsoid center at  $(-\mu, 0, 0)$  to the particle at  $(\tilde{x}, \tilde{y}, \tilde{z})$ , respectively, and  $r_1 = |\vec{r}_1|$ ,  $r_2 = |\vec{r}_2|$ .  $\tilde{C}_{20}, \tilde{C}_{22}, \tilde{C}_{40}$  are the spherical harmonics coefficients of the ellipsoid component. The system can be normalized by taking the length unit as  $d = |\vec{d}|$  and the time unit as  $\omega^{-1} = |\vec{\omega}|^{-1}$ . The normalized state vector is written as  $\vec{r}_n = (x, y, z)$ . In addition, the normalized spherical harmonic coefficients  $C_{20}, C_{22}$  and  $C_{40}$  can be derived from the shape of the ellipsoid. They are expressed as

$$\begin{cases} C_{20} = \frac{1}{5d^2} \left( c^2 - \frac{a^2 + b^2}{2} \right) \\ C_{22} = \frac{1}{20d^2} (a^2 - b^2) \\ C_{40} = \frac{15}{7} (C_{20}^2 + 2C_{22}^2) \end{cases}. \tag{3}$$

Since the ellipsoid component is totally symmetric, there are no odd terms. In addition, the higher-order spherical harmonics are ignored as their coefficients are usually very small, e.g.  $C_{42}$  and  $C_{44}$  are usually one or two orders of magnitude smaller than  $C_{40}$ <sup>2</sup>. Their contribution to the results is limited, whereas they introduce significant complexity for solving the dynamics. After normalization, the equations of motion for this dynamical system can be expressed as

$$\begin{cases} \ddot{x} = 2\dot{y} + \frac{\partial \Omega}{\partial x} \\ \ddot{y} = -2\dot{x} + \frac{\partial \Omega}{\partial y} \\ \ddot{z} = \frac{\partial \Omega}{\partial z} \end{cases}, \tag{4}$$

in which  $\Omega$  is the effective potential, written as

$$\Omega = \frac{x^2 + y^2}{2} + \delta \cdot \bar{U}_{se},$$

---

<sup>2</sup> It should be noticed that the spherical harmonics expansion here is only for the ellipsoid component, not for the entire body.

where  $\delta = GM/\omega^2 d^3$  is the ratio of the gravitational force to the centripetal force and  $\bar{U}_{se}$  is the normalized potential. It should be mentioned here that the RTBP can be determined by a single parameter, the mass ratio  $\mu$ , but the contact binary model has a second one which is related to the uncoupled rotation of the body, the parameter  $\delta$ . The value of  $\delta$  to some extent reflects the internal forces between the two components, as  $\delta = 1$  indicates the case that the two are just touching one another, without any internal forces; compression for  $\delta > 1$ ; and stretch for  $\delta < 1$ . In (Scheeres, 1994), there is a similar parameter  $\delta$  of the ellipsoid model, with the difference that the length  $d$  is defined as the semi-axis of the ellipsoid there.

### 3.3 Non-collinear EPs and their Stability

The EPs are defined as the point where all the accelerations are zero. They can be obtained by finding the roots of Eq.(4) numerically, and are denoted as  $(x_e, y_e, z_e)$ . The orbital motion relative to an arbitrary EP can be expressed as

$$\begin{cases} \ddot{\xi} - 2\dot{\eta} = \frac{\partial \Omega}{\partial \xi} \\ \ddot{\eta} + 2\dot{\xi} = \frac{\partial \Omega}{\partial \eta} \\ \ddot{\zeta} = \frac{\partial \Omega}{\partial \zeta} \end{cases}, \quad (5)$$

where  $(\xi, \eta, \zeta)^T = (x, y, z)^T - (x_e, y_e, z_e)^T$  is the position offset w.r.t. the EP. For dynamics around such an asteroid, the location and stability of the EPs are heavily dependent on the gravity field and the rotation rate of the body. Based on the assumption that the asteroid rotates uniformly along the  $z$ -direction, the second partial derivatives  $\Omega_{xz}, \Omega_{zx}, \Omega_{yz}, \Omega_{zy}$  evaluated at the EPs are all zero. Therefore, the motion in the  $xy$ -plane is uncoupled from that along the  $z$ -direction for the linearized system which can be expressed as follows

$$\begin{cases} \ddot{\xi} - 2\dot{\eta} = \Omega_{11}\xi + \Omega_{12}\eta \\ \ddot{\eta} + 2\dot{\xi} = \Omega_{21}\xi + \Omega_{22}\eta \\ \ddot{\zeta} = \Omega_{33}\zeta \end{cases}. \quad (6)$$

The partial derivatives  $\Omega_{ij}$  evaluated at the non-collinear EP are given in Appendix A. Now, given the parameters of 1996 HW1 (Appendix B), the EPs are illustrated in Fig.2.

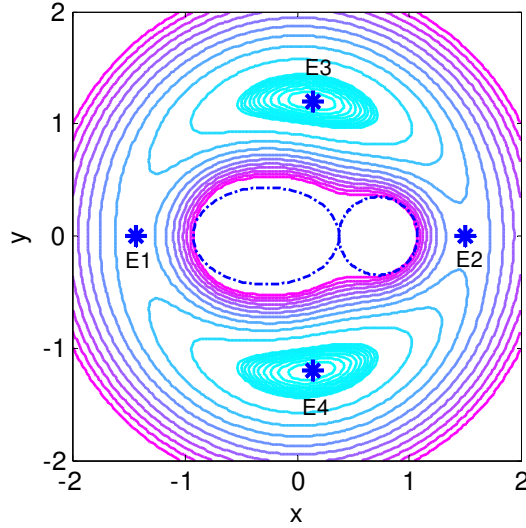


**Figure 2** The position of the EPs of system 1996 HW1; E3 and E4 are the non-collinear EPs<sup>3</sup>.

Once the EPs are obtained, their linear stability can be determined from the eigenvalues of the Jacobian matrix (Chicone, 1999). Since the motion in the  $xy$ -plane is independent of that along the  $z$ -direction, they can be studied separately. The characteristic equation in the  $xy$ -plane can be written as

$$\lambda^4 + (4 - \Omega_{11} - \Omega_{22}) \cdot \lambda^2 + \Omega_{11}\Omega_{22} - \Omega_{12}^2 = 0.$$

The  $xy$ -plane motion around the EP is stable only when the above equation has two pairs of purely imaginary characteristic roots, denoted by  $\pm i\omega_0, \pm iv_0$ . The following conditions need to be satisfied:

$$\begin{cases} C1 = 4 - \Omega_{11} - \Omega_{22} > 0 & (7a) \\ C2 = \Omega_{11}\Omega_{22} - \Omega_{12}^2 > 0 & (7b) \\ C3 = (4 - \Omega_{11} - \Omega_{22})^2 - 4(\Omega_{11}\Omega_{22} - \Omega_{12}^2) > 0 & (7c) \end{cases}.$$

For the motion in the  $z$ -direction, the characteristic equation is given as

$$\lambda^2 - \Omega_{33} = 0.$$

This motion is stable if  $\Omega_{33} < 0$ , and the characteristic root is represented as  $\pm iu_0$ . The three frequencies can be obtained as

$$\omega_0 = \sqrt{\frac{C1 - \sqrt{C3}}{2}}, v_0 = \sqrt{\frac{C1 + \sqrt{C3}}{2}}, u_0 = \sqrt{-\Omega_{33}}.$$

It is known that in the RTBP, the triangular EPs are linearly stable if the mass ratio  $\mu$  of the system is smaller than  $\mu_c = 0.03852$ . However, in our problem there is an additional parameter  $\delta$  (see Section 2) that will have an additional effect on the

<sup>3</sup> This figure is identical to Fig. 3 on page 25, with the difference that E1 and E2 have reversed their numbering. In this paper, the focus is on the non-equilibrium EPs E3 and E4. E1 and E2 presented here are only for notification.



stability of the non-collinear EPs. For each specific system, there is a critical value  $\delta_c$  (the bifurcation point for linear stability) which can be determined from numerical simulation. At this point, the system has one pair of pure imaginary eigenvalues of multiplicity two, which means that

$$(4 - \Omega_{11} - \Omega_{22})^2 - 4(\Omega_{11}\Omega_{22} - \Omega_{12}^2) = 0.$$

According to (Magri et al., 2011), the system 1996 HW1 has  $\mu = 0.27673$  and  $\delta = 2.1682$ . As a result, its non-collinear EPs are unstable. Compared with Figure 11 from (Magri et al., 2011), in which a full gravity field is applied, the locations of the EPs we obtained are quite close to theirs and the linear stability of the EPs are the same. This means that the main dynamics of the full gravity field is captured with this simplified model.

Given this value of  $\mu$ , the effect of  $\delta$  on the location and stability of the EPs can be identified. Fig.3a shows the location of the non-collinear EPs, where the red line represents the unstable EP and the blue line holds for the stable EP. The bifurcation point of this system is found to be  $\delta_c = 22.30624$ . The bifurcation diagram in Fig.3b describes the eigenvalues in the  $xy$ -plane.

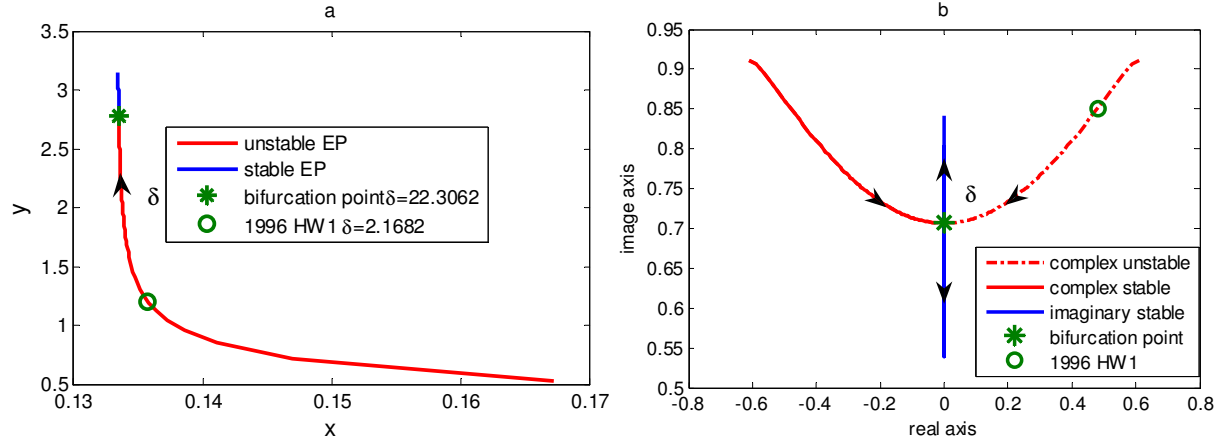


**Figure 3** The bifurcation diagram where the arrow represents the evolution of the system when  $\delta$  increases from 0.3 to 32.

The red lines represent the two pairs of conjugate complex eigenvalues. The red dotted line in the right half complex plane corresponds to the pair with a positive real component, while the red solid line in the left half plane holds for the pair with negative real parts. As  $\delta$  increases, the two pairs of complex eigenvalues evolve into pure imaginary eigenvalues as demonstrated by the blue line. Based on the characteristics of the stable and unstable non-collinear EPs, the motion in their vicinity can be studied in detail, which is addressed in the following sections.

### 3.4 Motion Around the Stable Non-collinear EPs

This section focuses on how the LP method is applied in our model, to obtain periodic and quasi-periodic orbits around the stable non-collinear EPs.

### 3.4.1 The Third-order Analytical Orbits

Following the LP method, the general procedure to construct the analytical solutions from low orders to high orders (to be defined later) is given. It is actually a recursion process which determines the coefficients of each order from the ones of lower orders. The solution of the linear system serves as the starting point. For the stable EPs, Eq.(6) have three pairs of pure imaginary roots. Since the out-of-plane motion is uncoupled from the in-plane motion, the general solution of the linearized system Eq.(6) can be expressed as

$$\begin{cases} \xi = \alpha \cos(\theta_1) + \beta \cos(\theta_2) \\ \eta = a_1 \alpha \cos(\theta_1) + b_1 \alpha \sin(\theta_1) + a_2 \beta \cos(\theta_2) + b_2 \beta \sin(\theta_2) , \\ \varsigma = \gamma \cos(\theta_3) \end{cases} \quad (8)$$

where  $\theta_1 = \omega_0 t + \phi_1$ ,  $\theta_2 = v_0 t + \phi_2$ ,  $\theta_3 = u_0 t + \phi_3$ , and  $\omega_0, v_0, u_0$  are the three frequencies mentioned in Section 3,  $\phi_1, \phi_2, \phi_3$  are the initial phase angles, and  $\alpha, \beta, \gamma$  are the amplitudes of the corresponding components. The coefficients in the solution have the following form

$$a_1 = \frac{\Omega_{12} \cdot b_1}{2 \cdot \omega_0}, \quad b_1 = -\frac{2\omega_0(\omega_0^2 + \Omega_{11})}{4\omega_0^2 + \Omega_{12}^2}, \quad a_2 = \frac{\Omega_{12} \cdot b_2}{2v_0}, \quad b_2 = -\frac{2v_0(v_0^2 + \Omega_{11})}{4v_0^2 + \Omega_{12}^2}.$$

When the nonlinear terms are taken into account, the motion can be expanded into trigonometric series of the amplitudes  $\alpha, \beta, \gamma$ . This is analogous to that of the collinear EPs (Jorba and Masdemont, 1999), with the difference that there are three frequencies here. The general form of the high-order solution of Eq.(5) can be written as

$$\begin{cases} \xi = \sum_{i,j,k=1}^{\infty} [\xi_{ijk}^{lmn} \cos(l\theta_1 + m\theta_2 + n\theta_3) + \bar{\xi}_{ijk}^{lmn} \sin(l\theta_1 + m\theta_2 + n\theta_3)] \alpha^i \beta^j \gamma^k \\ \eta = \sum_{i,j,k=1}^{\infty} [\eta_{ijk}^{lmn} \cos(l\theta_1 + m\theta_2 + n\theta_3) + \bar{\eta}_{ijk}^{lmn} \sin(l\theta_1 + m\theta_2 + n\theta_3)] \alpha^i \beta^j \gamma^k , \\ \varsigma = \sum_{i,j,k=1}^{\infty} [\varsigma_{ijk}^{lmn} \cos(l\theta_1 + m\theta_2 + n\theta_3) + \bar{\varsigma}_{ijk}^{lmn} \sin(l\theta_1 + m\theta_2 + n\theta_3)] \alpha^i \beta^j \gamma^k \end{cases} \quad (9)$$

in which  $\theta_1 = \omega t + \phi_1$ ,  $\theta_2 = v t + \phi_2$ ,  $\theta_3 = u t + \phi_3$  and  $\xi_{ijk}^{lmn}, \bar{\xi}_{ijk}^{lmn}, \eta_{ijk}^{lmn}, \bar{\eta}_{ijk}^{lmn}, \varsigma_{ijk}^{lmn}, \bar{\varsigma}_{ijk}^{lmn}$  are the coefficients to be determined at the order of  $N$ . Here, the order of the analytical solution is defined as the sum of the three power magnitudes,  $N = i + j + k$ . The numbers  $i, j, k$  are non-negative integers, and  $l, m, n$  are the coefficients of the frequencies and also integers. Due to the influence of the nonlinear terms, the frequencies are no longer constant and can be expanded in power series of amplitudes

$$\omega = \omega_0 + \sum_{i,j,k=1}^{\infty} \omega_{ijk} \alpha^i \beta^j \gamma^k, \quad v = v_0 + \sum_{i,j,k=1}^{\infty} v_{ijk} \alpha^i \beta^j \gamma^k, \quad u = u_0 + \sum_{i,j,k=1}^{\infty} u_{ijk} \alpha^i \beta^j \gamma^k \quad (10)$$

and  $\omega_{ijk}, v_{ijk}, u_{ijk}$  are also coefficients to be determined. Due to the characteristics of the LP method and the symmetries of our model, the following conditions are met:

- (1)  $\begin{cases} k \text{ is even, } \xi_{ijk}^{lmn} = \bar{\xi}_{ijk}^{lmn} = 0 \\ k \text{ is odd, } \xi_{ijk}^{lmn} = \bar{\xi}_{ijk}^{lmn} = \eta_{ijk}^{lmn} = \bar{\eta}_{ijk}^{lmn} = 0 \end{cases}$ .
- (2)  $|l| \leq i, |m| \leq j, |n| \leq k$  and  $l, m, n$  have the same parity with  $i, j, k$ , respectively. Considering the symmetries of the solution, in general  $l \geq 0$  is assumed, and  $m \geq 0$  is assumed if  $l = 0$ ,  $n \geq 0$  is assumed if  $l = m = 0$ .
- (3)  $\omega_{ijk}, v_{ijk}, u_{ijk}$  are non-zero only if  $i, j, k$  are all even numbers.

Suppose we already have the solution up to the order  $N - 1$ . We substitute it into Eq.(5), group all unknown terms of the order  $N$  at the left-hand side of the equation and all the known terms of the order  $N$  at the right-hand side, then we can solve the unknown terms from the known terms. Generally, the known terms of the order  $N$  are only determined by the solution up to the order  $N - 1$ , so the recursive process is valid. The first-order solution to start the recurrence process is

$$\xi_{100}^{100} = 1, \xi_{010}^{010} = 1, \eta_{100}^{100} = a_1, \bar{\eta}_{100}^{100} = b_1, \eta_{010}^{010} = a_2, \bar{\eta}_{010}^{010} = b_2, \zeta_{001}^{001} = 1.$$

Substitution of the solution up to the order  $N - 1$  into the right-hand part of Eq.(5) is straightforward. It does not produce any unknown terms of the order  $N$ . For the left-hand part of Eq.(5), the process is complicated. Take the  $\xi$  component as an example; how this process is proceeded is given in Appendix C. Similar results can be derived for  $\eta, \bar{\eta}, \zeta, \bar{\zeta}$ . Thus, equating the coefficients of the order  $N$  terms at both sides of the equation will give us the equations for the unknown coefficients, written in matrix form as

$$\begin{bmatrix} A_{11} & A_{12} & A_{13} & A_{14} \\ A_{21} & A_{22} & A_{23} & A_{24} \\ A_{31} & A_{32} & A_{33} & A_{34} \\ A_{41} & A_{42} & A_{43} & A_{44} \end{bmatrix} \begin{bmatrix} \xi_{ijk}^{lmn} \\ \bar{\xi}_{ijk}^{lmn} \\ \eta_{ijk}^{lmn} \\ \bar{\eta}_{ijk}^{lmn} \end{bmatrix} + \begin{bmatrix} \Delta_{\xi} \\ \Delta_{\bar{\xi}} \\ \Delta_{\eta} \\ \Delta_{\bar{\eta}} \end{bmatrix} = \begin{bmatrix} M_{ijk}^{lmn} \\ \bar{M}_{ijk}^{lmn} \\ N_{ijk}^{lmn} \\ \bar{N}_{ijk}^{lmn} \end{bmatrix}. \quad (11)$$

The components of matrix  $A_{4 \times 4}$  are expressed as

$$A_{11} = -\Lambda^2 - \Omega_{11}, A_{12} = 0, A_{13} = -\Omega_{12}, A_{14} = -2\Lambda, A_{21} = A_{12}, A_{22} = A_{11}, A_{23} = -A_{14}, A_{24} = A_{13},$$

$$A_{31} = -\Omega_{21}, A_{32} = 2\Lambda, A_{33} = -\Lambda^2 - \Omega_{22}, A_{34} = 0, A_{41} = -A_{32}, A_{42} = A_{31}, A_{43} = A_{34}, A_{44} = A_{33}.$$

where  $\Lambda = l\omega_0 + mv_0 + nu_0$ . The  $\Delta_i$  represents the expressions of frequencies at the order  $N - 1$  and solutions at order 1, and can be obtained from Tables 1 and 2 as

$$\begin{bmatrix} \Delta_{\xi} \\ \Delta_{\bar{\xi}} \\ \Delta_{\eta} \\ \Delta_{\bar{\eta}} \end{bmatrix} = \begin{bmatrix} -\omega_0 - b_1 \\ a_1 \\ -a_1\omega_0 \\ -b_1\omega_0 - 1 \end{bmatrix} \cdot 2\omega_{i-1jk} \delta_{l1} \delta_{m0} \delta_{n0} + \begin{bmatrix} -v_0 - b_2 \\ a_2 \\ -a_2v_0 \\ -b_2v_0 - 1 \end{bmatrix} \cdot 2v_{ij-1k} \delta_{l0} \delta_{m1} \delta_{n0}.$$

In addition, for the  $\zeta$  component, the equation is

$$B \cdot \begin{bmatrix} \xi_{ijk}^{lmn} \\ \bar{\xi}_{ijk}^{lmn} \end{bmatrix} + \begin{bmatrix} \Delta_{\zeta} \\ \Delta_{\bar{\zeta}} \end{bmatrix} = \begin{bmatrix} P_{ijk}^{lmn} \\ \bar{P}_{ijk}^{lmn} \end{bmatrix}, \quad (12)$$

where  $B = -\Lambda^2 - \Omega_{33}$ ,  $\Delta_\zeta = -2u_0 u_{ijk-1} \delta_{l0} \delta_{m0} \delta_{n1}$ ,  $\Delta_{\bar{\zeta}} = 0$ .

In Eqs. (11) and (12),  $M_{ijk}^{lmn}$ ,  $\bar{M}_{ijk}^{lmn}$ ,  $N_{ijk}^{lmn}$ ,  $\bar{N}_{ijk}^{lmn}$  and  $P_{ijk}^{lmn}$ ,  $\bar{P}_{ijk}^{lmn}$  are the known components of the equations of motion at the corresponding order. Some special cases should be remarked here:

- (1) when  $n \neq 0$ , the determinant of matrix  $\mathbf{A}$  is non-zero, and Eq.(11) can be solved directly.
- (2) when  $(l, m, n) = (1, 0, 0)$  or  $(l, m, n) = (0, 1, 0)$ , matrix  $\mathbf{A}$  is not full rank, then it is assumed that  $\xi_{ijk}^{lmn} = \bar{\eta}_{ijk}^{lmn} = 0$ , and  $\bar{\xi}_{ijk}^{lmn}$ ,  $\eta_{ijk}^{lmn}$ ,  $\omega_{i-1jk}$ ,  $v_{ij-1k}$  can be found.
- (3) when  $(l, m, n) = (0, 0, 0)$ , matrix  $\mathbf{A}$  is also not full rank, then it is assumed that  $\bar{\xi}_{ijk}^{lmn} = \bar{\eta}_{ijk}^{lmn} = 0$  and  $\xi_{ijk}^{lmn}$ ,  $\eta_{ijk}^{lmn}$  can be solved.
- (4) when  $(l, m, n) = (0, 0, 1)$ ,  $\zeta_{ijk}^{lmn} = \bar{\zeta}_{ijk}^{lmn} = 0$  is assumed and  $u_{ijk-1}$  is obtained.

Therefore, the  $N^{\text{th}}$ -order solution can be obtained by solving the above equations. Neglecting the possible resonances (which brings about small denominator problem), this process can be theoretically carried on to arbitrary order. The third-order solution is given in this paper. The coefficients of the solution are given in Appendix C, based on the parameters of system 1996 HW1 but with  $\delta = 30$ , in which case the non-collinear EPs are stable (Fig.3). With this solution in series expansion form, periodic and quasi-periodic orbits around the EPs are constructed.

### 3.4.2 Numerical Verification

To test the accuracy of the third-order analytical solution, numerical simulations are performed in the full model (Eq.(5)), the results of which are shown in Figs.4-9. They cover all possible motions in the vicinity of a stable non-collinear EP. All units in the figure are dimensionless and the non-collinear EP is located at the origin of the coordinate frame. The amplitudes are chosen such that the size of the orbit remains around the value of 0.1, and the integration time is selected to insure that the general characteristics of the orbital motion are properly reflected. Figs.4-6<sup>4</sup> illustrate the periodic orbits and the numerical orbits with one amplitude equal to 0.1, which also means that only one frequency plays a role for each plot. Figures 7-8 show quasi-periodic orbits with combinations of two frequencies. Fig.7 is the plot of general planar motion with  $\gamma = 0$ , while Fig.8 is comparable to a Lissajous orbit in the RTBP. Fig.9 illustrates the general three-dimensional quasi-periodic orbit. The error (in the right-hand part of these figures) is defined here as the distance between the analytical and the numerical orbit at each epoch. They are at the magnitude of  $10^{-5}$  in dimensionless units, which indicates that the third-order analytical solution is in very good agreement with its full numerical counterpart. Additionally, the errors of all these

<sup>4</sup> The orbits in Figs 4-5 are all in clockwise direction.

orbits are oscillating around some mean value, which proves that the motion in the vicinity of the stable EPs is indeed stable.

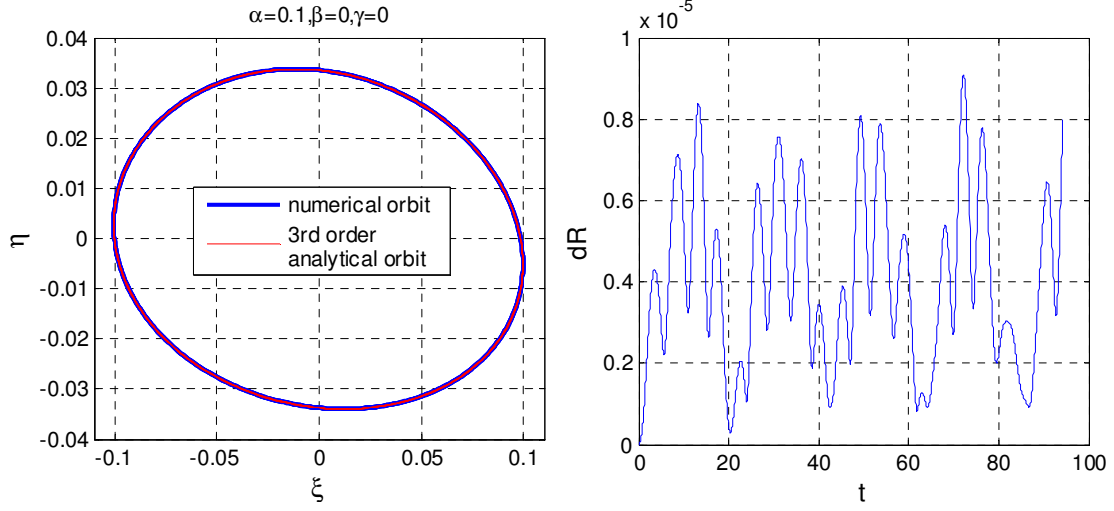


**Figure 4** The planar orbit with  $\alpha = 0.1, \beta = 0, \gamma = 0$  (left) and the orbit error (right) for a time duration of  $30\pi$ .

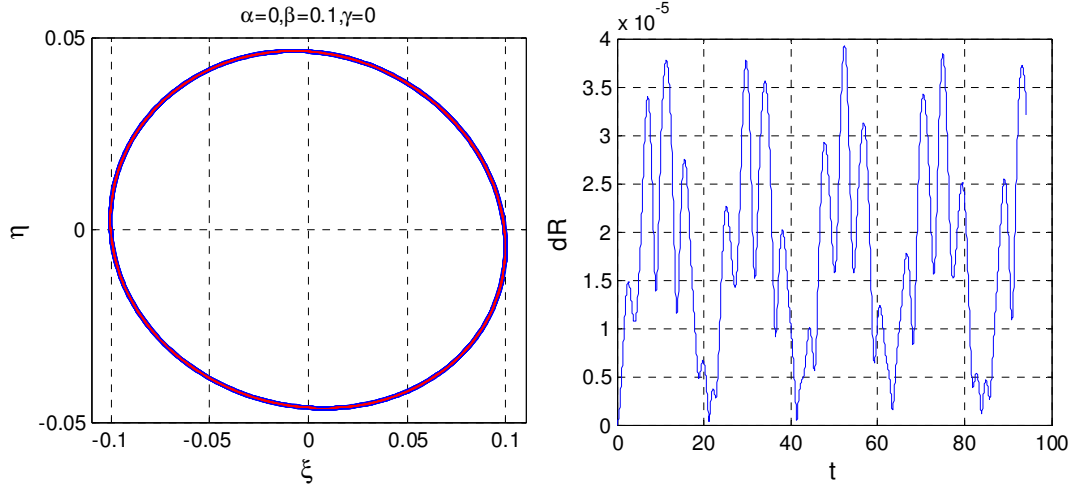


**Figure 5** The planar orbit with  $\alpha = 0, \beta = 0.1, \gamma = 0$  (left) and the orbit error (right) for a time duration of  $30\pi$ .

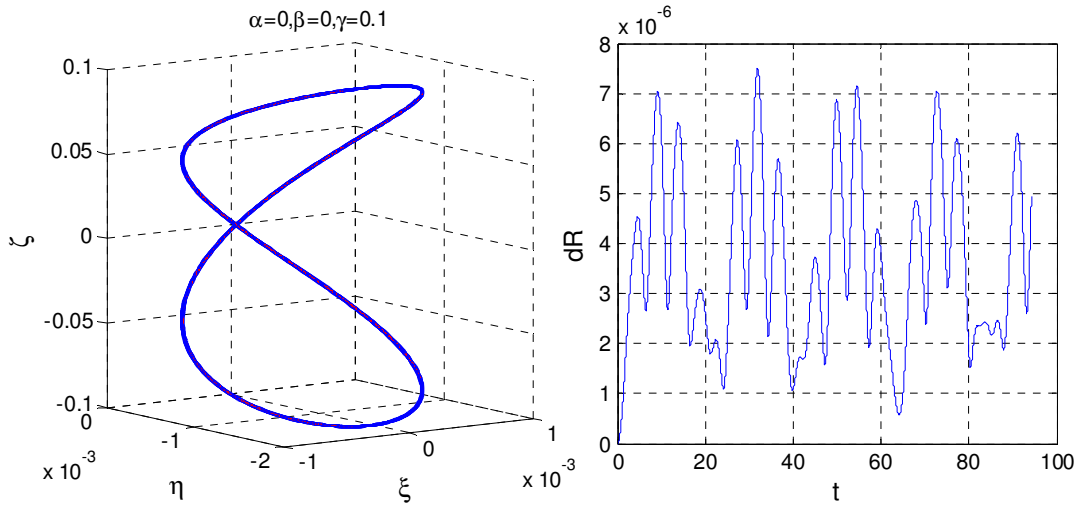


**Figure 6** The vertical orbit with  $\alpha = 0, \beta = 0, \gamma = 0.1$  (left) and the orbit error (right) for a time duration of  $30\pi$ .

## Orbital motion in the vicinity of the non-collinear equilibrium points

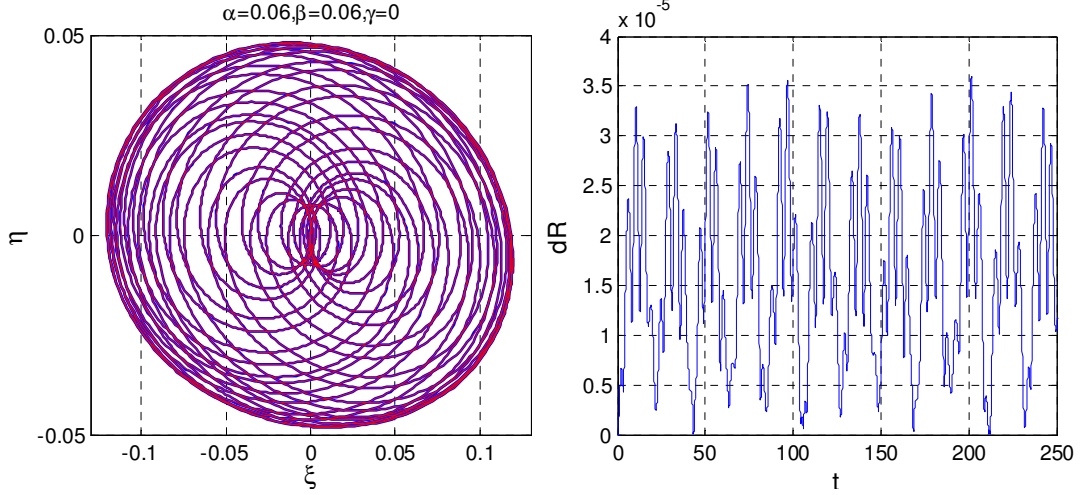


**Figure 7** The planar orbit with  $\alpha = \beta = 0.06, \gamma = 0$  (left) and the orbit error (right) for a time duration of  $80\pi$ .

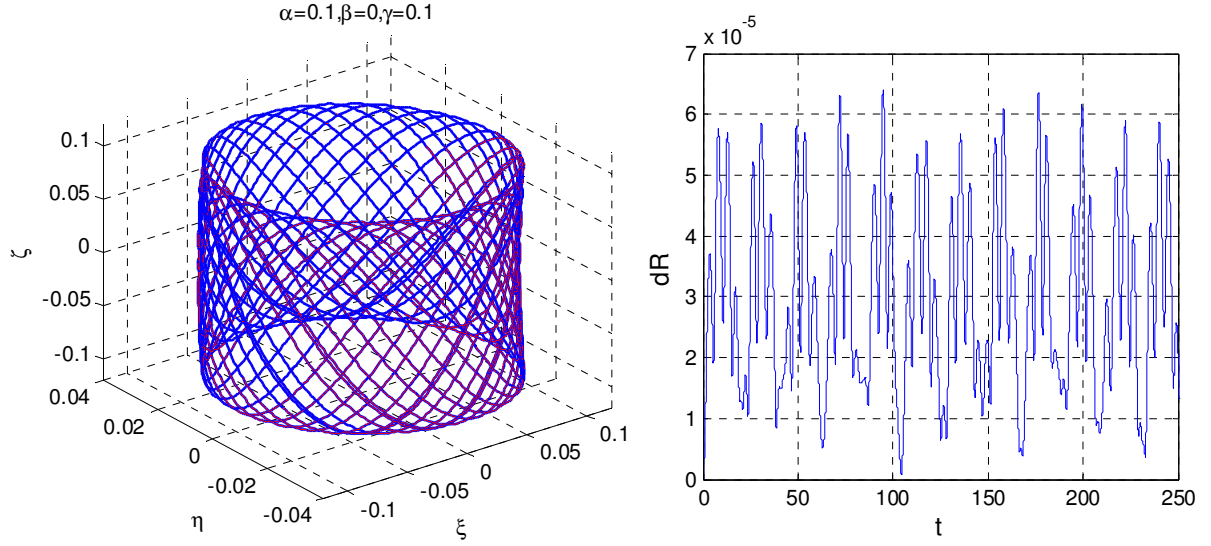


**Figure 8** The three-dimensional orbit with  $\alpha = \gamma = 0.1, \beta = 0$  (left) and the orbit error (right) for a time duration of  $80\pi$ .

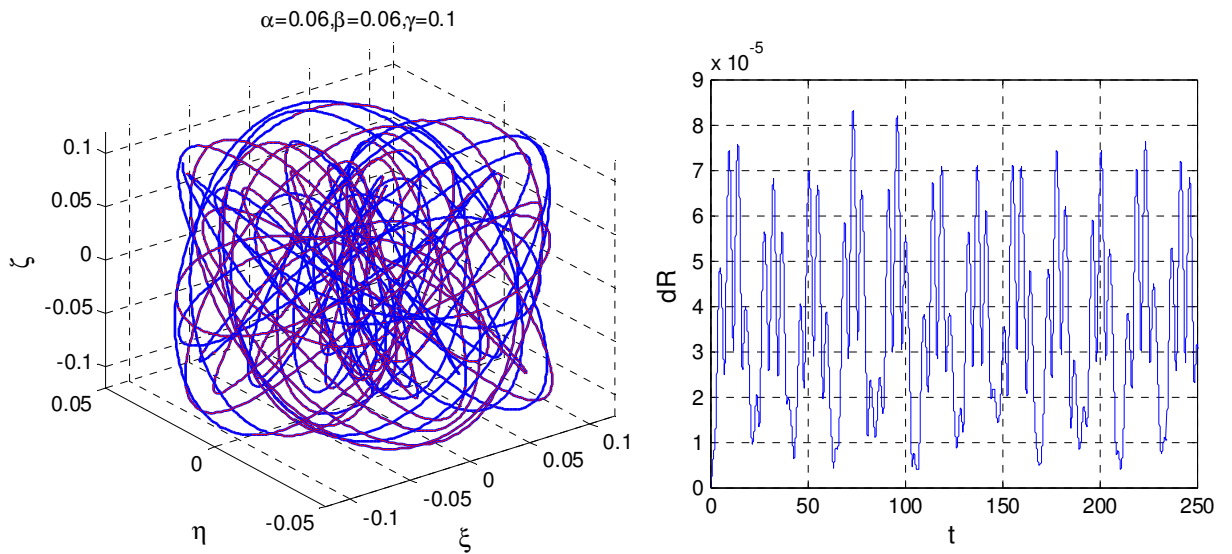


**Figure 9** The three-dimensional orbit with  $\alpha = \beta = 0.06, \gamma = 0.1$  (left) and the orbit error (right) for a time duration of  $80\pi$ .

It is also interesting to investigate how the orbit amplitude and  $\delta$  influence the error. By numerical simulation, a plot illustrating these relationships is given in Fig.10. It is seen that the maximum error grows when the orbit amplitude increases. This results from the fact that the third-order analytical solution is based on a Taylor-series expansion of the motion in the vicinity of an EP, which is obviously more valid for small deviations. For a given orbit amplitude, the error decreases as  $\delta$  becomes larger, which implies that the third-order analytical solution is more valid for a system with larger stability (slow rotation). In addition, benefiting from all these analyses, the design of orbits can be very straightforward.

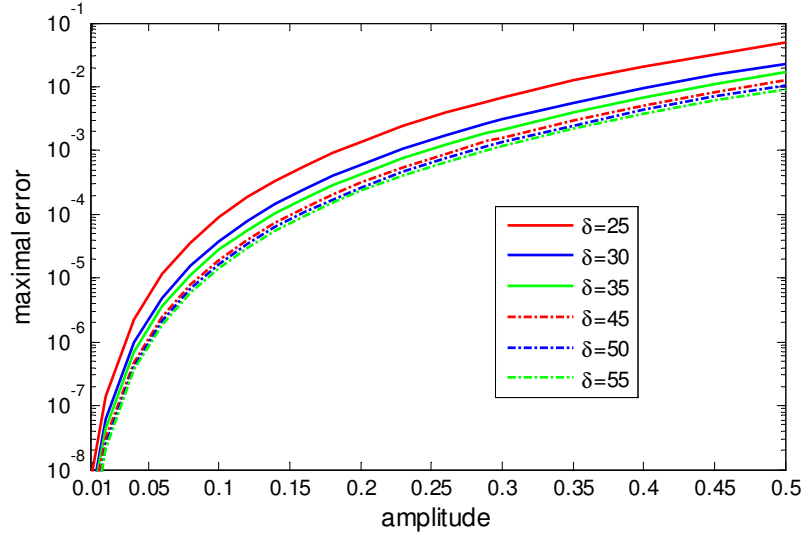


**Figure 10** The influence of orbit amplitude and parameter  $\delta$  on the error of the third-order analytical solution.

### 3.5 Motion around the Unstable Non-collinear EPs

For the unstable non-collinear EPs, the situation is quite different. Given a small deviation, the motion around the unstable EP is integrated for a time interval of  $5\pi$ , as shown in Fig.11. It diverges significantly, especially in the  $xy$ -plane, due to the property of instability of the non-collinear EPs.

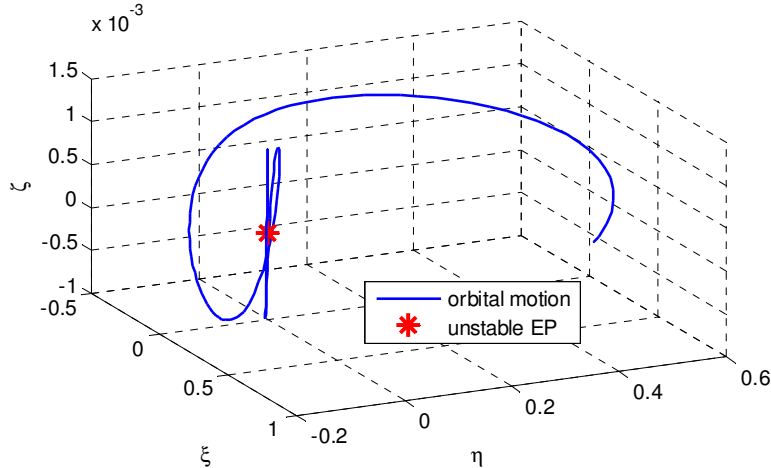


**Figure 11** Orbital motion in the vicinity of the unstable non-collinear EP.

Therefore, for a spacecraft exploration in this system, low-thrust control is to be introduced to stabilize the motion. A linear feedback control law is employed for stabilizing the unstable non-linear system, which is outlined in the next section.

### 3.5.1 Linear Feedback Control

Firstly, the linearized system with linear feedback control is written as (Slotine and Li, 1991)

$$\dot{\mathbf{X}} = \mathbf{E} \cdot \mathbf{X} + \mathbf{F} \cdot \mathbf{u}, \quad (14)$$

where  $\mathbf{X} = (\Delta\xi, \Delta\eta, \Delta\zeta, \Delta\dot{\xi}, \Delta\dot{\eta}, \Delta\dot{\zeta})$  is the deviation vector from the reference trajectory  $\mathbf{X}_{ref}$  and  $\mathbf{u} = (u_\xi, u_\eta, u_\zeta)^T$  is the control vector,  $\mathbf{E}_{6 \times 6}$  is the Jacobi matrix calculated along  $\mathbf{X}_{ref}$ , and  $\mathbf{F}_{6 \times 3}$  is the control coefficients matrix. The control law is usually defined as  $\mathbf{u} = -\mathbf{K} \cdot \mathbf{X}$ , in which  $\mathbf{K}_{3 \times 6}$  is the gain matrix. Therefore, Eq. (14) can be rewritten as  $\dot{\mathbf{X}} = (\mathbf{E} - \mathbf{F}\mathbf{K}) \cdot \mathbf{X}$ . By choosing an approximate gain matrix  $\mathbf{K}$ , the new linearized system can be forced to be stable. To meet the tracking accuracy and also the requirement of the allowed control force, a linear quadratic regulator (LQR) is applied to find the optimal control solution and the quadratic cost function is defined as (Gopal, 1993)

$$J = \int_0^\infty (\mathbf{X}^T \mathbf{Q} \mathbf{X} + \mathbf{u}^T \mathbf{R} \mathbf{u}) dt, \quad (15)$$

where  $\mathbf{Q}$  is a real positive semi-definite matrix and  $\mathbf{R}$  is a real symmetric positive definite matrix. Both are weighting matrices. They can be defined by the ‘Bryson’s Rule’ (Bryson, 1975)

$$\mathbf{Q} = \text{diag} \left\{ \frac{1}{\Delta X_{1max}^2}, \frac{1}{\Delta X_{2max}^2}, \dots, \frac{1}{\Delta X_{6max}^2} \right\}$$

$$\mathbf{R} = \text{diag} \left\{ \frac{1}{\Delta u_{1max}^2}, \frac{1}{\Delta u_{2max}^2}, \frac{1}{\Delta u_{3max}^2} \right\},$$

where  $\Delta X_{imax}, \Delta u_{jmax}$  are the maximum allowable amplitudes of the  $i^{\text{th}}$  and  $j^{\text{th}}$  component of  $\mathbf{X}$  and  $\mathbf{u}$ , respectively. Once  $\mathbf{Q}$  and  $\mathbf{R}$  are selected, the control gain matrix  $\mathbf{K}$  is obtained as

$$\mathbf{K} = \mathbf{R}^{-1} \mathbf{F}^T \mathbf{P},$$

where matrix  $\mathbf{P}_{6 \times 6}$  is the solution of the following Riccati matrix equation (Gopal, 1993)

$$\mathbf{E}^T \mathbf{P} + \mathbf{P} \mathbf{E} - \mathbf{P} \mathbf{F} \mathbf{R}^{-1} \mathbf{F}^T \mathbf{P} + \mathbf{Q} = 0.$$

Therefore, the optimal control force is written as

$$\mathbf{u} = -\mathbf{R}^{-1} \mathbf{F}^T \mathbf{P} \mathbf{X}.$$

### 3.5.2 Controlled Motion Tracking the Third-order Analytical Orbit

Here, the third-order analytical solution will serve as the reference trajectory. As shown in Section 3, the unstable EP has only one pure imaginary eigenvalue in the  $z$ -



direction. Therefore, the reference trajectory can be given by the third-order analytical solution with  $\alpha = \beta = 0$  and  $\gamma$  with a chosen value. Three cases will be studied for the control problem: (1) the spacecraft is exactly put on the reference orbit, in which situation there is no injection error; (2) an initial error, e.g.  $[10^{-4}, 10^{-4}, 0, 10^{-4}, -10^{-4}, 0]$ , is added to the initial state of the spacecraft; (3) the spacecraft is put on the stable manifold of the EP. For the last case, the local stable manifold of the EP is given as

$$\begin{cases} \xi(t) = e^{(-M \cdot t)} \cdot (\gamma_1 \cdot \cos(N \cdot t) + \gamma_2 \cdot \sin(N \cdot t)) \\ \eta(t) = \sigma \cdot e^{(-M \cdot t)} \cdot (\gamma_3 \cdot \cos(N \cdot t) + \gamma_4 \cdot \sin(N \cdot t)) \\ \zeta(t) = \zeta_3(t) \end{cases}, \quad (16)$$

in which

$$\begin{cases} \sigma = 1 / (M^2 - 4M \cdot \Omega_{12} + \Omega_{12}^2 + 4N^2) \\ \gamma_3 = -(2M^3 \cdot \gamma_1 - 2M^2 N \cdot \gamma_2 + 2MN^2 \cdot \gamma_1 + \Omega_{12} \Omega_{11} \cdot \gamma_1 + \Omega_{12} \cdot \gamma_1 \cdot N^2 - 2\Omega_{11} \cdot \gamma_2 \cdot N \\ \quad - 2 \cdot \gamma_2 \cdot N^3 - M^2 \Omega_{12} \cdot \gamma_1 + 2MN \cdot \Omega_{12} \cdot \gamma_2 - 2M \cdot \Omega_{11} \cdot \gamma_1) \\ \gamma_4 = -(2M^3 \cdot \gamma_2 + 2M^2 N \cdot \gamma_1 + 2MN^2 \cdot \gamma_2 + \Omega_{12} \Omega_{11} \cdot \gamma_2 - \Omega_{12} \cdot \gamma_2 \cdot M^2 - 2M \cdot \Omega_{11} \cdot \gamma_2 \\ \quad + 2 \cdot \gamma_1 \cdot N^3 + N^2 \Omega_{12} \cdot \gamma_2 - 2MN \cdot \Omega_{12} \cdot \gamma_1 + 2N \cdot \Omega_{11} \cdot \gamma_1) \end{cases}$$

where  $\gamma_1, \gamma_2, \gamma_3, \gamma_4$  are the amplitudes and  $M, N$  are the absolute values of the real and imaginary components of the complex eigenvalues,  $\zeta_3(t)$  is the third-order analytical solution in the  $z$ -direction. Based on the parameters of system 1996 HW1 with its value for  $\delta = 2.1682$ , the reference orbit and controlled motion as well as the control accelerations are given in Figs.12-14.

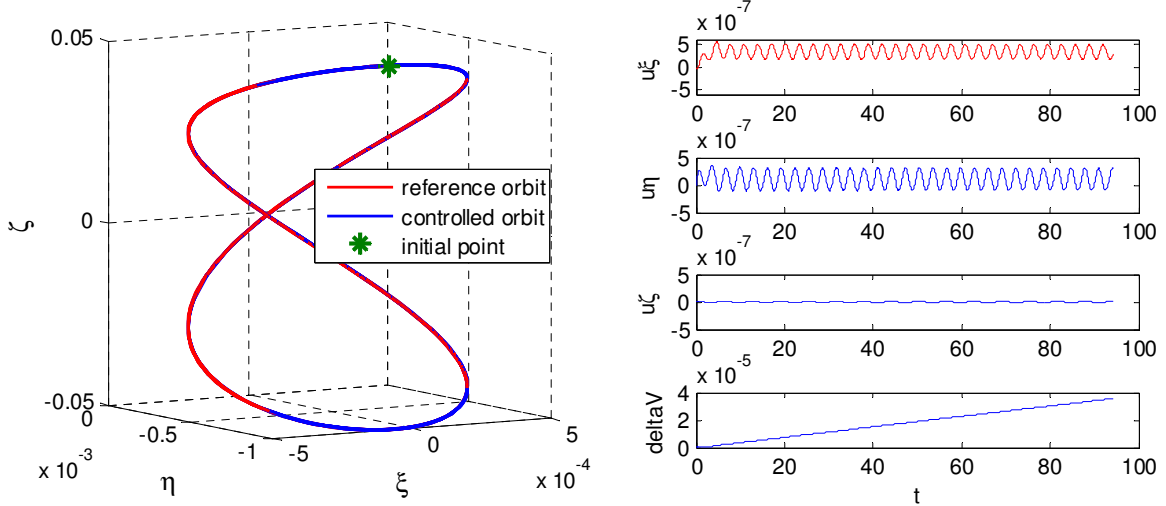


**Figure 12** The reference and controlled orbits, and the control accelerations for case 1.

### Orbital motion in the vicinity of the non-collinear equilibrium points

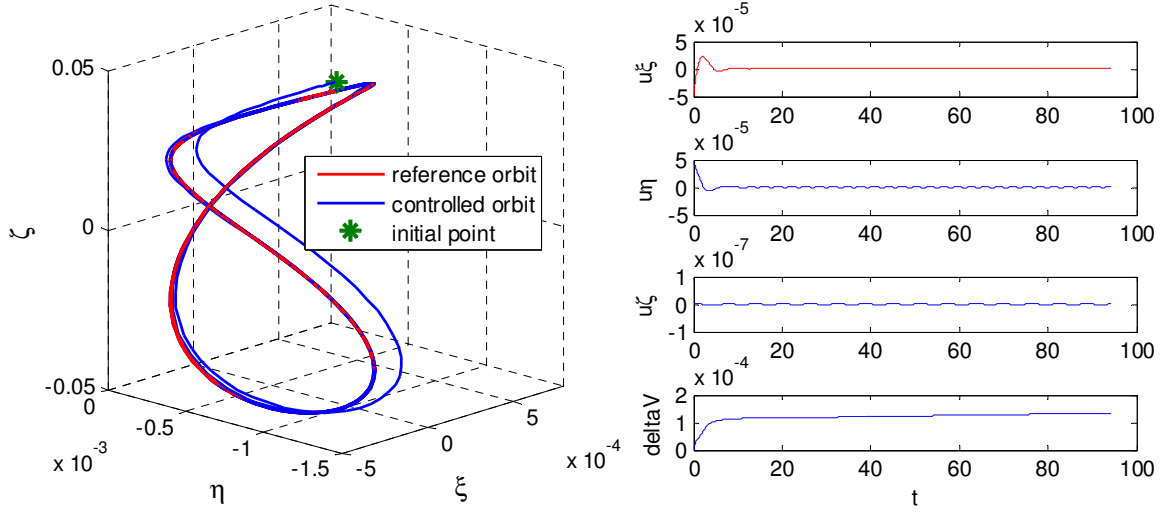


**Figure 13** The reference and controlled orbits, and the control accelerations for case 2.

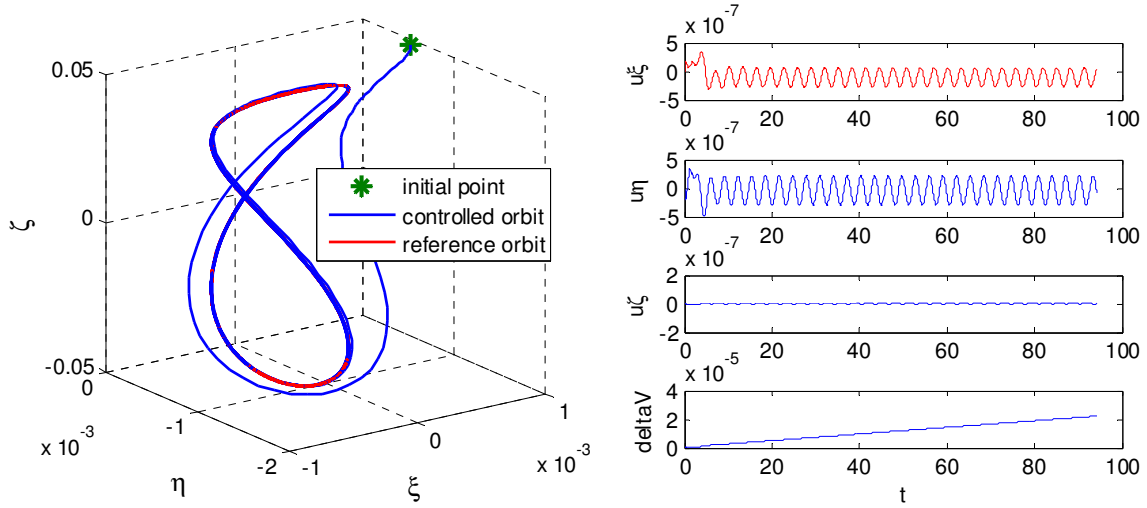


**Figure 14** The reference and controlled orbits, and the control accelerations for case 3.

For a time interval of 15 revolutions, the propellant needed for the above three cases in dimensionless units are  $3.56 \times 10^{-5}$ ,  $1.34 \times 10^{-4}$  and  $2.22 \times 10^{-5}$ , respectively. Going back to dimensional units, it is appealing to notice that about  $10^{-5}$  m/s propellant is required for the spacecraft to stay on this orbit for about 34.4 days, provided no initial offset is present, i.e. case (1). If the spacecraft is put on the local stable manifold of the EP, the consumption is slightly less than case (1) and significantly less than the case when there is a random error in the initial state, i.e. case (2). More generally, we find that the propellant consumption for cases (1) and (3) is close to each other and always smaller than that of case (2), for orbit amplitudes ranging from 0.01 to 0.1. From simulations, it is observed that for case (2) the magnitude of the control  $\Delta V$  is closely related to the magnitude of the initial error. However, since this study is more interested in the influence of the orbit amplitude and parameter  $\delta$  on the control effort, the exact value of the initial error in case (2) is not so important. Therefore, to avoid the calculation of manifolds in each simulation and also to eliminate the influence of the initial error, case (1) is selected for further study.

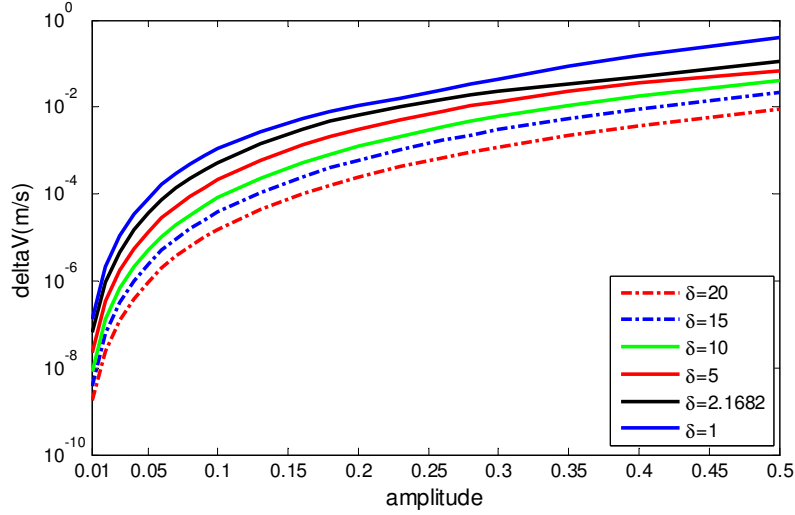


**Figure 15** The influence of orbit amplitude and parameter  $\delta$  on propellant consumption.

As shown in Fig.15, more propellant is needed when the orbit amplitude increases and when the rotation of the asteroid goes faster (smaller  $\delta$ ). Two reasons are responsible for this. One is obviously that more control force is required due to the larger instability of the orbit induced by the faster rotation of the asteroid. The other is due to the fact that the larger the amplitude of the orbit the larger the error of the analytical solution, which adds an extra artificial control effort to follow this solution. This is further studied in the following section.

### 3.5.3 Controlled Motion Tracking the Numerical Orbit

Firstly, exact periodic orbits (POs) are obtained by numerically modifying the third-order analytical solution. The differential correction (Russell and Lara, 2007, Lara and Russell, 2007) and the Levenberg-Marquardt method (Moré, 1978) are methods commonly used for numerical corrections. For this simulation, the latter one is applied. The difference between the third-order analytical orbits and the accurate POs is illustrated in Fig.16a. It is less than  $10^{-5}$  when the amplitude of the orbit is smaller than 0.1, and goes up to  $10^{-2}$  when the orbital amplitude enlarges to 0.5. When the asteroid rotates fast, the error becomes larger for orbits at the same amplitude. This is consistent with what was obtained for the situation of stable motion (Fig.10). In addition, the instability of the numerical POs is clarified by the stability index, which is defined as the sum of the norm of each pair of eigenvalues of the monodromy matrix of the PO (Chicone, 1999). If larger than 6, the orbit is unstable. The POs are highly unstable for the rapid rotation case, as illustrated in Fig.16b.

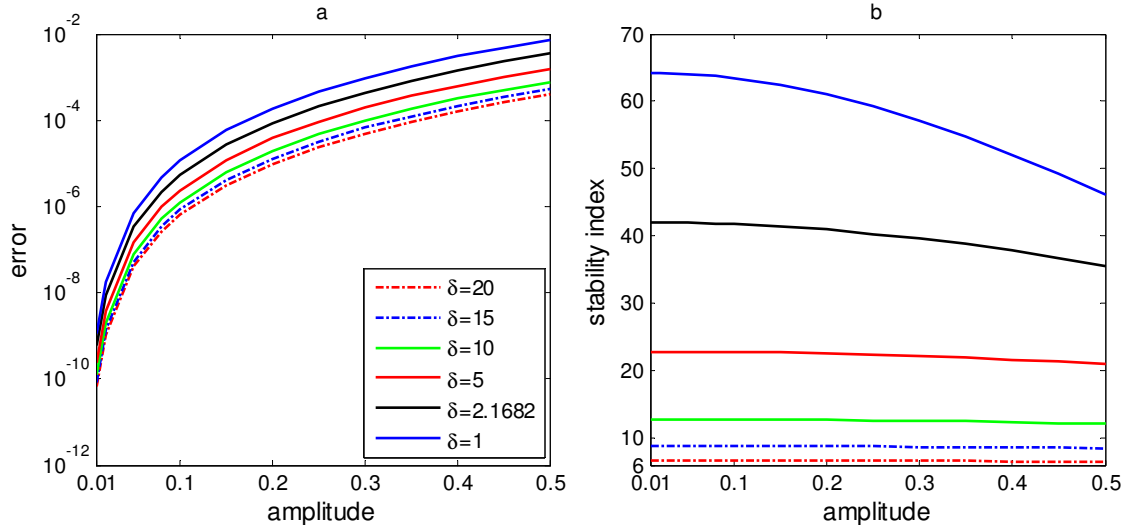


**Figure 16** The errors of the analytical orbits (left) and the stability index of the accurate numerical orbits (right) for different orbit amplitudes.

To have a detailed idea of how the error of the analytical PO affects the control effort, a comparison is made between the control force required to track the third-order analytical solution and to track the numerical PO. For the case of system 1996 HW1 and orbit amplitudes ranging from 0.1 to 0.5, Fig.17a illustrates that almost more than half of the propellant is introduced by the error of the analytical reference orbit for a time interval around  $4\pi$  (about two periods for each orbit). However, the percentage of the control force from tracking the analytical orbit will reduce gradually for longer time intervals, as more control effort is allocated for stabilizing the orbit, as shown in Fig.17b. Actually, this simulation emphasizes that an accurate numerical reference orbit should be used for large amplitude motions to reduce the control force.

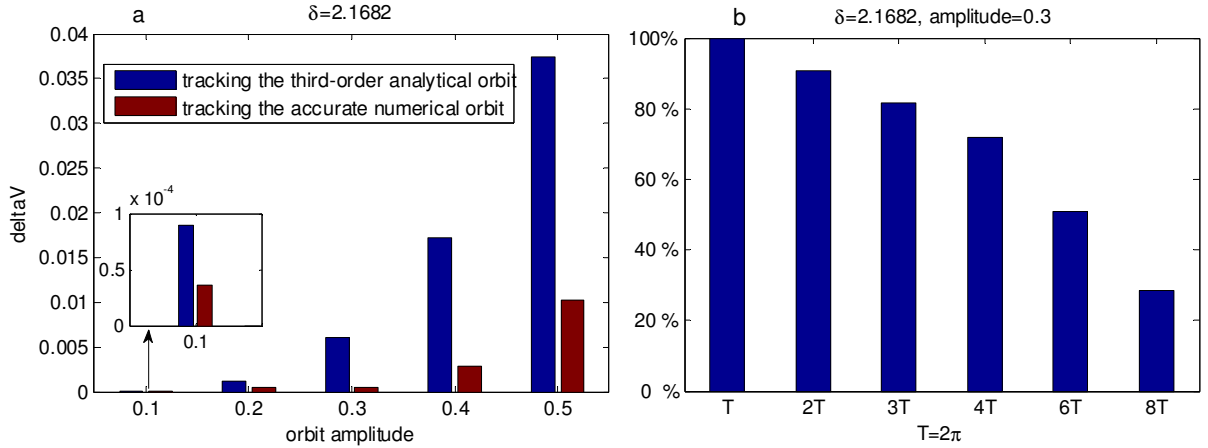


**Figure 17** The comparison of  $\delta V$  between tracking the third-order analytical solution and the numerical orbit for a time duration around  $4\pi$  (left); the percentage of propellant consumption for compensating the error of the analytical orbit (right) for different time intervals.

Nonetheless, the third-order analytical solution is of important value. It approximates the small-amplitude motion quite well, and also provides a very good

initial guess for the numerical search for the accurate numerical orbit when the orbital amplitude is large.

### 3.6 Conclusions

The orbital motion around the non-collinear EPs of a contact binary asteroid has been studied in this paper. With the asteroid represented by a combination of an ellipsoid and a sphere and sizes and mass taken from the system 1996 HW1, the locations and the linear stability of the EPs of the system are obtained first for different values of  $\delta$ .

For motions around the stable EPs, third-order analytical solutions have been constructed, by means of the LP method. Compared with numerical integration, they are found to be a good approximation for the motions in the vicinity of the stable EPs. However, the accuracy of this third-order analytical solution decreases when the orbital amplitude grows larger and the asteroid rotates faster, in which cases higher order solutions are probably more valid.

The motion around the unstable EPs is shown to be highly unstable. Therefore, for spacecraft exploration, a low-thrust control strategy based on the linear feedback control law has been employed to follow the third-order reference trajectory. Very little control effort is needed for all three simulated cases. For the spacecraft located on the local stable manifold of the EP, the propellant consumption is found to be approximately the same as the case without initial error. The injection error definitely brings about extra control effort. In addition, more propellant is required when the orbit amplitude increases and when the rotation of the asteroid goes faster, which is partially due to the increasing error of the analytical reference orbit. Thus, for large amplitude motion, the accurate orbit obtained from numerically modifying the analytical solution is used as the reference orbit. Consequently, the propellant consumption reduces compared to that tracking the less accurate third-order analytical solution. In conclusion, to save control effort, an accurate numerical orbit is recommended for a mission with large amplitude motion in a highly perturbed environment.

This study can also be extended to binary asteroids, planets and even star systems in which the primary body has an irregular gravity field.

### Acknowledgment

The authors thank the anonymous reviewers for their comments on improving this paper. The authors also owe their thanks to Dr. E. Mooij from Delft University of Technology for his helpful discussions on the control part of this research and Dr. P.N.A.M. Visser from Delft University of Technology for his comments on this study. This research is funded by the Chinese Scholarship Council.

## Appendix A

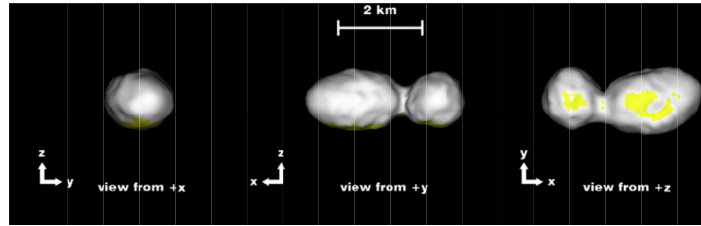
The second derivatives of the potential at the EPs located at  $(x_0, y_0, 0)$

$$\begin{aligned}\Omega_{11} &= 1 + \delta \left\{ 3 \frac{\mu R_1^2}{R_a^{5/2}} - \frac{\mu}{R_a^{3/2}} + 3 \frac{(1-\mu) R_2^2}{R_b^{5/2}} - \frac{1-\mu}{R_b^{3/2}} + (1-\mu) \left[ C_{20} \left( -\frac{15 R_2^2}{2 R_b^{7/2}} + \frac{3}{2 R_b^{5/2}} \right) + 6 \frac{C_{22}}{R_b^{5/2}} \right. \right. \\ &\quad \left. \left. - 60 \frac{C_{22} R_2^2}{R_b^{7/2}} + 105 \frac{C_{22} R_2^2 R_3}{R_b^{9/2}} - 15 \frac{C_{22} R_3}{R_b^{7/2}} + \frac{C_{40}}{8} \left( 105 \frac{R_2^2}{R_b^{9/2}} - \frac{15}{R_b^{7/2}} \right) \right] \right\} \\ \Omega_{12} &= \delta \left[ 3 \frac{\mu \sigma_1 R_1 y_0}{R_a^{5/2}} + (1-\mu) \left( \frac{3 \sigma_2 R_2 y_0}{R_b^{5/2}} - \frac{15 C_{20} \sigma_2 R_2 y_0}{2 R_b^{7/2}} + 105 \frac{C_{22} R_3 \sigma_2 R_2 y_0}{R_b^{9/2}} + \frac{105 C_{40} \sigma_2 R_2 y_0}{8 R_b^{9/2}} \right) \right] \\ \Omega_{22} &= 1 + \delta \left\{ 3 \frac{\mu y_0^2}{R_a^{5/2}} - \frac{\mu}{R_a^{3/2}} + 3 \frac{(1-\mu) y_0^2}{R_b^{5/2}} - \frac{1-\mu}{R_b^{3/2}} + (1-\mu) \left[ C_{20} \left( -\frac{15 y_0^2}{2 R_b^{7/2}} + \frac{3}{2 R_b^{5/2}} \right) - 6 \frac{C_{22}}{R_b^{5/2}} \right. \right. \\ &\quad \left. \left. + 60 \frac{C_{22} y_0^2}{R_b^{7/2}} + 105 \frac{C_{22} R_3 y_0^2}{R_b^{9/2}} - 15 \frac{C_{22} R_3}{R_b^{7/2}} + \frac{C_{40}}{8} \left( 105 \frac{y_0^2}{R_b^{9/2}} - \frac{15}{R_b^{7/2}} \right) \right] \right\} \\ \Omega_{33} &= \delta \left( -\frac{\mu}{R_a^{3/2}} - \frac{1-\mu}{R_b^{3/2}} + (1-\mu) \left( \frac{9 C_{20}}{2 R_b^{5/2}} - 15 \frac{C_{22} R_3}{R_b^{7/2}} - \frac{75 C_{40}}{8 R_b^{7/2}} \right) \right) \\ &\quad (A.1)\end{aligned}$$

in which  $R_3 = (x_0 + \mu)^2 - y_0^2$ ,  $R_a = (x_0 + \mu - 1)^2$ ,  $R_b = (x_0 + \mu)^2$ ,  
and  $\sigma_1 = \text{sign}(x_0 + \mu - 1)$ ,  $\sigma_2 = \text{sign}(x_0 + \mu)$ .

## Appendix B

The main physical parameters of 1996 HW1 (Magri et al., 2011).



Overall dimensions (km)	X: 3.78±0.05; Y: 1.64±0.1; Z: 1.49±0.15
Sidereal period (h)	8.76243±0.00004
Average sphere radius (km)	1.5
Triaxial ellipsoid principal axes size (km)	2.28×1.64×1.49
Bulk density (g·cm <sup>-3</sup> )	2.0

## Appendix C

The first and second derivatives of the  $\xi$  component:

$$\left\{ \begin{array}{l} \dot{\xi} = \omega \frac{\partial \xi}{\partial \theta_1} + v \frac{\partial \xi}{\partial \theta_2} + u \frac{\partial \xi}{\partial \theta_3} \end{array} \right. \quad (C.1a)$$

$$\left\{ \begin{array}{l} \ddot{\xi} = \omega^2 \frac{\partial^2 \xi}{\partial \theta_1^2} + v^2 \frac{\partial^2 \xi}{\partial \theta_2^2} + u^2 \frac{\partial^2 \xi}{\partial \theta_3^2} + 2\omega v \frac{\partial^2 \xi}{\partial \theta_1 \partial \theta_2} + 2\omega u \frac{\partial^2 \xi}{\partial \theta_1 \partial \theta_3} + 2vu \frac{\partial^2 \xi}{\partial \theta_2 \partial \theta_3} \end{array} \right. \quad (C.1b)$$

At the left-hand side of the equation, the derivative terms at order  $N$  come from two parts. One is from the frequency part at order  $N_f$ , and the other is from the partial derivatives part at order  $N_d$ . From Eq. (C.1a), the combinations of  $N_f$  and  $N_d$  are shown in Table C.1. Similarly, the combinations of  $N_f$  and  $N_d$  from Eq. (C.1b) are shown in Tables C.2a and C.2b.

 Table C.1 The terms at order  $N$  from the first derivatives.

$N_f$	$N_d$	$\omega \cdot \frac{\partial \xi}{\partial \theta_1}$	$v \cdot \frac{\partial \xi}{\partial \theta_2}$	$u \cdot \frac{\partial \xi}{\partial \theta_3}$
0	N	$-\omega_0 l \xi_{ijk}$	$-v_0 m \xi_{ijk}$	$-u_0 n \xi_{ijk}$
N-1	1	$-2b_1 \omega_{i-1jk} \delta_{l1} \delta_{m0} \delta_{n0}$	0	0

 Table C.2a The terms at order  $N$  from the second derivatives.

$N_f$	$N_d$	$\omega^2 \cdot \frac{\partial^2 \xi}{\partial \theta_1^2}$	$v^2 \cdot \frac{\partial^2 \xi}{\partial \theta_2^2}$	$u^2 \cdot \frac{\partial^2 \xi}{\partial \theta_3^2}$
0	N	$-\omega_0^2 l^2 \xi_{ijk}$	$-v_0^2 m^2 \xi_{ijk}$	$-u_0^2 n^2 \xi_{ijk}$
N-1	1	$-2\omega_0 \omega_{i-1jk} \delta_{l1} \delta_{m0} \delta_{n0}$	$-2v_0 v_{ij-1k} \delta_{l0} \delta_{m1} \delta_{n0}$	0

 Table C.2b The terms at order  $N$  from the second cross derivatives.

$N_f$	$N_d$	$\omega v \cdot \frac{\partial^2 \xi}{\partial \theta_1 \partial \theta_2}$	$\omega u \cdot \frac{\partial^2 \xi}{\partial \theta_1 \partial \theta_3}$	$vu \cdot \frac{\partial^2 \xi}{\partial \theta_2 \partial \theta_3}$
0	N	$-\omega_0 v_0 l m \xi_{ijk}$	$-\omega_0 u_0 l n \xi_{ijk}$	$-v_0 u_0 m n \xi_{ijk}$
N-1	1	0	0	0

In the above tables,  $\delta_{ij}$  is the Kronecker function defined as  $\delta_{ij} = 0$  if  $i \neq j$  and  $\delta_{ij} = 1$  if  $i = j$ .

Table C.3

The coefficients of the third-order solution based on the system 1996 HW1 with  $\delta = 30$ .

$i, j, k$	$l, m, n$	$\xi_{ijk}^{lmn}$	$\bar{\xi}_{ijk}^{lmn}$	$\eta_{ijk}^{lmn}$	$\bar{\eta}_{ijk}^{lmn}$
<b>First order</b>					
0 0 1	0 0 1	0	0	0	0
0 1 0	0 1 0	1	0	-0.035053982599398	-0.462561390510061
1 0 0	1 0 0	1	0	-0.039537507604550	-0.336524799123989
<b>Second order</b>					
2 0 0	0 0 0	-0.023806114920661	0	-0.053741389350147	0
	2 0 0	-0.016192214114086	0.035431401331960	-0.04459758386557	0.003759838927571
0 2 0	0 0 0	-0.021006982631613	0	-0.038383674187688	0
	0 2 0	-0.003915952890528	0.016657054924871	-0.043517860201724	-0.002029452661860
0 0 2	0 0 0	-0.000877747450392	0	-0.081689054179531	0
	0 0 2	-0.003434126850330	-0.078070935564490	-0.079513547812876	0.003416490374532
1 1 0	1 1 0	-0.011709442031593	0.039582384163479	-0.093135622475414	-0.002076374704935
	1 -1 0	-0.071866545748974	0.061834804112778	-0.102857914964174	-0.015387784859370

# Orbital motion in the vicinity of the non-collinear equilibrium points

Third order						
0 1 2	0 1 0	0	-0.254455536743036	-0.118039682453026	0	
	0 1 2	0.007553124943105	-0.000174979775855	-0.000184016696880	-0.008296739941255	
	0 1 -2	0.030236354551945	-0.000380069835466	-0.000684739985558	0.025453086732806	
1 0 2	1 0 0	0	0.258292868721213	0.085816387449906	0	
	1 0 2	0.009817337527766	-0.000282319704210	-0.000302255508270	-0.010613532662720	
	1 0 -2	0.018669336525655	0.000382335070366	-0.000672394037954	0.018179956333375	
1 2 0	1 0 0	0	-0.023168973443996	0.005885433654049	0	
	1 2 0	-0.009636398933641	-0.001840065809099	0.001846933760841	-0.013413088064179	
	1 -2 0	0.008171128122171	0.002687712210761	0.006910586800193	0.004789674411975	
2 1 0	0 1 0	0	-0.435139147907026	-0.185246194642733	0	
	2 1 0	-0.010238386420191	-0.002425723361892	0.002825269628812	-0.015119405158079	
	2 -1 0	0.047799298598753	-0.005380853876668	0.006962113291533	-0.020744877091795	
0 3 0	0 0 0	0	-0.250160272880210	-0.110317571405433	0	
	0 3 0	-0.003096643426563	-0.000554947829432	0.000540105182793	-0.004300085512299	
3 0 0	0 0 0	0	0.049726518676773	0.023948768284819	0	
	3 0 0	-0.003617421378978	-0.001217724734530	0.001544580406246	-0.006174181192942	

$i, j, k, l, m, n$	$\zeta_{ijk}^{lmn}$	$\bar{\zeta}_{ijk}^{lmn}$	$i, j, k, l, m, n$	$\zeta_{ijk}^{lmn}$	$\bar{\zeta}_{ijk}^{lmn}$
First order			0 2 1 0 2 -1	-	0.000570762759971
0 0 1 0 0 1	0	1		0.007691552844634	
Second order			2 0 1 0 0 1	0	0
			2 0 1 2 0 1	-	-0.001378172317923
0 1 1 0 1 1	-0.001745243543444	0.092712440784877		0.014594281836922	
			2 0 1 2 0 -1	-	0.003328262370502
0 1 1 0 1 -1	0.004267433115526	-0.22669852669720		0.002785187193666	
1 0 1 1 0 1	-0.001466326438136	0.116825844612141	0 0 3 0 0 1	0	0
			0 0 3 0 0 3	-	0
1 0 1 1 0 -1	-0.001745243543444	0.092712440784877		0.000124241324214	
Third order			1 1 1 1 1 1	-	-0.001146204733178
				0.023981112829593	
0 2 1 0 0 1	0	0	1 1 1 1 -1 1	-	-0.012350389128375
				0.035826340467038	
0 2 1 0 2 1	-0.010751558776951	-0.00048027511378	1 1 1 1 1 -1	-	0.001773914178153
				0.011862800003690	
			1 1 1 1 -1 -1	-	0.009327034565701
				0.001845253539161	

$i, j, k$	$\omega_{ijk}$	$\nu_{ijk}$	$u_{ijk}$
2 0 0	-0.020030813330247	0.024142612320952	0.001863199630957
0 2 0	-0.033184598445032	0.007740025281966	0.001878519971433
0 0 2	-0.026919160761714	0.019745386404717	-0.000506169348563





# Chapter 4 Modelling and Analysis of Periodic Orbits Around a Contact Binary Asteroid

---

J. Feng, R. Noomen, P.N.A.M. Visser, J. Yuan

Published in *Astrophysics and Space Science*, vol. 357, issue 2, p. 1-18, 2015

## Abstract

The existence and characteristics of periodic orbits (POs) in the vicinity of a contact binary asteroid are investigated with an averaged spherical harmonics model. A contact binary asteroid consists of two components connected to each other, resulting in a highly bifurcated shape. Here, it is represented by a combination of an ellipsoid and a sphere. The gravitational field of this configuration is for the first time expanded into a spherical harmonics model up to degree and order 8. Compared with the exact potential, the truncation at degree and order 4 is found to introduce an error of less than 10% at the circumscribing sphere and less than 1% at a distance of the double of the reference radius. The Hamiltonian taking into account harmonics up to degree and order 4 is developed. After double averaging of this Hamiltonian, the model is reduced to include zonal harmonics only and frozen orbits are obtained. The tesseral terms are found to introduce significant variations on the frozen orbits and distort the frozen situation. Applying the method of Poincaré sections, phase space structures of the single-averaged model are generated for different energy levels and rotation rates of the asteroid, from which the dynamics driven by the 4×4 harmonics model is identified and POs are found. It is found that the disturbing effect of the highly irregular gravitational field on orbital motion is weakened around the polar region, and also for an asteroid with a fast rotation rate. Starting with initial conditions from this averaged model, families of exact POs in the original non-averaged system are obtained employing a numerical search method and a continuation technique. Some of these POs are stable and are candidates for future missions.

## 4.1 Introduction

Orbital dynamics around asteroids has become more and more interesting for mission purposes. It also sheds light on our understanding of the evolution of the solar system. This paper focuses on one specific type of asteroid, i.e. the contact binary asteroid, which consists of two lobes that are in physical contact and which represents the mostly bifurcated body. Together with comets, the contact binary body is estimated to constitute 10-20% of all small solar system bodies (Harmon et al., 2011). Rosetta's target comet 67P/Churyumov-Gerasimenko was found to be probably a contact binary very recently (August 2014). (Richardson, 1980)

The irregular gravitational field induced by an asteroid can be modelled with several different methods (Scheeres, 2012). For the study outside of the circumscribing sphere, the method of a spherical harmonic expansion truncated at arbitrary degree and order can be used. When the distance becomes smaller, the polyhedron method of approximation of the shape of a body with triangular faces is more valid (Werner and Scheeres, 1997). Another option is to approximate the gravitational field by elementary geometrical shapes (e.g. ellipsoid), in which case closed-form potentials can be obtained.

Following the typical mass distribution of a contact binary, the model of a combination of an ellipsoid and a sphere is used in this study, as shown in Fig.1. This model breaks one axial symmetry, which is different from the geometrical shapes (a straight segment, two orthogonal segments, an ellipsoid, a cube, a thin bar) studied in (Elife and Lara, 2003, Bartczak et al., 2006, Bartczak and Breiter, 2003, Liu et al., 2011b, Halamek and Broucke, 1988). For this specific configuration, possible formation mechanisms and the relationship between the relative configuration and the rotational angular momentum have been studied in detail in (Scheeres, 2007). In addition, this simplified model already captures the main characteristics of the full gravitational field.

To gain some insight into the gravitational field of this configuration and the orbital dynamics around such a system, the spherical harmonics expansion is applied. As already mentioned, it is a good representation of a non-spherical gravitational field outside the circumscribing sphere. It has been applied extensively for studying orbital dynamics around planets and moons, for which the zonal and  $C_{22}$  terms are usually dominant and several magnitudes larger than the other tesseral terms. However, for orbital motion close to a contact binary asteroid, it is typically not sufficient to only include the zonal and  $C_{22}$  terms. Due to the highly non-spherical shape of the body, the other tesseral harmonics are much larger and more comparable with the zonal terms than in the case of planets and moons. For instance, the  $C_{30}$ ,  $C_{31}$  and  $C_{33}$  terms can easily be only one order of magnitude smaller than the  $C_{22}$  and  $C_{40}$  terms or even of the same magnitude, e.g. in the case of Eros and Itokawa (Scheeres et al., 2000, Yu and Baoyin, 2012b, Barnouin-Jha et al., 2006). Therefore, they should not be ignored during the analysis.

For studying the corresponding orbital dynamics with a spherical harmonics model, numerical (Hu and Scheeres, 2004, Russell and Lara, 2007, Russell and Lara, 2009, Lara and Russell, 2007), analytical (Liu et al., 2011a, Ceccaroni and Biggs, 2013, Coffey et al., 1994, San-Juan et al., 2004) and semi-analytical (Scheeres et al., 2000, Métris and Exertier, 1995) methods have been developed. Among them, the traditional averaging method has extensive applications, since it simplifies the system by averaging out the short-term effects while capturing the secular and long-term evolutions. Together with the Lagrange Planetary Equations (LPE), the effect of the

harmonics  $C_{20}$ ,  $C_{22}$ ,  $C_{30}$  and  $C_{40}$  on orbital elements has been studied by (Scheeres et al., 2000), and they are found to enlarge the orbital eccentricity. By applying the Lie transformations, high-altitude frozen orbits have been obtained analytically by (Ceccaroni and Biggs, 2013) for the fast-rotating asteroid Eros, with the harmonics truncated at degree 15.

Actually, the averaging process reduces the three degrees of freedom (3-DoF) to 2-DoF and even 1-DoF. The reduced system then can either be numerically integrated or be solved in closed form. The method of Poincaré sections is a good tool for solving the reduced 2-DoF by numerical integration, as it transforms the 2-DoF system to a two-dimensional map. Common applications can be found in (Lara, 1996, Broucke, 1994) for finding POs. Generally, frozen orbits can be obtained from the 1-DoF system (Coffey et al., 1994, Liu et al., 2011a). POs however can be generated from the 1-DoF system (Palacián, 2007), 2-DoF (Tzirti et al., 2010) and also 3-DoF systems (Lara, 1999, Lara and Russell, 2007). The eccentricity and pericenter of the frozen orbits always remain constant on average, while those of the POs have small deviations from the ‘mean’ value but will return to the same value after one period. POs, i.e. repeat ground track orbits in the rotating frame, were also found to be a subset of frozen orbits in inertial space (Lara, 1999). In addition, the POs can also be explored for determining the stability bounds (Lara and Scheeres, 2002). Since the propellant consumption for following these kinds of orbits is usually small, both of them are interesting for mission purposes.

Little research however has been done on finding POs with a  $4 \times 4$  spherical harmonics model for the highly irregular gravitational field of a contact binary asteroid with this configuration and also with different rotation rates. This will be the focus of this study. In addition, instead of following a global search method, the POs of the original system will be obtained from the Poincaré sections with a numerical search and correction method.

This paper is arranged as follows. In Section 2, the gravitational field potential of the ellipsoid-sphere configuration is expanded into a spherical harmonics model. In fact, this kind of expansion has been performed for some specifically shaped bodies, e.g. an ellipsoid or two spheres connected with each other (Balmino, 1994), both of which are three-axis symmetric. Therefore, the current work is the first attempt for expanding the gravitational field into spherical harmonics for a geometrical body of which one axis-symmetry has been broken. The general method for obtaining the spherical harmonics for a given body is introduced. In Section 3, the contact binary system 1996 HW1 (Magri et al., 2011) (one of the most bifurcated bodies ever found) serves as the study case for testing the accuracy of the truncation at degree and order 4, and further at degree and order 8. The expansion is also checked against the cases when varying the sizes of this configuration. In Section 4, the Hamiltonian including the  $4 \times 4$  harmonics and the rotation of the asteroid is obtained for the analysis of the

dynamics. It is reduced to a 1-DoF system by double-averaging, and frozen orbits are identified. The effects of the tesseral harmonics on these frozen orbits are examined. In Section 5, by applying Poincaré sections, the phase space structure of the 2-DoF system is obtained at various energy levels and at different rotation rates of the asteroid. In Section 6, with a numerical correction method and the initial conditions from the Poincaré maps, a number of POs can be obtained in the single-averaged model and successively in the full non-averaged model.

## 4.2 Shape Model and Geometrical Potential

In this study, the contact binary asteroid is modeled as a combination of an ellipsoid and a sphere, as shown in Fig.1.

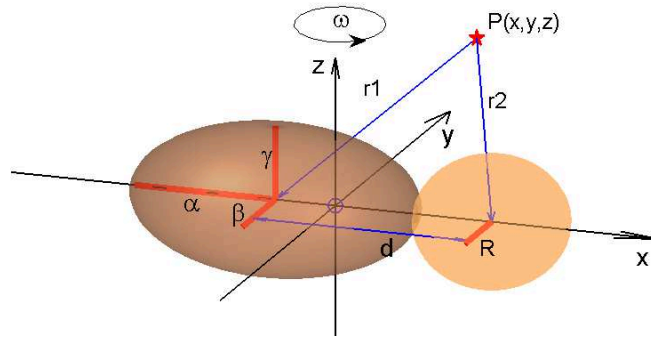


**Figure 1** The ellipsoid-sphere configuration and the body-fixed frame  $xyz$ .

The parameters that describe the configuration in Fig.1 are the three semi-axes of the ellipsoid  $\alpha, \beta, \gamma$  and the radius of the sphere  $R$ . The system is assumed to be homogeneous, with a constant density  $\rho$ . It is also assumed that the system rotates uniformly about the  $z$ -axis with a velocity  $\vec{\omega}$ . The vector from the center of mass of the ellipsoid to that of the sphere is denoted as  $\vec{d}$ , where  $|\vec{d}| = \alpha + R$ . The mass ratio  $\mu_0$  is defined as  $m_s/(m_s + m_e) = 1/(1 + \alpha\beta\gamma/R^3)$  ( $m_s$  and  $m_e$  are the mass of the sphere and the ellipsoid, respectively). Here the body-fixed frame is defined as the  $x$ -axis along the line connecting the mass centers of the two components with positive direction from ellipsoid to sphere, the  $z$ -axis along the rotation axis of the body with positive direction pointing along the angular velocity, and the  $y$ -axis obtained according to the right-hand rule. With this definition, the asteroid still has  $xy$  and  $xz$ -plane symmetry, while the  $yz$ -plane symmetry is broken. This makes the problem more complicated, compared to the individual sphere and ellipsoid geometries which have three planes of symmetry. The gravitational potential of this two-component asteroid can be written as

$$U_{se} = U_{sphere} + U_{ellipsoid} = G(m_s + m_e) \left[ \frac{\mu_0}{|\vec{r} - (1 - \mu_0)\vec{d}|} + (1 - \mu)U_e(\vec{r} + \mu_0\vec{d}) \right], \quad (1)$$

where  $\vec{r} = (x, y, z)$  is the position of a given point  $P$ , and  $U_{sphere}$  and  $U_{ellipsoid}$  are the potentials of the sphere and ellipsoid parts, respectively. The former one can be viewed as a point mass potential, while the later one is expressed as (MacMillan, 1958)

$$U_e(\mathbf{r}) = \frac{3}{4} \int_{\sigma}^{\infty} \phi(\mathbf{r}, v) \frac{dv}{\Delta(v)}$$

$$\phi(\mathbf{r}, v) = 1 - \frac{r_x^2}{\alpha^2 + v} - \frac{r_y^2}{\beta^2 + v} - \frac{r_z^2}{\gamma^2 + v},$$

$$\Delta(v) = \sqrt{(\alpha^2 + v)(\beta^2 + v)(\gamma^2 + v)}, \phi(\mathbf{r}, \sigma) = 0$$

where  $v$  is an internal variable for the calculation of  $U_e$  and  $\mathbf{r} = (r_x, r_y, r_z)$  is the independent variable of function  $U_e$ . The potential expressed here will serve as the baseline to verify the accuracy of the spherical harmonics expansion studied in the following section.

## 4.3 Spherical Harmonics Expansion

### 4.3.1 Method

The gravitational potential in spherical harmonics is usually expressed as follows (Kaula, 1966)

$$V = \frac{GM}{r} \left\{ 1 + \sum_{n \geq 2} \sum_{m=0}^n \left( \frac{R_e}{r} \right)^n P_{nm}(\sin \theta) [C_{nm} \cos(m\lambda) + S_{nm} \sin(m\lambda)] \right\}, \quad (2)$$

where  $GM$  is the gravitational constant of the asteroid;  $r, \theta$  and  $\lambda$  are spherical coordinates (the radial distance  $|\vec{r}|$  from the center of mass to a given point  $P$ , latitude and longitude, respectively) in the body-fixed frame;  $R_e$  is a characteristic physical dimension and is usually defined as half of the largest dimension of the whole body, equal to  $|\vec{d}|$  as defined in Section 2;  $P_{nm}$  is the associated Legendre polynomial.  $C_{nm}$  and  $S_{nm}$  are the coefficients of the spherical harmonics expansion which are determined by the mass distribution within the body. They can be expressed in terms of inertia integrals which are dependent on the geometric representation of the body. Assuming a homogeneous density of the body, the inertia integral  $I_{i,j,k}$  is defined as (MacMillan, 1958)

$$I_{i,j,k} = \rho \iiint x^i y^j z^k dx dy dz. \quad (3)$$

The triple integration is performed over the entire volume of the body. For bodies symmetric through the  $xy$ ,  $yz$  and  $xz$ -planes, the inertia integrals are zero if there is an odd number among  $i, j$  and  $k$ . Therefore, the un-normalized  $C_{nm}$  and  $S_{nm}$  in inertia integrals are expressed as follows (MacMillan, 1958)

$$C_{nm} = (2 - \delta_{0m}) \frac{(n-m)!}{(n+m)!} \cdot \frac{m!}{MR_e^n} \cdot \sum_{s=0}^i \sum_{j=0}^l \sum_{p,q,r} \frac{(-1)^{s+j} [2n-2j-1] j!}{(2s)! (m-2s)! (n-m-2j)! [2j] p! q! r!} \cdot I_{m+2p-2s, 2s+2q, n-m-2j+2r}$$

$$S_{nm} = (2 - \delta_{0m}) \frac{(n-m)!}{(n+m)!} \cdot \frac{m!}{MR_e^n} \cdot \quad (4)$$

$$\sum_{s=0}^t \sum_{j=0}^l \sum_{p,q,r} \frac{(-1)^{s+j} [2n-2j-1] j!}{(2s+1)! (m-2s-1)! (n-m-2j)! [2j] p! q! r!} \cdot I_{m+2p-2s-1, 2s+2q+1, n-m-2j+2r}$$

where

$$\delta_{0m} = \begin{cases} 1, m=0 \\ 0, m \neq 0 \end{cases}; \quad t = \begin{cases} m/2, m \text{ even} \\ (m-1)/2, m \text{ odd} \end{cases}; \quad l = \begin{cases} (n-m)/2, m \text{ even} \\ (n-m-1)/2, m \text{ odd} \end{cases};$$

$$\begin{cases} [2n] = 2n \cdot (2n-2) \cdot \dots \cdot 2; [0] = 1 \\ [2n-1] = (2n-1) \cdot (2n-3) \cdot \dots \cdot 1 \end{cases}; \quad \begin{cases} p \geq 0, q \geq 0, r \geq 0, \text{ integers} \\ p+q+r = j \end{cases}$$

For simplification, dimensionless units are used in the following study, where the length unit is  $Re$ , the gravitational parameter  $GM = 1$  and the resultant time unit  $T = \sqrt{R_e^3/GM}$ . From now on, the variables are in dimensionless units however with the same notation. The mathematical expressions for the configuration of this contact binary, which also define the limits of the inertia integral, can be written as

$$\begin{cases} \frac{(x+\mu_0)^2}{\alpha^2} + \frac{y^2}{\beta^2} + \frac{z^2}{\gamma^2} = 1, & -\alpha - \mu_0 \leq x \leq \alpha - \mu_0 \\ (x-1+\mu_0)^2 + y^2 + z^2 = R^2, & -R+1-\mu_0 \leq x \leq R+1-\mu_0 \end{cases} \quad (5)$$

With this method, the outcome of the associated spherical harmonics model has been tested against the analytical values available from literature, and in this way verified. For the study case of system 1996 HW1 (Appendix A), the coefficients up to degree and order 8 are obtained and given in Appendix B. It is found that higher-order zonal terms and some tesseral terms, e.g.  $C_{31}$ ,  $C_{40}$ ,  $C_{60}$ , have the same magnitude as  $C_{22}$ .

#### 4.3.2 Verification

For an ellipsoid, it is found that the external gravitational harmonics converge uniformly down to the surface when  $\alpha < \gamma\sqrt{2}$  (Balmino, 1994). For a general body the divergence is severe once the point of interest comes into the circumscribing sphere of the body (MacMillan, 1958). Therefore, the analysis of the dynamics based on the above spherical expansion will be restricted to the area outside the circumscribing sphere, which has a dimensionless radius of 1.0725 for system 1996 HW1. The accuracy of this expansion (up to degree and order 4 and 8) is verified by comparing it with the analytical potential formulation Eq.(1). The relative errors of the potential value and the radial acceleration on the circumscribing sphere and also on the sphere with a dimensionless radius equal to 2 are illustrated in Fig.2. The relative error here is defined as the absolute difference between the potential values or the acceleration from the spherical harmonics expansion and the analytical formulation, divided by the value of the latter one.

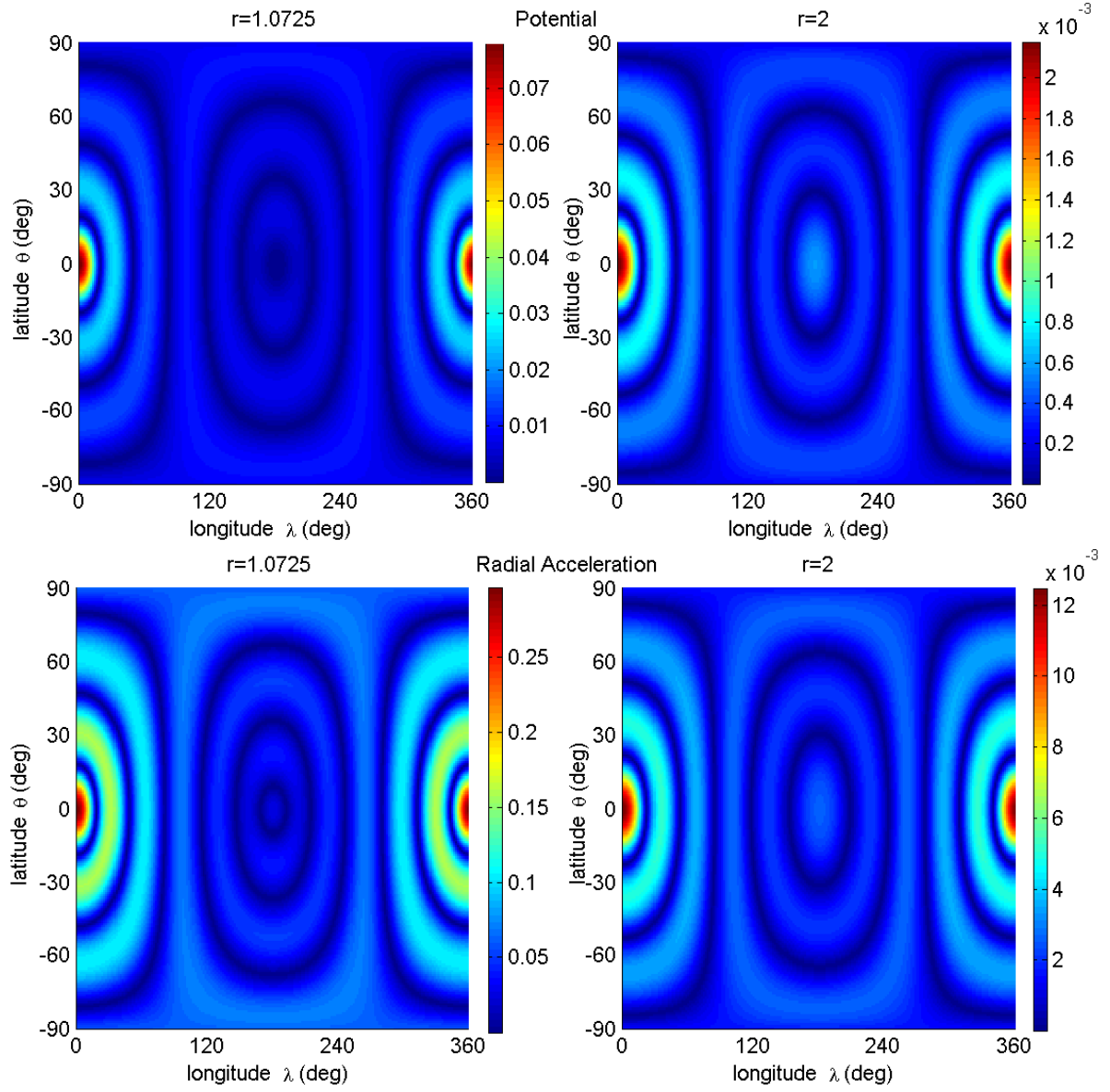


**Figure 2a** The relative error of potential (top) and radial acceleration (bottom) of the 4x4 spherical harmonics expansion for a radius equal to the one of the circumscribing sphere (left) and 2 (right).



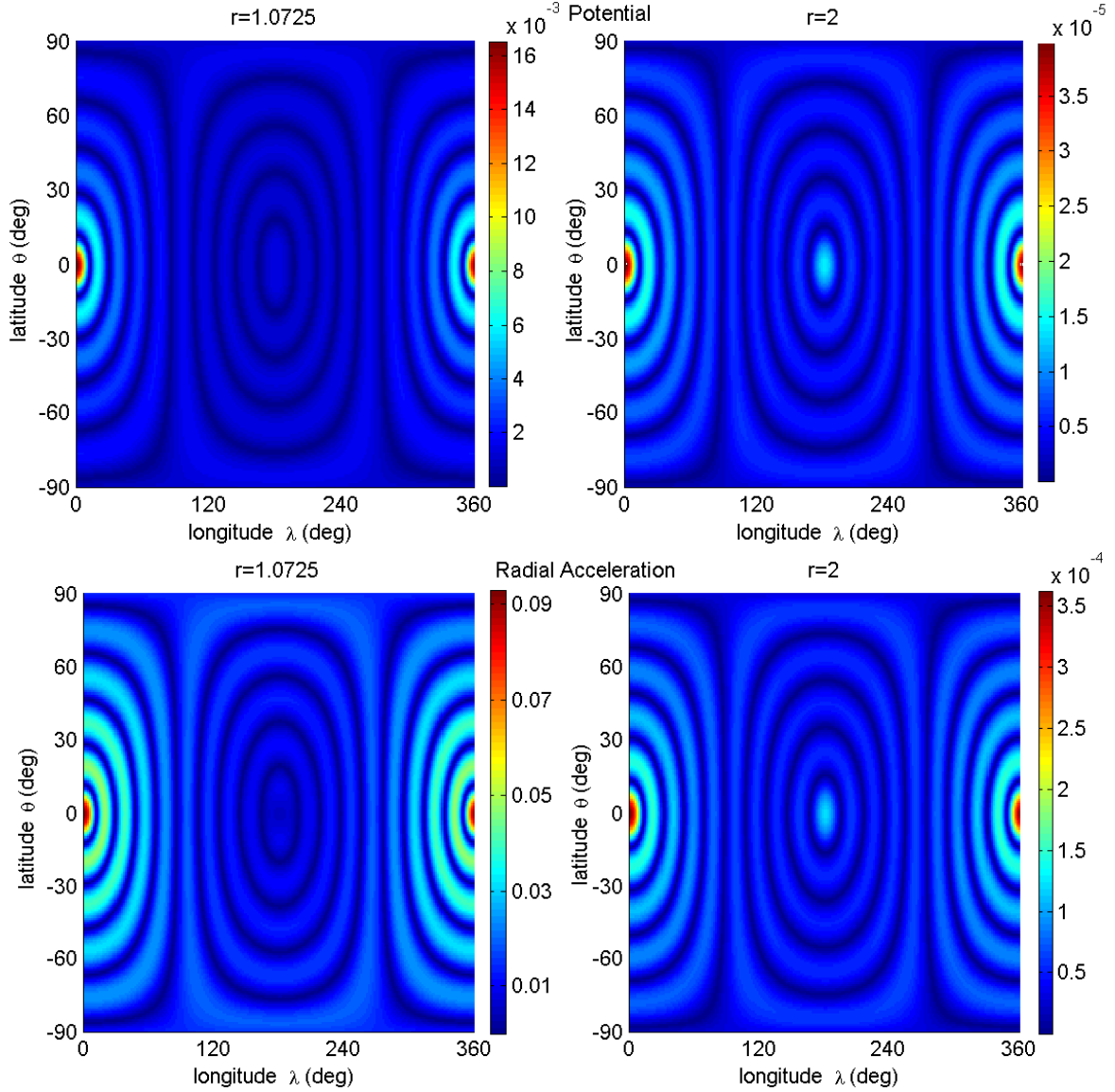


**Figure 2b** The relative error of potential (top) and radial acceleration (bottom) of the  $8 \times 8$  spherical harmonics expansion for a radius equal to the one of the circumscribing sphere (left) and 2 (right). Note the different colour scales.

For the truncation up to degree and order 4, Fig.2a (top) shows that the maximum error of the potential is about  $8 \times 10^{-2}$  on the circumscribing sphere and  $2 \times 10^{-3}$  at a radius of 2. In addition, for the  $8 \times 8$  expansion (Fig.2b, top), the potential error reduces to around  $2 \times 10^{-2}$  and  $4 \times 10^{-5}$ , respectively. As for the radial acceleration, the relative errors are all about one order of magnitude larger than those of the potential due to differentiation. This confirms the expectation that the higher the order of the truncation, the more accurate the expansion. For this irregularly shaped body, the largest errors appear at the outer edge of the smaller component along the most bifurcated direction ( $\lambda = 0^\circ$  or  $360^\circ$  and  $\theta = 0^\circ$ ) i.e. the positive  $x$ -axis; we call this point with the largest error ‘critical point’ from now on. For the radius larger than 2, the error reduces rapidly. In addition, it is concluded that the relative error of the expanded  $4 \times 4$  potential and the radial acceleration is much smaller than 0.3% and 1.5%, respectively, when

the distance to the center of mass of the system is larger than 2. Of course, the  $8 \times 8$  model performs better.

In addition, the influence of the configuration on the accuracy of the expansion is also checked. To that end, the radius of the sphere  $R$  is varied from zero to the value of the smallest semi-axis of the ellipsoid component (0.745 km, cf. Appendix A). The maximum relative errors of the expansions for the  $4 \times 4$  potential at five chosen radius are illustrated in Fig.3. When  $R$  is zero, the model reduces to that of the ellipsoid potential. Its largest relative error is at the magnitudes of  $10^{-2}$  (circumscribing sphere) and  $10^{-4}$  ( $r = 2$ ), respectively. For all study cases, the smallest relative error is at  $R = 0$ , while the largest one comes out for  $R = 0.46$  km. This implies that when  $R$  evolves from 0 to 0.745 km, at some radius near 0.46 km the most irregular (bifurcated) shape is generated, in which case the  $4 \times 4$  spherical harmonics approximation does not work so well at the singular point, and a higher-order truncation, e.g.  $8 \times 8$ , is required.

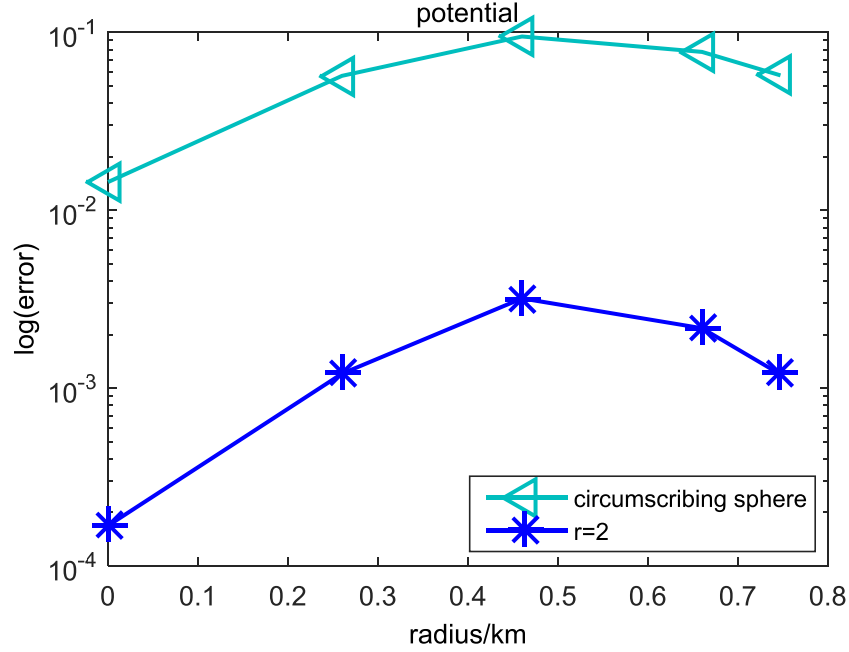


**Figure 3** The maximum relative error of the  $4 \times 4$  spherical harmonics expansion of the potential field at the circumscribing sphere and  $r = 2$  for the radius of the sphere at 0, 0.26, 0.46, 0.66, 0.745 km.

In summary, the spherical harmonics expansion up to degree and order 4 is a good approximation of the gravitational field of the contact binary asteroid especially for a dimensionless radius larger than 2. Therefore, in the following sections, the spherical harmonics truncated at this order are taken into account in the analysis of the dynamics of orbits. The initial conditions are chosen at a distance of no less than 2.

#### 4.4 Hamiltonian of the Truncated System

Taking into account the spherical harmonics up to degree and order 4, and the rotation of the asteroid at rate  $n_a$ , the Hamiltonian of the truncated system can be written as

$$\mathcal{H} = \mathcal{H}_0 + \mathcal{H}_{n_a} + \mathcal{H}_{C_{nm}} , \quad (6)$$

where  $\mathcal{H}_0$  is the unperturbed Keplerian part,  $\mathcal{H}_{n_a}$  comes from the rotation of the asteroid, and  $\mathcal{H}_{C_{nm}}$  represents the spherical harmonics perturbation. All terms of Eq.(6) in spherical coordinates are listed in Appendix C. For simplifying this dynamical system and also capturing its mean characteristics, an averaging method is applied. To this aim,  $\mathcal{H}$  is translated into a function of orbital elements  $(a, e, i, g, f, h)$ . Here  $a, e, i, f$  are the semi-major axis, eccentricity, inclination and true anomaly, respectively. In addition  $g = \omega$  is the argument of pericenter. The longitude of the ascending node  $\Omega$  in the frame co-rotating with the asteroid at rate  $n_a$  is expressed as  $h = \Omega - n_a t$ . The relations between orbital elements and spherical coordinates  $(r, \theta, \lambda)$  are given in Appendix D.

For studying the dynamics of a Hamiltonian system, it is convenient to use a canonical set of variables. One common set is the Delaunay variables, which are defined as follows (Chicone, 1999)

$$l = M, g = \omega, h = \Omega - n_a t, L = \sqrt{\mu a}, G = \sqrt{\mu a(1-e^2)}, H = \sqrt{\mu a(1-e^2)} \cos i ,$$

where  $G$  is the modulus of the angular momentum and  $H$  its projection on the z-axis. The equations of motion for a Hamiltonian system are expressed as

$$\begin{cases} \frac{dl}{dt} = \frac{\partial \mathcal{H}}{\partial L}, \frac{dL}{dt} = -\frac{\partial \mathcal{H}}{\partial l} \\ \frac{dg}{dt} = \frac{\partial \mathcal{H}}{\partial G}, \frac{dG}{dt} = -\frac{\partial \mathcal{H}}{\partial g} \\ \frac{dh}{dt} = \frac{\partial \mathcal{H}}{\partial H}, \frac{dH}{dt} = -\frac{\partial \mathcal{H}}{\partial h} \end{cases} . \quad (7)$$

Since Eq.(7) forms a system with six independent variables  $l, g, h, L, G, H$ , the Hamiltonian is a 3-DoF system. In the following study, the orbital elements are used in the averaging analysis, while the Delaunay variables will be employed in the numerical integration part.

#### 4.4.1 Single-averaged Model

By applying the change of variables

$$dM = \frac{r^2}{a^2(1-e^2)^{1/2}} df ,$$

$\mathcal{H}$  can be averaged over the mean anomaly  $M$  (or  $l$ ), and the averaged Hamiltonian  $\bar{\mathcal{H}}_{C_{nm}}$  up to degree and order 3 can be given as function of orbital elements (Tzirti et al., 2010)

$$\begin{aligned}
 \bar{\mathcal{H}}_0 &= -\frac{\mu}{2a} \\
 \bar{\mathcal{H}}_{n_a} &= -n_a \sqrt{\mu a (1-e^2)} c \\
 \bar{\mathcal{H}}_{C_{20}} &= -\frac{\mu C_{20} R_e^2 (1-3c^2)}{4a^3 (1-e^2)^{3/2}} \\
 \bar{\mathcal{H}}_{C_{22}} &= -\frac{3\mu C_{22} R_e^2 (1-c^2)}{2a^3 (1-e^2)^{3/2}} \cos(2h) \\
 \bar{\mathcal{H}}_{C_{3j}} &= -\frac{3\mu e C_{3i} R_e^3}{16a^4 (1-e^2)^2} \left[ K_{3j}^+ \cos(g+jh) + K_{3i}^- \cos(g-jh) \right], j=1,3
 \end{aligned}$$

where

$$c = \cos(i), K_{31}^\pm = 1 \pm 11c - 5c^2 \mp 15c^3, K_{33}^\pm = 30(1 \pm c - c^2 \mp c^3).$$

Extending the averaging of  $\mathcal{H}_{C_{nm}}$  to degree 4, the resultant Hamiltonian is obtained using MAPLE<sup>16</sup> and given as

$$\begin{aligned}
 \bar{\mathcal{H}}_{C_{40}} &= -\frac{3\mu C_{40} R_e^4}{128a^5 (1-e^2)^2} \left[ -(70s^4 - 60s^2) e^2 \cos(2g) + (35s^4 - 40s^2 + 8)(2+3e^2) \right] \\
 \bar{\mathcal{H}}_{C_{4j}} &= -\frac{45\mu e C_{4j} R_e^4}{32a^5 (1-e^2)^2} \left[ K_{4j}^+ \cos(2g+jh) e^2 + K_{4j}^- \cos(2g-jh) e^2 + K_{4j} \cos(jh)(2+3e^2) \right], \\
 & j=2,4
 \end{aligned}$$

where

$$\begin{aligned}
 s &= \sin(i), K_{42}^\pm = 1 \mp 5c - 6c^2 \pm 7c^3 + 7c^4, K_{42} = 1 - 8c^2 + 7c^4 \\
 K_{44}^\pm &= 14(-1 \mp 2c \pm 2c^3 + c^4), K_{44} = 14(1 - 2c^2 + c^4)
 \end{aligned}$$

Since  $M$  is averaged out,  $\mathcal{H}$  is reduced to a 2-DoF system with variables  $g$  and  $h$

$$\bar{\mathcal{H}} = \bar{\mathcal{H}}_0 + \bar{\mathcal{H}}_{C_{nm}} + \bar{\mathcal{H}}_{n_a}. \quad (8)$$

However, the system can be reduced further by a second averaging which is carried out in the next section.

#### 4.4.2 Double-averaged Model

It can be seen that in the single-averaged system the tesseral harmonics still include  $h = \Omega - n_a t$ , which is time related. Therefore, the Hamiltonian can be averaged a second time over  $h$ , denoted as  $\tilde{\mathcal{H}}$ . It can be shown that the corresponding tesseral terms are all eliminated, thus  $\tilde{\mathcal{H}}_{C_{nm}}$  only consists of contributions from zonal terms, which is actually the zonal approximation of the problem. The Hamiltonian is now reduced to 1-DoF and can be written as

$$\tilde{\mathcal{H}} = \bar{\mathcal{H}}_0 + \bar{\mathcal{H}}_{C_{20}} + \bar{\mathcal{H}}_{C_{40}} + \bar{\mathcal{H}}_{n_a}. \quad (9)$$

The four terms have already been given in Section 4.1.

#### (1) Frozen orbits

Substituting Eq.(9) into the Lagrange Planetary Equations (LPE) (Kaula, 1966), the derivatives of the orbital elements  $e$  and  $g$  can be obtained. With the perturbation from  $\bar{\mathcal{H}}_{C_{20}}$  and  $\bar{\mathcal{H}}_{C_{40}}$ , the derivatives of  $e$  and  $g$  from  $\bar{\mathcal{H}}$  are given as

$$\begin{aligned} \frac{de}{dt} &= \frac{-3R_e^4 \mu}{64a^7(1-e^2)^3 n} [C_{40}(70s^4 - 60s^2) \sin(2g)e] \\ \frac{dg}{dt} &= \frac{-3R_e^2 \mu}{128a^7(1-e^2)^4 n} \left\{ \begin{aligned} &32C_{20}a^2(5c^2 - 1)(1-e^2)^2 + 10C_{40}R_e^2 \cos(2g)[(2 - 16c^2 + 14c^4) \\ &+ (63c^4 - 56c^2 + 5)e^2] - 5C_{40}R_e^2[(12 - 144c^2 + 196c^4) + (189c^4 - 126c^2 + 9)e^2] \end{aligned} \right\} \end{aligned} \quad (10)$$

where  $n$  is the mean rotation rate of the orbit with semi-major axis  $a$ . Frozen orbits can be found by solving  $\dot{e} = \dot{g} = 0$ . Only for  $i_0 = 67.8^\circ$  or  $g = 0$  or  $\pm\pi/2$ ,  $\dot{e}$  equals zero. However, no solution for  $\dot{g} = 0$  is found at  $i_0$ . For the main problem based on  $C_{20}$  only and also the  $C_{20}+C_{30}$  dynamics studied in (Tzirti et al., 2010), frozen orbits exist at  $i = 63.4349^\circ$ , which is known as the critical inclination. However, the situation is different in the  $C_{20}+C_{40}$  dynamics, which is explained in the following part.

For  $g = 0$  and  $\pi/2$ , solutions for  $\dot{g} = 0$  can be obtained in the  $e - i$  plane as shown in Fig.4, in which the frozen eccentricities are all quite large in all cases, except for those close to the bifurcations. Therefore, only parts of them (in the inclination range around  $60 \sim 63.5^\circ$ ) are practical as they should not impact on the asteroid. In addition, the frozen eccentricity increases as  $a$  becomes larger. Compared with the case of  $g = \pi/2$ , for the case of  $g = 0$  the frozen orbit is slightly more eccentric for a given value of  $i$ , and the feasible range of  $i$  for a practical orbit becomes more narrow. For both situations, no solution exists around  $i = 70^\circ$  or at low inclinations due to this specific  $C_{20} + C_{40}$  dynamics.

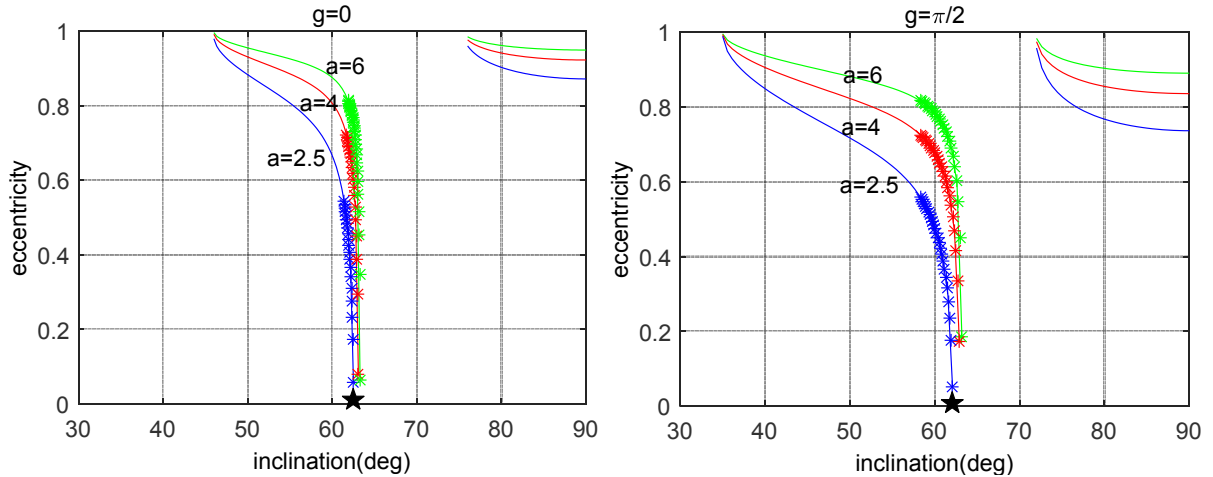


**Figure 4** Eccentricity-inclination diagrams for the double-averaged system with  $C_{20} + C_{40}$  dynamics at  $g = 0$  (left) and  $\pi/2$  (right). The stars represent the conditions where there is no intersection with the asteroid (1996 HW1). The two black pentagams represent the two bifurcations for  $a=2.5$ .

Coffey (Coffey et al., 1994) also studied the frozen dynamics including the  $C_{20}+C_{40}$  terms, but with the Lie perturbation method. Using the same values for  $C_{20}$  and  $C_{40}$ , Coffey's results are found to have two similar branches at both  $g = 0$  and  $\pi/2$ . There is approximately 1-5% difference between the results from his method and ours in this double-averaged model, due to the different averaging methods applied. The large difference appears at a large frozen eccentricity. According to his study, for the  $C_{20}+C_{40}$  dynamics, two families (for  $g = 0$  and  $g = \pi/2$ ) of solutions bifurcate around the critical inclination. As we can see from Fig.4, there are also two bifurcations (the two black pentagrams) from our results, one at  $i \approx 62.5071^\circ$  for  $g = 0$  and the other at  $i \approx 62.1144^\circ$  for  $g = \pi/2$ , at  $a = 2.5$ . They are also very close to the critical inclination of the main problem. Further, the bifurcation moves closer to the critical value ( $63.4349^\circ$ ) with the increase of  $a$ , since the perturbation from spherical harmonics is weakened when orbits are further away from the body. This is consistent with Coffey's theory and proves that the traditional averaging technique also describes the underlying dynamics quite well.

In general, frozen orbit of planetary problem have a small eccentricity and exists for a large inclination range. However, for asteroids the frozen eccentricity is large and is only present in a limited inclination range. This is probably due to the large  $C_{20}$  and  $C_{40}$  terms, which is always the case for highly irregular asteroids, e.g. 433 Eros and the contact binary in this study.

Similarly, the behaviour of the frozen orbits in this system but with different sizes as in Section 3.2 is also investigated and shown in Fig.5. Again the radius of the sphere  $R$  is changed from zero to 0.745 km. Several aspects can be noticed. Firstly, the deviations of the frozen eccentricities among different sizes are smaller for  $a = 4$  than those for  $a = 2$  (note the difference in scale of the y-axis). This means that  $R$  has a smaller influence on orbits for larger values of  $a$ , which is obvious since the irregular shape of the asteroid has less influence when one is further away. Secondly, at a specific value of  $a$ , the frozen eccentricity decreases as  $R$  reduces when  $R > 0.46$  km, and the opposite occurs when  $R < 0.26$  km. It is concluded that there is a transition radius somewhere in between these values, at the right side of which the frozen eccentricity is analogously proportional to the radius  $R$  and the opposite happens on the left side; again, due to the manifestation of the irregularity of the contact binary system. In summary, the frozen orbits are highly elliptic and the feasible ones exist at inclinations  $60 \sim 63.5^\circ$ .

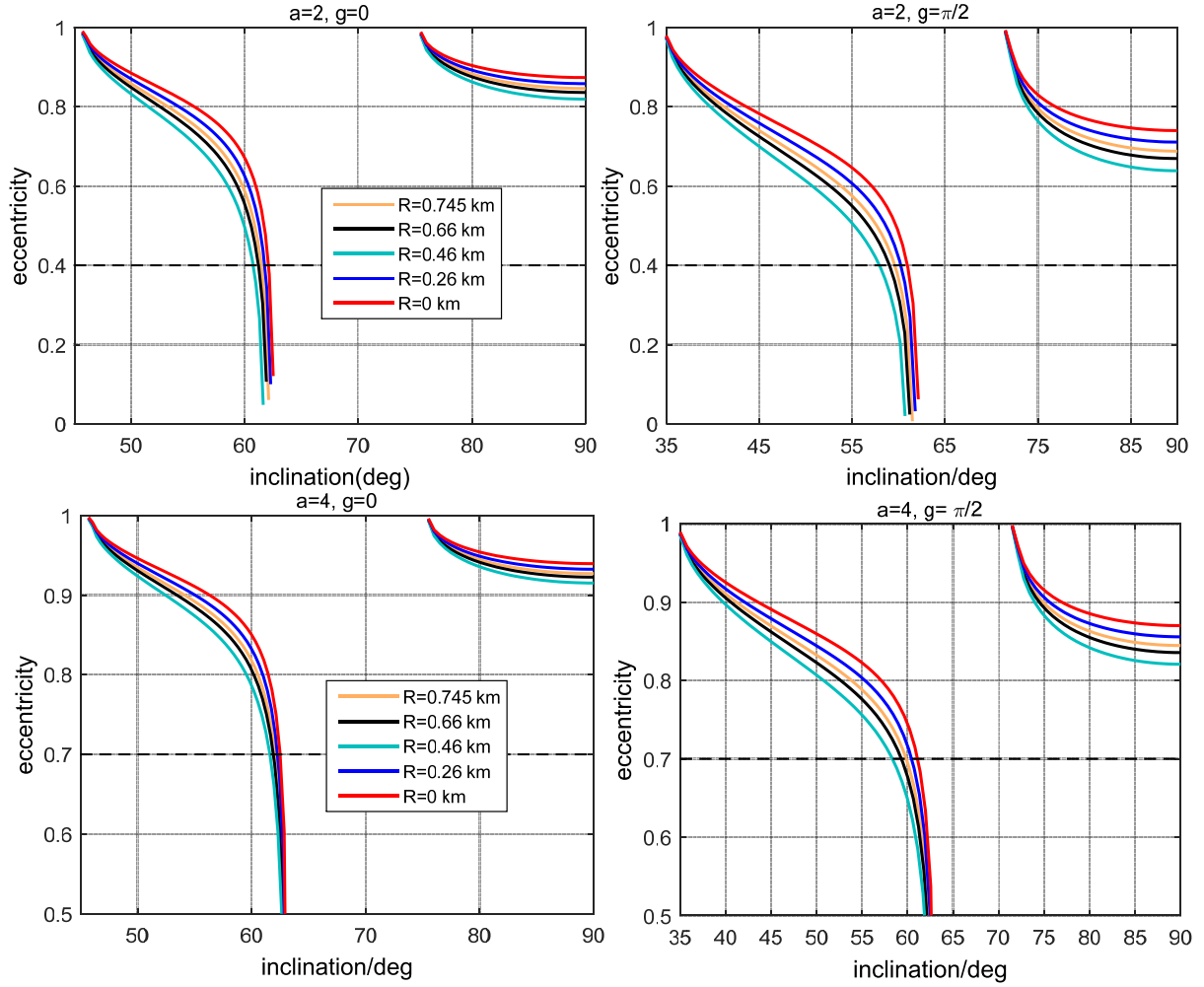


**Figure 5** Eccentricity-inclination diagrams for the double-averaged system with  $C_{20}$  and  $C_{40}$  at  $g = 0$  (left) and  $\pi/2$  (right), when the radius of the sphere varies from 0 to 0.745 km. The straight dashed lines indicate the value of impact eccentricity.

## (2) Effects of Tesseral Harmonics

To check the validity of the frozen orbits found in the previous section, a numerical integration is carried out under the influence of different subsets of the  $4 \times 4$  spherical harmonics in the non-averaged model. One example is given in Fig.6, where the evolutions of the orbital elements  $e, i, g$  are illustrated. The initial frozen condition is  $a = 2.5, e = 0.4772, g = 90^\circ, i = 60^\circ, \Omega = 90^\circ, \theta = 60^\circ$ . With the short-period perturbation of the dominant  $C_{20}, C_{40}, C_{22}$  terms added to the above mean values, the osculating elements are obtained for integration in the non-averaged dynamics<sup>5</sup>. A number of cases from Fig.4 have been simulated, and they have similar evolutions. It is also found that the more circular (close to the critical inclination) and the larger  $a$  of the orbit, the better behaviour of its evolution in the non-averaged  $C_{20}+C_{40}$  dynamics.

<sup>5</sup> The initial conditions are doubly-averaged orbital elements. The long-period perturbation arises from the secular change of  $g$ , which is zero for frozen orbits. Therefore, only the short-period perturbation is added to the initial conditions to get the osculating elements.

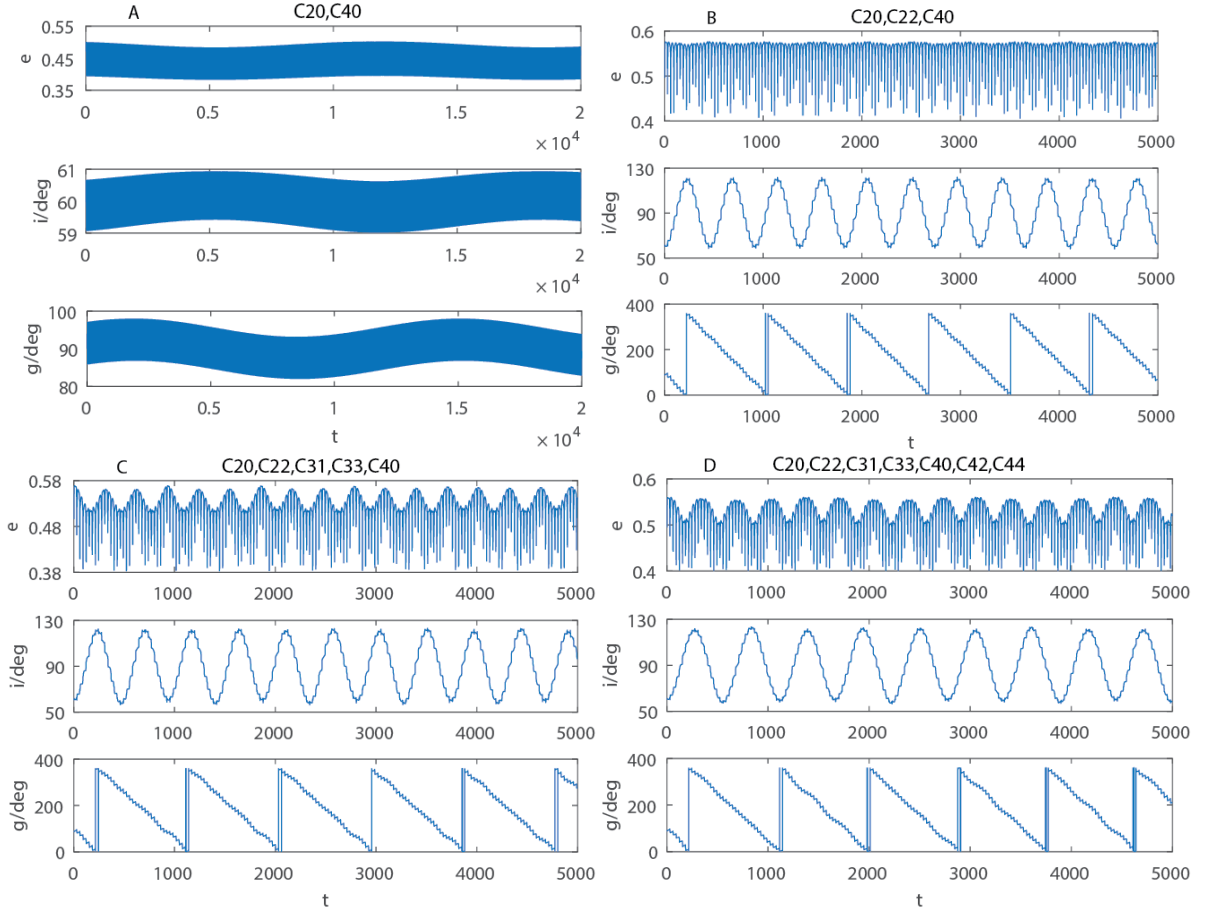


**Figure 6** The effects of different subsets of the  $4 \times 4$  spherical harmonics model on frozen orbits in the non-averaged  $4 \times 4$  model (time is dimensionless).

For the  $C_{20}$ ,  $C_{40}$  terms only (Fig. 6A), the short- and long-period oscillations appear as expected. The orbital elements evolve close to the mean value. When the  $C_{22}$  term is added, the inclination  $i$  has a large variation and perigee  $g$  circulates over the full range from  $0$  to  $360^\circ$  (Fig. 6B). After inclusion of the 3<sup>rd</sup> and 4<sup>th</sup> order tesseral harmonics (Figs. 6C and 6D), the general characteristic are kept except that the oscillations are obvious for the long-period evolution of  $e$ . Since the tesseral terms distort the frozen situation, their effect should be considered in the double-averaged model. However, they are all eliminated with the double averaging method applied in this study. The Lie-Deprit perturbation method studied in (Lara, 2008) is promising for solving this problem, where the effect of  $C_{22}$  is preserved after double averaging. In the following part, the dynamics of the single-averaged model is studied, where the tesseral terms are kept.

## 4.5 Poincaré Sections of the Single-averaged Model

The single-averaged model given by Eq.(8) is studied in this section. Since the time term is implicit, the averaged Hamiltonian  $\bar{\mathcal{H}}$  can be viewed as the integral of motion and is conserved. Since  $l = M$  has already been eliminated during the averaging,  $L$  and  $a$  remain constant as  $\partial \bar{\mathcal{H}} / \partial l = 0$ . To explore the global dynamics, the Poincaré map



method is employed. In the current study, the Poincaré section on which the flow is cut is defined as the  $G - g$  plane with  $h = \pi$  and  $\dot{h} < 0$  (which is always the case as time increases). Given an energy level of the system, i.e.  $\bar{\mathcal{H}}_{initial}$ , and an initial condition  $(L_0, g_0, G_0, h_0)$ , the value of  $H_0$  can be determined numerically. With this initial point, Eq.(7) is integrated over long time intervals, and the events when the solution crosses the  $G - g$  plane are recorded throughout the integration. To get a section fully filled with points, we chose a  $30 \times 30$  grid of initial values  $(g_0, G_0)$  for each given  $\bar{\mathcal{H}}_{initial}$  and  $L_0$ ; therefore the section corresponds to a range of  $e_0$  and  $i_0$ . Based on the physical parameters of system 1996 HW1, Figs.7 and 8 present some sections obtained for  $a = 2.5$  and 4, respectively, both at  $n_a = 0.01$ . The plots reflect the evolution of phase space of the single-averaged system at different orbital inclinations or energy values.

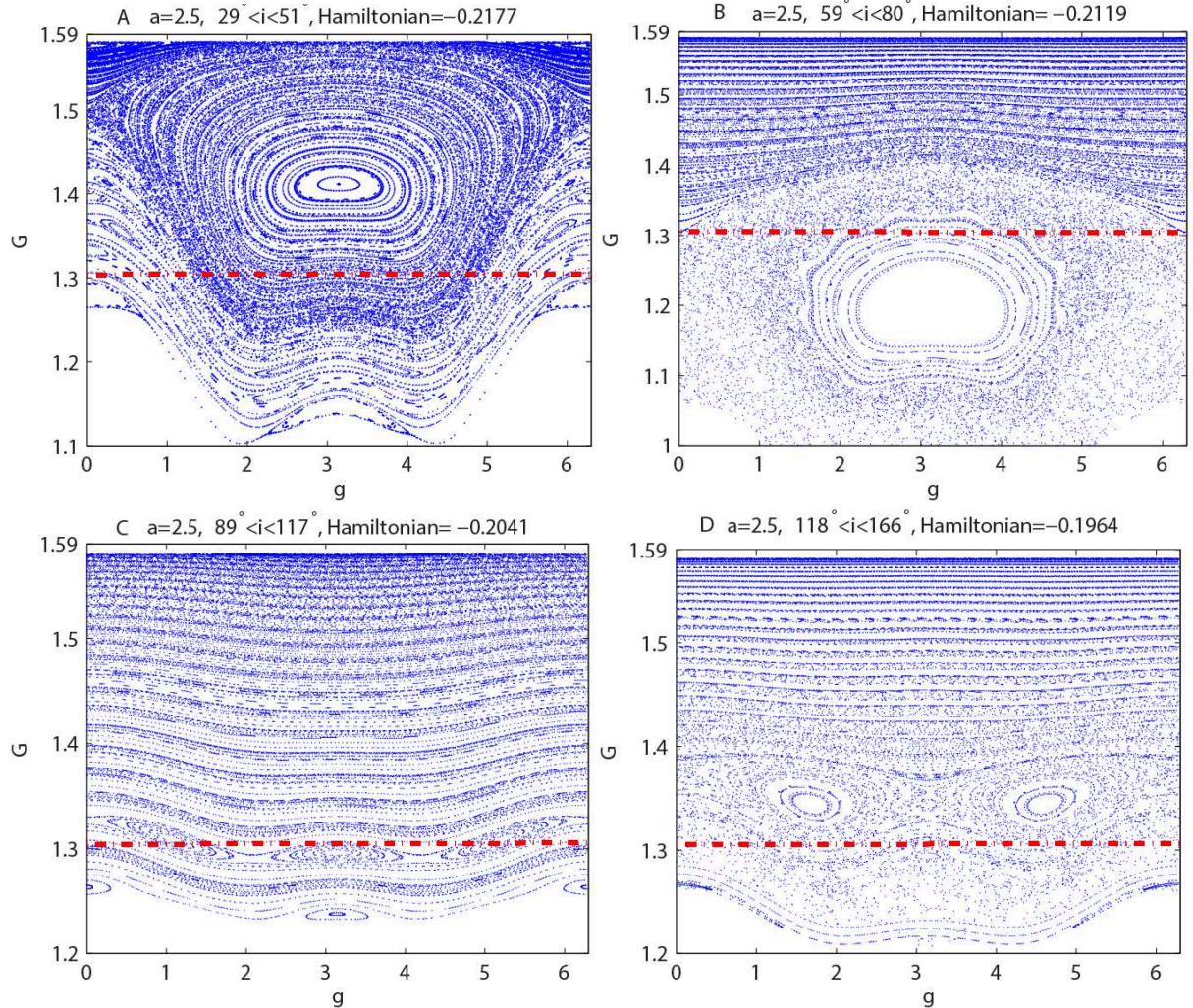


**Figure 7** Poincaré sections for  $a = 2.5$  under different energy levels; areas below the dashed line are the impact regions.

Since the orbital elements of a PO should return to the same values after one period of the orbit (which may cover multiple revolutions), it is actually a fixed point on the map, which can be identified from the center of an island. It is seen from Fig.7 that the phase space is very different for different energy levels. For  $29^\circ < i < 51^\circ$ , many

islands come forth both in the impact and non-impact regions, implying the existence of POs. One is weakly visible located at the top corner of the map with  $G = 1.58$  and  $g = 0$  or  $2\pi$ , while the largest one is at the center of the map with  $g = \pi$ . When the inclination increases (Fig.7B), the upper part of the map becomes regular without any island apparent, and the region around the largest island is chaotic. For the region around the polar case (Fig.7C), many islands emerge again but at the very bottom of the map. After that (Fig.7D), islands surrounded by large chaotic regions appear. Since the impact eccentricity  $e_{imp}$  for  $a = 2.5$  is 0.56, which corresponds to  $G = 1.31$ , small-eccentricity POs can be found at low inclinations (Fig.7A), while high inclinations only give rise to large-eccentricity ones (but still valid from an impact perspective, Fig.7D). However, the polar PO is not feasible as its eccentricity already exceeds  $e_{imp}$ , which is a restriction for practical usage as it might intersect with the asteroid at periapsis (Figs.7B,7C).

Now let us go to higher orbits at  $a = 4$ , with the corresponding  $e_{imp} = 0.725$  and  $G = 1.377$ . As shown in Fig.8, in general the sections for  $a = 4$  are more smooth, compared with those of  $a = 2.5$ . As expected, the 4×4 spherical harmonics' influence on orbits is weakened when the orbital altitude increases. Similarly, for  $0 < i < 90^\circ$  (Figs.8A and 8B), the islands move towards the bottom of the map with the increase of orbital inclination, implying the raise of eccentricity of the POs. No island appears near the polar region (Fig.8C). When it passes the polar region (Fig.8D), islands appear again and a new phase structure is generated. Compared with the maps for  $a = 2.5$ , the ones at higher altitude are already smooth due to the smaller influence of the irregular gravitational field on orbits. However, the same conclusion holds that the phase space is more smooth around the polar region than that close to the equatorial plane, implying the larger influence of the irregular gravitational field on the motion in the latter one. As a consequence, the feasible POs tend to appear at low and high inclinations rather than at the polar region.



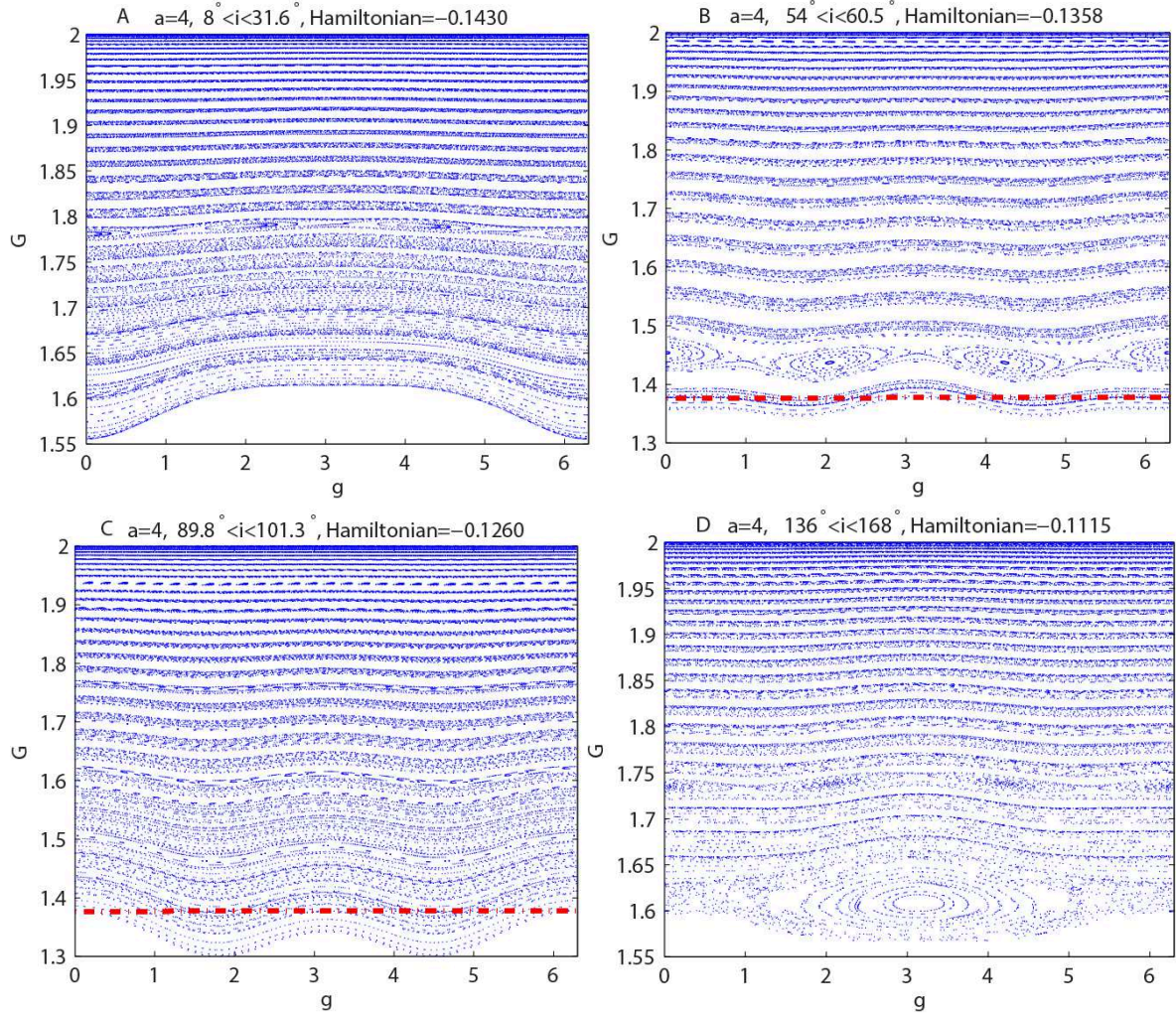


**Figure 8** Poincaré sections for  $a = 4$  under different energy levels; plots below the dashed line are the impact regions.

In addition, a similar analysis has also been performed for different system parameters of this configuration, as done in the study of frozen orbits (Section 3.2). It is found that the quantitative characteristics of the maps are similar to those above, for approximately the same  $a$  and inclination range if we vary the size of the sphere for this system configuration. Therefore, in the following sections, only the size of system 1996 HW1 is considered for simulations. What's more, some comparisons can be made with the frozen results obtained from Section 4. For the same  $a, i$  and  $g$  the POs have a close but slightly smaller eccentricity than that of the frozen orbits, and also POs appear in the inclination range where no frozen solution was to be found. This is due to the effects of inclusion of the tesseral harmonics as well as the rotation of the asteroid and also the resultant more abundant dynamics.

## 4.6 Periodic Orbits

The exact POs can be obtained by numerically modifying the raw initial condition read from the maps. In this section, the POs found in the single-averaged model and then in the non-averaged model are given respectively.

### 4.6.1 POs in the Single-averaged Model

Starting from the initial conditions given from the center of the islands in Figs.7 and 8, POs are found with the differential correction method (DC) (Russell and Lara, 2007, Lara and Russell, 2007). The evolution of their eccentricity vectors (defined as  $[e \cdot \sin(g), e \cdot \cos(g)]$ ) is given in Fig.9 for four different cases, all covering 5 periods of the orbit. It can be observed that all eccentricity vectors repeat their path completely. The paths in Figs.9A, 9B and 9D are all simple circles, as  $e$  has a sin/cos wave oscillation and  $g$  varies between 0 and  $2\pi$  throughout one period. However, the curve in Fig.9C is more complicated due to the non-trivial variation of  $e$  and also the oscillation of  $g$  is limited to the range from  $1.2\pi$  to  $1.9\pi$ .

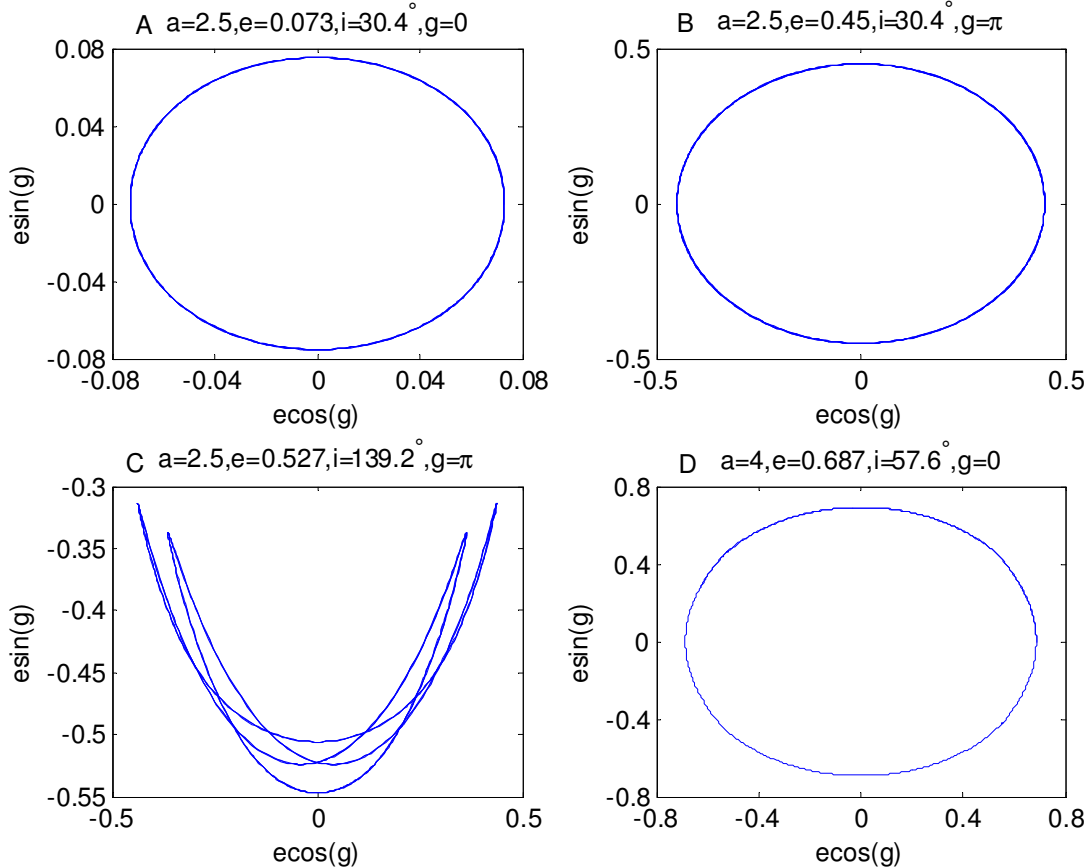


**Figure 9** Examples of the eccentricity vector evolution for 5 periods of the POs.

### 4.6.2 POs in the Non-averaged Model

One step further, the POs obtained in the single-averaged model can serve as initial conditions for identifying POs in the full non-averaged model given by Eq.(1). Here, the Levenberg-Marquardt method (Lourakis, 2005) is applied, which can be used for searching the zero root of a given system. Several families of POs are obtained, which

are illustrated in Fig.10<sup>6</sup>. In Fig.10, the blue orbit in each subfigure is modified from the corresponding initial conditions given by Fig.9. For example, the blue orbit in family A is originally from Fig.9A. With numerical continuation of energy, many orbits are found for each family. The two orbits at the ends of the continuation are given in red and green, respectively.

With the Floquet's Theory, their linear stabilities can be evaluated; a PO is stable if all the eigenvalues of its monodromy matrix have unity magnitude (Chicone, 1999). Since the monodromy matrix of a PO always has the eigenvalues in the form of  $\{1, 1, \lambda_1, 1/\lambda_1, \lambda_2, 1/\lambda_2\}$ , the stability index is commonly defined as  $s_i = |\lambda_i + 1/\lambda_i|$ ,  $i = 1, 2$ . The PO is linearly stable if  $s_i < 2$ , while linearly unstable if  $s_i > 2$ . Bifurcation might occur when  $s_i = 2$ . The linear stability diagrams for these four families of POs are given in Fig. 11.

For family A, the blue orbit and the 'circular' green one are both linearly stable, while the eccentric red one is unstable. The eccentric orbits of family B are all unstable. One direction of the continuation leads to an orbit that comes close to the equatorial plane (the green one), while the other (the red one) gradually approaches the polar region. All the orbits of family C are unstable and also highly inclined when they become smaller and closer to the asteroid. For family D in Fig.10D, the continuation ends at the equatorial plane with a stable yellow orbit. The orbits out of the plane are all unstable.

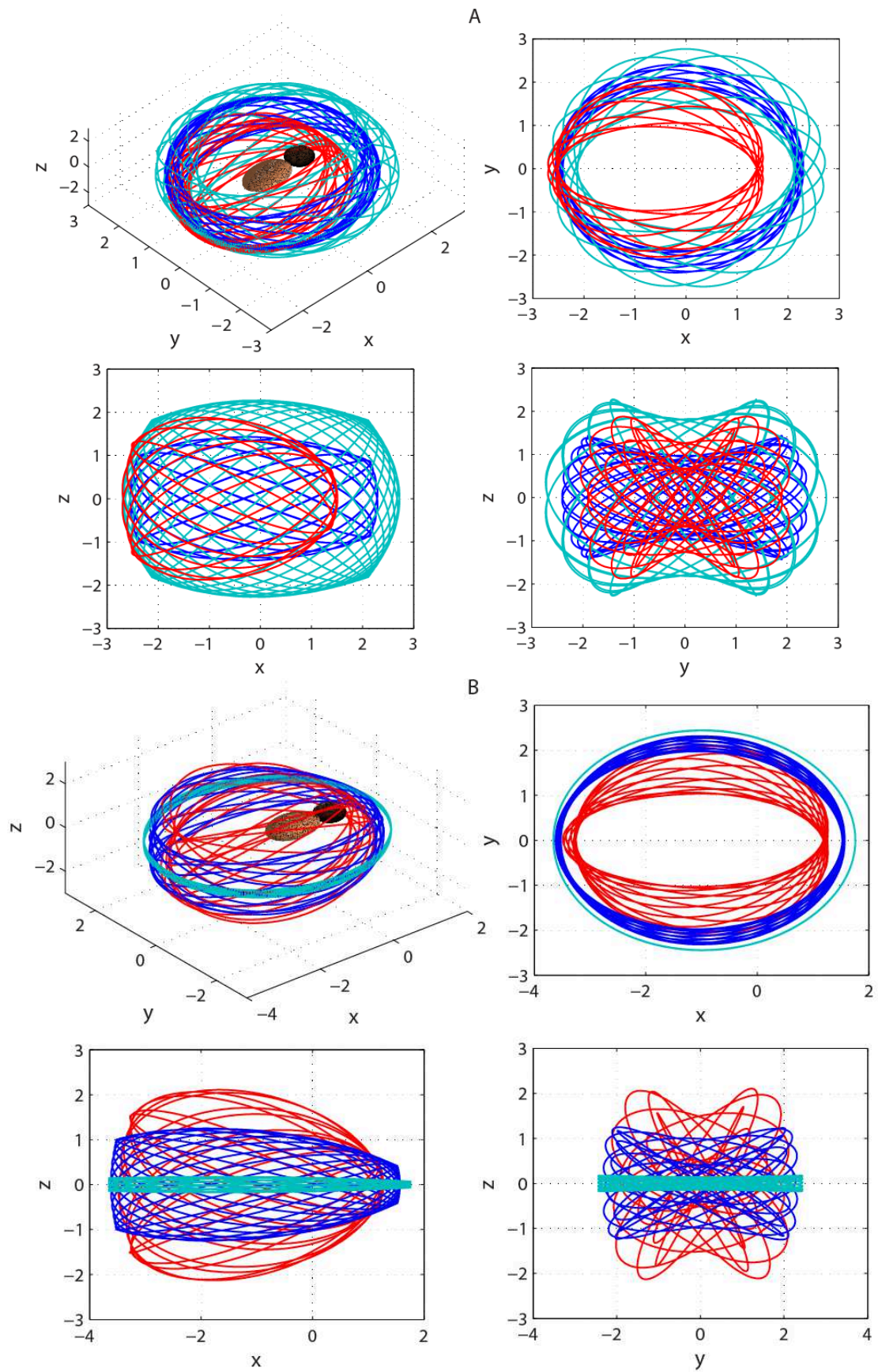
In all four families, the green orbits have the longest period while the red ones have the shortest period. The period is simply lengthened with the increase of energy. These families also share the same characteristic that the orbits become highly inclined in the close vicinity of the asteroid, resulting from the highly irregular gravitational field. In addition, all families of orbits have multiple revolutions within one period, and the initial conditions of all blue orbits are given in Appendix E. It can be noticed that the radius at some epoch along the orbits is smaller than 2, however this does not play a role since the simulation is already done in the full model (cf. Eq.(1)).

---

<sup>6</sup> Orbits of families A, B and E are all in counter-clockwise direction, while orbits of families C and D are in clockwise direction.



# Modelling and analysis of periodic orbits



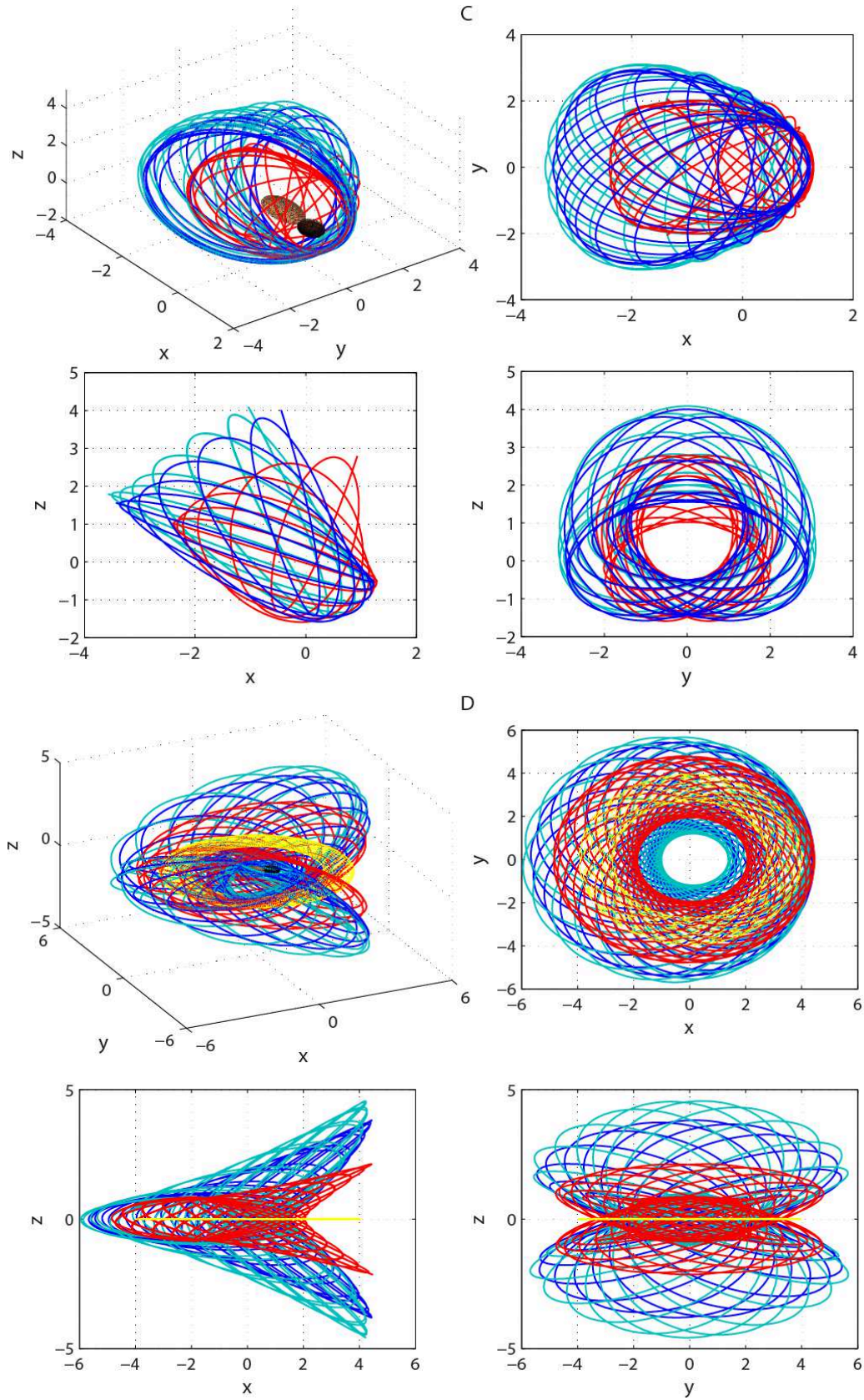


**Figure 10** Families of POs of the non-averaged system, represented as family A, B, C, D.

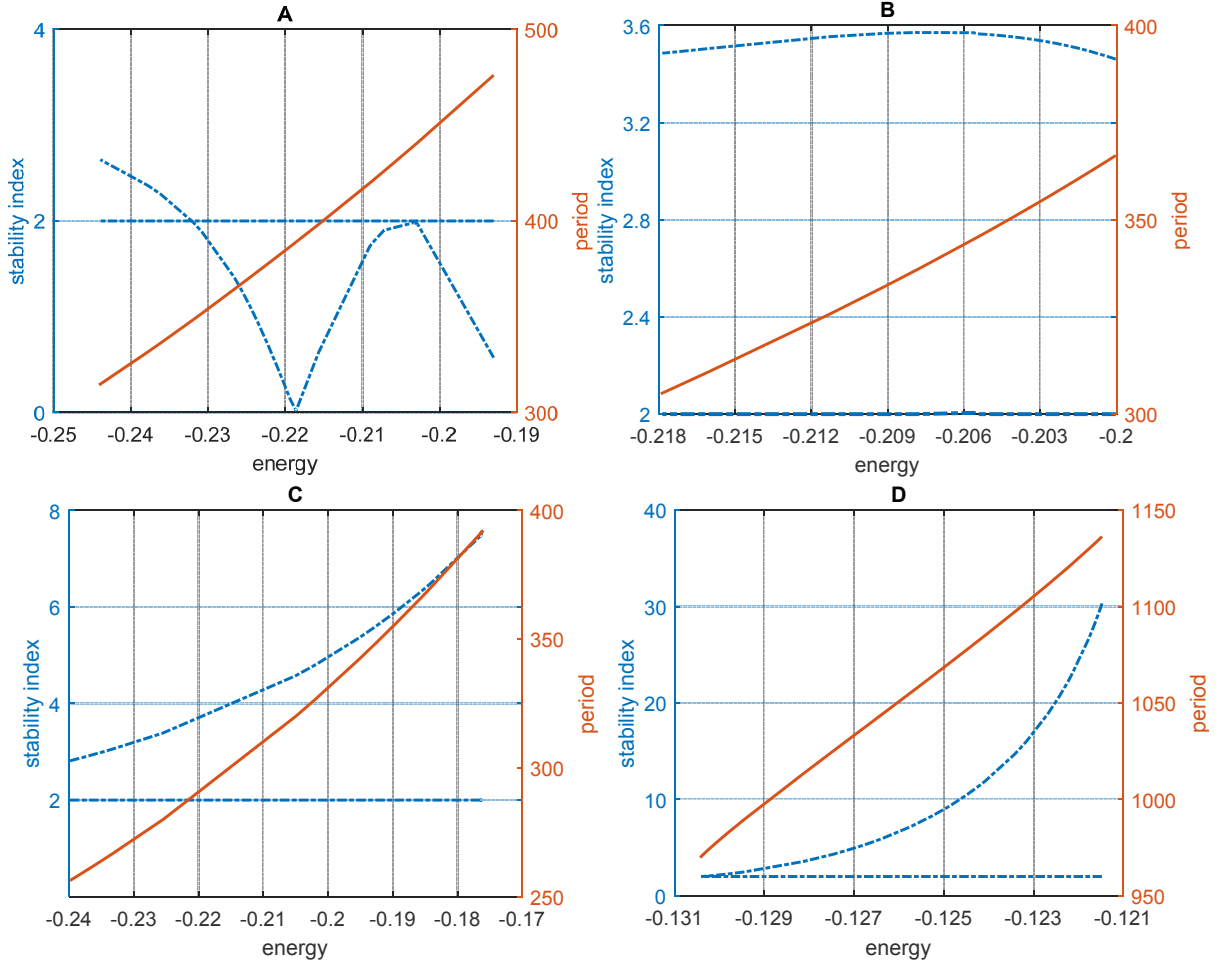


**Figure 11** The linear stability diagram of POs of families A, B, C, D. The two blue dashed lines are the stability index and the red line is the period.

#### 4.6.3 POs of Faster Rotating Asteroid

In fact, the rotation rate of the asteroid is suspected to have a more important effect on orbital dynamics than that of the size of this system configuration. Therefore, in this section, the work in Sections 5, 6.1 and 6.2 is repeated but with a rotation rate speeded from up  $n_a = 0.01$  to  $n_a = 0.1$ . Firstly, the case at  $a = 2.5$  is studied. The dynamical phenomena on these sections are found not to be as rich as those at  $n_a = 0.01$ . For low inclinations (Fig.12A), some ‘thin’ islands are apparent at the very bottom of the map, which are close to the impact eccentricity. The phase space is very regular and islands are absent for higher inclination cases, as shown in Figs.12B and 12C. Not depicted here, it is found that nearly no island exists at almost all the sections for larger values of  $a$ . This means that the faster rotation of the asteroid helps to reduce the effects of the highly irregular gravitational field on orbits and to smooth out the chaotic or irregular regions on the maps. Therefore, the case for a smaller value of  $a$  ( $a = 2$ ) is simulated and the results are shown in Figs.12D-F. Many islands and chaotic regions now appear again at the low inclination range, as shown in Fig.12D. Similarly, the islands gradually move towards the bottom with the increase of inclination and even disappear in the polar situation.



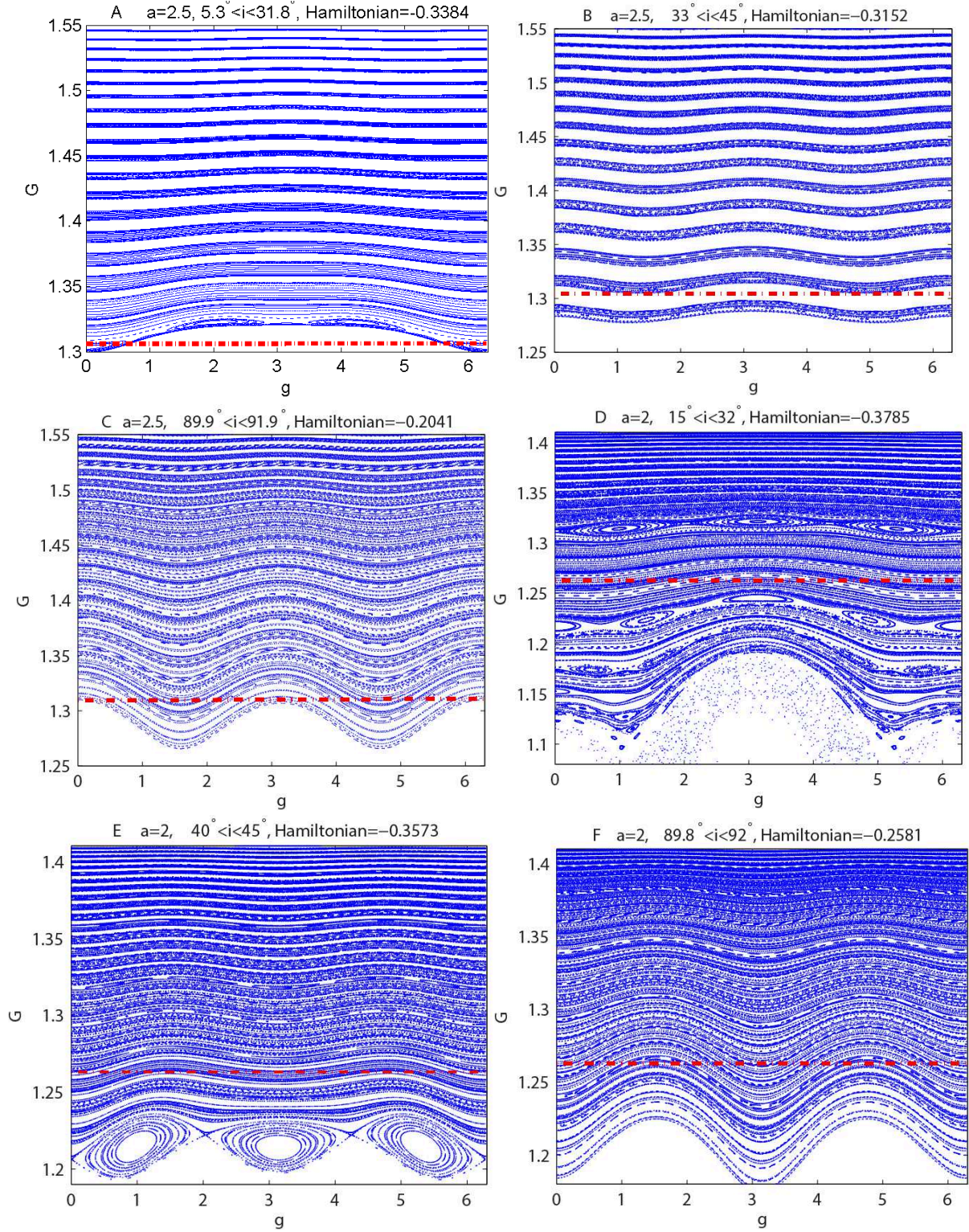


**Figure 12** Poincaré sections for  $a = 2.5$  and  $2$  at  $n_a = 0.1$  at different energy levels; areas below the dashed line are the impact regions.

In addition, it is found that the fast rotation of the asteroid smooths out the phase space. For instance, at  $a = 2.5$  but with  $n_a = 0.3$ , there is already no island on the Poincaré maps at different inclinations. The same phenomenon holds for larger  $a$  and  $n_a$ . This means that the rotation rate has a significant influence on the dynamics, rather than the limited effect from the size of the system.

The method for searching POs in the single-averaged model is the same for the case with  $n_a = 0.01$ . The evolution of the eccentricity vector over 5 periods of one sample PO, originally from Fig.12E, is given in Fig.13. It can be noticed that it has a similar pattern as those of Figs.9A, 9B and 9D. Similarly, with the initial conditions from Fig.13, the PO in the non-averaged model is obtained with the Levenberg-Marquardt method. With the continuation of energy, one family of orbits is obtained and illustrated in Fig.14. Their general configuration already differ from those in Fig.10, confirming that fast rotation of the asteroid does affect its surrounding orbit. All three orbits are unstable. The stability diagram of this family is given in Fig. 15. The green one is highly unstable, while the red one is slightly unstable, since one stability line is actually slightly above the line  $= 2$ , not exactly on it. For the continuation to the green orbits, the period decreases with the increase of energy probably due to the crossing of the bifurcation line ( $s = 2$ ). It should be mentioned here that it is more difficult in this situation to find the POs in the non-averaged model. This is probably due to the smaller accuracy of the spherical harmonics truncation at degree and order 4 when the orbit is really close to the asteroid and also the fact that more information is lost during the low-order averaging process when the rotation rate of the asteroid is increasing.

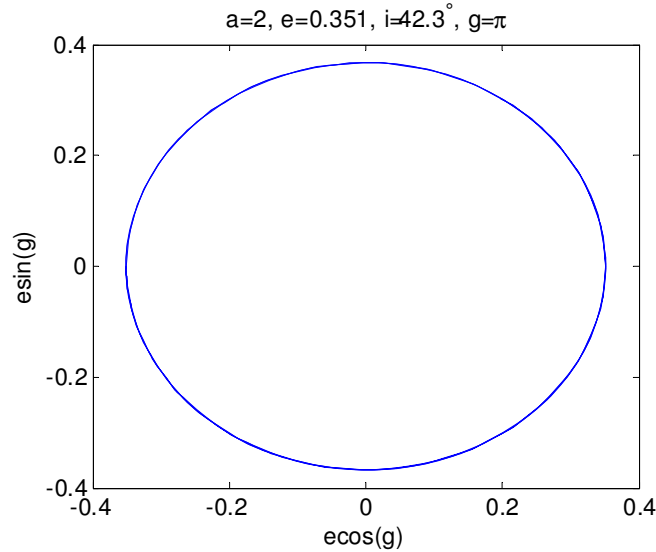


**Figure 13** The eccentricity vector evolution for 5 periods of the PO in the single-averaged model.

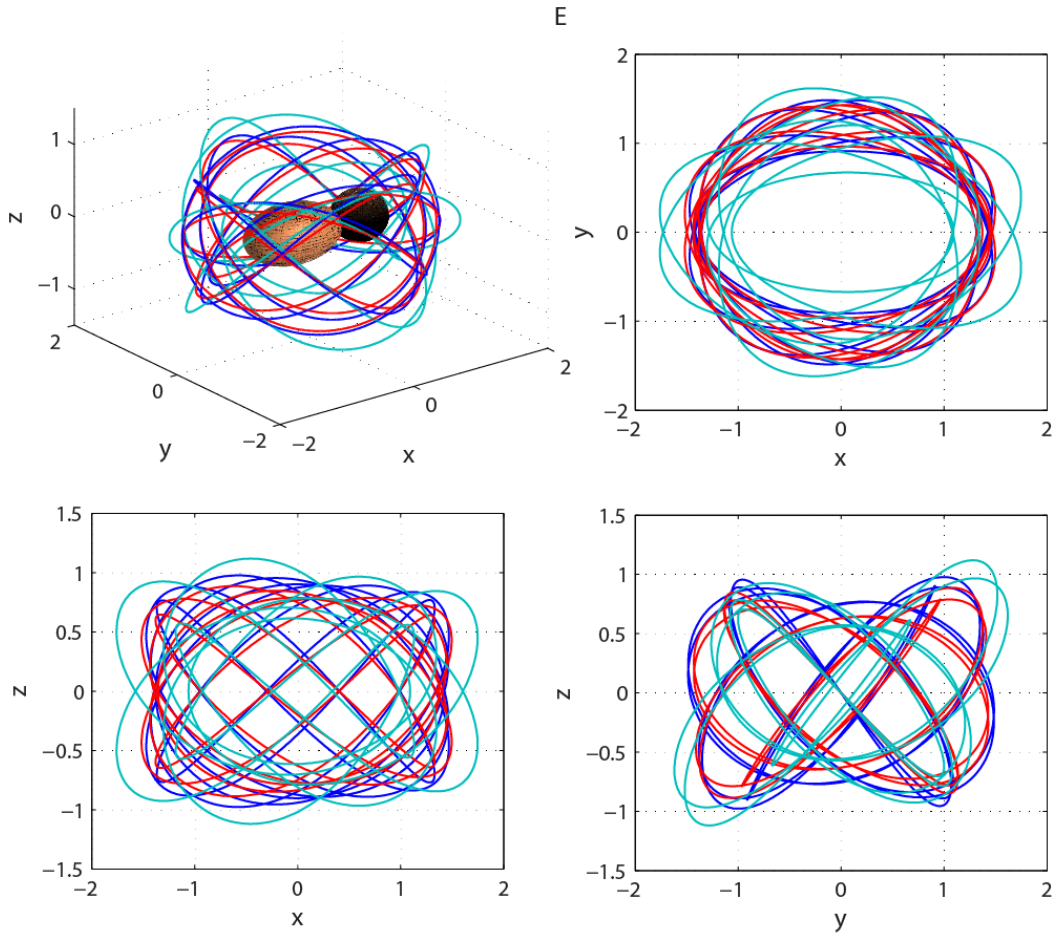


**Figure 14** POs of the original non-averaged system at  $n_a = 0.1$ .

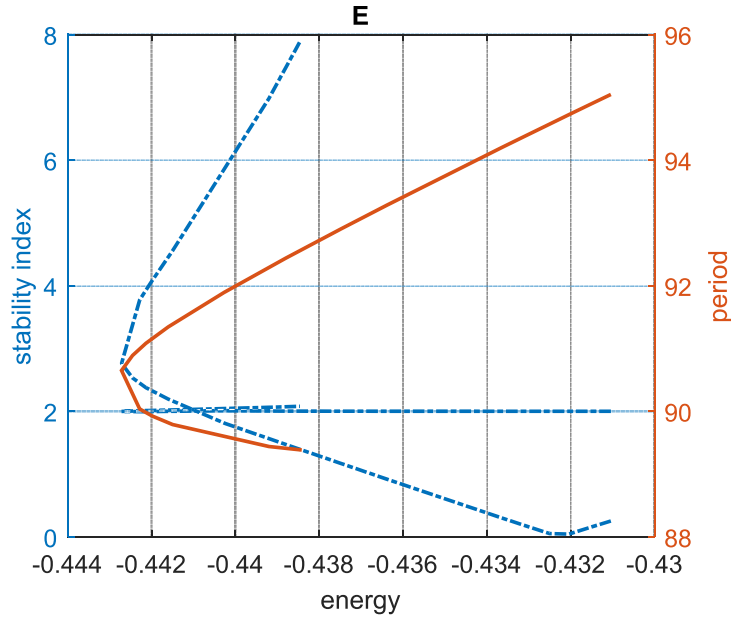


**Figure 15** The linear stability diagram of POs of family E. The two blue dashed lines are the stability index and the red line is the period.



## 4.7 Conclusions

The POs around a contact binary asteroid have been obtained with the spherical harmonics expansion, the averaged Hamiltonian and the numerical modification method. The highly irregular gravitational field is represented by the combination of an ellipsoid and a sphere, and then is expanded into a spherical harmonics model, which is shown to be a good approximation. For system 1996 HW1, the 8<sup>th</sup> and 4<sup>th</sup> degree and order expansions have relative errors of the potential of less than 2% and 8% at the circumscribing sphere, respectively. The relative errors of the 4×4 truncation are always smaller than 1% when the orbit radius is larger than 2, under different sizes of the system configuration. The radial acceleration has an error one magnitude larger than that of the potential. It is also found that some high-order terms also have a large magnitude, e.g.  $C_{31}$ ,  $C_{40}$ ,  $C_{60}$ , in comparison with that of planetary bodies and their moons.

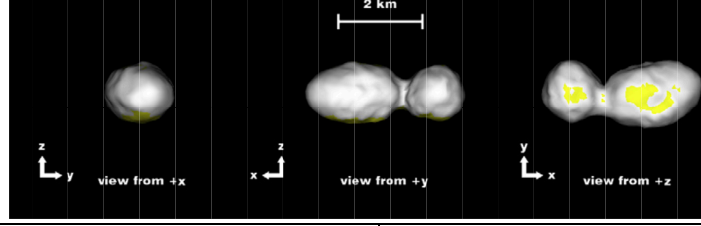
Frozen orbits are obtained from the double-averaged Hamiltonian including the 4<sup>th</sup> degree and order spherical harmonics. They are examined in the non-averaged model, and the tesseral terms are found to introduce large variations and distort the frozen situation. With Poincaré sections, the phase space structure of the single-averaged model is generated at different energy levels and rotation rates of the asteroid. The dynamics of the 4×4 harmonics is identified and POs are obtained. The disturbing effect of the highly irregular gravitational field on orbit motion is found to be reduced around the polar region as well as in the case of fast rotation of the asteroid. Further with the Levenberg-Marquardt method, some POs of the full non-averaged model are identified, of which the stable ones are interesting for future missions. In addition, this study provides a method for studying orbital dynamics around a highly bifurcated body represented by spherical harmonics.

## Acknowledgements

We acknowledge Prof. Martin Lara for his constructive comments for improving the quality of this paper. We thank Bart Root (Delft of Technology University) for his help on spherical harmonics expansion. We also give our acknowledgements to Dr. Stella Tzirti (University of Thessaloniki, Greece) for suggestions and help on the Poincaré section method. Great thanks are also given to Prof. Gerard Gomez (University of Barcelona, Spain) and Prof. Daniel J. Scheeres (University of Colorado, USA) for their suggestions and comments on this paper. This research is funded by the Chinese Scholarship Council (CSC).

## Appendix A

Table A1 The main parameters of 1996 HW1 (Magri et al., 2011).



Overall dimensions-full axes (km)	X: $3.78 \pm 0.05$ ; Y: $1.64 \pm 0.1$ ; Z: $1.49 \pm 0.15$
Sidereal period (h)	$8.76243 \pm 0.00004$
Average sphere diameter (km)	1.32
Triaxial ellipsoid principal axes size (km)	$2.46 \times 1.64 \times 1.49$
Bulk density ( $\text{g}\cdot\text{cm}^{-3}$ )	2.0

## Appendix B

The un-normalized dimensionless coefficients of the spherical harmonics expansion of the potential of 1996 HW1 up to degree and order 8.

Up to the degree and order 4			
$C_{00}$	1	$C_{32}$	0
$C_{10}$	0	$C_{33}$	$2.547 \times 10^{-3}$
$C_{11}$	0	$C_{40}$	$3.8779 \times 10^{-2}$
$C_{20}$	$-1.21847 \times 10^{-1}$	$C_{41}$	0
$C_{21}$	0	$C_{42}$	$-4.258 \times 10^{-3}$
$C_{22}$	$5.8547 \times 10^{-2}$	$C_{43}$	0
$C_{30}$	0	$C_{44}$	$5.16 \times 10^{-4}$
$C_{31}$	$-1.3964 \times 10^{-2}$		
Degree and order 5-8			
$C_{51}$	0.0048	$C_{73}$	$3.55379 \times 10^{-5}$
$C_{53}$	$-2.07134 \times 10^{-4}$	$C_{75}$	$-1.01047 \times 10^{-6}$
$C_{55}$	$2.16853 \times 10^{-5}$	$C_{77}$	$7.43626 \times 10^{-8}$
$C_{60}$	$-1.5481 \times 10^{-2}$	$C_{80}$	$6.693 \times 10^{-3}$
$C_{62}$	$7.69618 \times 10^{-4}$	$C_{82}$	$-1.92847 \times 10^{-4}$
$C_{64}$	$-2.52427 \times 10^{-5}$	$C_{84}$	$3.18426 \times 10^{-6}$
$C_{66}$	$2.05401 \times 10^{-6}$	$C_{86}$	$-7.46287 \times 10^{-8}$
$C_{71}$	$-1.752 \times 10^{-3}$	$C_{88}$	$4.57416 \times 10^{-9}$

## Appendix C

The terms of the Hamiltonian of the first 4<sup>th</sup> degree and order spherical harmonics in spherical harmonics are listed as follows

$$\begin{aligned}
 \mathcal{H}_0 &= -\mu/2a, \mathcal{H}_{n_a} = -n_a \sqrt{\mu a(1-e^2)} \cos(i) \\
 \mathcal{H}_{C_{20}} &= \frac{\mu R_e^2 C_{20}}{r^3} \left(1 - \frac{3}{2} \cos^2 \theta\right), \mathcal{H}_{C_{22}} = \frac{3\mu R_e^2 C_{22}}{r^3} \cos^2 \theta \cdot \cos 2\lambda \\
 \mathcal{H}_{C_{30}} &= \frac{\mu R_e^3 C_{30}}{2r^4} \sin \theta \cdot (5 \sin^2 \theta - 3), \mathcal{H}_{C_{31}} = \frac{3\mu R_e^3 C_{31}}{2r^4} \cos \theta \cdot \cos \lambda \cdot (4 - 5 \cos^2 \theta) \\
 \mathcal{H}_{C_{33}} &= \frac{16\mu R_e^3 C_{33}}{r^4} \cos^3 \theta \cdot \cos 3\lambda, \mathcal{H}_{C_{40}} = \frac{\mu R_e^4 C_{40}}{8r^5} (35 \sin^4 \theta - 30 \sin^2 \theta + 3) \\
 \mathcal{H}_{C_{42}} &= \frac{15\mu R_e^4 C_{42}}{2r^5} \cos^2 \theta \cdot \cos 2\lambda \cdot (6 - 7 \cos^2 \theta), \mathcal{H}_{C_{44}} = \frac{105\mu R_e^4 C_{44}}{r^5} \cos^4 \theta \cdot \cos 4\lambda
 \end{aligned} \tag{C.1}$$

where  $\mu = GM$  is the mass constant of the entire body.

## Appendix D

The relations between orbital elements and spherical coordinates are given as

$$\begin{aligned}
 \sin \theta &= \sin i \cdot \sin(f + g), \cos(f + g) = \cos \theta \cdot \cos(\lambda - h) \\
 \cos \theta &= \cos i \cdot \sin(f + g) \cdot \sin(\lambda - h) + \cos(f + g) \cdot \cos(\lambda - h) \\
 r &= \frac{a(1-e^2)}{1 + e \cos f}
 \end{aligned} \tag{D.1}$$

## Appendix E

Initial conditions of the blue periodic orbits in Figs.10 and 14.

Family (Rev.)	$x$	$y$	$z$	$\dot{x}$	$\dot{y}$	$\dot{z}$	$T$
A (17)	-2.55457397	5.64799031E-3	-3.53658923E-4	-1.28549893E-3	-0.47909409	0.37960782	388.99897129
B (14)	-3.62261850	1.60726159E-3	-1.00020805E-7	-3.11315611E-4	-0.32969659	0.20743635	345.00007481
C (14)	0.24122555	-1.33173497	-1.54128269	-0.41349405	-0.63862589	0.04199977	369.00019323
D (26)	-5.66707383	0.22824198	7.98840161E-16	2.16135142E-3	0.32293658	8.67487872E-3	1100.14960642
E (9)	1.37250344	-7.44797928E-4	1.08776131E-3	9.25774395E-4	0.69647207	-0.63225584	91.89849972



# Chapter 5 1:1 Ground-track resonance in a uniformly rotating 4<sup>th</sup> degree and order gravitational field

---

J. Feng, R. Noomen, X. Hou, P.N.A.M. Visser, J. Yuan

Submitted to *Celestial Mechanics and Dynamical Astronomy*, February 2016

## Abstract

Using a gravitational field truncated at the 4<sup>th</sup> degree and order, the 1:1 ground-track resonance is studied. To address the main properties of this 1:1 resonance, a 1-degree of freedom (1-DOF) system is firstly studied. It is completely integrable. Equilibrium points (EPs), stability and resonance width are obtained. Different from previous studies, the inclusion of non-spherical terms higher than degree and order 2 introduces new phenomena. For a further study about the 1:1 resonance, a 2-DOF system is introduced, which includes the 1-DOF system and a second resonance acted as a perturbation part. With the aid of Poincaré section, the generation of chaos in the phase space is studied in detail by addressing the overlap process of these two resonances with arbitrary combinations of eccentricity ( $e$ ) and inclination ( $i$ ). Retrograde orbits, near circular orbits and near polar orbits are found to have better stability against the perturbation of the second resonance. The situations of complete chaos are estimated in the  $e - i$  plane. By applying the maximum Lyapunov Characteristic Exponent (LCE), chaos is characterized quantitatively and same conclusions can be achieved. This study is applied to three asteroids 1996 HW1, Vesta and Betulia, but the conclusions are not restricted to them.

## 5.1 Introduction

The commensurability (usually a ratio of simple integers) between the rotation of the primary body and the orbital motion of the surrounding spacecraft or particle is called ground-track resonance. A large amount of research has been carried out about geosynchronous orbits. For example, a 2-DOF Hamiltonian system was modeled (Delhaise and Henrard, 1993) near the critical inclination perturbed by the inhomogeneous geopotential. Global dynamics were studied in terms of Poincaré maps in the plane of inclination and argument of pericenter. Chaotic motions were expected close to the separatrix of the resonance of the mean motion.

However, for ground-track resonances in the highly irregular gravitational field (mainly small solar system bodies), the studies are limited. Scheeres (1994) studied the stability of the 1:1 mean motion resonance with a rotating asteroid using a triaxial ellipsoid model, and applied it to Vesta, Eros and Ida. Later on, he studied the effect of the resonance between the rotation rate of asteroid Castalia and the true anomaly rate



of an orbiting particle at periapsis with a 2<sup>nd</sup> degree and order gravitational field (Scheeres et al., 1996). This kind of resonance was proven to be responsible for significant changes of orbital energy and eccentricity, and provides a mechanism for an ejected particle to transfer into a hyperbolic orbit or vice versa. By considering the 2<sup>nd</sup> degree and order gravitational field, Hu and Scheeres (2004) showed that orbital resonance plays a significant role in determining the stability of orbits. Further, by modelling the resonant dynamics in a uniformly rotating 2<sup>nd</sup> degree and order gravitational field as a 1-DOF pendulum Hamiltonian (Olsen, 2006), widths of the resonance were obtained in analytical expressions and also tested against numerical simulations for five resonances. They were found to be independent of the rotation rate and mass of the central body but strongly dependent on  $e$  and  $i$ . The retrograde orbits have a smaller resonance region than the prograde ones. In a slowly rotating gravitational field, the orbital stability was explained by the distance between the resonances but not by the strength of a specific one using the overlap criteria.

The resonant structure is explained with the truncated model for the equatorial and circular cases, respectively. Delsate (2011) built the 1-DOF Hamiltonian of the ground-track resonances of Dawn orbiting Vesta. The locations of the EPs and the resonance width were obtained for several main resonances (1:1, 1:2, 2:3 and 3:2). The results were checked against numerical tests. The 1:1 and 2:3 resonances were found to be the largest and strongest ones, respectively. The probability of capture in the 1:1 resonance and escape from it was found to rely on the resonant angle. Tzirti and Varvoglis (2014) extended Delsate's work by introducing  $C_{30}$  into the 1:1 resonance, which resulted in 2-DOF dynamics. The  $C_{30}$  term was found to create tiny chaotic layers around the separatrix but without significant influence on the resonance width. With the ellipsoid shape model (Compère et al., 2012), MEGNO (Mean Exponential Growth factor of Nearby Orbits) was applied as an indicator to detect stable resonant periodic orbits and also 1:1 and 2:1 resonance structures under different combinations of the three semi-axes of the ellipsoid. A 1-DOF resonant model parametrized by  $e$  and  $i$  was obtained with a truncated ellipsoidal potential up to degree and order 2.

For the previous studies, the limitations are either the gravitational field which is truncated at degree and order 2 or the orbit which is restricted to a circular or polar case. In this study, the harmonic coefficients up to degree and order 4 are taken into account for studying the 1:1 resonance at different combinations of  $e$  and  $i$ , which results in a 2-DOF model. Therefore, this paper is arranged as follows. Firstly, a 1-DOF Hamiltonian is built to investigate the main properties of the 1:1 resonance. The location of EPs and their stability are solved numerically for different combinations of  $e$  and  $i$  for Vesta, 1996 HW1 and Betulia. The resonance widths of the stable EPs are found numerically. Secondly, a 2-DOF Hamiltonian is introduced with the inclusion of a second resonance, which is treated as a perturbation on the 1-DOF Hamiltonian. Chaos is generated due to the overlap of the two resonances. By applying Poincaré

sections, for all three asteroids, the extent of the chaotic regions in the phase space is examined against the distance between the primary and second resonances and their respective strengths. The roles that  $e$  and  $i$  play on the evolution of chaos in the phase space are studied systemically. Finally, the maximal LCE (mLCE) of the orbits in the chaotic seas are calculated for a quantitative study.

## 5.2 Dynamical Modelling

### 5.2.1 Hamiltonian of the system

The gravity potential expressed in orbital elements  $(a, e, i, \Omega, \omega, M)$  is given by Kaula (1966) as

$$V = \frac{\mu}{r} + \sum_{n \geq 2} \sum_{m=0}^n \sum_{p=0}^n \sum_{q=-\infty}^{\infty} \frac{\mu R_e^n}{a^{n+1}} F_{nmp}(i) G_{npq}(e) S_{nmpq}(\omega, M, \Omega, \theta), \quad (1)$$

in which  $\mu$  and  $R_e$  are the gravitational constant and reference radius of the body, respectively.  $r$  is the distance from the point of interest to the center of mass of the body.  $F(i)$  and  $G(e)$  are functions of inclination and eccentricity, respectively. The complete list of them up to degree and order 4 can be found in Kaula (1966). In addition,  $n, m, p, q$  are all integers,  $\theta$  is the sidereal angle and

$$S_{nmpq} = \begin{bmatrix} C_{nm} \\ -S_{nm} \end{bmatrix}_{n-m \text{ odd}}^{n-m \text{ even}} \cos \Theta_{nmpq} + \begin{bmatrix} S_{nm} \\ C_{nm} \end{bmatrix}_{n-m \text{ odd}}^{n-m \text{ even}} \sin \Theta_{nmpq}$$

with Kaula's phase angle  $\Theta_{nmpq}$  written as

$$\Theta_{nmpq} = (n - 2p)\omega + (n - 2p + q)M + m(\Omega - \theta).$$

Given the Delaunay variables

$$l = M, g = \omega, h = \Omega, \\ L = \sqrt{\mu a}, G = L\sqrt{1 - e^2}, H = G \cos i,$$

the Hamiltonian of the system can be written as

$$\mathcal{H} = T - V + \dot{\theta}\Lambda, \quad (2)$$

in which  $T = -\mu^2/2L^2$  is the kinetic energy and  $\dot{\theta}$  is the rotation rate of the asteroid and  $\Lambda$  is the momentum conjugated to  $\theta$ . Resonances occur when the time derivative of  $\dot{\Theta}_{nmpq} \approx 0$ . The 1:1 resonance is studied in detail in the following sections.

### 5.2.2 1:1 Resonance

According to Kaula (1966), to study the 1:1 resonance, the resonant angle is introduced and defined as  $\sigma = \lambda - \theta$ , with the mean longitude  $\lambda = \omega + M + \Omega$ . This resonance occurs at  $\dot{\sigma} \approx 0$ , which means that the revolution rate (mean motion) of the orbit is commensurate with the rotation rate of the asteroid. In addition, it should be noticed that the solution of this 1:1 resonance includes the equilibrium points (EPs)

that are commonly studied in a rotating (or body-fixed) frame, and  $\sigma$  is the phase angle of the EPs in a rotating frame.

The spherical harmonics that contribute to this resonance are listed in Appendix A. To introduce the resonant angle  $\sigma$  in the Hamiltonian and also keep the new variables canonical, a symplectic transformation is applied

$$d\sigma L' + d\theta' \Lambda' = d\lambda L + d\theta \Lambda$$

and a new set of canonical variables is obtained as

$$\sigma, L' = L, \theta' = \theta, \Lambda' = \Lambda + L.$$

After averaging over the fast variable  $\theta'$ , the Hamiltonian for the 1:1 resonance truncated at the second order of  $e$  can be written as

$$\mathcal{H} = \mathcal{H}_0 + \mathcal{H}_1 + \mathcal{H}_2 + o(e^3),$$

where  $\mathcal{H}_k$  ( $k = 1, 2$ ) is the Hamiltonian at the  $k^{\text{th}}$  order of  $e$  and  $\mathcal{H}_0$  is expressed as

$$\begin{aligned} \mathcal{H}_0 = & -\frac{\mu^2}{2L^2} + \dot{\theta}(\Lambda' - L) - \frac{\mu^4 R^2}{L^6} [C_{20}(1-e^2)^{(-\frac{3}{2})} \left(-\frac{1}{2} + \frac{3s^2}{4}\right) \\ & + \frac{3}{4} \left(1 - \frac{5e^2}{2} + \frac{13e^4}{16}\right) (1+c)^2 (C_{22} \cos(2\sigma) + S_{22} \sin(2\sigma))] \\ & - \frac{\mu^5 R^3}{L^8} \left[ \left(1 + 2e^2 + \frac{239e^4}{64}\right) \left(-\frac{3}{4}(1+c) + \frac{15}{16}(1+3c)s^2\right) (C_{31} \cos \sigma + S_{31} \sin \sigma) \right. \\ & + \frac{15}{8} \left(1 - 6e^2 + \frac{423e^4}{64}\right) (1+c)^3 (C_{33} \cos(3\sigma) + S_{33} \sin(3\sigma))] \\ & - \frac{\mu^6 R^4}{L^{10}} [C_{40}(1-e^2)^{(-\frac{7}{2})} \left(\frac{3}{8} - \frac{15s^2}{8} + \frac{105s^4}{64}\right) \\ & + \left(1 + e^2 + \frac{65e^4}{16}\right) \left(-\frac{15}{8}(1+c)^2 + \frac{105}{8}(c+c^2)s^2\right) (C_{42} \cos(2\sigma) + S_{42} \sin(2\sigma))] \\ & + \frac{105}{16} \left(1 - 11e^2 + \frac{199e^4}{8}\right) (1+c)^4 (C_{44} \cos(4\sigma) + S_{44} \sin(4\sigma))] \end{aligned} \quad (3)$$

in which  $c = \cos(i)$ ,  $s = \sin(i)$  and  $L$  is used hereafter instead of  $L'$  for convenience. In terms of angular variables, it can be seen that  $\mathcal{H}_0$  is only dependent on the angle  $\sigma$ . Since  $\theta'$  is implicit in  $\mathcal{H}_0$ , its conjugate  $\Lambda'$  is a constant and can be dropped. Similarly,  $G$  and  $H$ , which are related to  $e$  and  $i$ , are constant as  $g, h$  are absent in  $\mathcal{H}_0$ . Therefore at a given combination of  $e$  and  $i$ ,  $\mathcal{H}_0$  is actually a 1-DOF system. However,  $\mathcal{H}_1$  and  $\mathcal{H}_2$  are functions of both  $\sigma$  and  $g$  and include angles  $j\sigma + kg$  ( $j = 1, 2, 3, k = \pm 1, \pm 2$ ), and therefore are 2-DOF systems. Their expressions are given in Appendix A and they are both zero at  $e = 0$  or  $i = 0$ .

According to our simulations, it is found that  $\mathcal{H}_1 \in \mathcal{O}(\epsilon^{3/2})$ ,  $\mathcal{H}_2 \in \mathcal{O}(\epsilon)$ , where  $\epsilon$  is the ordering parameter and ranges from  $10^{-2}$  to  $10^{-1}$ . Since the origin of our selected body-fixed frame is located at the center mass of the asteroid and the axes are aligned with the principal moments of inertia of the asteroid, the  $C_{21}$ ,  $S_{21}$  and  $S_{22}$  terms are all

zero, leading to the fact that the magnitude of  $\mathcal{H}_1$  is smaller than  $\mathcal{H}_2$ . Therefore,  $\mathcal{H}_0$  with resonant angle  $\sigma$  can be viewed as the primary resonance.  $\mathcal{H}_1$  and  $\mathcal{H}_2$  are the second resonances, which are expected to give rise to chaos.

## 5.3 Primary Resonance

### 5.3.1 EPs and Resonance Width

Firstly,  $\mathcal{H}_0$  is studied in detail. Its equilibria can be found by numerically solving

$$\dot{\sigma} = \frac{\partial \mathcal{H}_0}{\partial L} = 0, \dot{L} = -\frac{\partial \mathcal{H}_0}{\partial \sigma} = 0. \quad (4)$$

The linearized system is written as

$$\begin{bmatrix} d\ddot{\sigma} \\ d\ddot{L} \end{bmatrix} = \begin{bmatrix} \frac{\partial^2 \mathcal{H}_0}{\partial L \partial \sigma} & \frac{\partial^2 \mathcal{H}_0}{\partial L^2} \\ -\frac{\partial^2 \mathcal{H}_0}{\partial \sigma^2} & -\frac{\partial^2 \mathcal{H}_0}{\partial L \partial \sigma} \end{bmatrix} \begin{bmatrix} d\sigma \\ dL \end{bmatrix}.$$

The EPs are obtained by solving

$$\begin{cases} d\ddot{\sigma} = 0 \\ d\ddot{L} = 0 \end{cases}.$$

The linear stability of an EP can be determined from the Jacobian matrix evaluated at the EP. The resonant frequency can be approximated at a stable EP  $(\sigma_s, L_s)$  as  $\sqrt{\frac{\partial^2 \mathcal{H}_0}{\partial L^2} \cdot \frac{\partial^2 \mathcal{H}_0}{\partial \sigma^2} \Big|_{\sigma_s, L_s}}$ . Taking the Hamiltonian value corresponding to an unstable EP  $(\sigma_u, L_u)$ , denoted as  $\mathcal{H}_u$ , its level curve on the phase map is actually the separatrix that divides the motion into libration and circulation regions (Morbidei, 2002). Along this curve,  $L$  passes through its maximum  $L_{max}$  and also minimum  $L_{min}$  at  $\sigma = \sigma_s$ . The resonance width is then calculated as  $\Delta L = L_{max} - L_{min}$  and is therefore only valid for the stable EPs.

### 5.3.2 Numerical results

In this section, the EPs, their stability and the resonance width of asteroids Vesta, 1996 HW1 and Betulia are studied. They are selected because the first two asteroids are representatives of regular and highly bifurcated bodies, respectively, while Betulia has a triangular shape leading to large 3<sup>rd</sup> degree and order harmonics. The 4<sup>th</sup> degree and order spherical harmonics of the three asteroids are given in Appendix B. It is noted here that all the angles except for inclination in this study are in radians. First, the dynamics due to the 2<sup>nd</sup> degree and order harmonics ( $C_{20}$  and  $C_{22}$ ) is studied, hereafter denoted as  $\mathcal{H}_{0/2nd}$ .

#### (a) Vesta

As already mentioned in Section 2.2, the 1:1 resonance actually corresponds to the position of the EPs in the rotating frame. Fig.1 gives the mean semi-major axis of the 1:1 resonance in the  $e - i$  plane. The EPs with  $\sigma = 0$  are unstable, while the ones with  $\sigma = \pi/2$  are stable. The locations of the EPs are symmetric with respect to  $i = 90^\circ$ , due to the symmetry property of the 2<sup>nd</sup> degree and order gravitational field. It is closest to Vesta when the orbit is polar and then gradually moves further away when the orbit approaches the equatorial plane (either prograde or retrograde). The resonance width decreases with the increase of  $i$ , and finally becomes zero when  $i$  arrives at  $\pi$ . This can be explained by the coefficient of the resonant angle  $2\sigma$  in Eq.(3), denoted as  $f_{22}$

$$f_{22} = -\frac{3\mu^4 R^2}{4L^6} \cdot \left(1 - \frac{5e^2}{2} + \frac{13e^4}{16}\right) \cdot (1+c)^2.$$

When  $i$  approaches  $180^\circ$ , the term  $1 + c$  becomes zero and  $f_{22}$  also comes to zero. For a given value of  $i$ , the larger  $e$  the smaller  $f_{22}$  is and the resonance width also decreases (Fig.1). However, this phenomenon is weakened for larger  $i$  as its weight factor  $(1 + c)^2$  becomes smaller. This can clearly be observed from the contour map. In addition, our results for orbits at  $e = 0, i = 0$  or  $e = 0, i = 90^\circ$  are identical to those obtained in Delsate's study (Delsate, 2011).

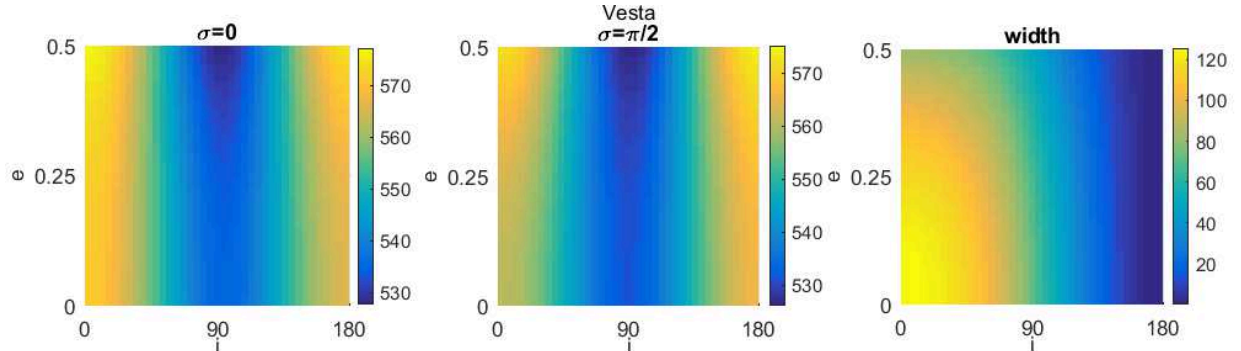


**Figure 1** The contour plots of mean semi-major axis (in km) of the unstable ( $\sigma = 0$ ) and stable ( $\sigma = \pi/2$ ) 1:1 resonance (the EPs) in the  $e - i$  plane and the corresponding resonance width of stable EPs.

To investigate the effects of higher-order terms, the Hamiltonian  $\mathcal{H}_0$  that includes the 4<sup>th</sup> degree and order harmonics is studied. Firstly, the phase portrait for some example orbits with different  $e$  and  $i$  is given in Fig.2. The four EPs are marked out as E1, E2, E3 and E4. The top three plots are actually the phase portrait of  $\mathcal{H}_{0/2nd}$  for comparison, and the remaining ones are those of  $\mathcal{H}_0$ . It can be seen that due to the inclusion of 3<sup>rd</sup> and 4<sup>th</sup> harmonics, the symmetry with respect to  $\sigma = \pi$  is broken and the EPs have a shift from  $\sigma = 0$  and  $\sigma = \pi/2$  but are still located in the near vicinity of them. For the subplots in the middle, with the enlargement of  $i$ , the two stable EPs gradually merge into one and the unstable EP around  $\sigma = \pi$  disappears, as a result of the increasing strength of harmonic coefficients other than  $C_{22}$ . The coefficient of the

$C_{31}$  term in Eq.(3) (denoted as  $f_{31}$ ) is a first-order expression of  $1 + c$  while for that of  $C_{22}$  it is of the second order  $(1 + c)^2$ :

$$f_{31} = -\frac{\mu^5 R^3}{L^8} \cdot \left(1 + 2e^2 + \frac{239e^4}{64}\right) \cdot \left(-\frac{3}{4}(1+c) + \frac{15}{16}(1+3c)s^2\right).$$

When  $i$  is large enough, the influence of  $C_{31}$  on the structure of the phase space exceeds that of  $C_{22}$ . Therefore the phase space is dominated by the phase angle  $\sigma$  of  $C_{31}$ , and the existence of only one stable EP can be easily understood. In addition, all four EPs disappear when  $i$  approaches  $\pi$ , which is due to the fact that all the coefficients of  $k\sigma$  ( $k = 1, 2, 3, 4$ ) in Eq.(3) become zero when  $i = 180^\circ$  because of the terms  $1 + c$  and  $s^2$  and the phase portrait is filled with straight lines. The transit inclination (from four EPs to two EPs) is approximately 2.5 at  $e = 0$  and slightly decreases to 2.2 at  $e = 0.5$ . This is explained by the fact that the  $C_{31}$  dynamics is strengthened when  $e$  becomes larger, which is witnessed by the fact that the large  $e$  promotes the merger of the two stable EPs shown in the bottom plots of Fig.2. In addition, the larger  $e$ , the smaller the value of the resonance width is, which can be explained by  $f_{22}$ . The resonance width for large  $i$  values is larger than that of the  $\mathcal{H}_{0/2nd}$  dynamics, which can be explained by the dynamics taken over by  $C_{31}$  from  $C_{22}$  in these regions. The exact  $\sigma$  values of the EPs and the resonance width are given as a contour map in the  $e - i$  plane in Appendix C.

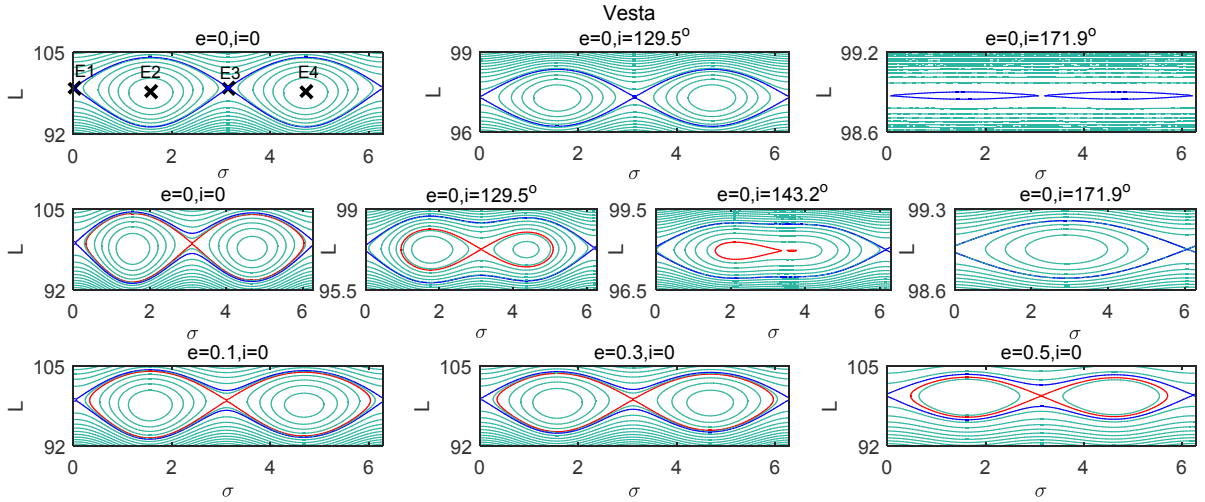


**Figure 2** The phase portrait of the Hamiltonian of Vesta. Top row:  $\mathcal{H}_{0/2nd}$  for  $e = 0$ ,  $i = 0, 129.5^\circ, 171.9^\circ$ ; middle row:  $\mathcal{H}_0$  for  $e = 0$ ,  $i = 0, 129.5^\circ, 143.2^\circ, 171.9^\circ$ ; bottom row:  $\mathcal{H}_0$  for  $i = 0$ ,  $e = 0.1, 0.3, 0.5$ . The blue and red lines are the separatrix (or the values of the Hamiltonian) of the unstable EPs.

### (b) 1996 HW1

For 1996 HW1, the phase portrait of  $\mathcal{H}_{0/2nd}$  and  $\mathcal{H}_0$  is given in Fig.3. There are four unstable EPs appearing in the equatorial plane ( $i = 0$ ), which is consistent with our previous studies (Feng et al., 2015b) and the results in (Magri et al., 2011). They are

also marked out as E1, E2, E3 and E4. For small  $i$ , there is no region for libration and therefore all the EPs are unstable. It can be seen that the instability of the four EPs is already determined by the dynamics of  $\mathcal{H}_{0/2nd}$ . The inclusion of other harmonics however causes a strong distortion of the phase space. Two of the unstable EPs become stable at  $i \approx 108.9^\circ$  for  $\mathcal{H}_{0/2nd}$  and at  $i \approx 120.3^\circ$  for  $\mathcal{H}_0$ , indicating the stability of the retrograde motion in this highly perturbed environment. In addition, the difference of these inclination values implies destabilizing effects of the highly irregular gravitational fields. Then the two EPs merge into one at  $i \approx 154.7^\circ$  also due to strong effects of  $C_{31}$  and finally disappear for the same reason: the effects of terms  $1 + c$  and  $s^2$ . The phase portrait is slightly influenced by  $e$  with the exception that the elongated orbit (with larger  $e$ ) has been less influenced by the high degree and order harmonics, as shown in the bottom subplots.

The  $\sigma$  of the EPs and the resonance width are only obtained for the situation where stable EPs exist and are given in Appendix C. The semi-major axis of the stable EPs and the unstable EPs are also given, indicated by  $a_s$  and  $a_u$ , respectively. After arriving at the maximum value at  $i \approx 128.9^\circ$ , the resonance width decreases and becomes zero when  $i$  approaches  $180^\circ$ . However, it is not affected by  $e$ , as the dynamics is mainly dominated by  $i$  rather than  $e$ . Therefore the most interesting range for resonance is within  $126^\circ < i < 171.9^\circ$ , which will be further studied in the next section.

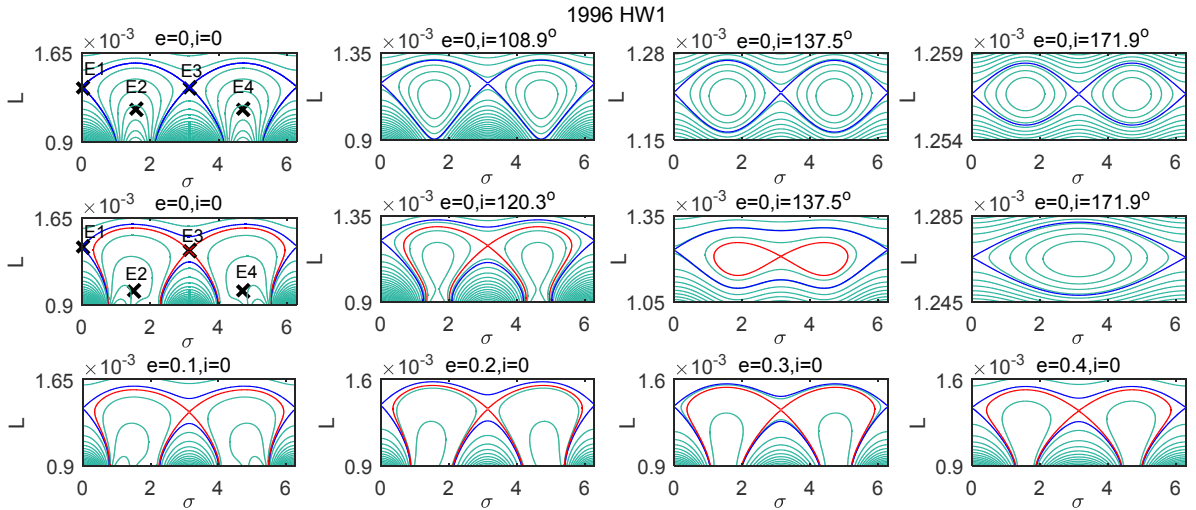


**Figure 3** The phase portrait of the Hamiltonian of 1996 HW1. Top row:  $\mathcal{H}_{0/2nd}$  for  $e = 0$ ,  $i = 0, 108.9^\circ, 137.5^\circ, 171.9^\circ$ ; middle row:  $\mathcal{H}_0$  for  $e = 0$ ,  $i = 0, 120.3^\circ, 137.5^\circ, 171.9^\circ$ ; bottom row:  $\mathcal{H}_0$  for  $i = 0$ ,  $e = 0.1, 0.2, 0.3, 0.4$ . The blue and red lines are the separatrix of the unstable EPs.

### (c) Betulia

The phase portrait of Betulia is given in Fig.4. Only four EPs (E1, E2, E3 and E4) appear for  $\mathcal{H}_{0/2nd}$ , while there are six EPs apparent in the equatorial plane for  $\mathcal{H}_0$  due

to the triangular shape of this body. Among them, E2, E4 and E6 are stable and E1, E3 and E5 are unstable. In Magri's study (Magri et al., 2007), six EPs were also obtained near the equatorial plane of Betulia, but using a polyhedron gravitational field. However, they found E6 unstable while it is stable (the right stretched island) from our phase portrait. The second difference is that their EPs are in general slightly closer to the body than ours. These distinctions primarily originate from the different gravitational fields applied in the studies. However, the gravitational field truncated at degree and order 4 applied in this study already captures the main dynamical properties of the complete gravitational field to a large extent at least for 1:1 resonant dynamics, which is the focus of our study.

As shown in the middle row of Fig.4, the phase portrait of  $\mathcal{H}_0$  changes significantly with the increase of  $i$ . There are actually three EPs within the left main island, which are illustrated as E2, E3 and E4 in the plot. Among them, E2 and E4 are stable, while E3 is unstable and the most inner red line is its separatrix. From  $i \approx 66.2^\circ$ , the unstable EP will disappear and the two stable ones start to merge, as can be seen clearly at  $i = 137.5^\circ$  with only two EPs left. Similarly, when  $i$  gets close to  $180^\circ$ , only one EP exists due to the dominant effect of  $C_{31}$ . In addition, because of the triangular shape of Betulia, the  $C_{31}$ ,  $S_{31}$  and  $S_{33}$  terms are large compared to other asteroids, e.g. Vesta and 1996 HW1. Although  $S_{33}$  is one order of magnitude smaller than  $C_{22}$ , the coefficients of their phase angles  $3\sigma$  and  $2\sigma$  respectively are comparable with each other for small  $e$  and  $i$ . It is the  $S_{33}$  term that introduces two more EPs and also makes the phase space asymmetric with respect to  $\sigma = \pi$ . With the increase of both  $e$  and especially  $i$ , the influence of  $C_{31}$  becomes much stronger than that of  $C_{22}$  and  $S_{33}$  and finally dominates the phase space, which is the same as the cases of Vesta and 1996 HW1. In addition, the right island where EP6 is located is always slightly larger than the left one. In the next section, the resonance width of Betulia is actually measured as the width of the larger one. The exact values of  $\sigma$  of the EPs, the corresponding semi-major axes and the resonance width are also given in Appendix C.



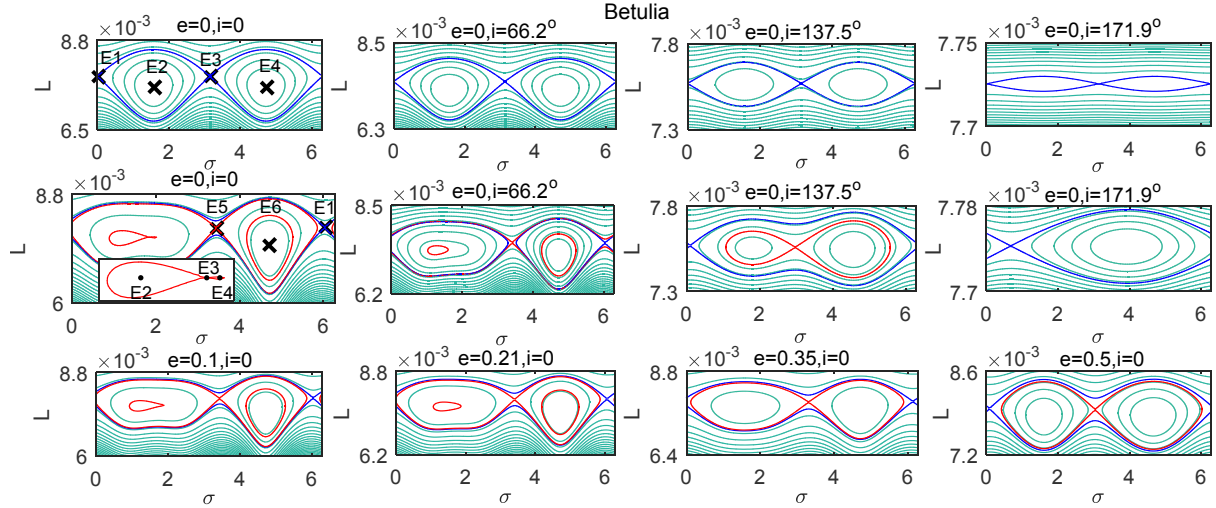


**Figure 4** The phase portrait of the Hamiltonian of Betulia including 4<sup>th</sup> degree and order harmonics. Top  $\mathcal{H}_{0/2nd}$  for  $e = 0$ ,  $i = 0, 66.2^\circ, 137.5^\circ, 171.9^\circ$ ; middle  $\mathcal{H}_0$  for  $e = 0$ ,  $i = 0, 66.2^\circ, 137.5^\circ, 171.9^\circ$ ; bottom  $\mathcal{H}_0$  for  $i = 0$ ,  $e = 0.1, 0.21, 0.35, 0.5$ . The blue and red lines are the separatrix of the unstable EPs.

In summary, this 1-DOF Hamiltonian  $\mathcal{H}_0$  captures the main dynamics of the system and is illustrated with the three study cases above. The strength of  $C_{31}$  exceeds  $C_{22}$  and dominates the structure of the phase space when  $i$  approaches  $180^\circ$ . The large  $S_{33}$  term not only brings about more EPs but also introduces significant asymmetry of the phase space with respect to  $\sigma = \pi$ . In addition, due to the  $1 + c$  term in the coefficients of all phase angles of  $\mathcal{H}_0$ , the resonance width of the retrograde orbits are found to be smaller than that of the prograde ones, which is consistent with Olsen's conclusion (Olsen, 2006). It was also found that the stability of the EPs is largely determined by the 2<sup>nd</sup> degree and order harmonics, especially for Vesta and 1996 HW1. However, the higher degree and order harmonics change the resonance width. The odd harmonics introduce new EPs to the system and break the symmetry of the 1:1 resonant dynamics.

## 5.4 Second Resonance

For a qualitative study about the effect of the second degree of freedom on the 1:1 resonant dynamics,  $\mathcal{H}_1$  and  $\mathcal{H}_2$  should be considered. However, the inclusion of all terms in  $\mathcal{H}_1$  and  $\mathcal{H}_2$  is far from trivial. For this study, the dominant term of  $\mathcal{H}_2$  is taken into account. The dominant term, which has the largest amplitude, is given by

$$\mathcal{H}_{2d} = -\frac{\mu^4 R^2}{L^6} \left[ F_{221} G_{212} (C_{22} \cos(2\sigma - 2g) + S_{22} \sin(2\sigma - 2g)) \right], \quad (5)$$

In the current study, only  $\mathcal{H}_0$  and the dominant term  $\mathcal{H}_{2d}$  are taken into account and the resulting 2-DOF Hamiltonian is written as

$$\mathcal{H}_{2dof} = \mathcal{H}_0 + \mathcal{H}_{2d}.$$

A new resonant angle  $2\sigma - 2g$  is introduced in the dynamics in addition to  $k\sigma$  ( $k = 1, 2, 3, 4$ ). A formal way to deal with this system is to treat  $\mathcal{H}_{2d}$  as a small

perturbation to the integrable system  $\mathcal{H}_{2dof} = \mathcal{H}_0$  (Henrard, 1990). However, in our study, the perturbation of  $\mathcal{H}_{2d}$  is not limited to small values, due to the large variations of  $e$  and  $i$ .

According to Chirikov (1979) and Morbidelli (2002), the dynamics of  $\mathcal{H}_{2dof}$  can be studied by observing the overlap process of nearby resonances using Poincaré maps. To a first approximation, each resonance is considered separately, namely only its own resonant angle is taken into account and the other one is neglected. The first resonance  $\mathcal{H}_{reson1}$  is actually  $\mathcal{H}_0$ , and the second resonance  $\mathcal{H}_{reson2}$  is defined as

$$\begin{aligned}\mathcal{H}_{reson2} &= -\frac{\mu^2}{2L^2} - \dot{\theta}L - \frac{\mu^4 R^2}{L^6} F_{201} G_{210} C_{20} + \mathcal{H}_{2d} \\ &= -\frac{\mu^2}{2L^2} - \dot{\theta}L - \frac{\mu^4 R^2}{L^6} (1-e^2)^{\left(-\frac{3}{2}\right)} \left(-\frac{1}{2} + \frac{3s^2}{4}\right) C_{20} \\ &\quad - \frac{\mu^4 R^2}{L^6} \frac{3}{2} \left(\frac{9e^2}{4} + \frac{7e^4}{4}\right) s^2 [C_{22} \cos(2\sigma - 2g) + S_{22} \sin(2\sigma - 2g)]\end{aligned}\quad (6)$$

which only includes one resonant angle  $2\sigma - 2g$ . Their locations need to be solved first and then the Poincaré maps of the single-resonance dynamics are computed respectively on the same section in the vicinity of their location. If  $\mathcal{H}_{2d}$  is small enough, the separatrix of  $\mathcal{H}_{reson2}$  is further away from that of  $\mathcal{H}_{reson1}$  and the two resonances are slightly influenced by each other. Tiny chaotic layers are probably generated around the separatrix. Otherwise, if  $\mathcal{H}_{2d}$  is large, the separatrix of the two resonances intersect, their dynamical domains overlap, and each resonance is significantly affected by the other one. The chaotic layers extend to large-region chaos that dominates the phase space. Since  $\mathcal{H}_{reson1}$  is the dominant dynamics of our 1:1 resonant model, the focus is put on how  $\mathcal{H}_{reson1}$  is influenced by  $\mathcal{H}_{reson2}$ , which can also be interpreted as how much the 1-DOF dynamics is affected by a perturbation.

#### 5.4.1 The location and width of $\mathcal{H}_{reson2}$

The location and width of  $\mathcal{H}_{reson1}$  have been obtained in Section 3. Since we want to apply Poincaré sections to study the dynamics, the section of the map is first defined here as  $g = \pi/2, \dot{g} > 0$  in the  $L - \sigma$  plane. Since  $\mathcal{H}_{reson1}$  has 1-DOF, its Poincaré map is the same with its phase portrait in the phase space. The location of  $\mathcal{H}_{reson2}$  on this section can be obtained by numerically solving

$$\begin{cases} 2\dot{\sigma} - 2\dot{g} = \frac{2\partial\mathcal{H}_{reson2}}{\partial L} - \frac{2\partial\mathcal{H}_{reson2}}{\partial G} = 0 \\ \mathcal{H}_{reson2}(\sigma_0, g_0, L^*, G^*) = \mathcal{H}_{separatrix} \end{cases}, \quad (7)$$

in which  $\sigma_0 = g_0 = \pi/2$ .  $\mathcal{H}_{separatrix}$  is the Hamiltonian value of the separatrix of  $\mathcal{H}_{reson1}$  which is also the energy constant of the section.  $L^*$  and  $G^*$  represent the variables that need to be solved. As  $\mathcal{H}_{reson2}$  itself is a 2-DOF system, the pendulum model cannot be applied for approximating its resonance width. Therefore, based on

the dynamical properties of the Poincaré map, a full numerical estimation is used. By integrating from the initial point  $(\sigma_0, g_0, L^*, G^*)$  for moderate iterations, a curve is obtained which is either the upper or the lower part of the separatrix of  $\mathcal{H}_{reson2}$  on the section. If it is the upper part,  $L_{max}$  is directly obtained by taking record of the maximum point of the curve.  $L_{min}$  is the minimum of the lower border obtained by integrating from the point  $(\sigma_0, g_0, L^* - \delta L, G)$  with a displacement from  $(\sigma_0, g_0, L^*, G^*)$  by  $\delta L$  depending on the dynamics studied and vice versa. The curves acquired are the separatrix of  $\mathcal{H}_{reson2}$ . Therefore, the width of  $\mathcal{H}_{reson2}$  is approximated by  $L_{max} - L_{min}$ , which is already good enough for the current study.

Given that the maxima and minima of  $\mathcal{H}_{reson1}$  and  $\mathcal{H}_{reson2}$  are denoted as  $L_{max1}, L_{min1}$  and  $L_{max2}, L_{min2}$ , respectively, the relative locations of the two resonances can be characterized by  $L_{min1} - L_{max2}$  and  $L_{min1} - L_{min2}$ . The former one, which is the distance between the lower borders of the two resonances, is positive if the two resonances are totally separated and becomes negative as the resonances start to overlap with each other. The latter one is actually the measurement of the extent of overlap of the two resonances. Its non-positive value indicates that one resonance is completely within the other one. For different combinations of  $e$  and  $i$ , the 2-DOF Hamiltonian  $\mathcal{H}_{2dof}$  is studied for 1996 HW1, Vesta and Betulia.

#### 5.4.2 1996 HW1

Since 1996 HW1 only has a limited inclination range ( $126^\circ \lesssim i < 180^\circ$ ) of libration motion of  $\mathcal{H}_{reson1}$  (shown in Fig.3), its second degree of freedom dynamics is studied first. In Fig.5, the upper plots give the separatrices of the two resonances on the Poincaré maps, which are the boundaries of their phase space. The bottom plots are the phase space of  $\mathcal{H}_{2dof}$  on the same section, both for  $i$  changing from  $171.9^\circ$  to  $143.2^\circ$  at the example  $e = 0.1$ . Fig.5 reflects the relationship of the distance between the two resonances  $\mathcal{H}_{reson1}$  and  $\mathcal{H}_{reson2}$  and the extent of chaotic region of  $\mathcal{H}_{2dof}$ .

##### (1) The effect of $i$

For  $i = 171.9^\circ$ , even though the resonances do not overlap (but are close), tiny chaotic layers appear in the vicinity of the separatrix of  $\mathcal{H}_{2dof}$ . When there is a small overlap at  $i = 166.2^\circ$ , the chaotic layer is extended but a large libration region still retains. With the increase of the overlap from  $i = 166.2^\circ$ , a large part of the phase space is occupied by chaos. The regular region shrinks to a limited area at the center of the phase space and meanwhile five islands appear around it, which is due to the high-order resonances between  $\mathcal{H}_{reson1}$  and  $\mathcal{H}_{reson2}$ . With the further decrease of  $i$  to  $158.7^\circ$ ,  $\mathcal{H}_{reson2}$  is almost completely inside  $\mathcal{H}_{reson1}$  and there are only three small KAM tori left, indicating the system is transiting to global chaos. In addition, the original stable EP becomes unstable as the center part is already chaotic. Although the dynamics is completely chaotic at  $i = 149^\circ$ , the chaos is still bounded by the

separatrix of  $\mathcal{H}_{reson1}$ . However, finally at  $i = 143.2^\circ$  the whole structure of  $\mathcal{H}_{reson1}$  could not be kept and the continuity of phase space is broken. It is noticed that this break is consistent with the break of the separatrix of  $\mathcal{H}_{reson2}$  at the same range of  $\sigma$ , implying a significant perturbation of  $\mathcal{H}_{reson2}$  on the total dynamics. The break of  $\mathcal{H}_{reson2}$ 's separatrix attributes to the fact that the time derivative of  $g$  (namely  $\dot{g}$ ) changes its sign from positive to negative after  $i$  crossing some specific value, and therefore it produces no crossings on the section which is defined as  $\dot{g} > 0$ . This phenomenon will be discussed in detail in the next section.

In summary,  $i$  has a great influence on the 2-DOF dynamics at constant  $e$ . When  $i$  decreases,  $\mathcal{H}_{reson2}$  is strengthened as it includes the term  $s^2$  (as seen in Eq.(6)) and its resonance width increases. However, its location does not deviate much. For  $\mathcal{H}_{reson1}$ , not only its width is increasing but also its location is moving downward. Ultimately, the two resonances totally overlap and have a strong interaction with each other. Nevertheless, the width of  $\mathcal{H}_{2dof}$  is determined by  $\mathcal{H}_{reson1}$ , which is seen from both  $L$  values, although the inner structure of the phase space has been totally affected.

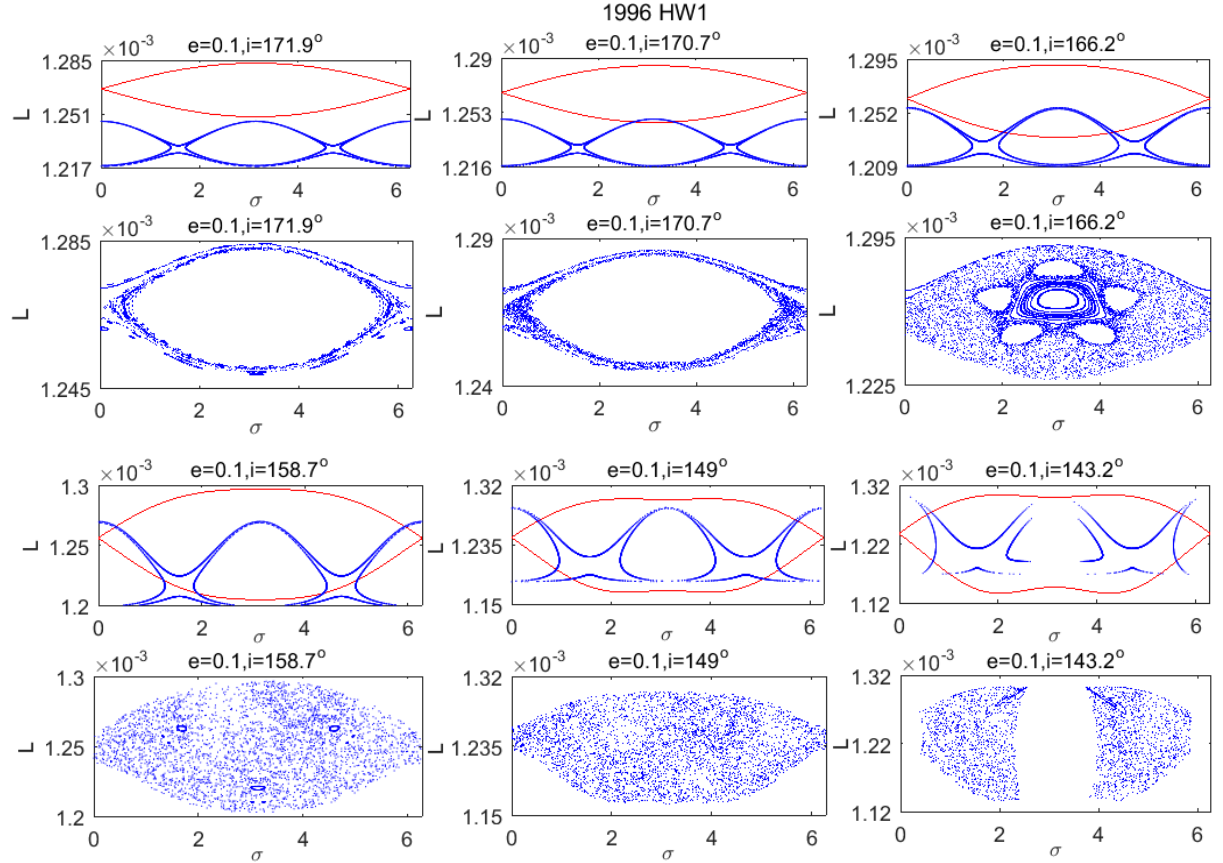


**Figure 5** First and third rows: the separatrices of resonances  $\mathcal{H}_{reson1}$  (red) and  $\mathcal{H}_{reson2}$  (blue) on the section  $g = \pi/2, \dot{g} > 0$ ; second and fourth rows: the phase space of the corresponding  $\mathcal{H}_{2dof}$ ; both for  $e = 0.1, i = 171.9^\circ, 170.7^\circ, 166.2^\circ, 158.7^\circ, 149^\circ, 143.2^\circ$ .

## (2) The effect of $e$

To study the effect of  $e$  on the dynamics, the contour map of the distance of the two resonances and also the width of the second resonance are given on the  $e - i$  plane in Fig.6. In the left plot, the yellow region indicates the situation of non-overlap and slight overlap. In the middle plot, the green and blue areas demonstrate the situation when  $\mathcal{H}_{reson2}$  moves totally inside  $\mathcal{H}_{reson1}$  and the overlap between the two is complete. The right plot demonstrates that the width of  $\mathcal{H}_{reson2}$  is also enlarged when  $e$  becomes large, which can be proven by the term  $(9e^2/4 + 7e^4/4)$  in  $\mathcal{H}_{reson2}$ . Therefore, the largest distance of  $\mathcal{H}_{reson1}$  and  $\mathcal{H}_{reson2}$  is witnessed at the down-right corner and  $\mathcal{H}_{reson2}$  approaches its highest location at the upper-left corner in the left plot. In addition, as  $e$  increases and  $i$  decreases,  $\mathcal{H}_{reson2}$  becomes stronger (as indicated by the resonance width) and has a significant influence on the dynamics of  $\mathcal{H}_{reson1}$ .

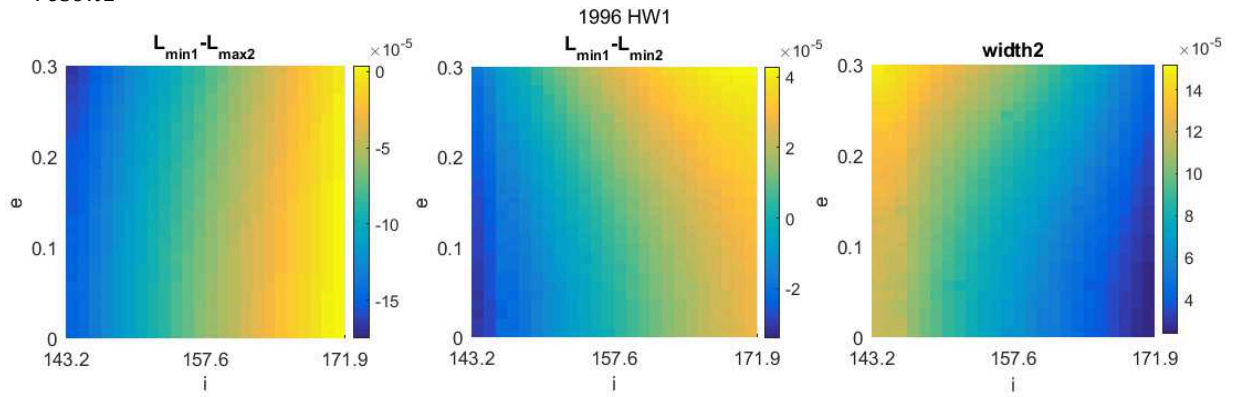


**Figure 6** The distance between  $\mathcal{H}_{reson1}$  and  $\mathcal{H}_{reson2}$  measured as  $L_{min1} - L_{max2}$  (left) and  $L_{min1} - L_{min2}$  (middle), and the width of  $\mathcal{H}_{reson2}$  (right).

Therefore, given a specific  $e$  and  $i$ , an estimation from this contour map can be made on when small chaotic layers appear and when large chaotic seas are expected. As an example, for  $e = 0.1$ , tiny chaotic layers are apparent at  $i = 171.9^\circ$  when the two resonances start to overlap; the last KAM tori disappear and the phase space is full with chaos around  $i = 158.2^\circ$ .

For a more complete understanding, the phase space of  $\mathcal{H}_{2dof}$  at  $e = 0.3$  with different  $i$  is given in Fig.7. As compared to Fig.5, the upper plots of Fig.7 show that the large  $e$  distorts the main island, which originally has circular or ellipsoidal shape. The chaos is more abundant and the size of the main island reduces and a new phase structure is generated at the bottom of the plot, due to the stronger influence of  $\mathcal{H}_{reson2}$ . In addition, the lower half of the chaos is thicker than the upper part, as it is more influenced by the perturbation from  $\mathcal{H}_{reson2}$  which approaches  $\mathcal{H}_{reson1}$  from the bottom direction. In addition, the islands appearing at the bottom area of the phase space can be explained by the direct interaction of  $\mathcal{H}_{reson1}$  and  $\mathcal{H}_{reson2}$  in that region. Furthermore, the lower three plots are full of chaos.

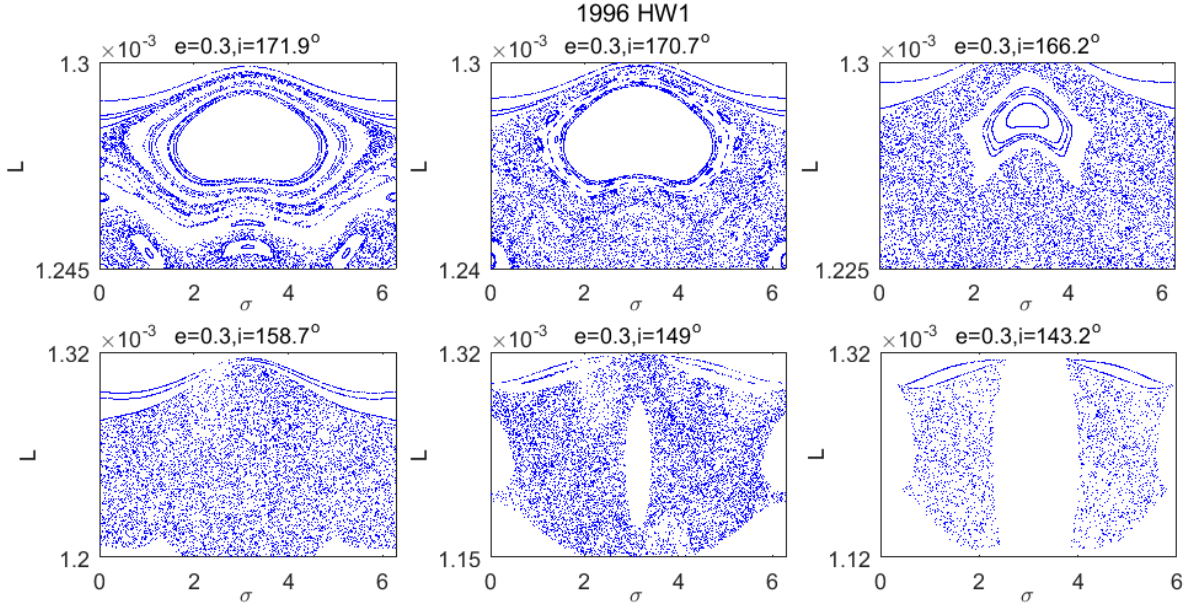


**Figure 7** The phase space of  $\mathcal{H}_{2dof}$  at  $e = 0.3$  for  $i = 171.9^\circ, 170.7^\circ, 166.2^\circ, 158.7^\circ, 149^\circ, 143.2^\circ$ .

For  $e = 0.3, i = 149^\circ$ ,  $\mathcal{H}_{reson2}$  is already comparable with  $\mathcal{H}_{reson1}$  on the dynamics of  $\mathcal{H}_{2dof}$ . Therefore, the center part of the phase space is not completely chaotic; limited regular (white) region appear which is actually part of the center island of  $\mathcal{H}_{reson2}$ .

### (3) Bounded chaotic regions

As mentioned in 4.2.1, tiny chaotic layers are generated in the vicinity of the separatrix. Their boundaries can be estimated, which is the topic of this section.

For small perturbations, it is known from (Morbidei, 2002) that the chaotic region covers areas spanned by the instantaneous separatrices for varying secular angles, which is  $g$  in our study. Its boundaries are estimated from the separatrices corresponding to the minimal and maximal resonant width. This is also known as the modulated-pendulum approximation. The small perturbation corresponds to the case of close approach and almost contact between  $\mathcal{H}_{reson1}$  and  $\mathcal{H}_{reson2}$ , and is therefore applicable to a situation with quite large inclination values. For 1996 HW1, Fig.8 illustrates this region at different eccentricities and inclinations.



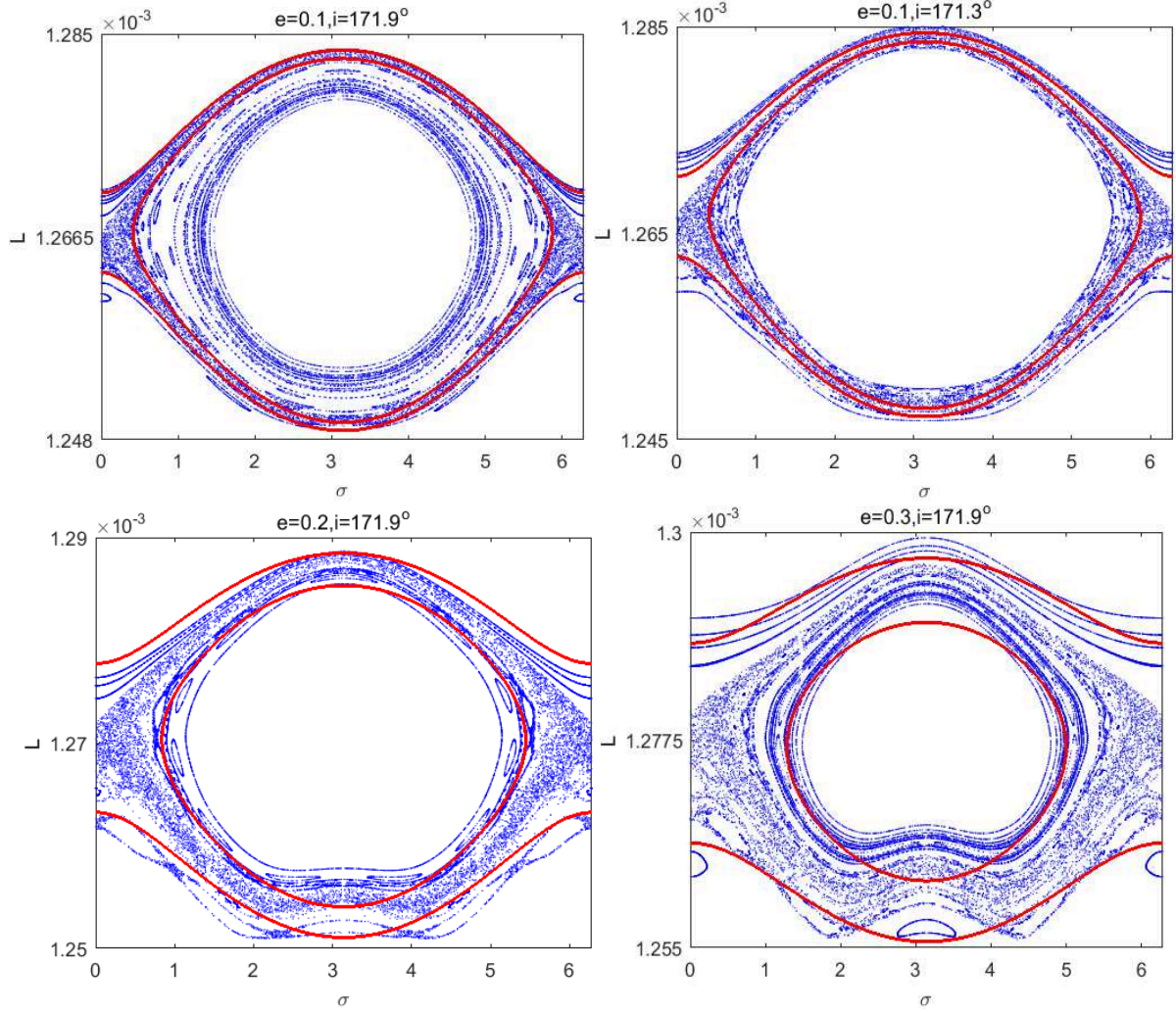


**Figure 8** The chaotic regions bounded by the separatrices (red lines) corresponding to the minimal and maximal resonant width for  $e = 0.1, i = 171.9^\circ, 171.3^\circ$ ;  $i = 171.9^\circ, e = 0.2, 0.3$ .

In each plot, the outer red lines represent the boundary corresponding to the Hamiltonian value of  $\mathcal{H}_{separatrix} + \mathcal{H}_{2d}(g = 0)$  which is the maximum resonance width. The inner red line is the inner boundary with the Hamiltonian value of  $\mathcal{H}_{separatrix} + \mathcal{H}_{2d}(g = \pi/2)$  which is the minimum resonance width. For  $e = 0.1, i = 171.9^\circ$ , in which case the perturbation from  $\mathcal{H}_{reson2}$  is the weakest (shown in Fig.5), the theory works perfectly since all chaos is restricted to the region between the two red lines. When the inclination decreases to  $171.3^\circ$ , the chaos is still well bounded but a small portion of it at the bottom area is already outside the red lines. For comparison, the cases of  $e = 0.2, i = 171.9^\circ$  and  $e = 0.3, i = 171.9^\circ$  are studied, in which situation the perturbations of  $\mathcal{H}_{reson2}$  are not small anymore. The chaotic region does not fit well within the red lines. The bottom part of the chaos is shifted upwards and is therefore outside the inner red line, due to the distortion of the phase space.

In summary, the chaotic layers are well estimated with the approximation theory for the small perturbation cases ( $i$  close to  $\pi$  and small  $e$ ). The strong perturbation of

$\mathcal{H}_{reson2}$  introduced by large  $e$  not only broadens the chaotic region, but also reshapes the phase space.

### 5.4.3 Vesta

#### (1) The effect of $i$

For Vesta, there is always a stable EP for different  $i$  and  $e$ . For the retrograde case, the distance between  $\mathcal{H}_{reson1}$  and  $\mathcal{H}_{reson2}$  and the phase space of  $\mathcal{H}_{2dof}$  for orbits with different  $i$  but the same  $e = 0.1$  is given in Fig.9. For  $i = 171.9^\circ$ , the dynamics of  $\mathcal{H}_{reson1}$  is hardly influenced since the two resonances are far apart and there is no interaction between them. With the decreasing of  $i$ , a significant chaotic region around the separatrix appears, even when the two resonances are just in contact (as seen at  $i = 160.4^\circ$ ). When  $\mathcal{H}_{reson2}$  completely evolves inside  $\mathcal{H}_{reson1}$ , the phase space becomes totally chaotic, as indicated at  $i = 149^\circ$ . Further at  $i = 129.2^\circ$ , the phase space becomes discontinuous and only scattered points are left without any recognizable dynamical structure (similar to the case for 1996 HW1 at  $i = 143.2^\circ$ ). The reason will be explained later this section.

The situation is quite different for the prograde case, as shown in Fig.10. It can be seen that  $\mathcal{H}_{reson2}$  is completely inside  $\mathcal{H}_{reson1}$  for all inclinations; also the width of  $\mathcal{H}_{reson2}$  increases as the orbit gets more inclined. When the strength of  $\mathcal{H}_{reson2}$  is very weak at  $i = 11.5^\circ$ , a very tiny chaotic layer is present around the separatrix. When  $\mathcal{H}_{reson2}$  becomes stronger at  $i = 34.4^\circ$ , new islands inside the two main libration regions are generated, in addition to the weak chaos. Finally, when  $\mathcal{H}_{reson2}$  is large enough at  $i = 45.8^\circ$ , the original phase structure is broken and the two main islands are filled with chaos but not connected anymore. Combined with the previous analysis, the extent of chaos is found to be not only related to the location of the two resonances, but their relative strength is also important. The dynamics of  $\mathcal{H}_{2dof}$  is determined by the evolution (location, stability and strength) of both  $\mathcal{H}_{reson1}$  and  $\mathcal{H}_{reson2}$  as well as their interaction.



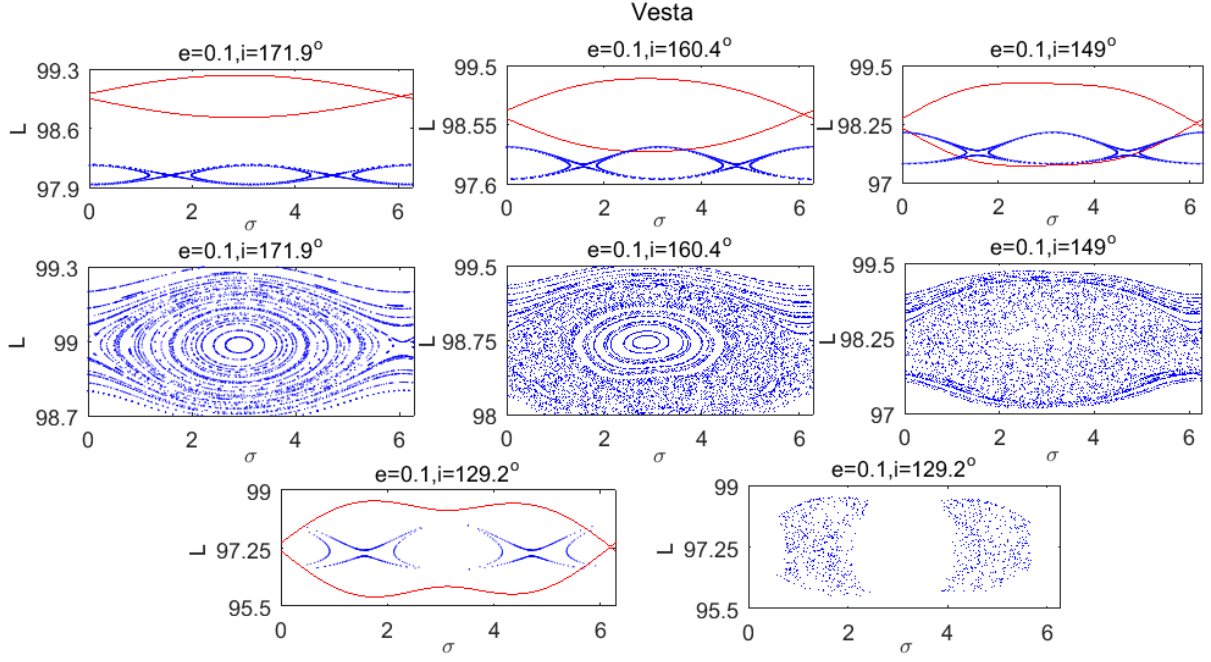


**Figure 9** First row: the separatrices of resonances  $\mathcal{H}_{reson1}$  (red) and  $\mathcal{H}_{reson2}$  (blue) on the section  $g = \pi/2, \dot{g} > 0$ ; second row: the phase space of the corresponding  $\mathcal{H}_{2dof}$ ; both for  $e = 0.1, i = 171.9^\circ, 160.4^\circ, 149^\circ$ ; third row: the separatrices and phase space for  $e = 0.1, i = 129.2^\circ$  (retrograde).

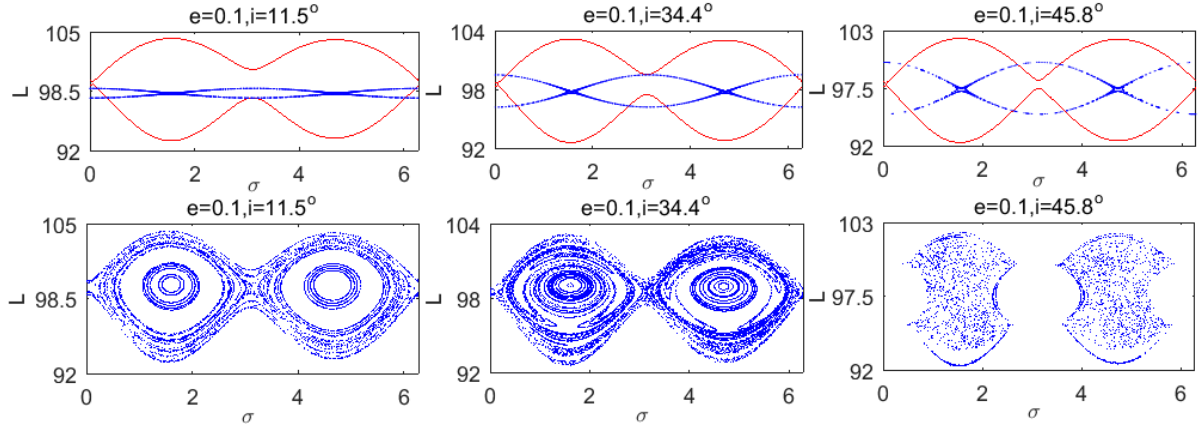


**Figure 10** First row: the separatrices of resonances  $\mathcal{H}_{reson1}$  (red) and  $\mathcal{H}_{reson2}$  (blue) on the section  $g = \pi/2, \dot{g} > 0$ ; Second row: the phase space of the corresponding  $\mathcal{H}_{2dof}$ ; both for  $e = 0.1, i = 11.5^\circ, 34.4^\circ, 45.8^\circ$  (prograde).

## (2) The effect of $e$

Fig.11 shows contour maps that can be used to analyze the impact of  $e$ . For the retrograde case, the effects of  $e$  and  $i$  on the evolution of the two resonances are similar to that of 1996 HW1, as shown in the bottom plots of Fig.11. The slight difference is that the maximum resonance width of  $\mathcal{H}_{reson2}$  is at  $e = 0.5$  and  $i \approx 137.5^\circ$  for Vesta rather than at the top-left corner for 1996 HW1, which can be explained by the non-linear property of the resonance width as a function of  $e$  and  $i$ . For the prograde case, instead of  $L_{min1} - L_{max2}$ ,  $L_{max1} - L_{max2}$  is obtained due to

the fact that the two resonances already completely overlap. It is always positive for  $L_{max1} - L_{max2}$  and negative for  $L_{min1} - L_{min2}$ . It must be mentioned that when  $i = 0$ , the width of  $\mathcal{H}_{reson2}$  is zero and the dynamics of  $\mathcal{H}_{reson1}$  is not affected. Therefore, we start our calculation from  $i = 0.6^\circ$ . The largest distances between the maximum and minimum boundaries of the two resonances are both at the left-bottom corner of the contour map, and the smallest distances between them at the right-top corner, which can be easily explained by the corresponding weakest and strongest perturbing effect of  $\mathcal{H}_{reson2}$ . In addition, the width of  $\mathcal{H}_{reson2}$  achieves its largest value at the largest inclination but smallest eccentricity. It can be noticed that the ranges of  $i$  stop at  $51.6^\circ$  and  $128.9^\circ$  for the prograde and retrograde orbits, respectively, due to the break of the separatrix of  $\mathcal{H}_{reson2}$  at  $51.6^\circ \lesssim i \lesssim 128.9^\circ$ .

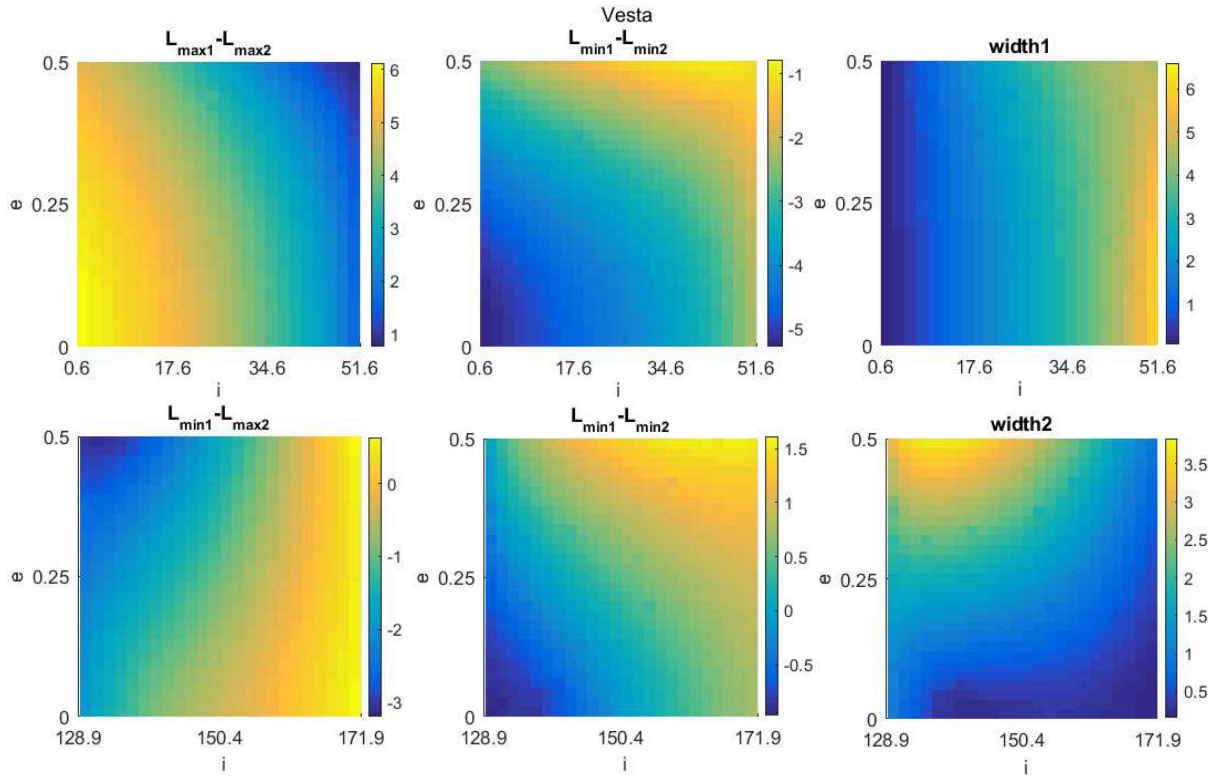


**Figure 11** The distance between  $\mathcal{H}_{reson1}$  and  $\mathcal{H}_{reson2}$  measured as  $L_{min1} - L_{max2}$  (left) and  $L_{min1} - L_{min2}$  (middle), and the width of  $\mathcal{H}_{reson2}$  (right) for the prograde (top) and retrograde (bottom) cases ( $i$  in radian).

For a complete understanding, the phase space of  $\mathcal{H}_{2dof}$  at  $e = 0.5$  is given in Fig.12. Similarly, compared to the phase space at  $e = 0.1$  (shown in Figs.9 and 10), the main island is strongly distorted and the chaotic region is significantly extended, due to the strong perturbation of  $\mathcal{H}_{reson2}$ . For  $e = 0.5, i = 149^\circ$ , the regular region at the center of the phase space again is actually part of the regular region of  $\mathcal{H}_{reson2}$ , due to the comparable influence of  $\mathcal{H}_{reson1}$  and  $\mathcal{H}_{reson2}$  on the dynamics of  $\mathcal{H}_{2dof}$ . Therefore, large  $e$  give rise to strong perturbations on the dynamics.

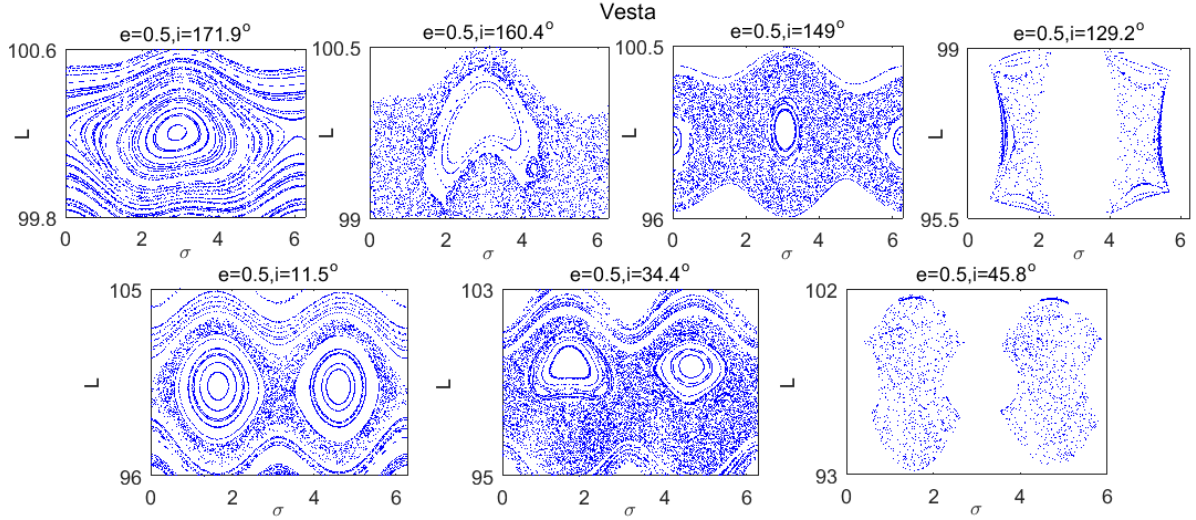


**Figure 12** The phase space of  $\mathcal{H}_{2dof}$  at  $e = 0.5$  for  $i = 171.9^\circ, 160.4^\circ, 149^\circ, 129.2^\circ, 11.5^\circ, 34.4^\circ, 45.8^\circ$ .

### (3) Near polar region

For the near polar region, the dynamical structure shrinks and almost disappears on our previously defined section, as can already be seen from the plots at  $i = 45.8^\circ$  and  $i = 129.2^\circ$  in Figs.9 and 10. This is due to the fact that the secular rate of  $g$  (Kaula, 1966)

$$\dot{g} = -\frac{3nR^2C_{20}}{a^2(1-e^2)^2}(4-5s^2)$$

changes sign at the critical inclinations  $i_{critical} = 63.4^\circ$  and  $116.6^\circ$ . In particular, it is negative for  $63.4^\circ < i < 116.6^\circ$ . Since this formula of  $\dot{g}$  is obtained from averaging the leading  $C_{20}$  perturbation and our current model includes additional harmonics terms, the sign of  $\dot{g}$  in our study does not change sharply at  $i_{critical}$  but has a transition process. However, the exact values of this transition are beyond the scope of this study. Some orbits may still have  $\dot{g} > 0$  while others already have  $\dot{g} < 0$ , which explains the break of the separatrix of  $\mathcal{H}_{reson2}$  on the section  $g = \pi/2, \dot{g} > 0$ . Therefore, we can define a new section for the near polar orbits with the only difference that  $\dot{g} < 0$ .

For similar simulations, results are shown in Fig.13. However, no  $(L^*, G^*)$  of  $\mathcal{H}_{reson2}$  can be found on this new section; and its Poincaré map rather than separatrix is included in plots labelled A. The two resonances have moderate overlap at the upper and lower boundaries of  $\mathcal{H}_{reson1}$ , which brings about limited chaotic regions closely attached to the separatrix. When  $\mathcal{H}_{reson2}$  reaches its strongest effect at  $i = 90^\circ$ , the chaos becomes more obvious and thick. For  $i = 68.8^\circ$  and  $108.9^\circ$ , the chaos is visible but less abundant. For  $i = 120.3^\circ$ , in addition to the chaos, islands are apparent in the circulation region of  $\mathcal{H}_{reson1}$ , where the two resonances have a strong modulation with each other.

In conclusion, the libration region of  $\mathcal{H}_{reson1}$  is hardly influenced by  $\mathcal{H}_{reson2}$ . From this point of view, the 1:1 resonance is more stable for near polar orbits at different eccentricities.

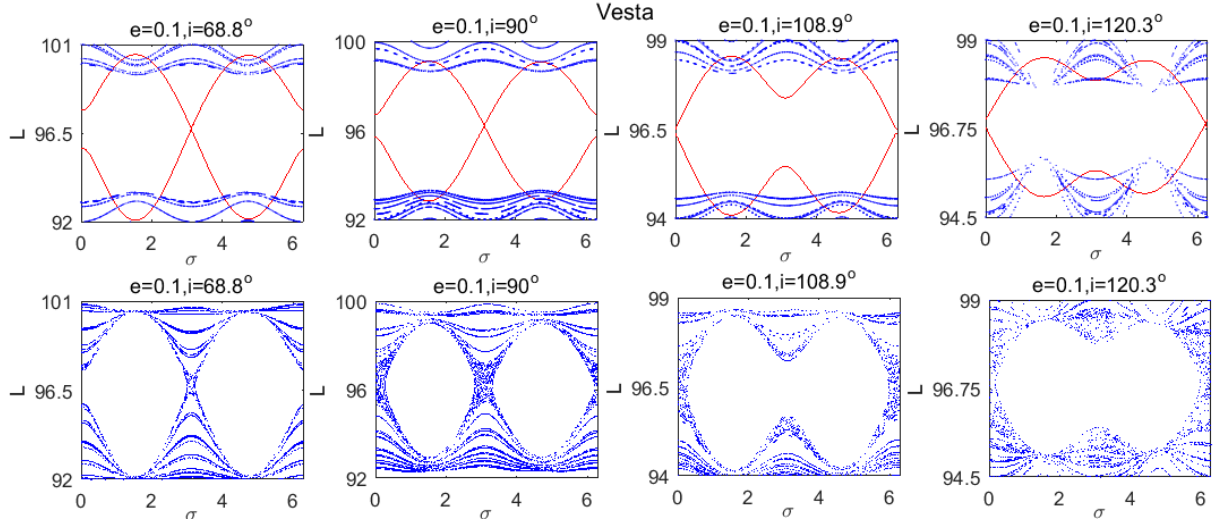


**Figure 13** First row: the separatrices of resonances  $\mathcal{H}_{reson1}$  (red) and  $\mathcal{H}_{reson2}$  (blue) on the section  $g = \pi/2, \dot{g} < 0$ ; second row: the phase space of the corresponding  $\mathcal{H}_{2dof}$ ; both for  $e = 0.1, i = 68.8^\circ, 90^\circ, 108.9^\circ, 120.3^\circ$ .

#### 5.4.4 Betulia

For both prograde and retrograde orbits, Betulia has very similar properties as Vesta, concerning the distance between the two resonances and the width of  $\mathcal{H}_{reson2}$ .

##### (1) The effect of $i$

The retrograde case is illustrated in Fig.14. The most obvious difference w.r.t. Fig.9 is that the phase space is not symmetric with respect to  $i = 90^\circ$  anymore. When the two resonances are further apart at  $i = 171.9^\circ$ ,  $\mathcal{H}_{reson1}$  is hardly influenced. When they are almost in contact with each other at  $i = 165^\circ$ , thick chaotic layers are present together with small islands in the phase space. Before complete overlap, there is a small KAM-tori left at  $i = 153.6^\circ$  and the center region of the phase space is also distorted. After that at  $i = 132^\circ$ , the phase space is totally chaotic and finally broken.

For the prograde case, the two resonances always totally overlap, as shown in Fig.15. When  $\mathcal{H}_{reson2}$  is tiny and weak at  $i = 11.5^\circ$ , the main structure of  $\mathcal{H}_{reson1}$  is kept, with the difference that small chaotic regions appear near the separatrix and again new islands are generated inside the right main island. As  $\mathcal{H}_{reson2}$  becomes stronger at  $i = 34.4^\circ$ , the overlapping part of  $\mathcal{H}_{reson1}$  is completely chaotic. Similarly, for  $i = 45.8^\circ$ , the phase space of  $\mathcal{H}_{reson1}$  is significantly broken and is left with large gap regions, even without complete break of the separatrix of  $\mathcal{H}_{reson2}$ . This indicates the strong perturbation of  $\mathcal{H}_{reson2}$  on the dynamics and the highly non-linear property of  $\mathcal{H}_{2dof}$ .

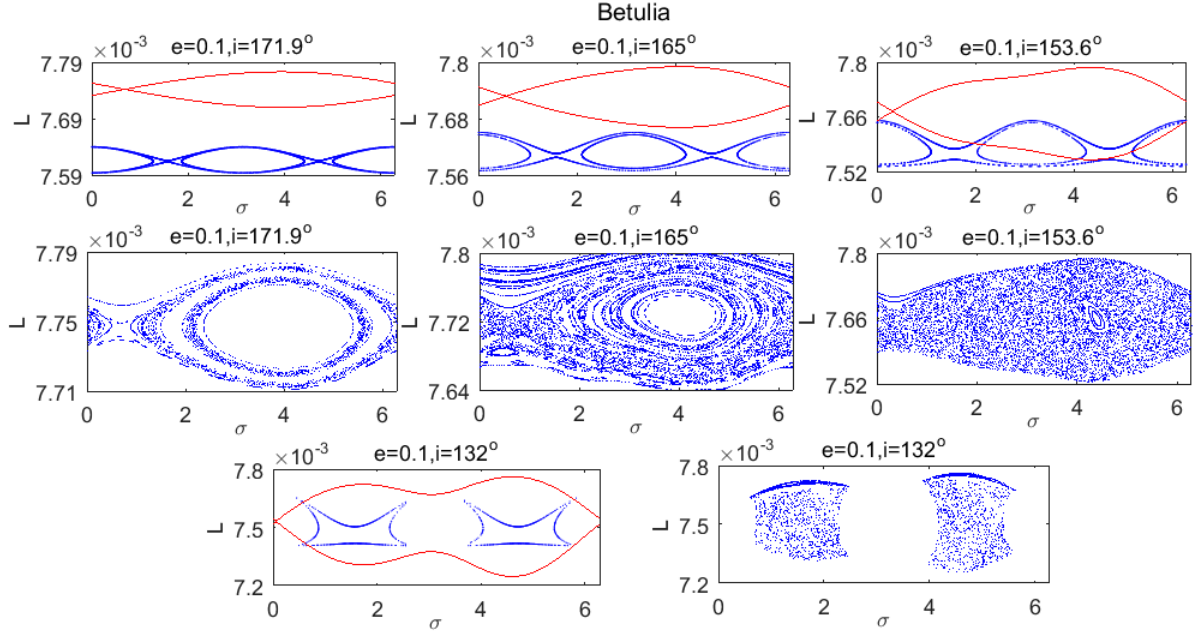


**Figure 14** First row: the separatrices of resonances  $\mathcal{H}_{reson1}$  (red) and  $\mathcal{H}_{reson2}$  (blue) on the section  $g = \pi/2, \dot{g} > 0$ ; second row: the phase space of the corresponding  $\mathcal{H}_{2dof}$ ; both for  $e = 0.1, i = 171.9^\circ, 165^\circ, 153.6^\circ$ ; third row: the separatrices and phase space for  $e = 0.1, i = 132^\circ$  (retrograde).

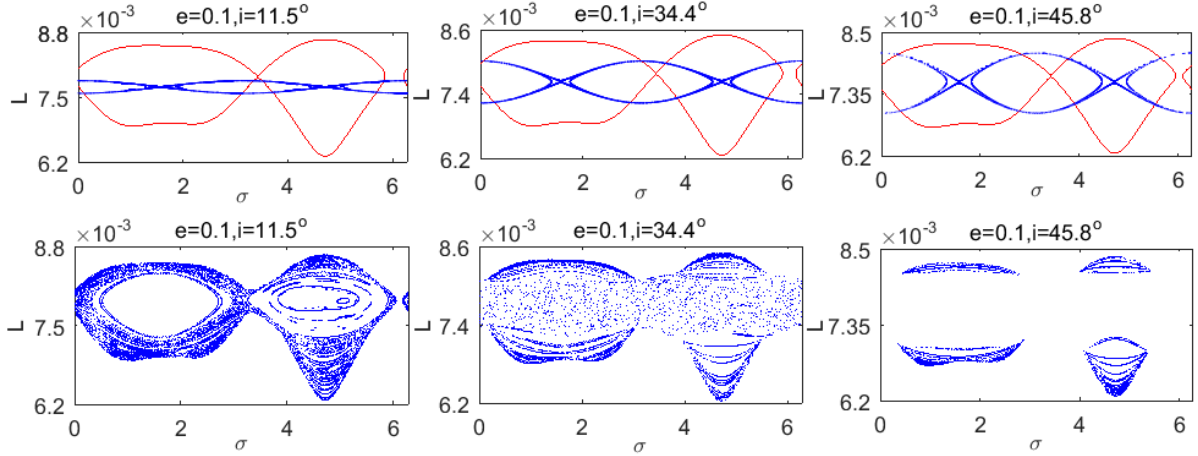


**Figure 15** First row: the separatrices of resonances  $\mathcal{H}_{reson1}$  (red) and  $\mathcal{H}_{reson2}$  (blue) on the section  $g = \pi/2, \dot{g} > 0$ ; second row: the phase space of the corresponding  $\mathcal{H}_{2dof}$ ; both for  $e = 0.1, i = 11.5^\circ, 34.4^\circ, 45.8^\circ$  (prograde).

For the near polar region, as illustrated in Fig.16, Betulia has a similar property as Vesta, considering that chaotic layers appear in the vicinity of the separatrix and also new islands are generated in the circulation region. However, for Betulia the three regions are weakly connected at  $i = 68.8^\circ$ . Furthermore, they become totally isolated at  $i = 90^\circ$ , due to the stronger modulation of  $\mathcal{H}_{reson2}$  compared to that of Vesta (Fig.13). Since the regular region is open, the originally stable EPs of  $\mathcal{H}_{reson1}$  probably change into unstable. At  $i = 108.9^\circ$  and  $120.3^\circ$ , the circulation region is full of chaos, which implies that the perturbation of  $\mathcal{H}_{reson2}$  and its interaction with



$\mathcal{H}_{reson1}$  in this region are stronger, compared to the cases at  $i = 68.8^\circ$  and  $90^\circ$ . Again, the general structure of the libration part of  $\mathcal{H}_{reson1}$  is kept.

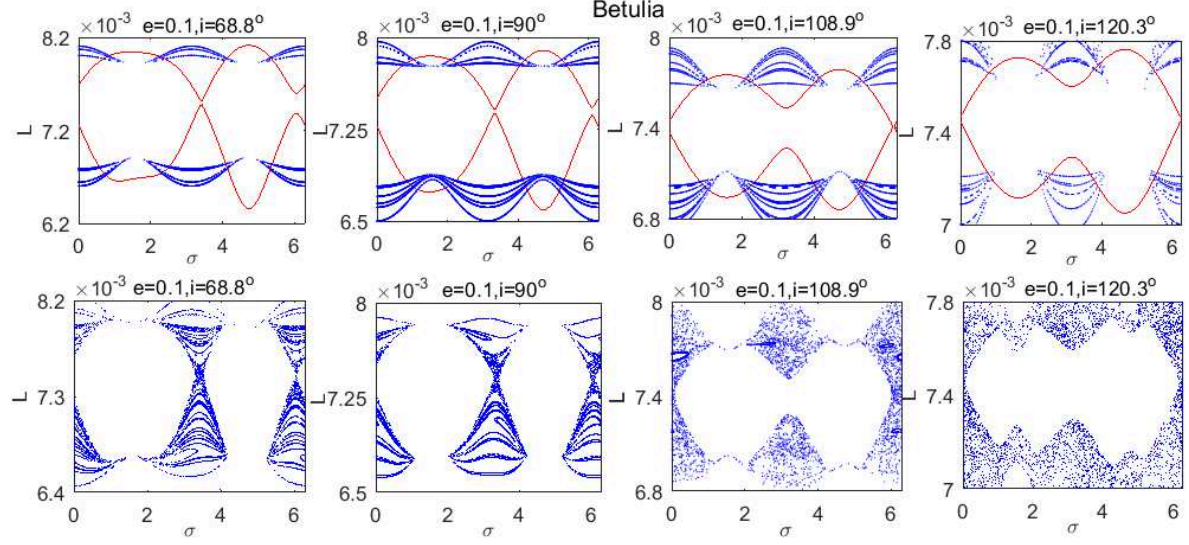


**Figure 16** First row: the separatrices of resonances  $\mathcal{H}_{reson1}$  and  $\mathcal{H}_{reson2}$  on the section  $g = \pi/2, \dot{g} < 0$ ; second row: the phase space of the corresponding  $\mathcal{H}_{2dof}$ ; both for  $e = 0.1, i = 68.8^\circ, 90^\circ, 108.9^\circ, 120.3^\circ$ .

## (2) The effect of $e$

In addition, it is also found that  $e$  shows the same effect on the dynamics of Betulia as for Vesta, both for the prograde and retrograde orbits. The mechanism is the same and is not explained in detail here. However, the phase space of  $\mathcal{H}_{2dof}$  at  $e = 0.5$  is included in Fig.17. For the first plot at  $i = 171.9^\circ$ , the main island is highly distorted although still without chaos. For  $i = 165^\circ$ , the distortion is more serious and large chaos appears. The phase space with a small area of regular region in the center already shows the property of  $\mathcal{H}_{reson2}$  at  $i = 153.6^\circ$ . For  $i = 11.5^\circ, 34.4^\circ, 45.8^\circ$ , the chaotic region is extended and new structures are generated.

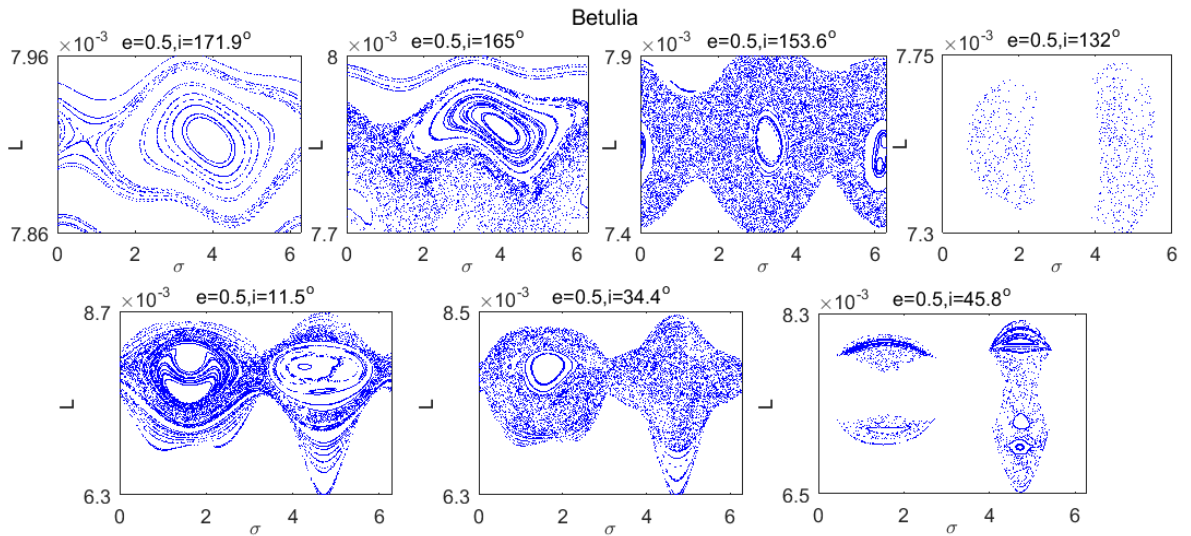


**Figure 17** The phase space of  $\mathcal{H}_{2dof}$  at  $e = 0.5$  for  $i = 171.9^\circ, 165^\circ, 153.6^\circ, 132^\circ, 11.5^\circ, 34.4^\circ, 45.8^\circ$ .

## 5.5 The Maximal Lyapunov Characteristic Exponent of Chaotic Orbits

In addition to the above study about the extent of chaotic layers, the chaos can also be characterized quantitatively by calculating the value of the maximal Lyapunov Characteristic Exponent (mLCE), which is indicator of the regular or chaotic properties of orbits (Skokos, 2010). Its basic idea is to measure the distance between two orbits that start close, until the infinite time  $t \rightarrow \infty$ . It characterizes the average growth rate of a small perturbation of the solution of a dynamical system and is defined as

$$\lambda = \lim_{t \rightarrow \infty} \frac{1}{t} \sum_0^t \ln \|\mathbf{v}(t)\|,$$

in which  $\mathbf{v}(t)$  is the deviation vector with respect to the given orbit at time  $t$ . It is also the solution of the corresponding variational equations of the dynamical system. If  $\lambda > 0$ , the orbit is chaotic; if  $\lambda = 0$ , the orbit is regular. The numerical algorithm applied here is the standard method originally developed by Benettin and Galgani (1979). Its detailed implementation can be found in Skokos (2010). It has to be mentioned that for regular orbits it might take a long time for  $\lambda$  to achieve zero. However, within a moderate time interval the tendency to zero is already visible.

Since it is obvious that large  $e$  introduces stronger chaos and the chaos of the three different asteroids is expected to be compared, the mLCE of orbits selected from the chaotic and regular regions (if there is no chaos) on the maps from Figs.5, 9, 10, 12 and 13 are given in Fig.18. These maps primarily indicate the effect of  $i$  on dynamics at  $e = 0.1$ . The total integration time for them is different, but has been chosen such that a stable value of all the mLCE can be achieved. To make the results more visible, the mLCE at the end of the integrations are magnified and are shown respectively as insets in the plots of Vesta and Betulia.

For the three asteroids, they share the same property that the more inclined the orbit, the larger mLCE value it has, indicating the stronger chaotic property. In addition, the mLCE values of the retrograde orbits are generally smaller than those of the prograde ones. For  $i = 171.9^\circ$ , there is no chaos on both the maps of Vesta and Betulia (shown in Figs.5 and 9). This is demonstrated in the value for the mLCE illustrated as dark blue at the bottom of inset which will finally tends to zero, the tendency of which can already be identified. The difference among the three asteroids can also be noticed. The resonant orbits around 1996 HW1 have the largest mLCE (at magnitude of  $10^{-5}$ ), the ones Betulia rank second (at magnitude of  $10^{-6}$ ), while orbits around Vesta show the smallest mLCE (mostly at magnitude of  $10^{-7}$ ). This can be explained by the different values of  $C_{20}$  and  $C_{22}$  induced from the irregular shape of the body. The more irregular the gravitational field, namely 1996 HW1 in our study, the relatively larger  $C_{20}$  and  $C_{22}$  and the resultant larger perturbation from  $\mathcal{H}_{reson2}$  it generates. Vesta is the

1:1 Ground-track resonance in a uniformly rotating 4<sup>th</sup> degree and order gravitational field

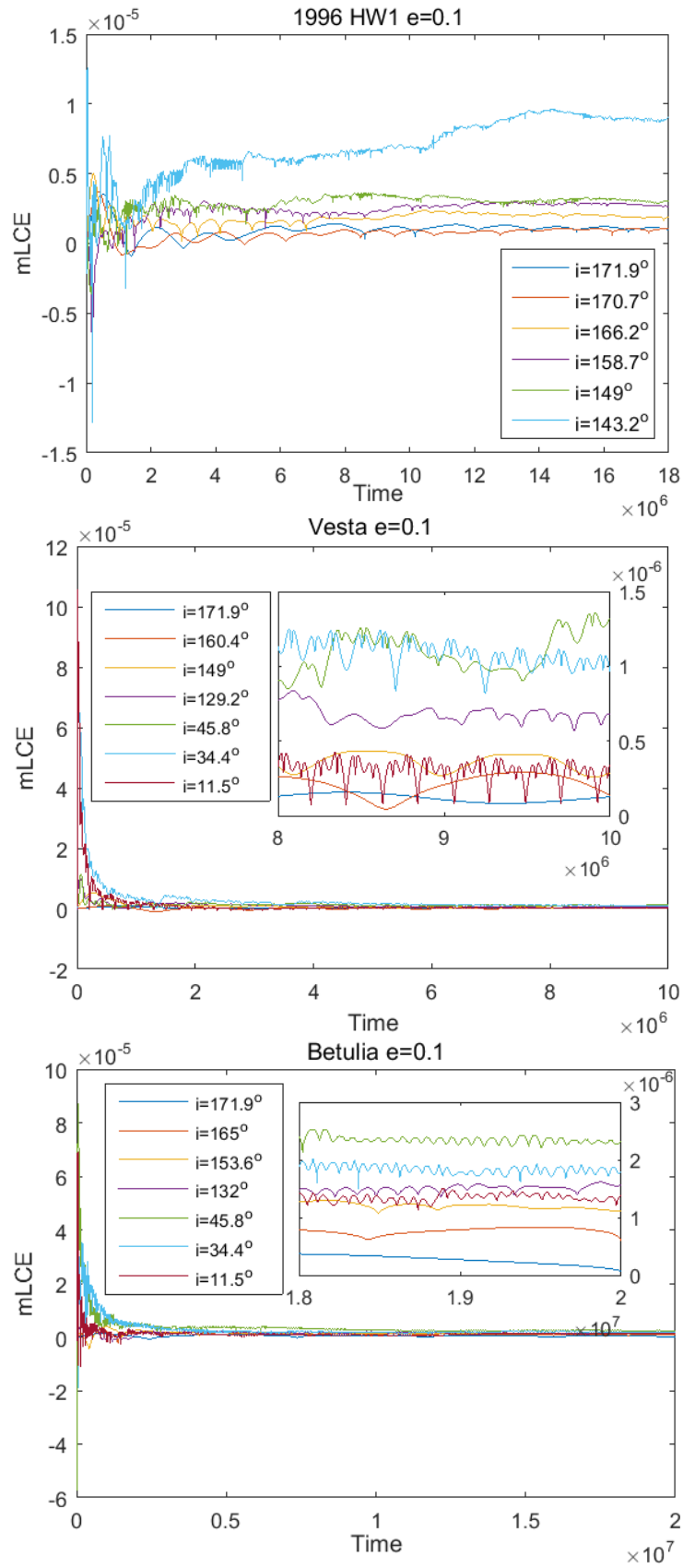


**Figure 18** The mLCE of regular and chaotic orbits from the Poincaré maps of  $\mathcal{H}_{2dof}$  for 1996 HW1, Vesta and Betulia.



most regular body and the influence of its second degree of freedom dynamics is limited. Betulia is in between.

In summary, the mLCE not only can identify the chaotic behavior of orbits, but also gives us a hint on their extent of chaotic property.

## 5.6 Conclusions

In this study, a 2-DOF Hamiltonian of the 1:1 resonant dynamics of a gravitational field up to degree and order 4 was built. The 1-DOF Hamiltonian  $\mathcal{H}_0$  was first studied by finding the EPs and examining their stability for non-circular and non-polar orbits of Vesta, 1996 HW1 and Betulia. This  $\mathcal{H}_0$  was proven to capture the main characteristics of the 1:1 resonant dynamics, which was proven by the three study cases. For  $\mathcal{H}_0$ ,  $i$  was found to play a significant role on the number of EPs. When  $i$  approaches  $\pi$ , there is only one stable EP left, due to the dominant strength of  $C_{31}$  over  $C_{22}$  on the structure of the phase space. The 2<sup>nd</sup> degree and order harmonics largely determine the stability of the EP, while the higher order terms either introduce new EPs and change the resonance width or break the symmetry of the dynamics.

By applying Poincaré maps, the 2-DOF Hamiltonian  $\mathcal{H}_{2dof}$  was then investigated. Two Hamiltonians  $\mathcal{H}_{reson1}$  and  $\mathcal{H}_{reson2}$  were defined in this 2-DOF model and their locations and widths were determined numerically for different combinations of  $e$  and  $i$ .

With the overlap criteria, the extent of chaotic regions was qualitatively explained by the distance between the two resonances as well as their resonance strength. For small  $e$  and  $i$  close to 0 or 180°, the dynamics of  $\mathcal{H}_{reson1}$  around the stable EP is hardly influenced for the situation when  $\mathcal{H}_{reson1}$  and  $\mathcal{H}_{reson2}$  are further apart. When  $i$  gets a bit further away from the equatorial plane,  $\mathcal{H}_{reson2}$  becomes close to and almost interacts with  $\mathcal{H}_{reson1}$ . Small-scale chaos (chaotic layers) were generated in the vicinity of the separatrix of  $\mathcal{H}_{2dof}$ , whose boundaries were well estimated by the modulated-pendulum approximation. When the two resonances have an obvious overlap for  $i$  getting close to the polar region, large chaos became apparent and new islands came forth in the phase space. However, for the near polar case, the libration region of  $\mathcal{H}_{reson1}$  is hardly influenced and is stable against perturbation of  $\mathcal{H}_{reson2}$ . Though the structure of the phase space is largely determined by  $i$ , the large  $e$  definitely give rise to strong perturbation of  $\mathcal{H}_{reson2}$ , which makes the main island distorted and the chaotic region extended. Therefore, the retrograde, near polar and near circular orbits show more stability against external perturbations.

In addition, the mLCEs of the chaotic and regular orbits were calculated, from which the above conclusion was proved quantitatively and the chaotic orbits around 1996 HW1 were revealed to have the strongest chaos, due to its highly irregular gravitational field.

This results and analyses in this paper serve as an example of studying the relationship among resonance overlap, extent of chaos and strength of the perturbing terms. The 2-DOF resonant dynamics of other main motion resonances, e.g. 1:2, 2:3, 3:2, can also be investigated with the approach applied in this paper. This research can also serve as the starting point for future study about the spacecraft's (or particle's) capture of and escape from mean motion resonances.

## Appendix A

Table A1 The primary zonal and tesseral terms contributing to the 1:1 resonance

$n$	2	2	3	3	4	4	4
$m$	0	2	1	3	0	2	4
$p$	1	0	1	0	2	1	0
$q$	0	0	0	0	0	0	0
$\Theta_{nmpq}$	0	$2\sigma$	$\sigma$	$3\sigma$	0	$2\sigma$	$4\sigma$

The expressions of  $\mathcal{H}_1$  and  $\mathcal{H}_2$  are given as

$$\begin{aligned}
\mathcal{H}_1 = & -\frac{\mu^4 R^2}{L^6} [F_{210} G_{20-1} (C_{21} \cos(\sigma + g) + S_{21} \sin(\sigma + g)) + F_{211} G_{211} (C_{21} \cos(\sigma - g) \\
& + S_{21} \sin(\sigma - g))] - \frac{\mu^5 R^3}{L^8} [F_{301} G_{31-1} (C_{30} \cos g + S_{30} \sin g) \\
& + F_{302} G_{321} (C_{30} \cos g - S_{30} \sin g)] \\
& - \frac{\mu^6 R^4}{L^8} [F_{411} G_{41-1} (C_{41} \cos(\sigma + g) + S_{41} \sin(\sigma + g)) \\
& + F_{412} G_{421} (C_{41} \cos(\sigma - g) + S_{41} \sin(\sigma - g)) \\
& + F_{430} G_{40-1} (C_{43} \cos(3\sigma + g) + S_{43} \sin(3\sigma + g)) \\
& + F_{431} G_{411} (C_{43} \cos(3\sigma - g) + S_{43} \sin(3\sigma - g))] \\
& \quad \quad \quad (A.1)
\end{aligned}$$

$$\begin{aligned}
\mathcal{H}_2 = & -\frac{\mu^4 R^2}{L^6} [F_{221} G_{212} (C_{22} \cos(2\sigma - 2g) + S_{22} \sin(2\sigma - 2g))] \\
& - \frac{\mu^5 R^3}{L^8} [F_{310} G_{30-2} (C_{31} \cos(\sigma + 2g) + S_{31} \sin(\sigma + 2g)) \\
& + F_{312} G_{322} (C_{31} \cos(\sigma - 2g) + S_{31} \sin(\sigma - 2g)) \\
& + F_{331} G_{312} (C_{33} \cos(3\sigma - 2g) + S_{33} \sin(3\sigma - 2g))] \\
& - \frac{\mu^6 R^4}{L^{10}} [F_{401} G_{41-2} (C_{40} \cos(2g) + S_{40} \sin(2g)) \\
& + F_{422} G_{422} (C_{42} \cos(2\sigma - 2g) + S_{42} \sin(2\sigma - 2g))] \\
& \quad \quad \quad (A.2)
\end{aligned}$$

## Appendix B

The tables below contain the values for the un-normalized spherical harmonic coefficients to degree and order 4 for Vesta derived from Tricarico and Sykes (2010), 1996 HW1 (Feng et al., 2015a) and Betulia derived from Magri et al. (2011). Although there is an update of the gravitational field of Vesta in Konopliv et al. (2014), the full

# 1:1 Ground-track resonance in a uniformly rotating 4<sup>th</sup> degree and order gravitational field

4×4 spherical harmonics are not directly available from it. In addition, the difference between the two is quite small.

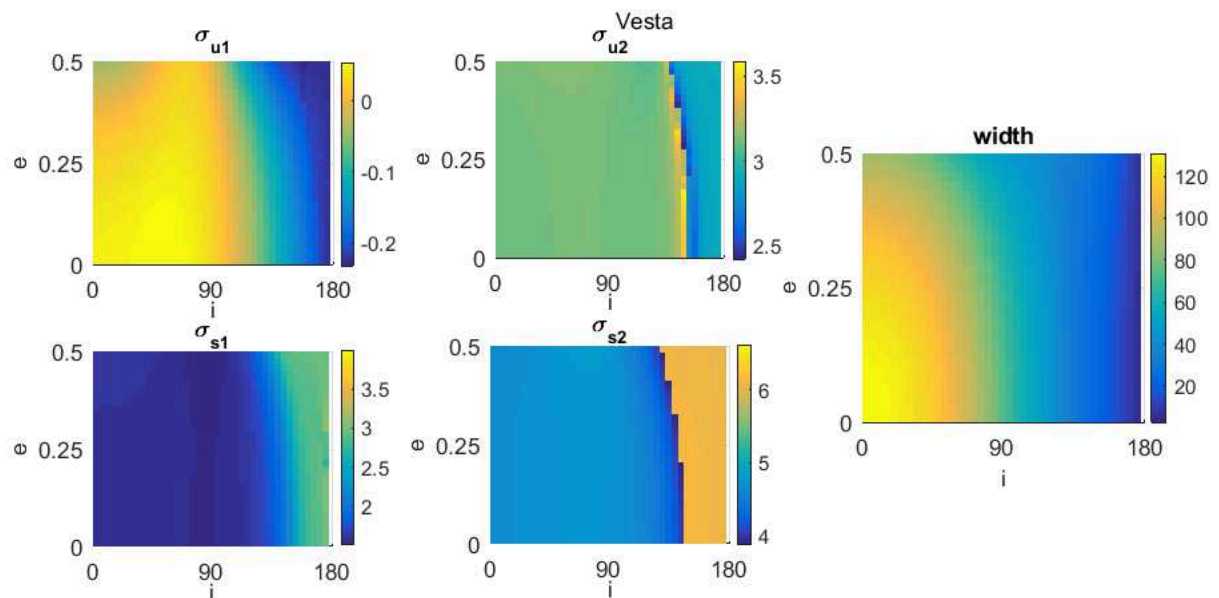
Vesta					
$C_{20}$	$-6.872555 \times 10^{-2}$	$S_{31}$	$1.825409 \times 10^{-4}$	$S_{41}$	$-1.347130 \times 10^{-4}$
$C_{21}$	0	$C_{32}$	$-3.162892 \times 10^{-4}$	$C_{42}$	$-3.152856 \times 10^{-5}$
$S_{21}$	0	$S_{32}$	$5.943231 \times 10^{-5}$	$S_{42}$	$6.551679 \times 10^{-5}$
$C_{22}$	$3.079667 \times 10^{-3}$	$C_{33}$	$2.565757 \times 10^{-5}$	$C_{43}$	$-3.113571 \times 10^{-5}$
$S_{22}$	0	$S_{33}$	$7.264998 \times 10^{-5}$	$S_{43}$	$-2.689264 \times 10^{-6}$
$C_{30}$	$6.286305 \times 10^{-3}$	$C_{40}$	$9.6 \times 10^{-3}$	$C_{44}$	$3.190457 \times 10^{-6}$
$C_{31}$	$-7.982112 \times 10^{-4}$	$C_{41}$	$6.394125 \times 10^{-4}$	$S_{44}$	$5.514632 \times 10^{-6}$

1996 HW1 (all $S_{nm}$ terms are zero)					
$C_{20}$	$-1.21847 \times 10^{-1}$	$C_{31}$	$-1.3964 \times 10^{-2}$	$C_{41}$	0
$C_{21}$	0	$C_{32}$	0	$C_{42}$	$-4.258 \times 10^{-3}$
$C_{22}$	$5.8547 \times 10^{-2}$	$C_{33}$	$2.547 \times 10^{-3}$	$C_{43}$	0
$C_{30}$	0	$C_{40}$	$3.8779 \times 10^{-2}$	$C_{44}$	$5.16 \times 10^{-4}$

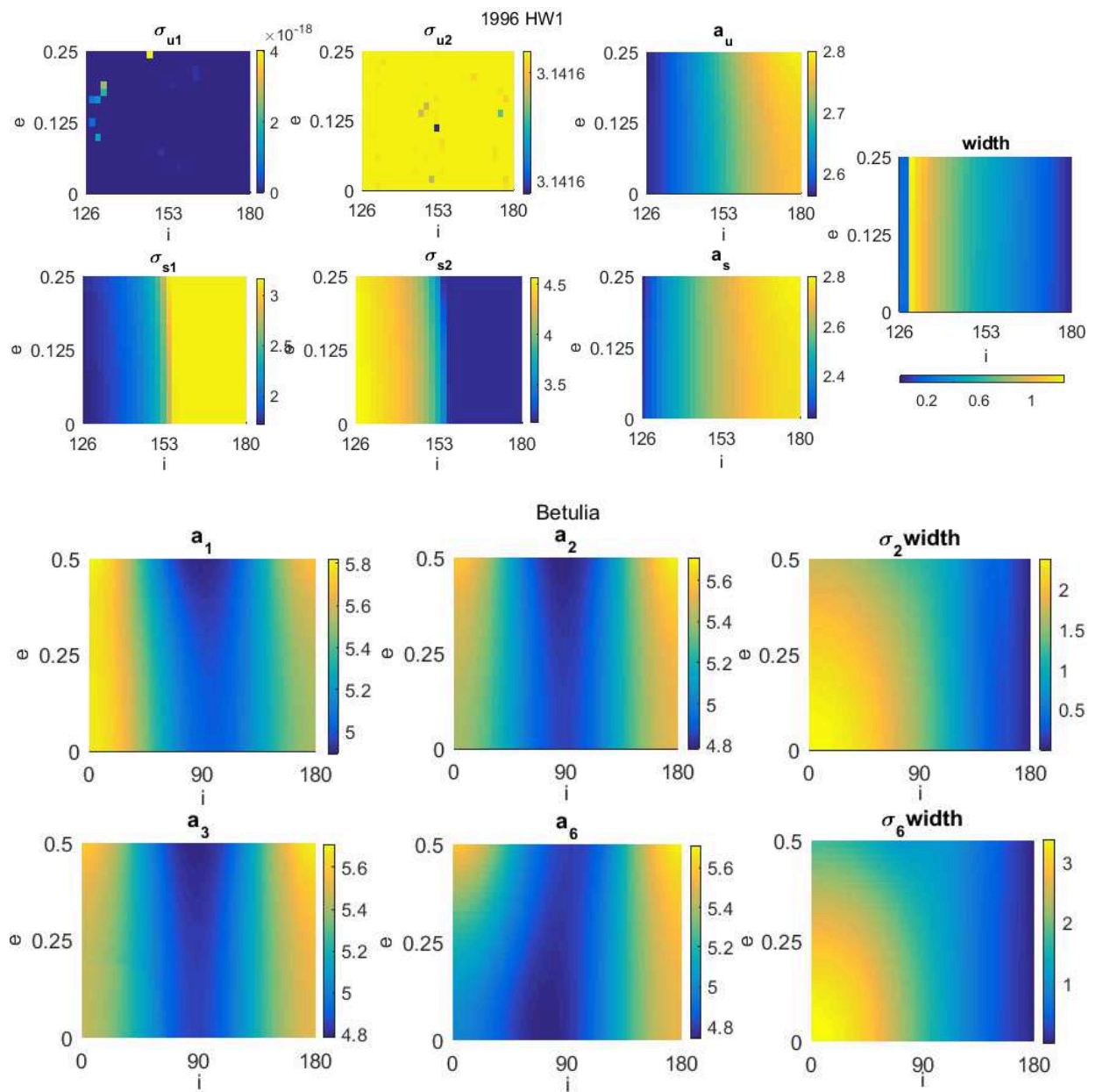
Betulia					
$C_{20}$	$-1.476131 \times 10^{-1}$	$S_{31}$	$-2.491845 \times 10^{-3}$	$S_{41}$	$-5.428366 \times 10^{-4}$
$C_{21}$	0	$C_{32}$	$-5.879324 \times 10^{-3}$	$C_{42}$	$-1.599034 \times 10^{-3}$
$S_{21}$	0	$S_{32}$	$2.931994 \times 10^{-3}$	$S_{42}$	$5.556629 \times 10^{-5}$
$C_{22}$	$1.711891 \times 10^{-2}$	$C_{33}$	$3.182376 \times 10^{-4}$	$C_{43}$	$1.775273 \times 10^{-4}$
$S_{22}$	0	$S_{33}$	$-3.910856 \times 10^{-3}$	$S_{43}$	$2.49498 \times 10^{-4}$
$C_{30}$	$9.543225 \times 10^{-3}$	$C_{40}$	$4.2618 \times 10^{-2}$	$C_{44}$	$-3.298214 \times 10^{-5}$
$C_{31}$	$-2.738977 \times 10^{-3}$	$C_{41}$	$-6.251823 \times 10^{-4}$	$S_{44}$	$3.024807 \times 10^{-5}$

## Appendix C

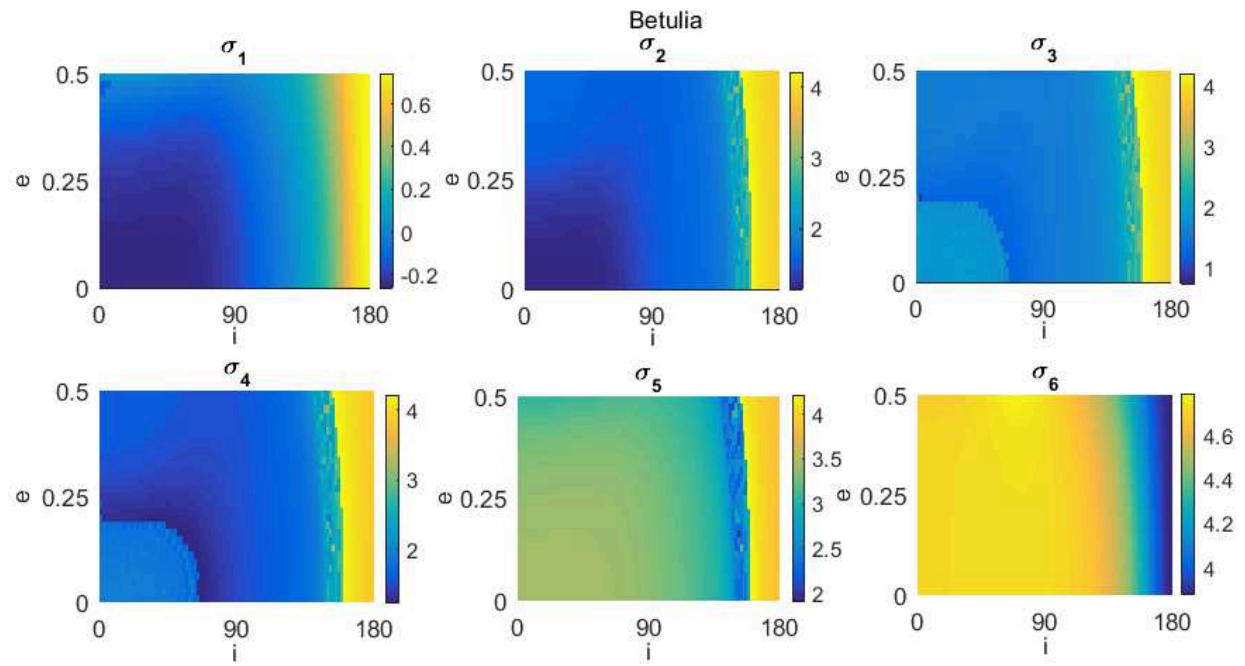
The location of EPs and resonance width at different combinations of  $e$  and  $i$  for Vesta, 1996 HW1 and Betulia



# 1:1 Ground-track resonance in a uniformly rotating 4<sup>th</sup> degree and order gravitational field



# 1:1 Ground-track resonance in a uniformly rotating 4<sup>th</sup> degree and order gravitational field



# Chapter 6 Conclusions and Recommendations

---

This thesis mainly investigated the dynamical environment in the vicinity of contact binary asteroid systems, or more specifically: the orbital motion of an accompanying spacecraft or particle. With the asteroid shape modeled by the combination of an ellipsoid and a sphere, the phase space around the asteroids was characterized by investigating the EPs, POs and their stability numerically. The influences of the system configuration and rotation rate on the phase space were also studied. One step further, a third-order analytical solution was constructed for the motion around the non-collinear EPs. Then putting the focus back on the entire asteroid system, the 3-dimensional POs were found for different rotation rates of the body. Lastly, for a generalized study about the effect of the irregular gravitational field on the 1:1 resonance dynamics, the gravitational field truncated at degree and order 4 was applied and the resulting 2-DOF Hamiltonian was studied by interpreting the extent of chaos in phase space with the overlap of the two resonances and their relative strength, for different combinations of eccentricity and inclination.

As presented in the previous chapters, the research questions were all addressed and conclusions on them are given in this chapter, which is followed by recommendations for future work.

## 6.1 Conclusions

### **(a) The phase space of the entire system has been characterized in Chapter 2**

First, to approximate the gravitational field of contact binary asteroids, a combination of an ellipsoid and a sphere was used. System 1996 HW1 was discussed to be the best study case. Under the assumption of constant density, its gravitational potential directly obtained from the combination of a spherical potential and a closed-form ellipsoidal potential. Four unstable EPs were found, the location and stability of which are highly consistent with the result from a polyhedron model.

Analogous to the RTBP, families of Lyapunov, Halo-like and vertical POs around the EPs were obtained numerically. It was found that the closer the PO to the EP, the more unstable it is, due to the instability of the EP and its surrounding motion. The relative size and shape of each lobe (also called system configuration) has a very weak influence on the stability of the four EPs, while the fast rotation of the asteroid transits the non-collinear EPs from stable to unstable. Two families of equatorial POs were found. The retrograde family A orbits, which are prograde in the inertial frame, became highly unstable when coming close to the asteroid. Retrograde family B orbits however can remain stable even when they almost touch the surface of the asteroid, and they are preferable orbits to be used in real missions.

The fast rotation of an asteroid does have a stabilizing effect to diminish the perturbation from the irregular gravitational field on equatorial orbits, which is in contrast to its influence on the stability of the non-collinear EPs. Polar resonant orbits in  $N$  commensurability with the rotation of the asteroid were obtained, which provide good coverage of the polar region of the body. From these simulations, the general properties of orbital motion in the vicinity of a contact binary asteroid system were characterized.

**(b) The analytical solution of the motion in the vicinity of the EPs has been constructed in Chapter 3**

As a natural next step, a third-order analytical solution of the motion around the non-collinear EPs was constructed with the LP method. Compared with numerical integration, this solution was proven to be a good approximation of such motion. However, its accuracy decreases when the amplitude of the motion becomes large and when the asteroid rotates rapidly, due to the fact that the LP method is based on a linear expansion of the motion. As already mentioned, the non-collinear EPs change to unstable when the asteroid rotates faster; and the motion in their vicinity is highly unstable. It was also found that the vertical orbital motion becomes more unstable when the asteroid rotates faster. With linear feedback control, a low-thrust control strategy was employed to stabilize the motion to follow the reference trajectory.

The larger the amplitude of the motion and the faster the rotation of the asteroid, the more propellant is required for stabilizing the motion. Therefore, from a practical concern on propellant consumption, it is recommended to have an accurate (i.e. numerical) nominal trajectory for a mission with large-amplitude motion around the EPs in a highly perturbed environment.

**(c) The dynamics in a truncated gravitational field has been addressed in terms of frozen orbits and POs in Chapter 4**

With such a shape model, the spherical harmonics expansion was shown to be a good approximation of the gravitational field for identifying frozen orbits and 3-dimensional POs. It was found that for a truncation at degree and order 4, the relative errors are smaller than 1% when the distance to the asteroid is larger than twice its reference radius, for different configurations. Particularly for 1996 HW1, the 8<sup>th</sup> and 4<sup>th</sup> degree and order expansions have relative errors of less than 2% and 8% at the circumscribing sphere, respectively. Terms  $C_{31}$ ,  $C_{40}$  and  $C_{60}$  were found to have large magnitudes, compared to the corresponding terms of planetary bodies and their moons.

Therefore, the Hamiltonian that takes into account 4<sup>th</sup> degree and order spherical harmonics was built. Frozen orbits were obtained from the double-averaged Hamiltonian, in which only zonal harmonics appear to play a role. By examining these orbits in the non-averaged model, tesseral harmonics were revealed to introduce large variations in the orbit and distort the frozen conditions. With the aid of Poincaré maps,

the structure of the phase space of the single-averaged Hamiltonian (including tesseral terms) was investigated at different energy levels and rotation rates of the asteroid, from which POs were obtained. Among them, the stable POs are most interesting for mission purposes. In addition, it was discovered that the perturbing effect of the highly irregular gravitational field on orbital motion is relatively weak around the polar region and for the situation when the asteroid rotates fast.

**(d) The 1:1 resonance dynamics in a rotating 4<sup>th</sup> degree and order gravitational field has been investigated in Chapter 5**

For a further and generalized study about the dynamics of a 4<sup>th</sup> degree and order gravitational field, the 1:1 ground-track resonance dynamics was investigated with a 2-DOF Hamiltonian. This resonance dynamics is dominated by a 1-DOF Hamiltonian that is included in the original 2-DOF model. The location, stability and width of this 1:1 resonance were assessed for orbits with arbitrary eccentricity and inclination. The 2<sup>nd</sup> degree and order harmonics were found to largely determine the stability, while the 3<sup>rd</sup> and 4<sup>th</sup> order terms were revealed to change the resonance width, introduce new locations of the resonance and break the symmetry of this 1:1 resonance dynamics. This study was applied to three asteroids: Vesta, 1996 HW1 and Betulia. The findings were in good agreement with the known results of the equatorial resonant orbits, proving that the 1-DOF Hamiltonian captures the main dynamics of the system.

For the 2-DOF Hamiltonian, a second resonance was identified in addition to the main resonance studied above, and was treated as a perturbation term. By applying Poincaré sections, the extent of chaos in the phase space was quantitatively shown to be determined by both the overlap of the two resonances and the strength of each resonance. Large regions with chaos are generated when the two resonances have a significant overlap and the perturbing resonance is stronger. When the two resonances are close but not connected yet, small chaotic layers appear around the separatrix of the main resonance; their boundaries were estimated with the modulated-pendulum approximation. The resonance width of the retrograde orbits was shown to be smaller than that of the prograde ones. In addition, the polar region again was found to be less influenced by the perturbation from the second resonance.

As already discussed, the research questions that were presented in the introduction chapter have been addressed in Chapters 2, 3, 4 and 5. In summary, several general conclusions can be drawn here:

- (1) The shape model of the combination of an ellipsoid and a sphere works well for studying the general dynamical environment in the vicinity of contact binary asteroid systems;
- (2) Compared to that of the system configuration, the rotation rate of the asteroid does have a significant influence on the phase space. The fast rotation does have a stabilizing effect on the nearby orbital motion, i.e. the equatorial orbits and the 3-



dimensional orbits around the entire system, except for the region where resonances occur (especially the 1:1 resonance). It is known that the non-collinear EPs, which belong to the 1:1 resonance, transit to unstable when the asteroid rotates more rapidly.

(3) Orbits near the polar region are found to be relatively stable and robust against the perturbations from the irregular gravitational field and from the second resonance.

(4) The extent of the chaotic regions is determined by both the distance between the resonances and their respective strengths.

The models and methods employed in this thesis have a wide application to investigate the dynamical environment of other systems, e.g. binary asteroid systems, planet-moon systems and even binary star systems.

## 6.2 Recommendations

There are still many open questions that need to be tackled in the field of orbital motion within a highly bifurcated gravitational field.

First, although our shape model of a combined ellipsoid and sphere is a good approximation, a high-fidelity gravitational model if available, e.g. the polyhedron model, is recommended for a more accurate exploration of the dynamical environment of a specific contact binary system, e.g. comet 67P. For real mission operations, it is hard to get the detailed gravitational field before the spacecraft's arrival at the target body. Monte Carlo analysis might be required to identify the stable region of orbital motion around the contact binary body, to assist with selecting robust mission orbits. Furthermore, as the two lobes of a contact binary system in general have a different origin and probably possess different densities, it is suggested to take this into account and to check its effects on the dynamical environment.

As an extension of this work about a third-order analytical solution of the motion in the vicinity of the non-collinear EPs, a higher-order solution is appreciated for large-amplitude motion and for the fast rotation of the asteroid. For this kind of study, a truncated gravitational field is still recommended to obtain a generalized result that can be applied to other highly irregular gravitational environments (not only for contact binary systems). Afterwards, a full validation can be performed by numerical integration. The analytical solution of motion around the collinear EPs can also be constructed with this gravitational model and the methods developed in this study.

In addition to the orbital dynamics, the long-term motion of ejecta particles is also worthwhile to be studied, not only for identifying the accumulation of particles on the surface of the asteroid but also for investigating the capture and ejecta dynamics of the body. For this purpose, the polyhedron model is suggested, as it is the most accurate one for motions on the surface and in close vicinity of the asteroid. For contact binary bodies, one of the most appealing areas is the neck region, where the two lobes merge into each other. Detailed exploration of the surface motion of a particle in this region

as well as its geophysical and chemical environment can help to uncover the formation process of contact binary bodies.

Except for the irregular gravitational field of the asteroid, there is also a perturbation from solar radiation pressure (SRP) on the spacecraft. If the spacecraft has a large area-to-mass ratio or flies at a moderate distance to the asteroid, SRP is expected to give rise to a significant perturbation on the stability of orbits. Together with the irregular gravitational field from the body, control strategies need to be studied for maintaining the desired orbital motion around the body. Furthermore, SRP can also be taken advantage of to design so-called solar-terminator orbits, which might be a good candidate of orbits that have a good coverage of the neck region. However, for spacecraft orbiting comets, with perturbations from SRP and outgassing (especially when the comet is at its perihelion) as well as the weak gravitational field of the comet, new characteristics of the dynamical environment are expected to be generated, together with new challenges for an orbital mission.

For the spacecraft passage through resonance, its orbit might become chaotic or it is captured into the resonance. Therefore, the probabilities of capture escape need to be investigated for the 1:1 resonance, as it is always recognized as the largest one. Delsate (2011) already did some preliminary numerical analysis for Dawn around Vesta, and found these probabilities to be closely related to the phase of the resonant angle. However, a systematic study is required to obtain a general conclusion for orbits with arbitrary eccentricity and inclination. Except for the 1:1 resonance, other resonances are also interesting to study. For example, for Vesta, the 2:3 resonance was shown to be strongest and to post a great influence on orbital eccentricity (Delsate, 2011). The main resonances and their strengths should be identified in the presence of a highly irregular gravitational field, together with the corresponding capture and escape probabilities. In addition, a new structure of phase space is generated in the chaotic region, which is the result of high-order resonances. This phenomenon is also interesting to address. Last but not least, the effect of the rotation rate of the asteroid on the width of main resonances should also be studied, for the completeness of the investigation of the effect of the rotation rate on dynamics of nearby orbiting objects.



# References

---

- ABELL, P., CARNELLI, I., CARRY, B., CHENG, A., DROLSHAGEN, G., FONTAINE, M., GALVEZ, A., KOSCHNY, D., KUEPPERS, M., MICHEL, P., MURDOCH, N., REED, C. & ULAMEC, S. 2012. Asteroid Impact & Deflection Assessment (AIDA) Mission Opportunities and Tests in a US-Europe Space Mission Cooperation. [http://esamultimedia.esa.int/docs/qsp/completed/AIDA\\_MissionRationale\\_InterimRelease.pdf](http://esamultimedia.esa.int/docs/qsp/completed/AIDA_MissionRationale_InterimRelease.pdf).
- BALMINO, G. 1994. Gravitational potential harmonics from the shape of an homogeneous body. *Celestial Mechanics and Dynamical Astronomy*, 60, 331-364.
- BARNOUIN-JHA, O., KUBOTA, T., SHIRAKAWA, K., KAWAGUCHI, J., UO, M., GASKELL, R., MUKAI, T., SCHEERES, D., ABE, S. & ISHIGURO, M. The actual dynamical environment about Itokawa. AIAA/AAS Astrodynamics Specialist Conference and Exhibit, 2006.
- BARTCZAK, P. & BREITER, S. 2003. Double material segment as the model of irregular bodies. *Celestial Mechanics and Dynamical Astronomy*, 86, 131-141.
- BARTCZAK, P., BREITER, S. & JUSIEL, P. 2006. Ellipsoids, material points and material segments. *Celestial Mechanics and Dynamical Astronomy*, 96, 31-48.
- BELLEROSE, J. & SCHEERES, D. 2008. *The restricted full three body problem: applications to binary asteroid exploration*, The University of Michigan, ProQuest.
- BELTON, M. J., CHAPMAN, C. R., KLAASEN, K. P., HARCH, A. P., THOMAS, P. C., VEVERKA, J., MCEWEN, A. S. & PAPPALARDO, R. T. 1996. Galileo's encounter with 243 Ida: An overview of the imaging experiment. *Icarus*, 120, 1-19.
- BENETTIN, G. & GALGANI, L. 1979. *Lyapunov characteristic exponents and stochasticity*. Cargese.
- BENNER, L. A., NOLAN, M. C., OSTRO, S. J., GIORGINI, J. D., PRAY, D. P., HARRIS, A. W., MAGRI, C. & MARGOT, J.-L. 2006. Near-Earth Asteroid 2005 CR37: Radar images and photometry of a candidate contact binary. *Icarus*, 182, 474-481.
- BOTTKE, W. F. 2002. *Asteroids III*, University of Arizona Press.
- BRITT, D., YEOMANS, D., HOUSEN, K. & CONSOLMAGNO, G. 2002. Asteroid density, porosity, and structure. *Asteroids III*.
- BROSCHART, S. B. & VILLAC, B. F. 2009. Identification of non-chaotic terminator orbits near 6489 Golevka. *Advances in Astronautical Sciences*, 134, 861-880.
- BROUCKE, R. 1969. Stability of periodic orbits in the elliptic, restricted three-body problem. *AIAA Journal*, 7, 1003-1009.
- BROUCKE, R. 1994. Numerical integration of periodic orbits in the main problem of artificial satellite theory. *Celestial Mechanics and Dynamical Astronomy*, 58, 99-123.
- BROZOVIC, M., BENNER, L. A., MAGRI, C., OSTRO, S. J., SCHEERES, D. J., GIORGINI, J. D., NOLAN, M. C., MARGOT, J.-L., JURGENS, R. F. & ROSE, R. 2010. Radar observations and a physical model of contact binary Asteroid 4486 Mithra. *Icarus*, 208, 207-220.
- BRYSON, A. E. 1975. *Applied optimal control: optimization, estimation and control*, CRC Press.
- BYRAM, S. M. & SCHEERES, D. J. 2009. Stability of Sun-synchronous orbits in the vicinity of a comet. *Journal of Guidance, Control, and Dynamics*, 32, 1550-1559.
- CECCARONI, M. & BIGGS, J. 2013. Analytic perturbative theories in highly inhomogeneous gravitational fields. *Icarus*, 224, 74-85.

- CHAPPAZ, L. & HOWELL, K. 2015. Exploration of bounded motion near binary systems comprised of small irregular bodies. *Celestial Mechanics and Dynamical Astronomy*, 123, 123-149.
- CHAUVINEAU, B., FARINELLA, P. & MIGNARD, F. 1993. Planar orbits about a triaxial body: Application to asteroidal satellites. *Icarus*, 105, 370-384.
- CHICONE, C. C. 1999. *Ordinary differential equations with applications*, Springer.
- CHIRIKOV, B. V. 1979. A universal instability of many-dimensional oscillator systems. *Physics Reports*, 52, 263-379.
- COFFEY, S. L., DEPRIT, A. & DEPRIT, E. 1994. Frozen orbits for satellites close to an Earth-like planet. *Celestial Mechanics and Dynamical Astronomy*, 59, 37-72.
- COMPÈRE, A., LEMAÎTRE, A. & DELSATE, N. 2012. Detection by MEGNO of the gravitational resonances between a rotating ellipsoid and a point mass satellite. *Celestial Mechanics and Dynamical Astronomy*, 112, 75-98.
- DANKOWICZ, H. 1994. Some special orbits in the two-body problem with radiation pressure. *Celestial Mechanics and Dynamical Astronomy*, 58, 353-370.
- DELHAISE, F. & HENRARD, J. 1993. The problem of critical inclination combined with a resonance in mean motion in artificial satellite theory. *Celestial Mechanics and Dynamical Astronomy*, 55, 261-280.
- DELSATE, N. 2011. Analytical and numerical study of the ground-track resonances of Dawn orbiting Vesta. *Planetary and Space Science*, 59, 1372-1383.
- ELIPE, A. & LARA, M. 2003. A simple model for the chaotic motion around (433) Eros. *The Journal of the Astronautical Sciences*, 51, 391-404.
- FARQUHAR, R. W. 1970. The control and use of libration-point satellites. National Aeronautics and Space Administration.
- FARQUHAR, R. W. & KAMEL, A. A. 1973. Quasi-periodic orbits about the translunar libration point. *Celestial Mechanics*, 7, 458-473.
- FENG, J., NOOMEN, R., VISSER, P. N. & YUAN, J. 2015a. Modeling and analysis of periodic orbits around a contact binary asteroid. *Astrophysics and Space Science*, 357, 1-18.
- FENG, J., NOOMEN, R. & YUAN, J. 2015b. Orbital Motion in the Vicinity of the Non-collinear Equilibrium Points of a Contact Binary Asteroid. *Planetary and Space Science*, 117, 1-14.
- FERRAZ-MELLO, S. 2007. *Canonical perturbation theories: degenerate systems and resonance*, Springer Science & Business Media.
- FUJIWARA, A., KAWAGUCHI, J., YEOMANS, D., ABE, M., MUKAI, T., OKADA, T., SAITO, J., YANO, H., YOSHIKAWA, M. & SCHEERES, D. 2006. The rubble-pile asteroid Itokawa as observed by Hayabusa. *Science*, 312, 1330-1334.
- GABERN, F., KOON, W., MARSDEN, J. & SCHEERES, D. 2006. Binary asteroid observation orbits from a global dynamical perspective. *SIAM Journal on Applied Dynamical Systems*, 5, 252-279.
- GERMAN, D. & FRIEDLANDER, A. L. A simulation of orbits around asteroids using potential field modelling. *Spaceflight Mechanics*, 1991. 1183-1201.
- GÓMEZ, G. 2001. *Dynamics and Mission Design Near Libration Points: Advanced methods for triangular points*, World Scientific.
- GÓMEZ, G. & MARCOTE, M. 2006. High-order analytical solutions of Hill's equations. *Celestial Mechanics and Dynamical Astronomy*, 94, 197-211.
- GÓMEZ, G., MARCOTE, M. & MONDELO, J. 2005. The invariant manifold structure of the spatial Hill's problem. *Dynamical Systems: An International Journal*, 20, 115-147.

- GOPAL, M. 1993. *Modern control system theory*, New Age International.
- GURFIL, P. & MELTZER, D. 2006. Stationkeeping on unstable orbits: generalization to the elliptic restricted three-body problem. *The Journal of the Astronautical Sciences*, 54, 29-51.
- HALAMEK, P. & BROUCKE, R. 1988. *Motion in the potential of a thin bar*. PhD dissertation, University of Texas, Austin.
- HARMON, J. K., NOLAN, M. C., GIORGINI, J. D. & HOWELL, E. S. 2010. Radar observations of 8P/Tuttle: A contact-binary comet. *Icarus*, 207, 499-502.
- HARMON, J. K., NOLAN, M. C., HOWELL, E. S., GIORGINI, J. D. & TAYLOR, P. A. 2011. Radar observations of comet 103P/Hartley 2. *The Astrophysical Journal Letters*, 734, L2.
- HARTMANN, W. K. & CRUIKSHANK, D. P. 1978. The nature of Trojan asteroid 624 Hektor. *Icarus*, 36, 353-366.
- HENRARD, J. 1990. A semi-numerical perturbation method for separable Hamiltonian systems. *Celestial Mechanics and Dynamical Astronomy*, 49, 43-67.
- HIRABAYASHI, M., MORIMOTO, M. Y., YANO, H., KAWAGUCHI, J. I. & BELLEROSE, J. 2010. Linear stability of collinear equilibrium points around an asteroid as a two-connected-mass: Application to fast rotating Asteroid 2000EB 14. *Icarus*, 206, 780-782.
- HIRABAYASHI, M. & SCHEERES, D. 2013. Recursive computation of mutual potential between two polyhedra. *Celestial Mechanics and Dynamical Astronomy*, 117, 245-262.
- HOU, X. & LIU, L. 2010. On quasi-periodic motions around the triangular libration points of the real Earth–Moon system. *Celestial Mechanics and Dynamical Astronomy*, 108, 301-313.
- HOU, X. & LIU, L. 2011. On quasi-periodic motions around the collinear libration points in the real Earth–Moon system. *Celestial Mechanics and Dynamical Astronomy*, 110, 71-98.
- HOWELL, K. C. 1984. Three-dimensional, periodic, ‘halo’ orbits. *Celestial Mechanics*, 32, 53-71.
- HU, W. & SCHEERES, D. 2004. Numerical determination of stability regions for orbital motion in uniformly rotating second degree and order gravity fields. *Planetary and Space Science*, 52, 685-692.
- HUDSON, R. S. 1994. Shape of Asteroid 4769 Castalia (1989 PB). *Science*, 263, 18.
- HUSSMANN, H., OBERST, J., WICKHUSEN, K., SHI, X., DAMME, F., LÜDICKE, F., LUPOVKA, V. & BAUER, S. 2012. Stability and evolution of orbits around the binary asteroid 175706 (1996 FG3): Implications for the MarcoPolo-R mission. *Planetary and Space Science*, 70, 102-113.
- JIANG, Y., BAOYIN, H., LI, J. & LI, H. 2014. Orbits and manifolds near the equilibrium points around a rotating asteroid. *Astrophysics and Space Science*, 349, 83-106.
- JORBA, A. & MASDEMONT, J. 1999. Dynamics in the center manifold of the collinear points of the restricted three body problem. *Physica D: Nonlinear Phenomena*, 132, 189-213.
- KAULA, W. M. 1966. *Theory of satellite geodesy: applications of satellites to geodesy*, Massachusetts, Blaisdell Publishing Company.
- KONOPLIV, A., ASMAR, S., PARK, R., BILLS, B., CENTINELLO, F., CHAMBERLIN, A., ERMAKOV, A., GASKELL, R., RAMBAUX, N. & RAYMOND, C. 2014. The Vesta gravity field, spin pole and rotation period, landmark positions, and ephemeris from the Dawn tracking and optical data. *Icarus*, 240, 103-117.
- LARA, M. 1996. On numerical continuation of families of periodic orbits in a parametric potential. *Mechanics research communications*, 23, 291-298.

- LARA, M. 1999. Searching for repeating ground track orbits: A systematic approach. *The Journal of the Astronautical Sciences*, 47, 177-188.
- LARA, M. 2003. Repeat ground track orbits of the Earth tesseral problem as bifurcations of the equatorial family of periodic orbits. *Celestial Mechanics and Dynamical Astronomy*, 86, 143-162.
- LARA, M. 2008. Simplified equations for computing science orbits around planetary satellites. *Journal of Guidance, Control, and Dynamics*, 31, 172-181.
- LARA, M. & ELIPE, A. 2002. Periodic orbits around geostationary positions. *Celestial mechanics and dynamical astronomy*, 82, 285-299.
- LARA, M. & RUSSELL, R. 2007. Computation of a science orbit about Europa. *Journal of Guidance, Control, and Dynamics*, 30, 259-263.
- LARA, M. & SCHEERES, D. J. 2002. Stability bounds for three-dimensional motion close to asteroids. *The Journal of the Astronautical Sciences*, 50, 389-409.
- LAURETTA, D., BARTELS, A., BARUCCI, M., BIERHAUS, E., BINZEL, R., BOTTKE, W., CAMPINS, H., CHESLEY, S., CLARK, B. & CLARK, B. 2015. The OSIRIS - REx target asteroid (101955) Bennu: Constraints on its physical, geological, and dynamical nature from astronomical observations. *Meteoritics & Planetary Science*, 50, 834-849.
- LEI, H. & XU, B. 2013. High-order analytical solutions around triangular libration points in the circular restricted three-body problem. *Monthly Notices of the Royal Astronomical Society*, 434, 1376-1386.
- LIU, X., BAOYIN, H. & MA, X. 2011a. Analytical investigations of quasi-circular frozen orbits in the Martian gravity field. *Celestial Mechanics and Dynamical Astronomy*, 109, 303-320.
- LIU, X., BAOYIN, H. & MA, X. 2011b. Equilibria, periodic orbits around equilibria, and heteroclinic connections in the gravity field of a rotating homogeneous cube. *Astrophysics and Space Science*, 333, 409-418.
- LOURAKIS, M. I. 2005. A brief description of the Levenberg-Marquardt algorithm implemented by levmar. *Foundation of Research and Technology*, 4, 1-6.
- MACMILLAN, W. D. 1958. *The theory of the potential*, New York, Dover.
- MAGRI, C., HOWELL, E. S., NOLAN, M. C., TAYLOR, P. A., FERNÁNDEZ, Y. R., MUELLER, M., VERVACK JR, R. J., BENNER, L. A., GIORGINI, J. D., OSTRO, S. J., SCHEERES, D. J., HICKS, M. D., RHOADES, H., SOMERS, J. M., GAFTONYUK, N. M., KROUPRIANOV, V. V., KRUGLY, Y. N., MOLOTOV, IGOR E., B., MICHAEL W., MARGOT, J.-L., BENISHEK, VLADIMIR, P.-B., VOJISLAVA, G., ADRIAN, HIGGINS, D., KUŠNIRÁK & PETER, P., DONALD P. 2011. Radar and photometric observations and shape modeling of contact binary near-Earth Asteroid (8567) 1996 HW1. *Icarus*, 214, 210-227.
- MAGRI, C., OSTRO, S. J., SCHEERES, D. J., NOLAN, M. C., GIORGINI, J. D., BENNER, L. A. M. & MARGOT, J.-L. 2007. Radar observations and a physical model of Asteroid 1580 Betulia. *Icarus*, 186, 152-177.
- MARCHIS, F., DURECH, J., CASTILLO-ROGEZ, J., VACHIER, F., CUK, M., BERTHIER, J., WONG, M., KALAS, P., DUCHENE, G. & VAN DAM, M. 2014. The puzzling mutual orbit of the binary Trojan Asteroid (624) Hektor. *The Astrophysical Journal Letters*, 783, L37.
- MARUYA, M., OHYAMA, H., UO, M., MURANAKA, N., MORITA, H., KUBOTA, T., HASHIMOTO, T., SAITO, J. & KAWAGUCHI, J. I. Navigation shape and surface topography model of Itokawa. AIAA Guidance, Navigation, and Control Conference, 2006.

- MASSIRONI, M., SIMIONI, E., MARZARI, F., CREMONESE, G., GIACOMINI, L., PAJOLA, M., JORDA, L., NALETTO, G., LOWRY, S. & EL-MAARRY, M. R. 2015. Two independent and primitive envelopes of the bilobate nucleus of comet 67P. *Nature*, 526, 402-405.
- MCMAHON, J. W. & SCHEERES, D. J. 2013. Dynamic limits on planar libration-orbit coupling around an oblate primary. *Celestial Mechanics and Dynamical Astronomy*, 115, 365-396.
- MEISS, J. D. 2007. *Differential dynamical systems*, USA, Siam.
- MÉTRIS, G. & EXERTIER, P. 1995. Semi-analytical theory of the mean orbital motion. *Astronomy and Astrophysics*, 294, 278-286.
- MICKENS, R. E. 1981. *An introduction to nonlinear oscillations*, Cambridge University Press.
- MORBIDELLI, A. 2002. Modern celestial mechanics: aspects of solar system dynamics. London: Taylor & Francis.
- MORÉ, J. J. 1978. The Levenberg-Marquardt algorithm: implementation and theory. *Numerical analysis*. Springer.
- MOULTON, F. R., BUCHANAN, D., BUCK, T., GRIFFIN, F. L., LONGLEY, W. R. & MACMILLAN, W. D. 1920. *Periodic orbits*, Washington, Carnegie Institution of Washington.
- MULLER, P. M. & SJOGREN, W. L. 1968. Mascons: Lunar mass concentrations. *Science*, 161, 680-684.
- NASA. 2015a. <https://www.nasa.gov/feature/last-of-pluto-s-moons-mysterious-kerberos-revealed-by-new-horizons>. [Accessed October 2015].
- NASA. 2015b. <https://www.nasa.gov/content/what-is-nasa-s-asteroid-redirect-mission>. [Accessed April 2016].
- NASA. 2016. <http://neo.jpl.nasa.gov/risk/a101955.html>. [Accessed April 2016].
- NATHUES, A., HOFFMANN, M., SCHAEFER, M., LE CORRE, L., REDDY, V., PLATZ, T., CLOUTIS, E., CHRISTENSEN, U., KNEISSL, T. & LI, J.-Y. 2015. Sublimation in bright spots on (1) Ceres. *Nature*, 528, 237-240.
- NELSON, M. L., BRITT, D. T. & LEBOSKY, L. A. 1993. Review of asteroid compositions. *Resources of Near-Earth Space*, 493-522.
- OLSEN, Ø. 2006. Orbital resonance widths in a uniformly rotating second degree and order gravity field. *Astronomy & Astrophysics*, 449, 821-826.
- OSINGA, H. & KRAUSKOPF, J. G.-V. B. 2007. Numerical continuation methods for dynamical systems. Springer.
- OSTRO, S. J., HUDSON, R. S., ROSEMA, K. D., GIORGINI, J. D., JURGENS, R. F., YEOMANS, D. K., CHODAS, P. W., WINKLER, R., ROSE, R. & CHOATE, D. 1999. Asteroid 4179 Toutatis: 1996 radar observations. *Icarus*, 137, 122-139.
- OSTRO, S. J., MARGOT, J.-L., BENNER, L. A., GIORGINI, J. D., SCHEERES, D. J., FAHNESTOCK, E. G., BROSCART, S. B., BELLEROSE, J., NOLAN, M. C. & MAGRI, C. 2006. Radar imaging of binary near-Earth asteroid (66391) 1999 KW4. *Science*, 314, 1276-1280.
- PALACIÁN, J. 2007. Dynamics of a satellite orbiting a planet with an inhomogeneous gravitational field. *Celestial Mechanics and Dynamical Astronomy*, 98, 219-249.
- PARK, R. S., WERNER, R. A. & BHASKARAN, S. 2010. Estimating small-body gravity field from shape model and navigation data. *Journal of Guidance, Control, and Dynamics*, 33, 212-221.
- PRAVEC, P., HARRIS, A. W. & MICHALOWSKI, T. 2002. Asteroid rotations. *Asteroids III*. University of Arizona Press.



- PRAVEC, P., SCHEIRICH, P., KUŠNIRÁK, P., ŠAROUNOVÁ, L., MOTTOLA, S., HAHN, G., BROWN, P., ESQUERDO, G., KAISER, N. & KRZEMINSKI, Z. 2006. Photometric survey of binary near-Earth asteroids. *Icarus*, 181, 63-93.
- PRESS, W. H. 2007. *Numerical recipes 3rd edition: The art of scientific computing*, Cambridge University Press.
- PRIETO-LLANOS, T. & GOMEZ-TIERNO, M. A. 1994. Stationkeeping at libration points of natural elongated bodies. *Journal of Guidance, Control, and Dynamics*, 17, 787-794.
- RIAGUAS, A., ELIPE, A. & LARA, M. 1999. Periodic Orbits Around a Massive Straight Segment. *Celestial Mechanics and Dynamical Astronomy*, 73, 169-178.
- RICHARDSON, D. L. 1980. Analytic construction of periodic orbits about the collinear points. *Celestial Mechanics*, 22, 241-253.
- RUSSELL, C., RAYMOND, C., CORADINI, A., MCSWEEN, H., ZUBER, M., NATHUES, A., DE SANCTIS, M., JAUMANN, R., KONOPLIV, A. & PREUSKER, F. 2012. Dawn at Vesta: Testing the protoplanetary paradigm. *Science*, 336, 684-686.
- RUSSELL, R. P. & LARA, M. 2007. Long-lifetime lunar repeat ground track orbits. *Journal of Guidance, Control, and Dynamics*, 30, 982-993.
- RUSSELL, R. P. & LARA, M. 2009. On the design of an Enceladus science orbit. *Acta Astronautica*, 65, 27-39.
- SAN-JUAN, J. F., ABAD, A., LARA, M. & SCHEERES, D. J. 2004. First-order analytical solution for spacecraft motion about (433) Eros. *Journal of Guidance, Control, and Dynamics*, 27, 290-293.
- SCHEERES, D. 1994. Dynamics about uniformly rotating triaxial ellipsoids: Applications to asteroids. *Icarus*, 110, 225-238.
- SCHEERES, D. 2002. Stability of Binary Asteroids. *Icarus*, 159, 271-283.
- SCHEERES, D. 2006. Relative Equilibria for General Gravity Fields in the Sphere-Restricted Full 2-Body Problem. *Celestial Mechanics and Dynamical Astronomy*, 94, 317-349.
- SCHEERES, D. 2007. Rotational fission of contact binary asteroids. *Icarus*, 189, 370-385.
- SCHEERES, D. 2012. *Orbital Motion in Strongly Perturbed Environments*, Springer.
- SCHEERES, D., BROSCART, S., OSTRO, S. & BENNER, L. 2004. The dynamical environment about Asteroid 25143 Itokawa: target of the Hayabusa Mission. *AIAA/AAS Astrodynamics Specialist Conference and Exhibit*.
- SCHEERES, D. & MARZARI, F. 2002. Spacecraft Dynamics in the Vicinity of a Comet. *Journal of the Astronautical Sciences*, 50, 35-52.
- SCHEERES, D., MILLER, J. & YEOMANS, D. 2003. The orbital dynamics environment of 433 Eros: A case study for future asteroid missions. *InterPlanetary Network Progress Report*, 42, 1-26.
- SCHEERES, D., OSTRO, S., HUDSON, R. & WERNER, R. 1996. Orbits close to asteroid 4769 Castalia. *Icarus*, 121, 67-87.
- SCHEERES, D., OSTRO, S. J., HUDSON, R., DEJONG, E. M. & SUZUKI, S. 1998. Dynamics of orbits close to asteroid 4179 Toutatis. *Icarus*, 132, 53-79.
- SCHEERES, D., WILLIAMS, B. & MILLER, J. 2000. Evaluation of the dynamic environment of an asteroid: Applications to 433 Eros. *Journal of Guidance, Control, and Dynamics*, 23, 466-475.
- SCHEERES, D. J., FAHNESTOCK, E. G., OSTRO, S. J., MARGOT, J.-L., BENNER, L. A., BROSCART, S. B., BELLEROSE, J., GIORGINI, J. D., NOLAN, M. C. & MAGRI, C. 2006. Dynamical configuration of binary near-Earth asteroid (66391) 1999 KW4. *Science*, 314, 1280-1283.

- SIERKS, H., BARBIERI, C., LAMY, P. L., RODRIGO, R., KOSCHNY, D., RICKMAN, H., KELLER, H. U., AGARWAL, J., A'HEARN, M. F., ANGRILLI, F., AUGER, A.-T., BARUCCI, M. A., BERTAUX, J.-L., BERTINI, I., BESSE, S., BODEWITS, D., CAPANNA, C., CREMONESE, G., DA DEPPO, V., DAVIDSSON, B., DEBEL, S., DE CECCO, M., FERRI, F., FORNASIER, S., FULLE, M., GASKELL, R., GIACOMINI, L., GROUSSIN, O., GUTIERREZ-MARQUES, P., GUTIÉRREZ, P. J., GÜTTLER, C., HOEKZEMA, N., HVIID, S. F., IP, W.-H., JORDA, L., KNOLLENBERG, J., KOVACS, G., KRAMM, J. R., KÜHRT, E., KÜPPERS, M., LA FORGIA, F., LARA, L. M., LAZZARIN, M., LEYRAT, C., LOPEZ MORENO, J. J., MAGRIN, S., MARCHI, S., MARZARI, F., MASSIRONI, M., MICHALIK, H., MOISSEL, R., MOTTOLA, S., NALETTO, G., OKLAY, N., PAJOLA, M., PERTILE, M., PREUSKER, F., SABAU, L., SCHOLTEN, F., SNODGRASS, C., THOMAS, N., TUBIANA, C., VINCENT, J.-B., WENZEL, K.-P., ZACCARIOTTO, M. & PÄTZOLD, M. 2015. On the nucleus structure and activity of comet 67P/Churyumov-Gerasimenko. *Science*, 347.
- SKOKOS, C. 2010. The Lyapunov characteristic exponents and their computation. *Dynamics of Small Solar System Bodies and Exoplanets*. Springer.
- SLOTINE, J.-J. E. & LI, W. 1991. *Applied nonlinear control*, New Jersey, Prentice-Hall.
- SZEBEHELY, V. 1967. *Theory of orbits: the restricted three body problem*, Academic Press San Diego.
- TAKEUCHI, T. 2009. Small Bodies in Planetary Systems. *Lecture Notes in Physics*, 758, 1.
- TRICARICO, P. & SYKES, M. V. 2010. The dynamical environment of Dawn at Vesta. *Planetary and Space Science*, 58, 1516-1525.
- TZIRTI, S., TSIGANIS, K. & VARVOGLIS, H. 2010. Effect of 3rd-degree gravity harmonics and Earth perturbations on lunar artificial satellite orbits. *Celestial Mechanics and Dynamical Astronomy*, 108, 389-404.
- TZIRTI, S. & VARVOGLIS, H. 2014. *Motion of an Artificial Satellite around an Asymmetric, Rotating Celestial Body: Applications to the Solar System*. PhD dissertation, Aristotle University of Thessaloniki.
- VASILKOVA, O. 2005. Three-dimensional periodic motion in the vicinity of the equilibrium points of an asteroid. *Astronomy & Astrophysics*, 430, 713-723.
- VEVERKA, J., ROBINSON, M., THOMAS, P., MURCHIE, S., BELL, J., IZENBERG, N., CHAPMAN, C., HARCH, A., BELL, M. & CARCICH, B. 2000. NEAR at Eros: Imaging and spectral results. *Science*, 289, 2088-2097.
- WAKKER, K. 2010. Fundamentals of Astrodynamics. *Lecture Notes*. The Netherlands: Delft University of Technology.
- WERNER, R. A. 1994. The gravitational potential of a homogeneous polyhedron or don't cut corners. *Celestial Mechanics and Dynamical Astronomy*, 59, 253-278.
- WERNER, R. A. 1997. Spherical harmonic coefficients for the potential of a constant-density polyhedron. *Computers & Geosciences*, 23, 1071-1077.
- WERNER, R. A. & SCHEERES, D. J. 1997. Exterior gravitation of a polyhedron derived and compared with harmonic and mascon gravitation representations of asteroid 4769 Castalia. *Celestial Mechanics and Dynamical Astronomy*, 65, 313-344.
- WHITELEY, R. J., THOLEN, D. J. & HERGENROTHER, C. W. 2002. Lightcurve analysis of four new monolithic fast-rotating asteroids. *Icarus*, 157, 139-154.
- WIGGINS, S. 2003. *Introduction to applied nonlinear dynamical systems and chaos*, Springer Science & Business Media.
- WIGGINS, S. 2013. *Global bifurcations and chaos: analytical methods*, Springer Science & Business Media.

## References

- WOO, P., MISRA, A. & KESHMIRI, M. 2013. On the planar motion in the full two-body problem with inertial symmetry. *Celestial Mechanics and Dynamical Astronomy*, 117, 263-277.
- YONGLIAO, Z., WEI, L. & ZIYUAN, O. 2014. China's Deep-space Exploration to 2030. *Chinese Journal of Space Science*, 34, 516-517.
- YU, Y. & BAOYIN, H. 2012a. Generating families of 3D periodic orbits about asteroids. *Monthly Notices of the Royal Astronomical Society*, 427, 872-881.
- YU, Y. & BAOYIN, H. 2012b. Orbital dynamics in the vicinity of asteroid 216 Kleopatra. *The Astronomical Journal*, 143, 62.
- ZHAO, Y., JI, J., HUANG, J., HU, S., HOU, X., LI, Y. & IP, W.-H. 2015. Orientation and rotational parameters of asteroid 4179 Toutatis: new insights from Chang'e-2's close flyby. *Monthly Notices of the Royal Astronomical Society*, 450, 3620-3632.

# Curriculum Vitae

Jinglang Feng was born in Henan, China, on May 5, 1987. From 2005 to 2008, she studied at the Honoring College of Northwestern Polytechnical University (NWPU), Xi'an, China, for successive undergraduate and graduate programs for selected students. After finishing three years study about a wide range of fundamental courses and primary research training, she got the freedom to choose any major in NWPU. From 2008 to 2011, she studied at the School of Astronautics for her Master degree. She conducted her master thesis about perturbation analysis on orbits of lunar spacecraft. In 2011, she joined the Astrodynamics and Space Missions group at the Faculty of Aerospace Engineering, Delft University of Technology, The Netherlands, as a PhD candidate.

During her PhD, she focused on research about orbital dynamics around contact binary asteroid systems. A systematic study on the dynamical environment around such kind of bodies was performed, which led to the preparation of this dissertation. Her research interests also include celestial mechanics and solar system dynamics. She also served as reviewer for the scientific journal *Planetary and Space Science*.



# List of Author's Publications

## Journal Articles

Feng, J., Noomen, R., Visser, P. N., & Yuan, J. (2015). Modeling and analysis of periodic orbits around a contact binary asteroid. *Astrophysics and Space Science*, 357(2), 1-18.

Feng, J., Noomen, R., & Yuan, J. (2015). Orbital Motion in the vicinity of the non-collinear equilibrium points of a contact binary asteroid. *Planetary and Space science*, 117, 1-14.

Feng, J., Noomen, R., Visser, P. N., & Yuan, J. (2016). Numerical analysis of orbital motion around a contact binary asteroid system. *Advances in Space Research* (accepted).

Feng, J., Noomen, R., Hou, X., Visser, P. N., & Yuan, J. (2016). 1:1 Ground-track resonance in a uniformly rotating 4<sup>th</sup> degree and order gravitational field. *Celestial Mechanics and Dynamical Astronomy* (submitted).

## Conference Papers

Feng, J., Noomen, R., Ambrosius, B. A. C., & Yuan, J. (2013). Orbital Dynamics in the Vicinity of Contact Binary Asteroids. *International Astronautical Conference*, Beijing, IAC-13-C1.9.4x18311.

Feng, J., Noomen, R., Ambrosius, B. A. C., & Yuan, J. (2014). Third-order Analytical Solutions around Non-collinear Equilibrium Points of a Contact Binary Asteroid. *AIAA/AAS Astrodynamics Specialist Conference*, 4-7 August 2014, San Diego, CA.

